2016

Fabrication of high quality periodic structures through convective assembly procedures

Midhun Joy
Lehigh University

Fabrication of high quality periodic structures through convective assembly procedures

by

Midhun Joy

Presented to the Graduate and Research Committee
of Lehigh University
in Candidacy for the Degree of
Doctor of Philosophy
in
Chemical Engineering

Lehigh University
September 2016

Certificate of Approval

Approved and recommended for acceptance as a dissertation in partial fulfillment of the requirements of the degree of Doctor of philosophy.

_____

Date

_____ _____

James F. Gilchrist, *Ph.D.*
Dissertation advisor

Mark A. Snyder, *Ph.D.*
Dissertation advisor

_____

Accepted date

Committee Members:

_____

James F. Gilchrist, *Ph.D.*
Committee chair

_____

Mark A. Snyder, *Ph.D.*
Committee member

_____

Martin P. Harmer, *Ph.D.*
Committee member

_____

Hugo S. Caram, *Ph.D.*
Committee member

Acknowledgements

Today, when I finish five years of my PhD life, I am really thankful to some great people I have come across in my life for their inspiration, guidance, support and help without which this dissertation would not have been possible. No words of acknowledgment would be sufficient to express my gratitude towards my advisors, colleagues, friends and family for devoting their time and energy, inspiring me to be successful as a researcher.

I am immensely grateful to my advisors Prof. James F. Gilchrist and Prof. Mark A. Snyder for mentoring me throughout the past five years as a doctoral student- both as research advisors who would always guide me in my research and also as friends with whom I could confide my personal struggles. I am deeply indebted to my advisors for taking me as a group member in spite of the lack of any experimental background and constantly motivating me when I encountered several obstacles during my research years. The bulk of my dissertation would not have been possible, if not for my advisors who inspired me to explore uncharted territories and perform detailed studies when I came across certain unexpected observations during the course of my experiments. Thank you Professors for your patience with me, for your guiding and supporting hands, for inspiring me to take up challenges, teaching me to be systematic as a researcher and persuading me to have belief and confidence in my capabilities.

I would like to express my sincere gratitude to the members of my dissertation committee- Prof. Hugo S. Caram and Prof. Martin A. Harmer for their valuable suggestions and insights regarding the research work. Also, the discussions on crystallography and crystal defects which I had with Prof. Chris Kiely deserves special acknowledgement,

without which I would not have been able to gain a mechanistic understanding of the periodic patterns reported in the dissertation – the discussions enabled a theoretical analysis as well as model building tasks which replicated the observed patterns. Also, I would like to express my gratitude to the faculty at the department of chemical engineering at Lehigh University who taught me various courses during the span of my PhD research. Moreover, my PhD research at Lehigh University would not have been possible, but for the funding I received from various sources during the course of my studies. I would like to acknowledge the research funding received from Lehigh University (Gotshall Research Fellowship) as well as the funding from NSF, Power Optics LLC, Pennsylvania Nanomaterials Commercialization Center and CBET: Energy for Sustainability.

I am equally indebted to my lab mates in both Prof. Gilchrist's lab as well as Prof. Snyder's lab who made me feel at ease when I joined the lab and have been an unrelenting source of guidance and help since then. I am greatly thankful for the guidance I received from Pisist Kumnorkaew (Pao) who patiently taught me even the basics of doing experiments, never losing his temper in spite of several chemical spills and innumerable experiments which went awry, teaching me to perform experiments in an efficient, focused and systematic manner. I would also like to thank my other lab mates, namely, Dr. Daniels for his suggestions regarding particles and for allowing me to use the chemicals and instruments of EPI lab, Alex, Zheng, Bonny & Cooper for their training on various lab instruments and particle synthesis, Erg for training me to use SEM and his valuable help and suggestions regarding the vibration-assisted convective deposition project and Tharanga who trained me on using the confocal microscope. Also valuable is the research

guidance and help I have received from Dan, Minseok, Kedar, Naval and Megha, who were always willing to spare their time to help me out in my projects.

Also, thanks to John Caffrey who developed the designs for various experimental set-ups and fabricated them, William Mushock (Bill) who was always happy to help with whatever issues I had with SEM. I would also like to thank the professors and students who allowed me to use their instruments and trained me on them- Prof. Manoj Choudhary, Partho and Aditi for their help with contact angle measurements and high speed imaging, Prof. Anand Jagota and Dadhichi Paretkar for profilometer and spin coating instruments, Prof. Xuanhong Chengand Krissada (Chai) for plasma-based surface treatment, Prof. Nelson Tansu and Wei Sun for the use of farfield measurement setups and RamaraoVemula for resolving instrumentation issues with various setups. Thanks are also due to my classmates and staff in the department, especially Barbara, Tracey and Janine who were always willing to help me out whenever I was in need.

My life as a graduate student at Lehigh would not have been the same if not for my friends who gave me several memories of fun and excitement outside my research life – Rinosh, Ashwin, Abhinay, Antony, Rahul, Vivek, Anoop, Avinash, Prasad, Hari..just to mention a few in the long list of my friends who took turns to teach me driving and to take me for shopping and other outdoor activities. My friends outside Lehigh University also deserve a special mention for devoting their time and resources for me. I am not sure if I could ever thank properly Sr. Clare and Sr. Clarice for all that they have done for me, giving me a home away from home in the U.S and being ever ready to help me out in my life- the innumerable dinners prepared for me as well as for the several dozens of gifts on all occasions of my life. Also deserving special mention is Mr. Linson and family as well

as Prisca Vidanage for the several rides, whenever in need. On this occasion, I would also like to thank Prof. Niket Kaisare, who being my advisor during Masters program motivated me to do PhD and was instrumental in my applying for and gaining admission at Lehigh University. Thank you all.

It also gives me immense pleasure to thank my family for all that they have done for me. My parents, who always loved me and strived to provide the best for me as well as my brothers Jithin and Nidhin who have given me uncountable childhood memories. I would also like to mention my wife, Grace who entered into my life as a partner-for-life during the last semester of my PhD program and has been a great source of love, inspiration and support since then. Equally loving and caring have been my in-laws, especially my close friend and brother-in-law Roger. Above all, I would like to acknowledge the bountiful blessings I have received from Almighty God, who has made His presence, love and power felt throughout my life through several instances which I had often passed over to just being lucky or a mere coincidence.

To my advisors, colleagues, friends and my family – I thank you all from the bottom of my heart.

Midhun Joy

Table of Contents

List of tables

List of figures

Abstract

Techniques aimed at scalable realization of periodic structures from self-assembly of constituent building blocks, an approach that could supplant microfabrication procedures, are often constrained by the lack of diversity in packing arrangements achievable with assembly of simple constituents (e.g., spherical particles). In this work, we present a strategy to effectively pattern colloidal crystalline assemblies at two characteristic scales; achieving extensive non-classical particle packing amidst fully periodic, banded structural defects. We first introduce a scalable and robust approach to fabricate non-hexagonal crystals comprised of mono-sized spherical particles through introduction of periodically oscillating flow-fields during convective particle deposition. Through this technique, we report the discovery of extensive and tunable square-packed arrangements of monosized particles i.e., (100) fcc facets oriented parallel to the underlying substrate in self-assembled colloidal structures. Besides forming large (100) fcc crystalline domains with relatively few defects, the process also results in colloidal crystals having negligible variation in thickness while simultaneously yielding controlled proportions of both hexagonal and square-packed arrangements. The formation of domains of (100) fcc symmetry structures as a result of added vibration is robust across a range of micron-scale monosized spherical colloidal suspensions (e.g., polystyrene, silica) as well as substrate surface chemistries (e.g., hydrophobic, hydrophilic). In-situ visualization during self-assembly process as well as colloidal-crystal fabrication realized at varying frequency and amplitudes of vibration gives clues toward the mechanism of this flow-driven self-assembly method.

In the second part of the work, we explore the introduction of volume defects in the uniformly-packed particle assemblies. Here, unlike randomly generated defects in packing structures, we demonstrate the formation of continuous, periodic banded defects comprised of particles with an fcc (110) packing configuration, and with tunable band periodicity. Studies aimed at discerning the specific effects of vibration conditions and meniscus properties help establish a mechanistic picture of the formation of fcc (110) banded structures based on stress relaxation in crystals through generation and movement of dislocations. The final chapters of the dissertation discuss how the convective assembly techniques could be efficiently used towards fabricating various devices for energy conversion and storage.

The dissertation has been organized as follows:

Chapter 1 of the dissertation provides an introduction to the self-assembly techniques, with primary focus on the characteristics and an in-depth analysis of the convective assembly technique. The fundamentals of the technique as well as various inherent process conditions are discussed, along with the characteristics of the colloidal crystal assemblies thus obtained. The chapter further sheds an insight into the limitations of the technique with regards to the limited structural diversity and quality considerations of the obtained crystal.

Chapter 2 of the research dissertation demonstrates the fabrication of colloidal crystals with a square packing arrangement which corresponds to the (100) face of an fcc crystal oriented parallel to the substrate. The technique derives its motivation from the use of vibration-aided convective assembly techniques, which was previously investigated in the

group. The chapter outlines the fabrication methodology as well as the analysis routines for investigating the properties of the assembled structures. Various potential uses of these structures have also been outlined in the chapter.

Chapter 3 strives to gain a mechanistic understanding of the self-assembled square packed crystals. Various experiments were designed and implemented for a detailed understanding of the observed structures, the objective behind the study being the potential to extend the convective assembly technique to yield further diversity in structural arrangements. Investigation of the mechanism relied on a systematic analysis of the assembled structures with varying proportions of square and hexagonally packed regions as well as the in-situ confocal experiments performed at the experimental conditions to simulate a similar growth environment.

In **Chapter 4** of the dissertation, we report the observation of periodic volume defects in square-packed crystals, an observation which has high potential to develop optical waveguides. The chapter provides an in-depth analysis of these defects and the factors which determine the frequency and extent of these defects in the square-packing regions. Various analysis routines were developed to quantify the defects in the sample and to characterize them. The chapter also details a mechanistic understanding behind the nucleation and propagation of these defectors based on stress-relaxation in crystals.

Chapter 5 of the report deals with incorporating the convective assembly techniques towards device fabrication, the emphasis of the work being on Dye sensitized solar cells (DSSC). The chapter provides a brief outline of the working principle of DSSC and its various components, which demands an individual as well as combined optimization for enhancement of the overall device performance. The chapter investigates the incorporation

of convex and concave micro lens structures in DSSC and the resulting variation in the photon path of incident radiation. Studies were also performed to investigate and identify a suitable architecture for scaling up the DSSC technology for commercial applications.

Chapter 6 of the dissertation reports the work performed in designing semi-conductor oxide membranes for high temperature applications in thermal batteries. The work outlines various methodologies which were adopted to fabricate these porous structures, varying from stabilization of magnesium oxide nanoparticles in aqueous solution and subsequent infiltration into the pore spaces of the colloidal crystal assembly as well as in-situ fabrication technique involving suitable precursor salt. The limitations of the structures thus obtained for membrane applications are discussed as well as possible methods to overcome them for commercial applications.

1

Introduction

The current focus on device miniaturization and performance optimization for applications involving microelectronics, optics, information technology etc. demands atypical fabrication approaches, which could yield functional materials with precise desired properties. Moreover, deriving optimal performance from a device prerequisite that the inherent structure of various functional components is fabricated to the desired specifications, with high precision and minimal defects. One of the key features which differentiates these advanced functional materials from their conventional counterparts is the presence of highly periodic structures which imparts its observed physical, chemical, magnetic and optical properties, thereby placing a significant emphasis on devising suitable fabrication procedures for its production. In addition to the requirements of precision, cost, tunability and reproducibility, the selection of a suitable technology also demands an ability to scale it up from laboratory set up to industrial scale, without loss of quality of the generated structures.

1.1 Self-assembly procedures for advanced functional materials

Self-assembly refers to the spontaneous assembly of individual building blocks into ordered structures over extended length scales as a result of the interactions between the building blocks. The individual building blocks in self-assembly processes can vary in size from molecules, molecular clusters, polymeric particles as well as polymeric clusters, and with time scales of assembly varying from couple of minutes to several days. The self-assembly processes which can be widely observed in nature in the formation of molecular clusters, globular proteins as well as living cells[1] are responsible for the formation, evolution and subsistence of living organisms. The molecular self-assembly processes in nature occurs spontaneously under the influence of non-covalent and weakly covalent interactions like Vander Waals forces, electrostatic interactions, hydrogen bonding etc. with the resulting structures being driven by thermodynamic considerations. Furthermore, these self-assembly processes could be utilized in generating structures with precise order and functionalization for robust engineering applications involving microelectronics, sensors, biological systems as well as high performance information storage and transmission devices.

"Spontaneous" self-assembly processes, although tenable for fabricating several periodic structures, are of limited usability to obtain functional materials owing to long characteristic time scales involved and limited interaction-forces between the constituent particles. Hence, obtaining assemblies for device fabrication demands a careful modulation of the interaction between the building blocks involved, commonly referred to as "directed" self-assembly techniques. This can be achieved either by modification and control of the intrinsic interactions between the constituent particle through a pre-designed control of its

surface and volume properties like shape, surface potential, surface functionalization with specific functional groups or DNA molecules, or by assembly performed under the influence of an external environment to generate a wide variety of non-equilibrium structures. The choice of external forces in the latter procedure depends on the nature of building blocks involved as well as the final desired structure and may involve either templated surfaces or external fields like electric fields, magnetic fields, flow fields, capillary forces, gravitational fields or a combination of several forces.

The directed self-assembly techniques[2] offers a less-expensive, more robust and faster alternative as a bottom-up technique in comparison to the top-down approaches currently used to obtain functional materials with desired properties, the currently established one being lithography based microfabrication techniques using a high-energy electron beam[3] , x-rays[4] or lasers[5]. The lithographic procedures are based on the removal of certain regions of the substrate along well-defined patterns, the resulting voids being filled later with suitable refractive index materials. The accuracy of the lithographic procedures are however limited to almost four lattice depths[3,6], which hinders its application for thicker photonic crystals. Another microfabrication procedure commonly employed for photonic-crystal fabrication uses laser halographic technique on a photoresist substrate, in which certain regions of the photoresist are rendered insoluble using interference patterns generated using multiple laser beams[7,8], The required lattice patterns can be obtained on the photoresist by varying the intensities and polarization vectors of the laser beams resulting in various interference patterns[7]. The limitation of this approach for large-scale fabrication of photonic crystals arises from the spherical aberration effects due to refractive-index mismatch at the air-photoresist interface[9], which

needs to be compensated using additional prisms[8] or liquid-crystal based spatial light modulator[9]. Nevertheless, these procedures remain prohibitively expensive for commercial fabrication of photonic crystals due to the procedures involved.

The phenomenon of self-assembly of particles offers a versatile and convenient technique to modulate the structural, surface, optical and electronic properties of various materials. This technique derives its prominence over micro-fabrication techniques with its scalability, cheaper materials and processes involved and its versatility for a wide range of processes and materials. The versatility of this technique is further supported by the fact that the self-assembly processes are massively parallel, involving several million particles undergoing assembly at any instant of time. While lithography based fabrication procedures are two-dimensional in nature, the self-assembly processes are multi-dimensional, in addition to yielding features with a much higher resolution than that could be achieved even with the best state-of-art lithographic procedure.

1.2 Colloidal crystal structures through self-assembly procedures

Colloidal crystals refer to a periodic arrangement of particles uniformly dispersed in a solution to generate two-dimensional or three-dimensional uniform structures, with the constituent particles varying in size from a couple of nanometers to micrometer scale. Analogous to the packing of atoms in atomic crystals, these colloidal crystal assemblies can be widely observed in nature in opals as well as iridescent colors observed in insects and birds. While the former is a colloidal assembly of monosized silica particles, the iridescence arises due to the same order of magnitude of the periodicity of the inherent structures as the wavelength of visible light, thereby giving rise to Bragg diffraction of

visible light wavelengths from various colloidal crystal planes. The properties of colloidal crystal can be suitably modulated by varying the properties of individual particles as well as the structural assembly, yielding periodic arrangements which has its application as chemical sensors, photonic materials, data transmission devices as well as optical applications. In addition, they provide a useful tool to investigate the fundamental processes associated with crystal growth. In comparison to its counterpart atomic crystals, the building blocks of colloidal crystals are an order of magnitude larger (nanometer to micrometer scale) compared to atoms (angstrom scale). This leads to a corresponding order of magnitude reduction in the characteristic time associated with the processes responsible for the formation of these structures, making it possible to observe and investigate them – thus making these colloidal crystal assemblies suitable candidates as model systems for studying atomic crystals.

The engineering of atomic packing in colloidal crystal materials offers a versatile tool for altering the physical, chemical, electronic and optical properties of materials, and has received further impetus with the invention of photonic crystals[10,11]. Photonic crystals, commonly referred to as 'semiconductors of light'[12] possess a periodic three-dimensional architecture with respect to the variation in dielectric constant in their structure, with the periodicity comparable to the wavelength of light. This makes it a useful tool in optical and photonic applications for modulating the characteristics of incident light radiations by virtue of its photonic band gap (PBG), the range of frequencies of the incident light, the propagation of which through the structure is blocked by the crystal in all directions. The photonic crystals are employed in optical devices like LEDs for enhanced light extraction[13], improved light absorption in photovoltaic cells[14], manipulation of laser light[15] and photonic

crystal fibers[16] for data-transmission, data- storage and medical devices. The photonic properties of this colloidal crystal assembly of particles can be tuned to obtain various PBGs by varying the lattice parameter, void fraction of the periodic structures, refractive indices of the materials involved or by obtaining new structures by infiltration of the void space with a suitable precursor salt yielding an inverse-opal structure[17].

The colloidal crystals are characterized based by the properties of individual particles generating the structure, their number of layers, packing arrangement of constituent particles within the crystal and uniformity of the dominant packing configuration over extended length scales, each of which plays a dominant role in determining the final properties of the overall crystal. An ideal colloidal crystal assembly corresponds to a uniform implementation of the desired packing configuration over the entire region of assembly, with minimal defects within the region of interest, and involving time scales suited for commercial scale utilization of the technology.

(a)

(b)

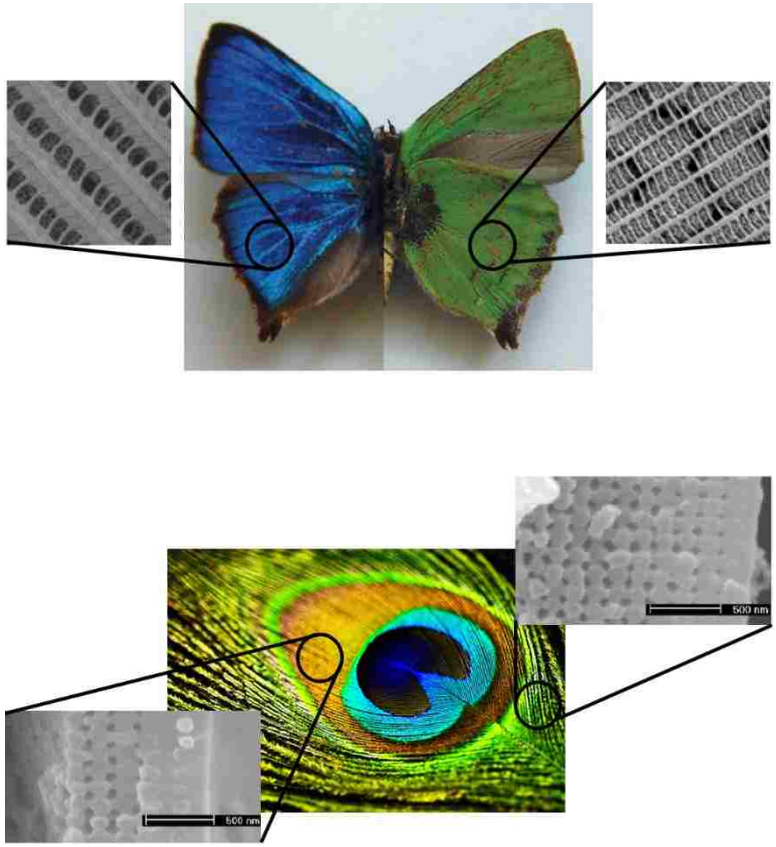

(c)

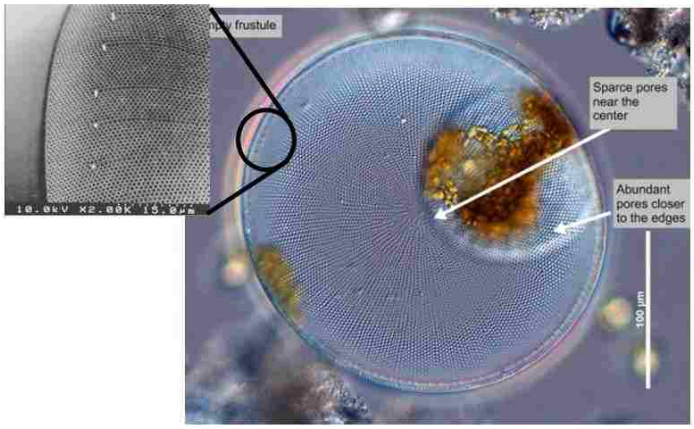

Figure 1.1: Photonic crystals in nature (a) Iridescence patterns from wings of a male butterfly of *C. remus* with left hand image showing the back side and right image displaying the front side of the wing[18] (b) Structural colors observed and high magnification images of the green and brown barbules[19] of a peacock feather (image adapted from *http://animalworld.tumblr.com/post/5162595961/peacock-feather-interference-bragg*) (c) High resolution image of the silica wall[20] of diatom *Coscinodiscus granii* (diatom image adapted from *https://www.eoas.ubc.ca/research/phytoplankton/diatoms/centric/coscinodiscus/c_granii.html/*)

Various methods have been proposed, investigated and optimized for the fabrication of uniform colloidal crystal assemblies, employing various driving forces, generating uniform crystals over a time span varying from couple of seconds to several days. In addition to uniform and continuous colloidal crystals, these procedures can also be used to develop coatings with unique features like periodic bands[21], stripes or streaks. The current methods for colloidal crystal fabrication utilizes gravitational, shearing[22–24], capillary[25,26] as well as electro/magnetic[27–29] forces with procedures which include, but are not limited to sedimentation, solvent evaporation, electrophoretic deposition, spin coating, shear alignment and convective assembly techniques. Although these techniques yield uniform crystal assemblies in laboratory scale experiments, their potential for scale-up for commercial applications remains limited due to the lack of control over the number of layers, complex fabrication procedures with limited scale-up capabilities and inability to maintain uniform packing arrangement over large areas of the substrate.

Two currently established procedures which can inexpensively yield colloidal crystals over large areas in a continuous fashion is sedimentation and convective deposition techniques. The sedimentation processes, although inexpensive and highly scalable, suffers from the limitation of large time scales involved and insufficient control over the number of layers, the former limitation overcome to a certain extent by employing a positive pressure and solution being continuously sonicated. In comparison, the convective assembly based techniques can yield roll-to-roll coatings of uniform crystal assemblies with a high control over the number of layers.

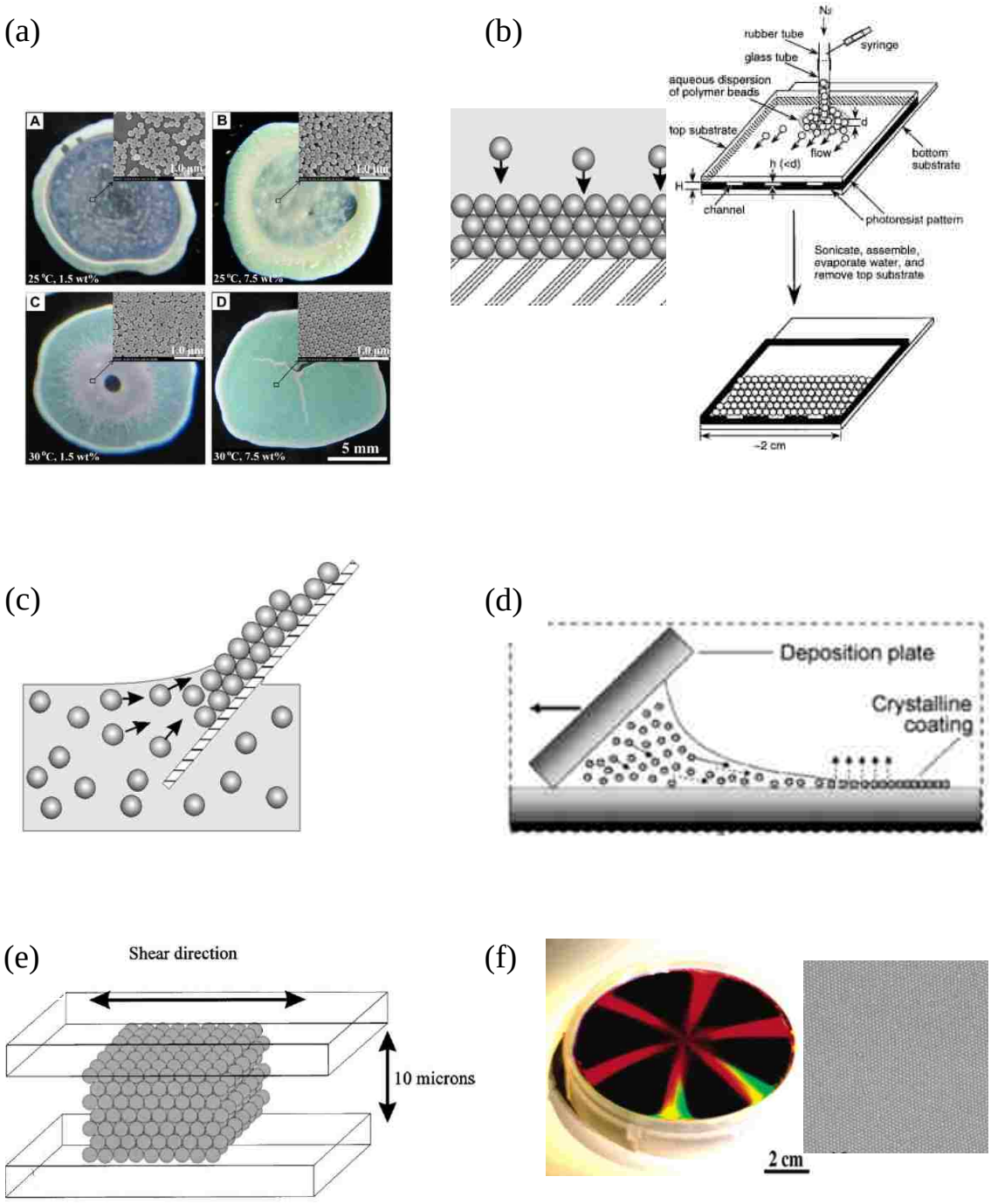

Figure 1.2: Fabrication of colloidal crystals through directed self-assembly procedures (a) Colloidal assembly generated by drop drying on a suitable substrate[30] (b) Gravitational settling of colloidal crystal, enhanced by positive pressure and sonication[31] (c) Dip coating process for colloidal crystal fabrication (d) Convective assembly procedure involving horizontal dragging of thin film over the substrate[26] (e) Shear alignment technique utilizing an oscillating parallel plate geometry[23] and (f) Spin coating technique to generate 3D ordered nanocomposite film on a silicon wafer[32]. (Figures shown were adapted from the corresponding references)

1.3 Convective self-assembly of particles into colloidal crystals

The fabrication of uniformly thick colloidal crystals can be successfully achieved using convective deposition procedures[21,33,34], the inter-particle forces coupled with the hydrodynamic interactions between the solvent and the colloidal particles resulting in the crystallization of particles in the suspension into a long-range ordered crystalline arrangement. The process, which involves an interplay of convective flux of colloidal particles towards the drying front and capillary forces between the particles, has been demonstrated to be successful in generating colloidal crystal films with high degree of control over the number of constituting layers. The self-assembly of mono-sized particles into ordered aggregates always results in a close-packed arrangement, with varying preference for the formation of a hexagonally close-packed structure (hcp) or a face-centered cubic structure (fcc) with a change in the number of layers[35–37].

1.3.1 Background of conventional convective self-assembly processes

The experimental setup for a conventional convective self-assembly procedure is given in Figure 1.3 along with a representative sketch of the thin film generated by the deposition blade.

The convective assembly processes for colloidal crystal fabrication involves horizontally dragging a liquid meniscus of the desired colloidal suspension confined within an inclined restraining surface (deposition blade) over the desired flat medium (substrate). The linear translation of the meniscus with respect to the substrate is achieved using a stage connected to a linear motor and can be set to the desired speed to modulate the number of layers in the crystal assembly. The thin liquid film resulting from this set-up tapers down

with a definite curvature to the substrate, creating a straight three-phase contact line on the substrate. The assembly of particles dispersed in a uniform suspension into an ordered film in convective deposition technique occurs by a combination of "Coffee –ring effect[38]" and "cheerio effect[39]", the former referring to the evaporation driven flux of particles towards the three phase contact line of the suspension meniscus and the latter referring to the interaction between particles confined within the thin film region. The horizontal dragging of liquid meniscus across the substrate generates a trailing thin film region bordered by the three-phase contact line, maintained as a straight line by the shape of the deposition blade. The evaporation of solvent from the thin film generates a convective flux of particles towards the substrate-liquid-air contact line. Once the particles are confined within the thin film region, inter-particle attraction leads to a deflection of the thin film meniscus, generating capillary forces which tries to pack the particles into a configuration with minimized surface energy. This results in a particle assembly with a close packed configuration, observed as a hexagonal packing structure in the case of two-dimensional particle assemblies.

The formation of monolayer colloidal crystals by convective self-assembly can be described using the Nagayama equation[33] to obtain the optimal meniscus withdrawal velocity (v_w) as :

$$v_w = v_c = \frac{\beta l J_E \varphi}{h(1-\epsilon)(1-\varphi)}$$

The growth-rate of the colloidal crystal (v_c) with height (h) and porosity (ϵ) depends on solvent-particle interaction parameter (β), drying length (l), evaporation flux (J_E) and

particle volume fraction (φ). A simplification of the above equation for the formation of multilayered colloidal crystals by convective self-assembly yields:

$$v_w = v_c = \frac{\beta l J_E \, \varphi}{0.605 \, N \, d \, (1 - \varphi)}$$

with $'N'$representing the number of layers and composed of particles with diameter 'd'.

The capillary force interactions, however plays a less significant role in the formation of a multilayered colloidal assembly. The formation of a multilayered colloidal crystal structure in convective assembly procedures is characterized by a planar growth front at which the incoming particles are added and a drying front, beyond which the colloidal particles occupy a definite time-invariant lattice position in the crystal. The growth front for a multilayer crystal in convective assembly is shown to resemble a (311) fcc plane at an orientation of 100^{o} with respect to the substrate[40]. The region between the growth front and the drying front possesses a wet film of colloidal assembly in which the void spaces are saturated with the solvent. Evaporation of the solvent occurs through the multiple menisci generated between the particles of the surface layer in the wet film region, resulting in a flux of colloidal particles towards the growth front and directed into the voids in between the particles on the growth front by the "convective steering" mechanism. The particles which constitute the colloidal crystal thus acts as a scaffold for the incoming particles, the flow of which is regulated by the convective flux[40–43].

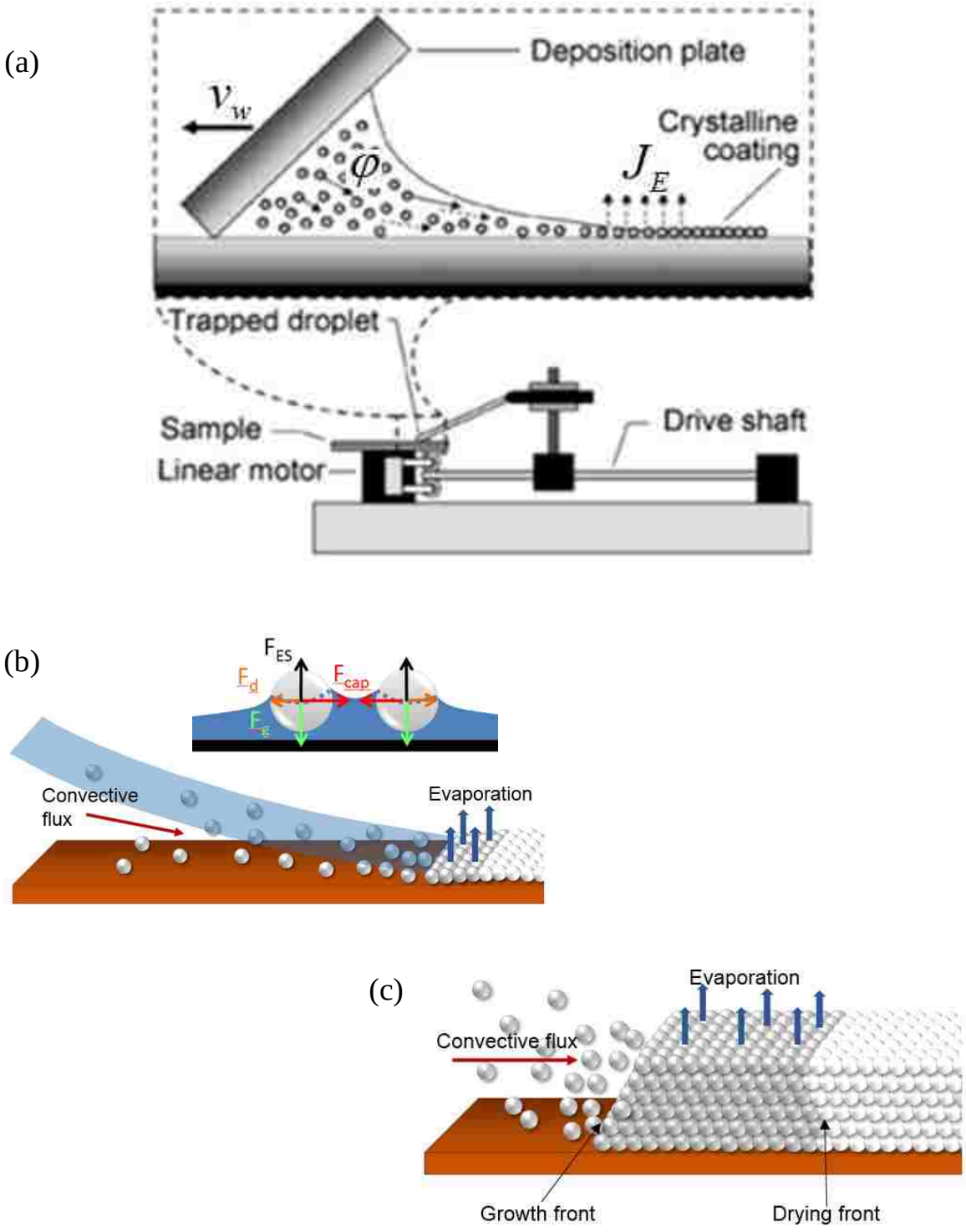

Figure 1.3: Convective deposition technique involving horizontal dragging of meniscus(a) Experimental set-up for convective self-assembly[26] (b) Monolayer assembly of colloidal particles by convective flux of particles towards the drying front with the inset figure showing the capillary forces acting on particles and (c) Multilayer assembly of colloidal particles by "convective steering" mechanism

1.3.2 Morphology of particle assemblies in convective deposition

The morphology of assemblies obtained by convective deposition techniques consists of close packed assembly of particles which corresponds to the densest packing configuration. These observed assemblies can be broadly classified into three types – sub monolayer, monolayer and multilayer, characterized using the parameters – surface coverage (ρ) and local-bond order (ψ), which is denoted as ψ_6 for hexagonal packing.

$$\rho = \frac{Area\ occupied\ by\ paricles}{Total\ area\ of\ surface} = \frac{N\ \frac{\pi d^2}{4}}{\frac{Void\ fraction}{A}}$$

$$\psi_{6,i} = \frac{1}{6}\sum_{k=1}^{6} e^{6\,i\,\theta_{kj}}$$

where N denotes the number of particles identified, d is the diameter of each particle and A is the total area of substrate. While ρ signifies the fractional area of the analyzed substrate which is covered with particles, ψ_6 denotes how close the analyzed packing is to an ideal hexagonal arrangement.

A 'monolayer' deposition is characterized by a uniform deposition of the particles in the colloidal suspension into a single-layered hexagonal arrangement on the surface of the substrate. These monolayer coatings are obtained at an optimal withdrawal velocity of the substrate, which corresponds to the crystallization velocity for a given concentration of the suspension, particle diameter and evaporation flux as described by Nagayama equation. An ideal monolayer is characterized by a complete particle coverage on the substrate (ρ =1) with perfectly crystalline packing configuration ($\psi_6 = 1$).

At withdrawal speeds higher than the crystallization velocities, "sub monolayer" coatings are formed on the substrate which contains incomplete particle coverage on the surface. These coatings are characterized by islands of particles, randomly distributed on the surface of the substrate, occurring either as isolated islands of couple of particles ($v_w \ll v_c$, 'random monolayers in Figure 1.4(a)) or as interconnected islands of several hundreds of particles ($v_w < v_c$, 'ordered monolayers' in Figure 1.4(a)). While the former is characterized by a predominantly string-like arrangement of particles, the larger islands have a localized hexagonal packing of particles within them. The formation of submonolayer regions can be attributed to the dewetting of the thin film from the surface[44], resulting from the absence of a continuous particle film on the surface which would pin the thin film meniscus to the substrate. At high withdrawal velocities, there is rupturing of the thin film due to evaporation and dewetting of the surface, confining particles to isolated islands on the substrate surface and generating close packed assemblies by capillary bridging.

Conversely, much lower withdrawal velocities results in multilayer assembly of particles. Although each individual domain has hexagonal packing arrangement of particles, the regions in which the thickness transition occurs are observed to have a square packing assembly, which can be observed as thin long stripes in the assembly. The formation of this non-hexagonal packing arrangement at transition regions is represented in Figure 1.4(b), the mechanism being attributed to the confinement of colloidal particles into the wedge-shaped volume between two hexagonal domains. This confinement effect can be utilized in the controlled generation of square packing, which would be discussed further in Chapter 2.

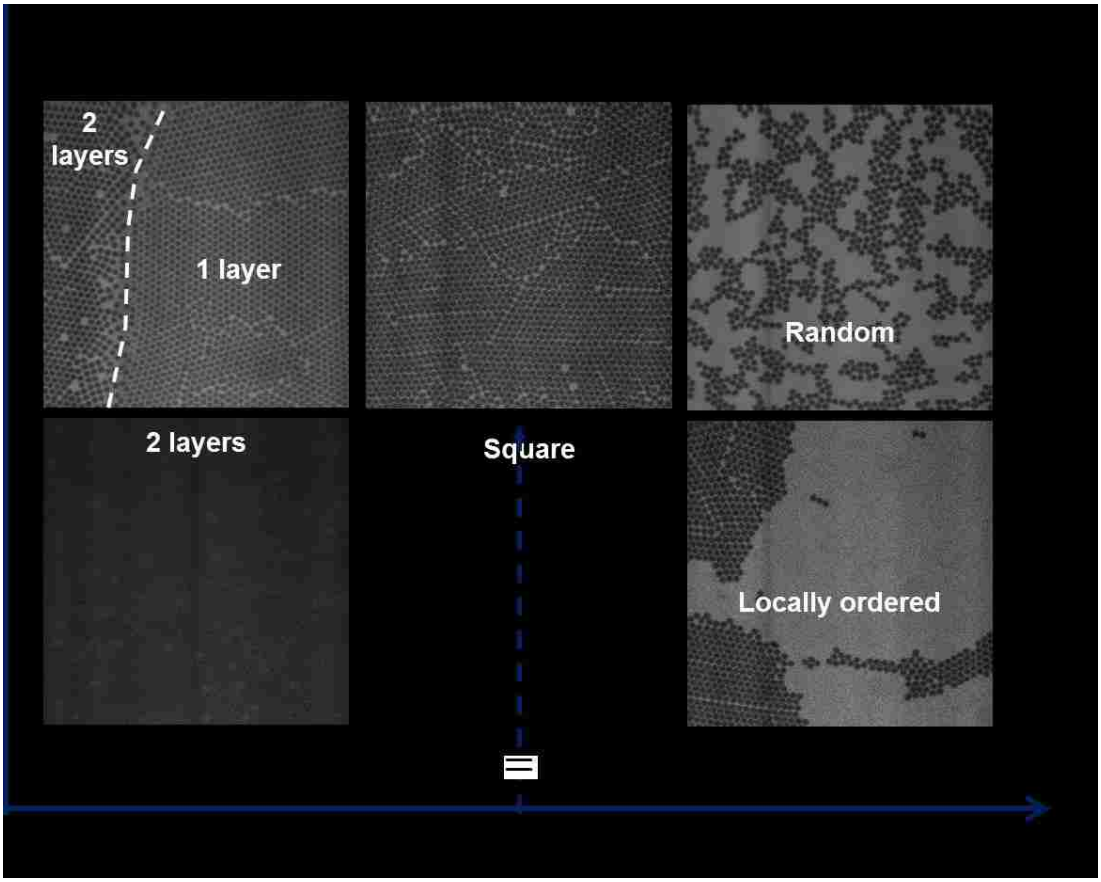

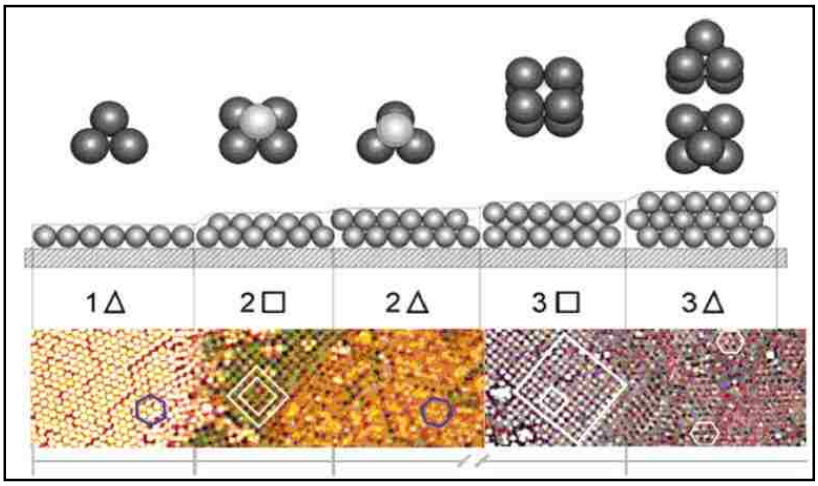

Figure 1.4: Morphology of particle assemblies obtained by convective deposition (a) Velocity-structure plot showing the formation of monolayer, submonolayer and multilayer at various withdrawal speeds with respect to crystallization velocity (superscript denoting the number of layers ie,1) (b) Formation of square-packing at transition regions in multilayer crystals[26] with the hexagonal packing and square arrangement in various regions denoted as (Δ) and (□) respectively. (Figure shown was adapted from the corresponding reference)

1.3.3 Limitations of Convective deposition techniques

The limitations of the convective deposition technique can be ascribed to the lack of robustness of the technique, quality of the particle assemblies and limited structural diversity obtained by the technique. As can be observed in Figure 1.4(a), a monolayer particle assembly can be obtained only when the withdrawal velocity of the meniscus is equal to the crystallization velocity. This demands a tuning of the procedure to identify the optimal withdrawal velocities, with a narrow window of the same for a suspension comprised of particles with a definite particle diameter, concentration and external conditions which determines the evaporation flux.

Another inherent limitation of the convective assembly procedure, which could be generalized for other self-assembly techniques as well, is the occurrence of varying fractions of both hexagonally close-packed structure (hcp) and face-centered cubic structure (fcc) stacking sequences[37] in the final close packed structure. Both hcp and fcc packing structures have a negligible difference of 0.005 RT/mole[45] in their free energy values which results in the final crystal to be composed of a combination of both hcp and fcc stacking sequences, and is often referred to as random hexagonal close packed (rhcp) arrangement. Such transitions between the packing sequences in the crystal inevitably leads to stacking faults in the crystals[46], which effects the overall properties of the structure and is particularly detrimental in photonic applications. Furthermore, although close-packed assemblies are generated within all the layers of the structure, they are associated with significantly small ‘domains’. A ‘domain’, which could be described as comprised of particles with the same packing configuration and orientation, is limited to several micrometers in dimensions, which makes these assemblies unsuitable for various

microelectronic components. In addition, when employed for multilayer fabrication, the convective deposition technique tends to generate streaks at low deposition rates, attributed to the instabilities which may be generated within the thin film region. The generation of these streaks often limits the quality of structures, reducing the area with the desired coating thickness as well as wasting of suspension.

The limited structural diversity derived in convective assembly techniques also limits their ability to act as a substitute for the microfabrication techniques in commercial applications. The attainable structures are limited to hexagonal packing of particles parallel to the substrate in all the layers of the crystal assembly. Even though square packed structures are observed in the regions of thickness transition within the crystal, they are not large enough to warrant a useful utilization of the same for practical applications.

1.4 Vibration-assisted convective self-assembly

The addition of external vibrational motion[47] to the linear translation of the substrate plays a pivotal role in regulating the packing characteristics of colloidal crystals in convective assembly process. The addition of periodic vibration to convective assembly was originally investigated in the group by Muangnapoh et. al[47] to discern the effect of inevitable external vibrations when the convective assembly process was implemented in a commercial environment. The experiments however revealed that the addition of low frequency and high amplitude vibrations to the convective assembly process results in an unexpected enhancement in the robustness of the procedure, yielding monolayer depositions of colloidal particles with an enlarged window of substrate withdrawal velocities. Furthermore, when convective assembly processes were used in the fabrication of multilayered colloidal crystals, the addition of external vibrations to the procedure results in a crystalline arrangement of particles possessing a high degree of uniformity in their number of layers, and with packing characteristics which were highly altered in comparison to the usual convective assembly based self-assembly procedures.

1.4.1 Analysis of experimental set-up

The experimental set-up for the convective deposition process aided by external vibration is shown schematically in Figure 1.5(a). Similar to the conventional convective deposition process, vibration-assisted deposition involves a uniform horizontal movement of a thin film of the suspension over the desired substrate, with the velocity regulated to control the number of layers in the packing assembly. In addition to the uniform and unidirectional horizontal movement, the substrate in this case is periodically vibrated in the same translational plane achieved by using a mechanical driver. The waveform of the

external vibrations, along with its frequency and amplitude can be suitably controlled by employing a signal generator.

The position of the substrate at any instant of time in vibration-assisted deposition, $x(t)$is a sum of the uniform unidirectional component and the periodic vibration component.

$$x(t) = v_w t + x_{vib}(t)$$

where v_w represents the time-independent uniform withdrawal velocity of the thin film and $x_{vib}(t)$ represent the displacement due to a periodic waveform at the given instant.

Assuming a sinusoidal input wave of amplitudeA_0 and frequency ω

$$x(t) = v_w t + A_0\, Sin(\omega t)$$

The resultant trajectory of the substrate over a definite time interval is represented by Figure 1.5(b).

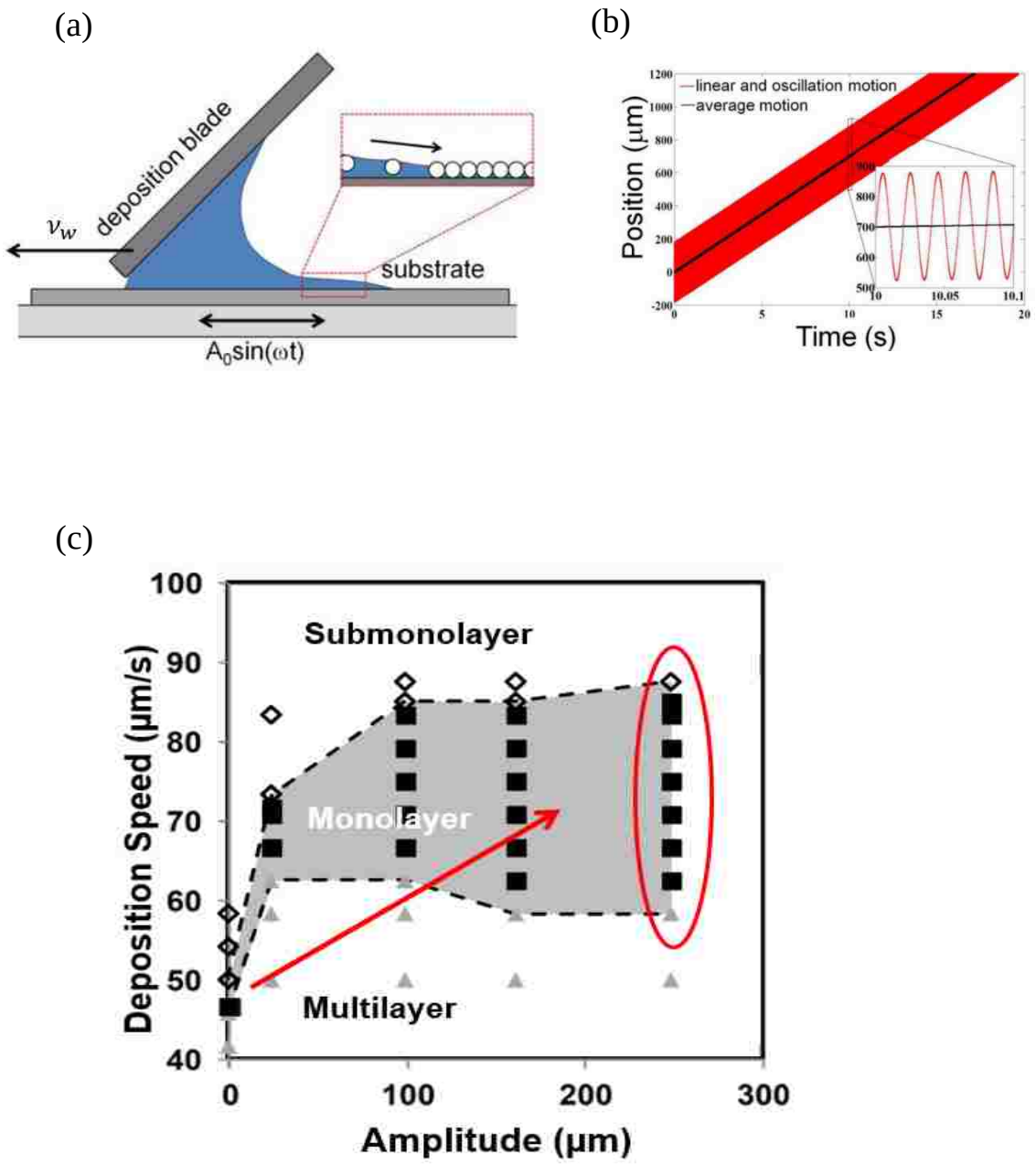

Figure 1.5: Experimental set-up and phase diagram for vibration assisted convective deposition(a) Schematic of the experimental procedure (b) Displacement curve of the substrate during vibration-assisted deposition and (c) Phase diagram for the particle assemblies during the process. The enhancement of the monolayer deposition speed and window is highlighted in the figure

1.4.2 Crystal assembly in vibration-assisted deposition

The utilization of additional lateral vibrations imparts a higher degree of robustness to the convective deposition techniques, with the twin benefits of yielding a monolayer deposition at higher speeds as well as a larger window of withdrawal speeds which would result in a monolayer assembly. This enhancement in performance could be observed from the assembled structure phase diagram in Figure 1.5(c). The monolayer deposition speed, which was confined to a narrow window for a particle suspension concentration and particle diameter unconventional convective deposition can be observed to have increased several times, along with a growing window for monolayer deposition with increase in amplitude. This generation of monolayer assemblies at faster speeds and enhanced deposition window can be attributed to enhanced evaporation flux of solvent from the thin film region due to the high amplitude low-frequency vibrations.

In addition to the enhanced robustness, significant improvement in the quality of assembled films with respect to surface coverage and crystallinity parameters could also be observed in vibration assisted deposition, the latter arising due to the effect of lubrication forces in the thin film region. The lateral acceleration of the substrate in periodic fashion results in variations in curvature of thin film meniscus, varying the Laplace pressure in the thin film region[47]. As a result, the particles confined within the thin film experience lubrication forces which provides sufficient time for the particles to assemble before they are deposited on the substrate.

The use of vibration was also observed to generate atypical packing assemblies in colloidal crystals. Contrary to the pure hexagonal packed structures attainable in convective deposition as well as other self-assembly techniques, vibration-assisted

deposition was successful in generating particle assemblies with a square packing configuration, an analysis of which revealed the existence of fcc (100) packing parallel to the substrate. A detailed explanation on the above observation has been presented in chapter 2, with a discussion on the mechanism in Chapter 3 of the dissertation.

1.5 References

1. Whitesides, G. M. & Grzybowski, B. Self-assembly at all scales. *Science (80-.).* **295,** 2418–2421 (2002).

2. Grzelczak, M., Vermant, J., Furst, E. & Liz-Marzán, L. Directed self-assembly of nanoparticles. *ACS Nano* **4,** 3591–3605 (2010).

3. Cheng, C. C. & Scherer, A. Fabrication of photonic band-gap crystals. *J. Vac. Sci. Technol. B* **13,** 2696–2700 (1995).

4. Feiertag, G. *et al.* Fabrication of photonic crystals by deep x-ray lithography. *Appl. Phys. Lett.* **71,** 1441–1443 (1997).

5. Zhou, G., Ventura, M. J., Vanner, M. R. & Gu, M. Fabrication and characterization of face-centered-cubic void dots photonic crystals in a solid polymer material. *Appl. Phys. Lett.* **86,** 011108 (2005).

6. Michael C. Wanke, Olaf Lehmann, Kurt Muller, Qingzhe Wen, M. S. Laser Rapid Prototyping of Photonic Band-Gap Microstructures. *Science (80-.).* **275,** 1284–1286 (1997).

7. Campbell, M., Sharp, D., Harrison, M., Denning, R. & Turberfield, A. Fabrication of photonic crystals for the visible spectrum by holographic lithography. *Nature* **404,** 53–6 (2000).

8. Miklyaev, Y. V. *et al.* Three-dimensional face-centered-cubic photonic crystal templates by laser holography: fabrication, optical characterization, and band-structure calculations. *Appl. Phys. Lett.* **82,** 1284 (2003).

9. Cumming, B. P., Jesacher, A., Booth, M. J., Wilson, T. & Gu, M. Adaptive aberration compensation for three-dimensional micro-fabrication of photonic crystals in lithium niobate. *Opt. Express* **19,** 9419–25 (2011).

10. Yablonovitch, E. Inhibited Spontaneous Emission in Solid-State Physics and Electronics. *Phys. Rev. Lett.* **58,** 2059–2062 (1987).

11. John, S. Strong Localization of Photons in Certain Disordered Dielectric Superlattices. *Phys. Rev. Lett.* **58,** 2486–2489 (1987).

12. Yablonovitch, E. Photonic Crystals: Semiconductors of light. *Sci. Am.* **285,** 47–55

(2001).

13. Yik-Khoon Ee, Ronald A. Arif, Nelson Tansu, Pisist Kumnorkaew, J. F. G. Enhancement of light extraction efficiency of InGaN quantum wells light emitting diodes using SiO2/polystyrene microlens arrays. *Appl. Phys. Lett.* **91,** 221107 (2007).

14. Guldin, S. *et al.* Dye-sensitized solar cell based on a three-dimensional photonic crystal. *Nano Lett.* **10,** 2303–2309 (2010).

15. John, S. Why trap light? *Nat. Mater.* **11,** 997–999 (2012).

16. Russell, P. Photonic crystal Fibers. *Science (80-.).* **299,** 358–362 (2003).

17. Arpin, K. a *et al.* Multidimensional architectures for functional optical devices. *Adv. Mater.* **22,** 1084–1101 (2010).

18. Biró, L. P. *et al.* Living photonic crystals: Butterfly scales — Nanostructure and optical properties. *Mater. Sci. Eng. C* **27,** 941–946 (2007).

19. Zi, J. *et al.* Coloration strategies in peacock feathers. *Proc. Natl. Acad. Sci.* **100,** 12576–12578 (2003).

20. Fuhrmann, T., Landwehr, S., El Rharbl-Kucki, M. & Sumper, M. Diatoms as living photonic crystals. *Appl. Phys. B Lasers Opt.* **78,** 257–260 (2004).

21. Ghosh, M., Fan, F. & Stebe, K. J. Spontaneous pattern formation by dip coating of colloidal suspensions on homogeneous surfaces. *Langmuir* **23,** 2180–2183 (2007).

22. Shklover, V., Braginsky, L. & Hofmann, H. Domain structure and optical properties of colloidal photonic crystal. *Mater. Sci. Eng. C* **26,** 142–148 (2006).

23. Amos, R., Rarity, J., Tapster, P., Shepherd, T. & Kitson, S. Fabrication of large-area face-centered-cubic hard-sphere colloidal crystals by shear alignment. *Phys. Rev. E* **61,** 2929–2935 (2000).

24. Solomon, T. & Solomon, M. J. Stacking fault structure in shear-induced colloidal crystallization. *J. Chem. Phys.* **124,** 134905 (2006).

25. Cong, H. & Cao, W. Colloidal crystallization induced by capillary force. *Langmuir* **19,** 8177–8181 (2003).

26. Prevo, B. G. & Velev, O. D. Controlled, rapid deposition of structured coatings from micro- and nanoparticle suspensions. *Langmuir* **20,** 2099–2107 (2004).

27. Winkleman, A., Gates, B. D., McCarty, L. S. & Whitesides, G. M. Directed self-assembly of spherical particles on patterned electrodes by an applied electric field. *Adv. Mater.* **17,** 1507–1511 (2005).

28. Lumsdon, S. O., Kaler, E. W., Williams, J. P. & Velev, O. D. Dielectrophoretic assembly of oriented and switchable two-dimensional photonic crystals. *Appl. Phys. Lett.* **82,** 949–951 (2003).

29. Snezhko, A. & Aranson, I. S. Magnetic manipulation of self-assembled colloidal asters. *Nat. Mater.* **10,** 698–703 (2011).

30. Zhou, C., Han, J. & Guo, R. A facile strategy to colloidal crystals by drying condensed suspension droplets. *J. Colloid Interface Sci.* **397,** 80–87 (2013).

31. Park, S. H., Qin, D. & Xia, Y. Crystallization of Mesoscale Particles over Large Areas. *Adv. Mater.* **10,** 1028–1032 (1998).

32. Jiang, P. & McFarland, M. J. Large-scale fabrication of wafer-size colloidal crystals, macroporous polymers and nanocomposites by spin-coating. *J. Am. Chem. Soc.* **126,** 13778–13786 (2004).

33. Dimitrov, A. S. & Nagayama, K. Continuous convective assembling of fine particles into two-dimensional arrays on solid surfaces. *Langmuir* **12,** 1303–1311 (1996).

34. Cong, H. & Cao, W. Colloidal Crystallization Induced by Capillary Force. *Langmuir* **19,** 8177–8181 (2003).

35. Dushkin, C. D., Nagayama, K., Miwa, T. & Kralchevskyt, P. A. Colored Multilayers from Transparent Submicrometer Spheres. *Langmuir* **9,** 3695–3701 (1993).

36. Galisteo-López, J. F. *et al.* Self-assembled photonic structures. *Adv. Mater.* **23,** 30–69 (2011).

37. Meng, L. *et al.* The role of thickness transitions in convective assembly. *Nano Lett.* **6,** 2249–2253 (2006).

38. Deegan, R. D. *et al.* Capillary flow as the cause of ring stains from dried liquid drops. *Nature* **389,** 827–829 (1997).

39. Vella, D. & Mahadevan, L. The 'Cheerios effect'. *Am. J. Phys.* **73,** 817 (2005).

40. Brewer, D. D. *et al.* Mechanistic principles of colloidal crystal growth by evaporation-induced convective steering. *Langmuir* **24,** 13683–13693 (2008).

41. Born, P., Munoz, A., Cavelius, C. & Kraus, T. Crystallization mechanisms in convective particle assembly. *Langmuir* **28,** 8300–8308 (2012).

42. Gasperino, D., Meng, L., Norris, D. J. & Derby, J. J. The role of fluid flow and convective steering during the assembly of colloidal crystals. *J. Cryst. Growth* **310,** 131–139 (2008).

43. Malaquin, L., Kraus, T., Schmid, H., Delamarche, E. & Wolf, H. Controlled particle placement through convective and capillary assembly. *Langmuir* **23,** 11513–11521 (2007).

44. Ohara, P. C. & Gelbart, W. M. Interplay between Hole Instability and Nanoparticle Array Formation in Ultrathin Liquid Films. *Langmuir* **14,** 3418–3424 (1998).

45. Woodcock, L. V. Entropy difference between the face-centred cubic and hexagonal close-packed crystal structures. *Nature* **385,** 141–143 (1997).

46. Junhu Zhang, Zhiqiang Sun, B. Y. Self-assembly of photonic crystals from polymer colloids. *Curr. Opin. Colloid Interface Sci.* **14,** 103–114 (2009).

47. Muangnapoh, T., Weldon, A. L. & Gilchrist, J. F. Enhanced colloidal monolayer assembly via vibration-assisted convective deposition. *Appl. Phys. Lett.* **103,** 181603 (2013).

2

Flow-templated fabrication of FCC (100) colloidal crystal structures

2.1 Introduction

Interest in colloidal crystallization has long been the focus of fundamental studies wherein thermodynamic and kinetic analogies are commonly drawn to atomic systems[1]. In contrast to equilibrium molecular particle assembly[2] dominated by intermolecular and interparticle forces,[3,4] non-equilibrium colloidal self-assembly[5] can be efficiently tailored through modulation of gravitational[6], shear[7–9], as well as electromagnetic[10,11] fields. Among non-equilibrium techniques, convective assembly of colloidal particles[12–15] enables realization of colloidal crystal films with fine control over film thickness (i.e., mono- to multi-layer) and extensive order (i.e., colloidal crystallinity) spanning scales of square millimeters or larger by exploiting evaporation-driven flow in a thin film.

Unique photonic[16–18], magnetic[19,20], and structural[21] applications are reliant, however, upon realization of colloidal assemblies with non-hexagonal packing symmetries oriented parallel to the underlying substrate for achievement or enhancement of specific physical properties. Yet the larger free energy of these structures relative to hexagonally symmetric and face centered cubic close-packed structures, hcp and fcc, respectively, makes them challenging to realize without imposition of external fields or epitaxial fabrication utilizing complex boundary templating. Although non-close packed colloidal phases (e.g, bcc) have been observed in addition to hexagonally close packed (hcp) phases

for specific particle volume fractions and charge screening in concentrated suspensions of charge stabilized particles[22], extraction of these assemblies from solution tends to eliminate bcc packing favoring close-packed symmetries. Primarily colloidal crystals with hexagonally symmetric packing in all constituent layers parallel to the substrate upon which they are asembled[6–8,12–15] result. Since hcp and face-centered cubic (fcc) structures differ negligibly (e.g., 0.005 RT/mole)[23] in their corresponding free energies, the resulting colloidal crystals tend to be comprised of coexisting hcp and fcc phases. Here, we refer to this mixture of hexagonal symmetries as "random hexagonally close packed" or rhcp arrangements.

The cubic particle symmetry desired for various applications is the same as that which is presented by the (100) facet of an fcc crystal. The spontaneous formation of square-packed colloidal domains by particle self-assembly, the (100) facets of fcc crystals, has been reported at boundaries marking the transition between adjacent hexagonally-packed domains of different multi-layer thickness[12,13,24,25]. Yet, the localization of such faceting to transition regions precludes its scalability to areas greater than several particle diameters. Only particle assembly performed under highly controlled growth conditions on pre-patterned substrates reproducibly yields structures with (100) fcc oriented colloidal-crystal planes. These substrate-patterning approaches[26–33], referred to as colloidal epitaxy,[26] have exploited various template morphologies to obtain square-packed structures. Because these templating procedures require precise control of the pitch and the diameter of fabricated template features with respect to the colloidal-particle size[28], the achievable extent of the epitaxially grown (100) fcc domains over the predominant (111)

fcc oriented packing being generated in the neighboring, unpatterned regions[31] is severely limited.

In this work, we report the discovery of extensive and tunable square-packing (i.e., (100) fcc facets oriented parallel to the underlying substrate) in self-assembled colloidal structures realized simply by the introduction of external oscillatory motion of the substrate during convective assembly of multilayer colloidal crystals. This substrate motion alters flow-patterns of the colloidal particles confined within the liquid film during convective assembly. Besides forming large (100) fcc crystalline domains with relatively few defects, the process also results in colloidal crystals having negligible variation in thickness while simultaneously yielding controlled proportions of both hexagonal and square-packed arrangements.

2.1.1 Applications of square packing

The presence of multiple void architectures, octahedral and tetrahedral voids in hexagonally packed colloidal crystal samples gives rise to stacking faults in the crystal, resulting in a high defect density in the final assembly. This is disadvantageous in applications which demands high quality periodic and ordered arrangement of constituent particles in the assembly, notably for photonic applications. The twinning effect associated with multiple packing sequences in the fabricated crystal can be eliminated if the packing conforms to a configuration which ensures a unique void architecture throughout the assembled structure, which would guarantee the same packing sequence in all the layers. Although this could be realized in diverse ways, the only arrangement which would yield this objective and simultaneously provide the densest packing of particles is the fcc (100)

arrangement, characterized by a square-like arrangement of the adjacent particles in each plane and has the void structure entirely restricted to a single geometry. This enables a regular repetition of the same packing arrangement in all the layers, generating crystals with highly reduced defect densities, making it a better candidate for photonic applications.

In addition, these square-packed colloidal crystals also serve as a basic structure to derive multiple complex structures like diamond cubic structure which are associated with a complete photonic band gap. The crystallographic modification of the colloidal assembly also provides a tool to alter the optical and magnetic properties of these crystals, with the resulting nanostructured applications for unique optical-response materials and high density data storage devices incorporating magnetic nanoparticles. The larger void spacing associated with this structure imparts better structural stability for the corresponding inverse structure, with improved performance for catalytic applications involving high stress-environments. The characteristic square-packed arrangement in fcc(100) structures also yields a non-close-packed arrangement on the surface-layer of the crystal (ref) which opens up avenues for exploring its incorporation in surface sensors and surface-responsive materials.

2.1.2 Current approaches towards fabricating square-packed structures

The procedures for obtaining self-assembled structures with a (100) orientation of the colloidal-crystal planes, resembling square packing of particles in a single plane, makes use of templated self-assembly procedures, in which the crystal nucleation and growth is carried out in pre-patterned templates. The templated approaches for specifically oriented fcc structures varies from chemically-patterned surfaces with selective regions for colloidal condensation[34], electrophotographic techniques for the desired charge patterning of the surface[35] and the surface modification of the substrate using microfabrication techniques. Of the various templating approaches, only the surface patterning procedures have been successful in the synthesis of high-quality crystals[36].

Template-directed self-assembly procedures on microfabricated substrates, referred to as colloidal epitaxy have been demonstrated for the fabrication of (100) oriented fcc crystals by using gravitational settling or convective assembly. Nucleation of the colloidal crystal assembly is initiated at distinct locations depending on the template, which then gradually grows into a continuous domain. The surface morphologies for the growth of oriented fcc crystals include square grating[27,28], pillar patterns on silicon substrate[30,31], regular arrays of square-pyramidal grooves or V- shaped grooves[32], square-grid patterned glass substrates[29] as well as pyramidal posts created on a PU surface. Although successful in creating continuous domains of square orientation, these procedures requires high-precision direct-write processes[3738] or lithographic procedures[39] to obtain the prerequisite template for crystallization to occur, which greatly hinders their scalability. These procedures also require a precise control of the pitch and the diameter of the feature[28] with respect to the colloidal-particle size. Even with precise feature characteristics, an accurate

epitaxial growth of (100) orientation is difficult to obtain on the patterns, and requires optimal substrate orientation and crystal growth environment[31] to favor the formation of (100) orientation over the predominant (111) orientation. Moreover, these procedures are based on layer-by layer assembly with each layer acting as a template for the next layer. This demands strong coupling between the layers to maintain the (100) orientation[32] and has the additional drawback that the presence of defect in a layer affects subsequent packing in all the layers formed above it. A gradual reduction in the area of square packing is also observed with progressing number of layers[29].

A variation of the templated procedure involves the use of an applied electric field to arrange the particles on a patterned electrode surface[36], but was only partially successful in generating defect-free crystals. Ann yet another procedure for obtaining square-packed colloidal crystals involves modifying the ends of DNA linkers in DNA-assisted colloidal crystallization[40], which is however prohibitively expensive due to the materials and procedures involved.

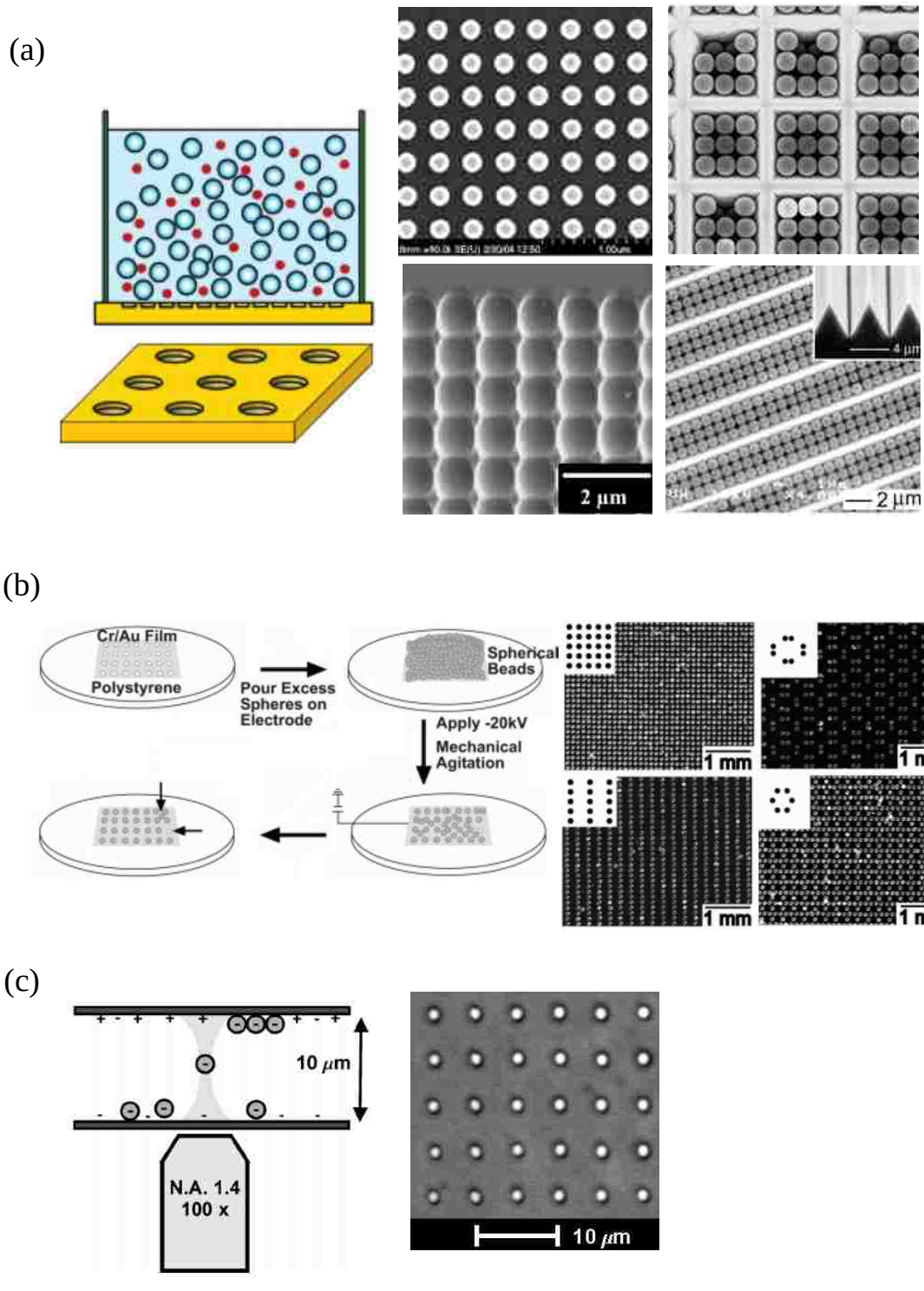

Figure 2.1: Fabrication approaches for square packed structures(a) Colloidal epitaxy method, anticlockwise from left : schematic of the assembly process[29], patterned silica substrate[31], FIB patterned glass substrate[29],V-shaped grooves and square pyramidal pits[32] (b) Colloidal particle assembly achieved by an external electric field[36] and (c) Assembled structure using optical tweezers[41]. (Figures shown were adapted from the corresponding references)

2.2 Experimental Section

2.2.1 Methods

Vibration assisted convective deposition was employed to assemble particles from aqueous solutions into multi-layer colloidal crystal films. The experimental setup described previously[42] employs a glass microscope slide as a coating blade, fixed at an angle of 45^{o} and ~5 mm above an underlying substrate. The bottom edge of the blade was made hydrophobic through attachment of Parafilm so as to confine small volumes (200 µl) of colloidal solutions in the angle between the blade and substrate. In addition to linear translation of the substrate, characteristic of conventional convective deposition processes[13], colloidal crystalline depositions in this work were carried out with the addition of controlled in-plane vibrations imposed in the same direction as that of the meniscus withdrawal. This was achieved through combination of a linear mechanical driver (kdScientific) and a mechanical driver (PASCO SF-9324) coupled with a waveform sinusoidal signal generator (Agilent 33220A).

Colloidal crystalline films were prepared in an enclosed chamber under controlled temperature (nominally 24^{o}C) and humidity conditions (nominally 20 %, but systematically varied from 4 % to 90 %). Nominal depositions were prepared from a 10 % w/w suspension of 0.93 µm or 1.5 µm polystyrene (PS; Thermo-scientific) or silica particles (Fiber Optic Center Inc.) in water on 45 mm x 50 mm microscope cover-glass (Fisherbrand) or glass-supported PS substrates. The latter was prepared by convective deposition of 0.30 µm PS particles (10 % w/w) into ca. 2 µm films (14 µm/s at a humidity of 20 %) followed by melting at 240^{o}C for 45 min. In all cases, glass substrates were pre-

treated with piranha solution and subsequently rinsed with distilled water and dried prior to deposition. Colloidal crystalline film thickness, *N*, was tuned by controlling the rate of linear translation of the substrate, v_w(2–10 μm/s), and relative humidity (i.e., evaporative solvent flux, j_e) according to the equation (1) proposed by Dimitrov and Nagayama[12]

$$N = \frac{\beta l}{0.605}\frac{j_e \varphi}{v_w d(1-\varphi)} \qquad (1)$$

where βl is a constant, φ is the suspension concentration and d is the diameter of particles in the suspension.. Nominal waveform generation, $A_0 sin(\omega t)$, was carried out at a frequency of ω=40 Hz and amplitude of ca. A_0=1200 μm.

Colloidal crystalline films were analyzed using white light irradiation and scanning-electron microscopy (SEM) on a Hitachi 4300 instrument to assess particle packing at the top-most layer of the film, and by laser scattering (λ=532 nm, 15 mm^2 spot size) by the films supported on glass substrates for insight into the bulk crystallinity and crystal symmetry. The colloidal crystal samples were also analyzed using laser scanning confocal microscopy (CLCM, Visitech) after wetting samples with 8 mM Rhodamine-B dye in DMSO. CLSM scans were taken at sequential axial positions along the direction of coating as well as through the thickness of the colloidal crystal film. Confocal images were processed using IDL to identify the individual particle locations[43,48] in the crystal assembly, and, subsequently, the number of particle layers comprising the colloidal crystalline film and the local crystal symmetry (e.g., hexagonally close packed, hcp; face centered cubic, fcc; mixtures thereof defined here as random hexagonally close packed, rhcp).

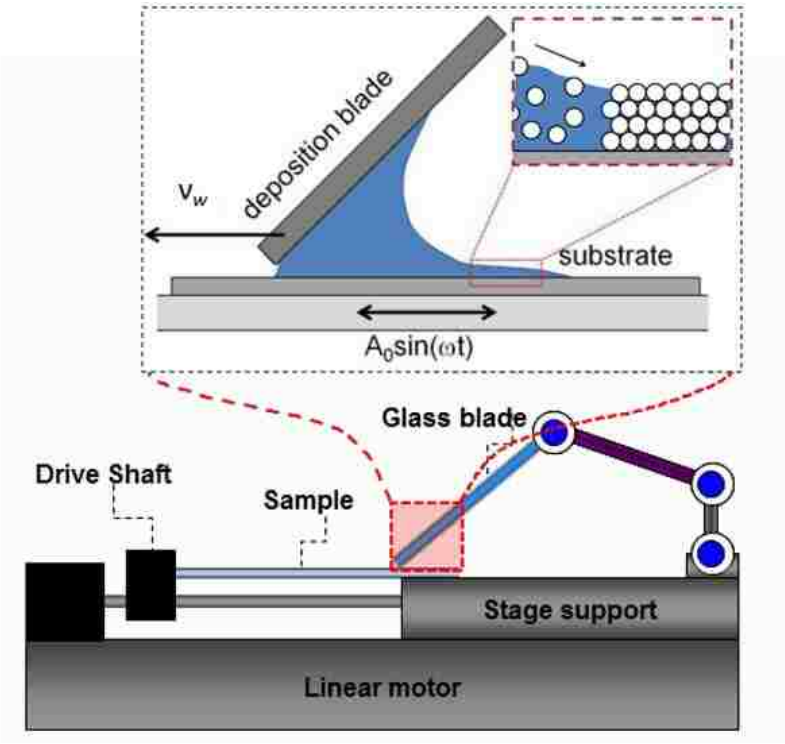

Figure 2.2: Experimental set-up for vibration-assisted assembly of colloidal crystals

2.2.2 Image Analysis Procedure

Multiple confocal scans of the sample were performed both in the lateral direction (direction of deposition) and longitudinal direction (perpendicular to deposition direction). The image stack was then analyzed using the particle tracking algorithm developed by John C. Crocker and Eric R. Weeks[1] to identify the centroid locations of the particles.

1. Identification of particles containing four and six nearest neighbors

This is achieved by first scaling the particle co-ordinates of the features present in a frame in terms of the particle diameter. A spherical cavity with radii of 0.8 and 1.2 particle-diameter units was assumed around each particle, followed by grouping of particles which have 6 and 4 nearest neighbors (defined as the particles whose centroid lies within the above assumed spherical cavity). Based on the number of nearest neighbors (NN), the color scheme as shown in Figure 2.3b is used to represent the various types of features.

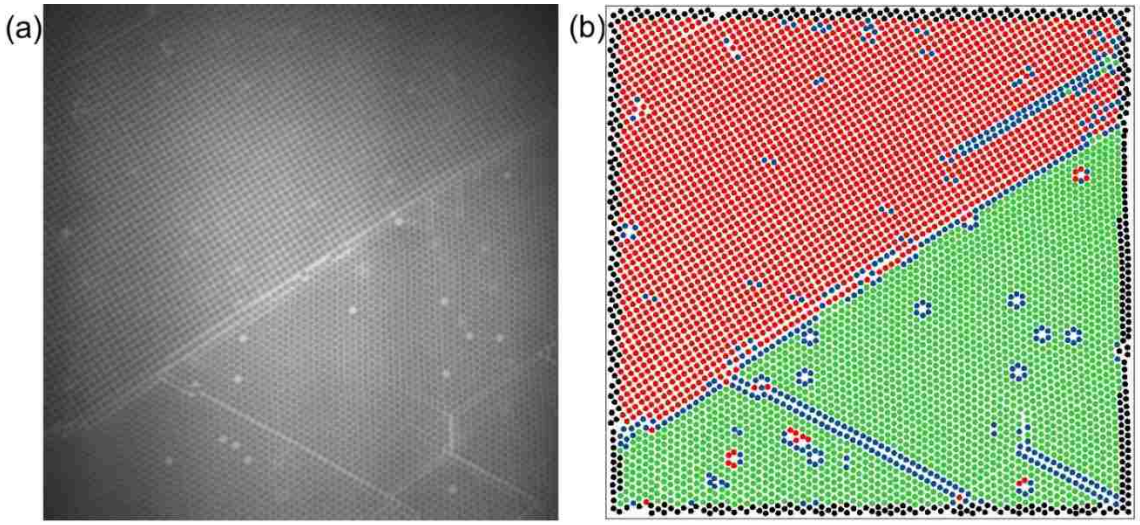

Figure 2.3:Tracking of particle centroid locations and identification of number of nearest neighbors (a) Representative confocal image with both square and hexagonal packed regions. (b) Reconstructed image with particles grouped into square-packed regions with four nearest neighbors (red), hexagonally-packed regions with six nearest neighbors (green), particles with neither four nor six nearest neighbors (blue) and particles at the boundary of the frame (black)

2. Recalculation to account for the inaccurate estimation of the particle type

The absence of particles in some locations, either due to a defect in packing during the colloidal-crystal assembly or being out of focus during the confocal scans results in a void space in what is actually a hexagonal or a square domain. This results in an inaccurate estimation of the particle type if its description is based only on its number of nearest neighbors and can be observed in Figure 2.3b as isolated green-color particles in the square-packed region or isolated red-colored particles around a void in the hexagonally-packed region. This inaccuracy in the estimation of the particle type is accounted for by using the local-bond order(ψ) of the particles constituting the rhcp or fcc(100) regions:

$$\psi_{N,j} = \frac{1}{N}\sum_{k=1}^{N} e^{N\, i\, \theta_{kj}}$$

where *N* is the number of neighbors for a particle 'j', 'i' is the complex conjugate and θ_{kj} denotes the angle between the centroid locations of particles 'j' and 'k'. A particle with a perfect hexagonal arrangement has six nearest neighbors in its plane, with $N = 6$ and$\theta_{kj} = 60^o$ $(for\ k = 1,2,3 \ldots 6)$, resulting in $\psi_6 = 1$. Similarly, a particle with perfect square arrangement has $\theta_{kj} = 90^o$ $(for\ k = 1,2,3,4)$ with $\psi_4 = 1$.

To obtain an estimate of the cut-off values for ψ_6 and ψ_4 which can accurately compartmentalize the particles as belonging to hexagonally-packed and square-packed regions respectively, a sample confocal image was considered which contained almost equal proportions of both packing arrangements (Figure 2.3a), and particles were classified into groups merely by counting the number of nearest neighbors. Histograms were obtained for $|\psi_6|^2$ (for particles observed to have 6 nearest neighbors) and $|\psi_4|^2$ (for particles with 4 NN), the plots for which are given in Figure 2.4a.

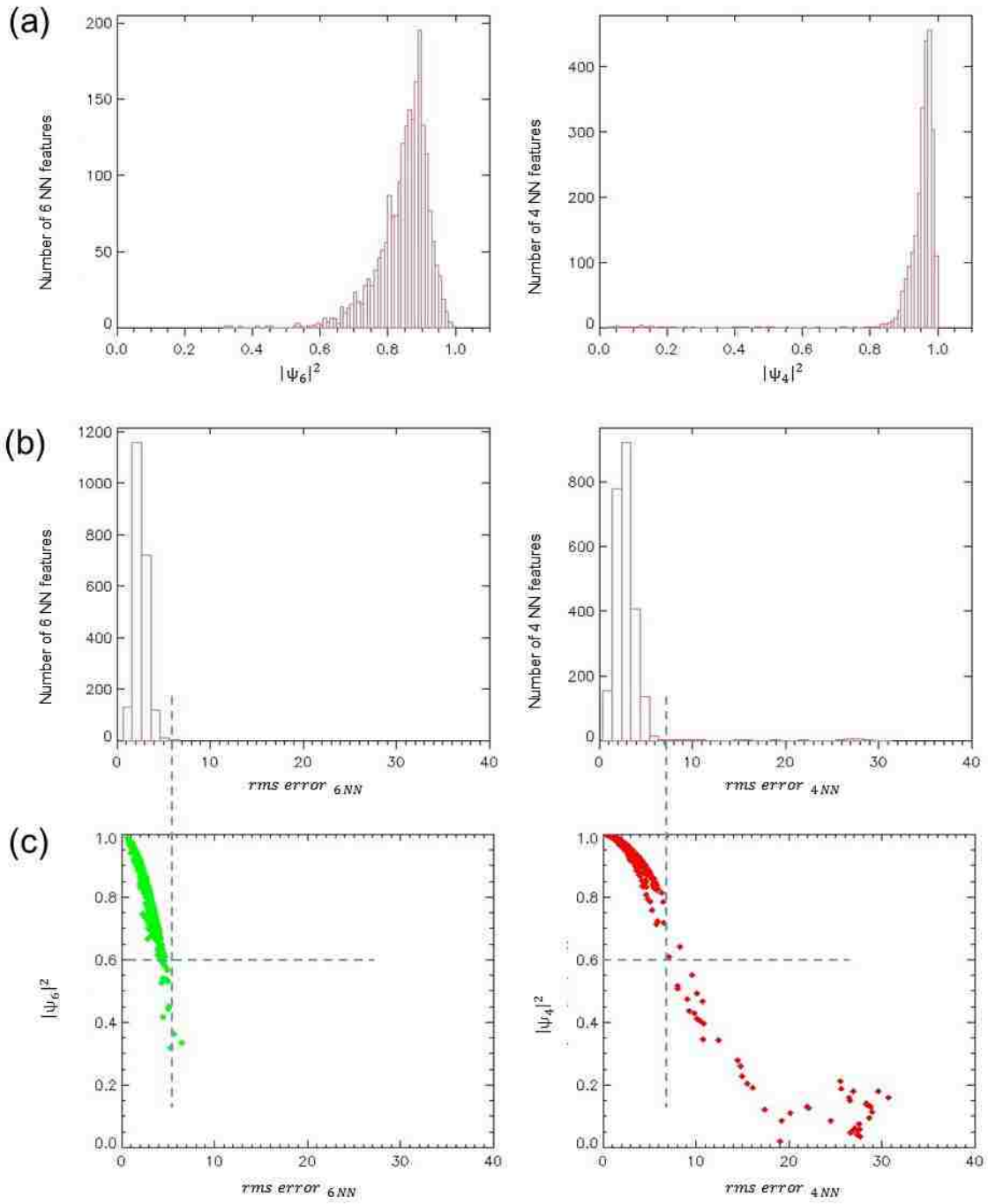

Figure 2.4: Calculations to identify the threshold $|\psi_6|$ and $|\psi_4|$values for 6 NN and 4 NN particles respectively (a) Histograms for $|\psi_6|^2$ (for particles observed to have 6 nearest neighbors) and $|\psi_4|^2$ (for particles with 4 NN) (b) Histograms for '*rms error*' for 6 NN and 4 NN particles respectively (c) Plot of $|\psi|^2$ vs '*rms error*' for both categories of particles

The histograms in Figure 2.4a displayed an asymptotic decay for the $|\psi|^2$ values and is not much helpful in defining a threshold- $\psi\ value$. This makes it essential to define a modified parameter: 'rms error' to measure how close the particle packing is to the perfect hexagonal or square packing-type (characterized by individual bond angles of 60^o and 90^o respectively).

The rms error associated with a particle 'j' having 6 NN is given by:

$$rms\ error_{\ 6\ NN\ ,j} = \sqrt{\frac{1}{6}\sum_{k=1}^{6}\left(\theta_{jk} - 60\right)^2}$$

Similarly, the rms error associated with a particle 'j' having 4 NN is given by:

$$rms\ error_{\ 4\ NN\ ,j} = \sqrt{\frac{1}{4}\sum_{k=1}^{6}\left(\theta_{jk} - 90\right)^2}$$

The rms error values for particles having 6 NN lies in the range of 0 to 6, while that for particles having 4 NN have an upper threshold of 7, barring a few outliers (Figure 2.4b,c). This translates to a $|\psi|^2$ value of 0.6, or a $|\psi|$value of 0.77 for both $|\psi_6|$ and $|\psi_4|$, a threshold chosen so as to capture most of the features of both 6 NN and 4 NN category.

For the particle grouping as described by Figure 2.3b, a set of recalculation is done for each of the particle based on their ψ values, resulting in the removal of particles with a $|\psi|$value less than 0.77 from the 6 NN or the 4 NN grouping. The color-coded representation of the particles after the ψ value-based recalculation is depicted by the colored image in **Error! Reference source not found.**a, with the particles not satisfying t he ψ- criteria added to the group of blue-colored particles.

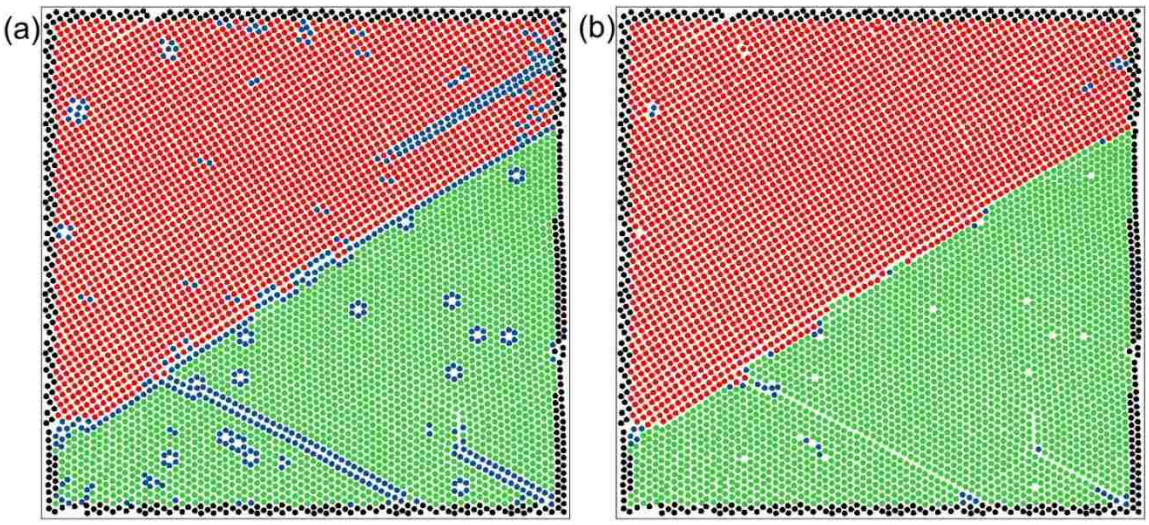

Figure2.5: Modified particle representation after (a) First recalculation based on $|\psi|$ values (b) Second recalculation of blue-colored particles based on its neighboring particles

3. Recalculation to modify the description of blue-colored particles based on the description of its neighbors (to account for the blue-colored particles, which are usually particles lying at the domain boundaries or associated with void spaces)

A blue-colored particle is added to the list of particles with 6 NN if:

(i) The number of neighbors belonging to the 6 NN grouping > Number of neighbors belonging to 4 NN grouping

(ii) There are atleast 2 neighbors belonging to 6 NN grouping with $|\psi_6| \geq 0.77$

Similarly, it is added to the list of particles with 4 NN if:

(i) The number of neighbors belonging to the 4 NN grouping ≥ Number of neighbors belonging to 6 NN grouping

(ii) There is atleast 1 neighbor belonging to 4 NN grouping with $|\psi_4| \geq 0.77$

A pictorial representation of the same is given by Figure 2.5b.

2.3 Results and Discussion

Figure 2.6 shows a direct comparison between representative multi-layered polystyrene colloidal crystals prepared on glass substrates by blade-based convective deposition methods with (Figure 1e-h) and without (Figure 2.6a-d) lateral oscillation of the substrate. White light irradiation (Figure 2.6a,e) of each colloidal crystal reveals iridescent reflections indicative of polycrystallinity, but with marked differences in the corresponding extent of the single crystalline sub-domains. Specifically, vibration-mediated assembly appears to dramatically increase the size of the constituent single crystal domains to extensive millimeter and even centimeter scales (Figure 2.6e). Laser diffraction through these glass-supported samples, carried out using a 532 nm wavelength laser with a 15 mm^2 spot size, confirms the millimeter-scale of the single crystalline domains (i.e., containing more than 10^7 particles with similar packing arrangement and orientation) achieved through vibration-mediated convective assembly (Figure 2.6f,g). In contrast, Figure 2.6b shows the characteristic ringed diffraction pattern from polycrystalline colloidal crystals assembled by conventional (i.e., vibration-free) convective deposition, derived from lattice mismatch of smaller grains of near exclusive hexagonal symmetry[6–8,12–15] as shown in more detail in the scanning electron microsocpy (SEM) images in Figure 2.6c,d.

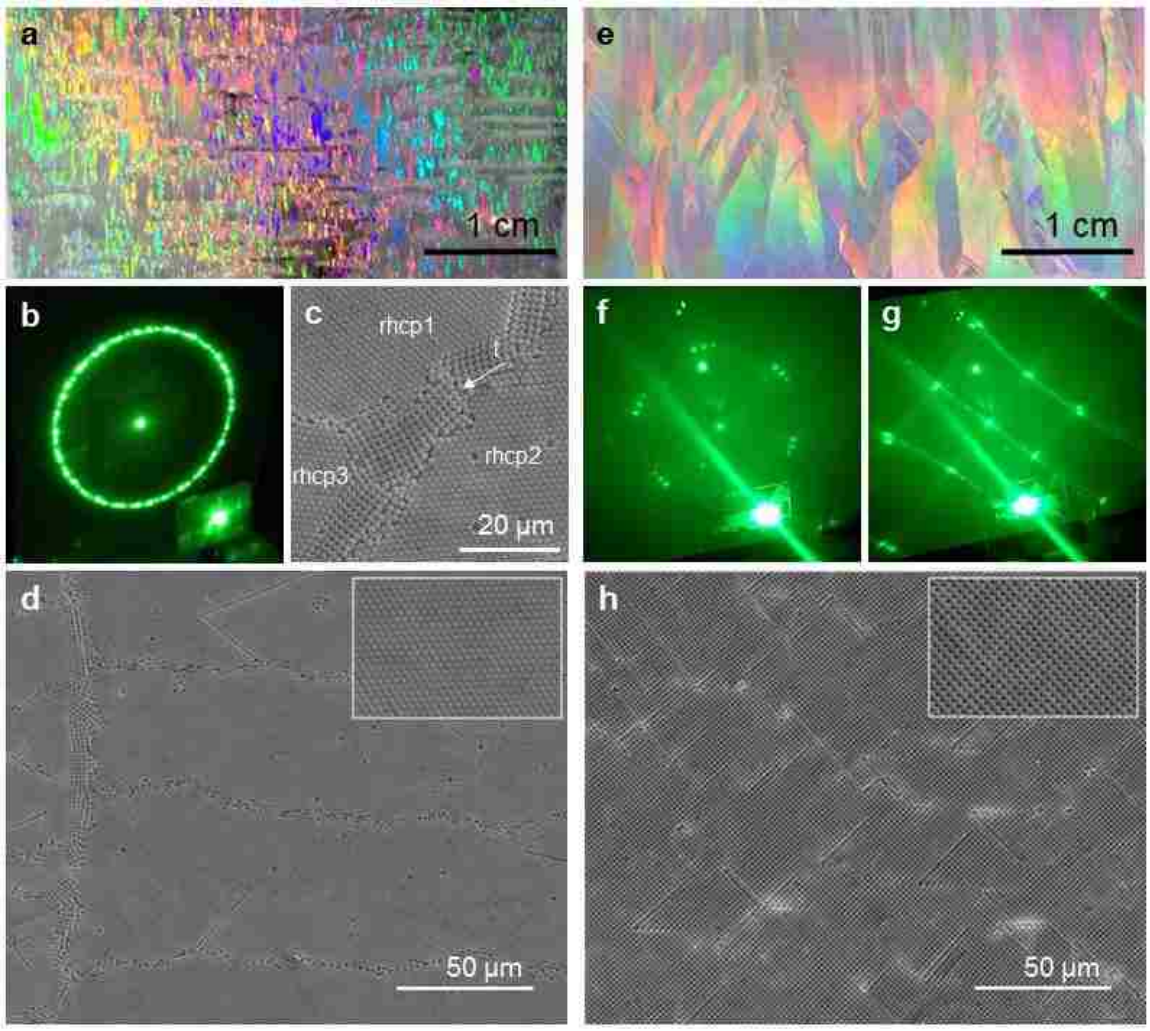

Figure 2.6:Comparison of colloidal-crystals assembled by conventional (a-d) and vibration-mediated (e-h)convective deposition (a,e) White light irradiation of representative colloidal crystals comprised of 1.5 µm polystyrene particles on glass substrates reveals differences in characteristic scales of polycrystallinity, with laser diffraction (15 mm^2 spot size) through the sample and corresponding SEM images of the colloidal crystal surface, indicating (b-d) micron-scale lattice-mismatched domains of rhcp symmetry with localized transition (shown as 't' in (c)) regions of square/cubic symmetry in the case of conventionally assembled colloidal crystals. The laser-diffraction experiments for samples obtained by vibration-mediated assembly shows a decidedly enlarged mm-scale domains of (f) hexagonal and (g,h) square/cubic symmetries. SEM images in (d,h) indicate the extent of the single crystallinity, with insets showing magnified views of the respective rhcp and square/cubic symmetries.

Laser diffraction from samples assembled by vibration-mediated methods reveals a surprising co-existence of domains with two distinct crystalline symmetries. In addition to crystalline domains of hexagonal symmetry (diffraction with 60^o angular spacing, Figure 2.6f), commonly observed in colloidal crystals assembled by conventional methods (Figure 2.6c,d), domains yielding diffraction patterns with angular spacing of 90^o (Figure 2.6g) are also observed. Taken together with the large laser spot size, the latter indicates the existence of extensive crystalline domains of square/cubic symmetry as shown in the SEM image in Figure 2.6h, the formation of which has not previously been reported without reliance on external fields, complex and multi-step epitaxial growth, or as highly localized artefacts of only a few particle diameters arising due to thickness transitions between hexagonally symmetric grains.(e.g., region '*t*', Figure 2.6c).

The coexistence of domains of rhcp and square/cubic symmetry is further explored in Figure 2.7a, where a lower magnification SEM image of the top surface of a representative colloidal crystal obtained by vibration-assisted convective deposition of 0.93 μm polystyrene (PS) particles reveals domains with distinct variation in brightness corresponding to two distinct colloidal crystalline arrangements at the surface. Whereas darker regions possess a hexagonal arrangement of particles corresponding to the (111) plane of the close-packed structure (rhcp), a square-arrangement of particles is observed at the surface of brighter regions, as shown in the inset to Figure 2.7a. Complemented by the laser diffraction analysis (Figure 2.6f,g), which indicates the persistence of such structures throughout the thickness of the colloidal crystal, and the contact between all adjacent particles, the square packing of particles at the surface of these domains is consistent with the structural symmetry associated with the (100) facet of an fcc crystal.

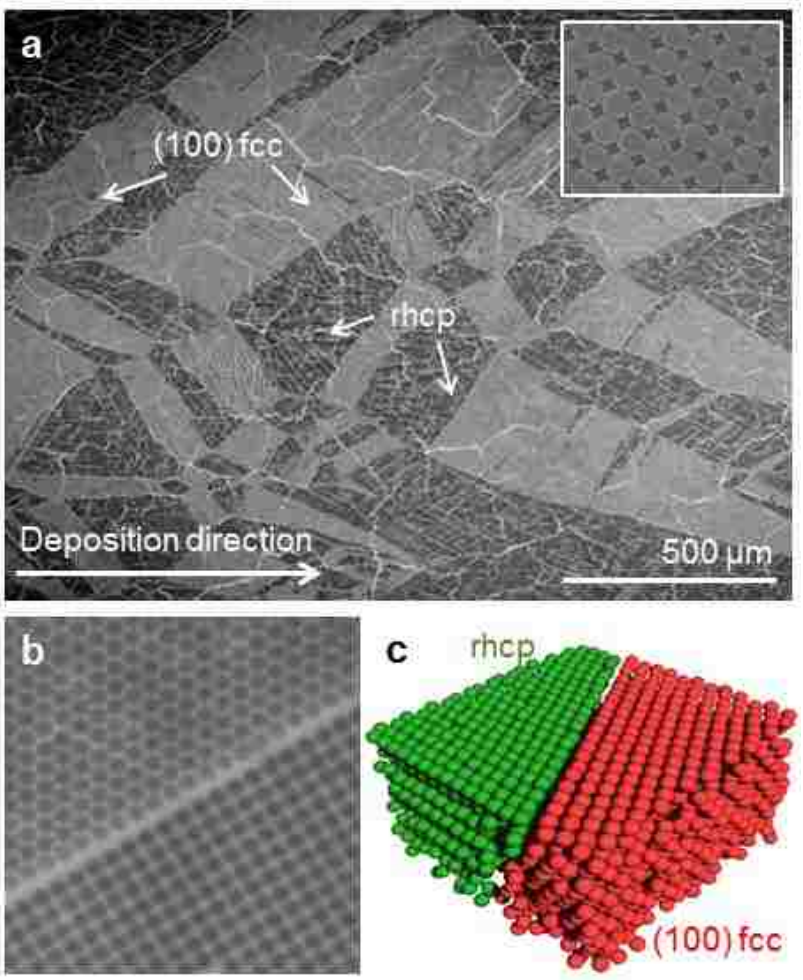

Figure 2.7: Structural analysis of multi-layer cubic colloidal-crystals achieved by vibration-assisted convective assembly carried out by (a) SEM analysis of the top surface of the colloidal crystal (square packing of ' (100) fcc' domains shown in inset), (b) CLSM imaging of adjacent single crystalline domains at the crystal-substrate interface, and (c) 3D reconstruction of the colloidal crystalline structure at a representative grain boundary. Analysis is shown for representative assemblies of 0.93 µm polystyrene (PS) particles.

Beyond the laser diffraction experiments, quantification of the bulk crystallinity was carried out by confocal laser scanning microscopy (CLSM) (Figure 2.7b), a technique enabling collection of optical slices through the thickness of the colloidal crystal and its subsequent 3D-reconstruction (Figure 2.7c). Whereas the SEM image shown in Figure 2a was collected at the top surface of the colloidal crystal, Figure 2.7b shows a representative optical slice of adjacent single crystalline domains collected at a focal plane positioned at the interface between the colloidal crystal and the underlying substrate. The confocal image clearly shows the two distinct particle arrangements in the adjacent single crystalline domains consistent with the rhcp and (100) fcc symmetries observed at the surface. 3D rendering of the corresponding series of confocal images spanning the thickness of the colloidal crystal is shown in Figure 2.7c, with analysis of particle positions confirming the hexagonal and (100) fcc crystal symmetries (see supplemental information). The transition between the adjacent (100) fcc and rhcp domains appears to occur along a sharp, well-defined grain boundary (Figure 2.7c) extending vertically through the thickness of the crystal (i.e., perpendicular to the underlying substrate and crystal surface). The vertical orientation of the grain boundary, consistent with all such measured boundaries in the colloidal crystals prepared in this study by the vibration-assisted convective deposition approach, lies in clear contrast to epitaxial (100) fcc assemblies reported previously[26–33]. In the case of the latter, the generation of square-packed regions progresses similar to a pyramidal structure from the substrate/crystal surface[29] leading to sequential reduction in the effective area of the square-packed surface structure with increasing thickness of the colloidal crystal.

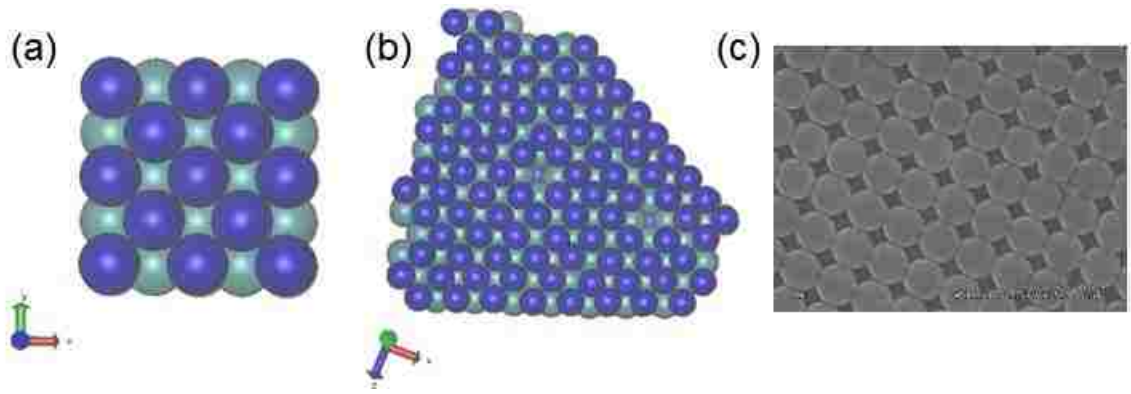

Figure 2.8: Comparison of planar views of as-obtained square-packed structure with that of (100) fcc structure (a) Ideal (100) fcc structure generated by VMD (b) VMD rendering of actual particles constituting square-packed region (c) SEM image of the sample

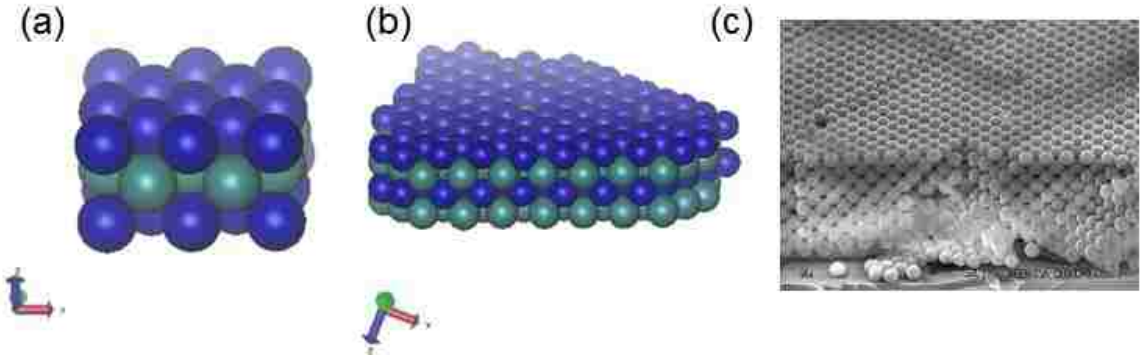

Figure 2.9: Comparison of cross-sectional views of as-obtained square-packed structure with that of (100) fcc structure (a) Ideal (100) fcc structure generated by VMD (b) VMD rendering of actual particles constituting square-packing (c) SEM image of the sample

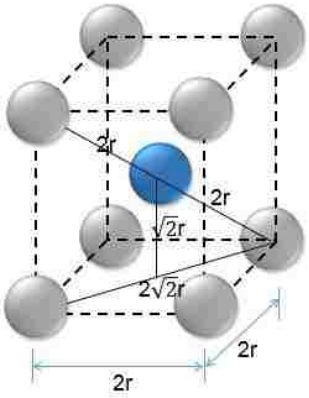

Figure 2.10: Schematic of a (100) fcc unit cell

For square-packed structure obtained with 0.93 µm PS particles, the distance between consecutive layers, averaged over multiple unit cells were found to be 0.64 µm, which matches with the theoretical value of 0.657 µm with an error of 2 % owing to the optical resolution limit of the instrument. Also, the packing fraction of actual structure obtained by CLSM analysis was found to be 76 %, which is almost equal to that of the fcc structure.

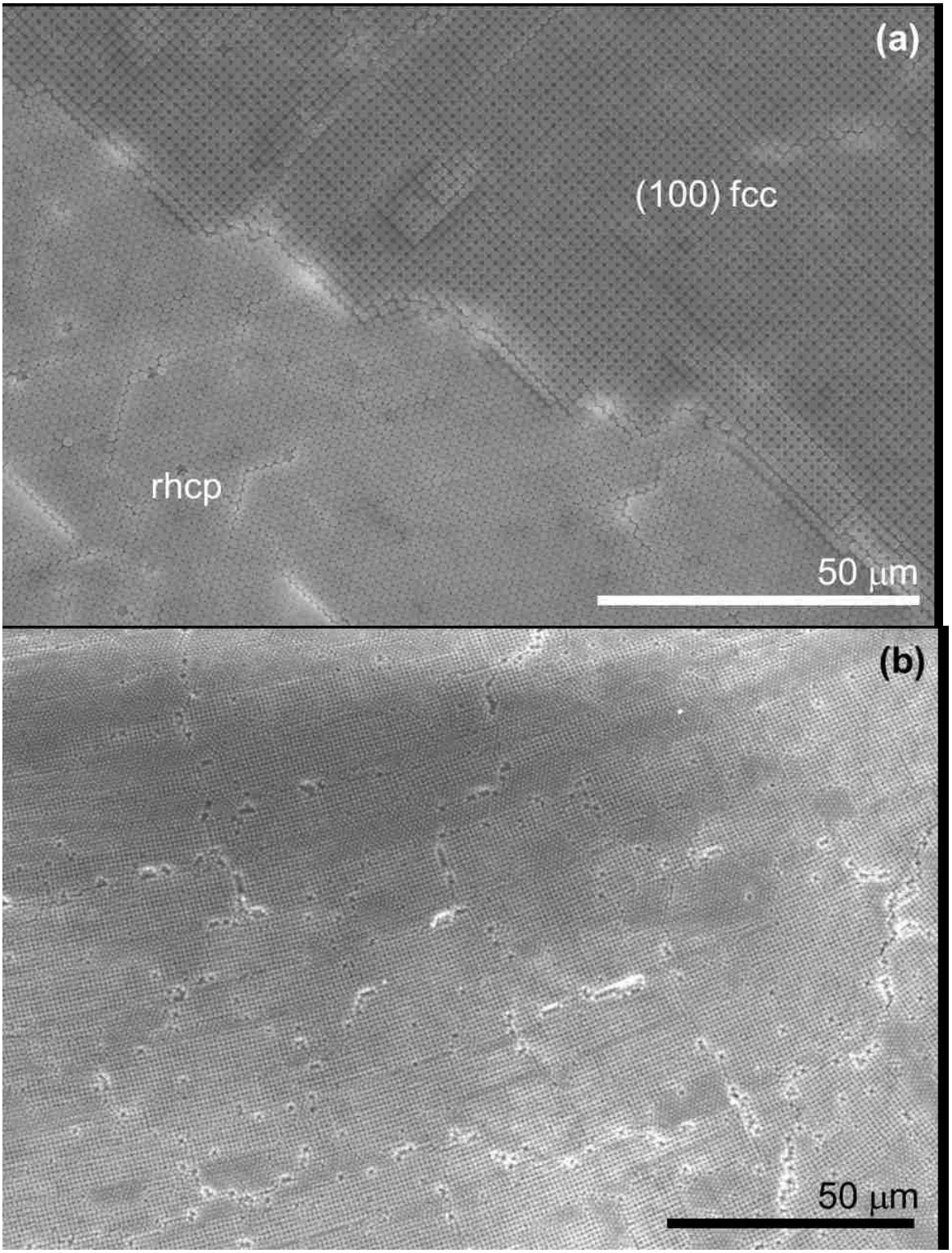

Figure 2.11: (100) fcc domains realized by vibration-assisted convective deposition of (a) 1.5 μm polystyrene particles and (b) 1 μm silica particles.

2.3.1 Effect of colloidal crystal thickness and substrate on generation of FCC (100)

The simultaneous generation of extensive domains of both square and hexagonally packed structures in multi-layer colloidal crystals assembled via vibration-assisted convective deposition stands in striking contrast to other reports on pure rhcp mono- and multi-layer colloidal crystalline structures from vibration-free[12–15] deposition methods. Similarly, only pure hexagonally assembled regions were obtained when vibration-assisted approaches[42] were used to generate mono-layer colloidal crystals. This underscores the apparent sensitivity of the constituent particle symmetry to the vibrations imposed during convective deposition, and the potential additional role of colloidal crystal thickness in controlling the existence, persistence, and extent of the unique (100) fcc domains.

For initial insight into the latter, we have systematically varied the multi-layer thickness of vibration-assisted, convectively deposited colloidal crystals, and have employed extensive CLSM and complementary particle identification and tracking algorithms to quantify properties such as particle-particle connectivity, crystal symmetry, and crystal orientation. Figure 2.12 depicts how the fraction of square-packed (100) fcc crystalline domains varies with the number of layers in multi-layer colloidal crystal assemblies. Here, the thickness of the colloidal crystal was tuned by controlling either the deposition speed (open symbols, Figure2.12) or the evaporative solvent flux (i.e., by relative humidity; filled symbols, Figure2.12). Both factors have been established by previous works[12] to independently tune the thickness of convectively deposited colloidal crystals. The fraction of square packing in the crystal assembly increases with a stronger than linear trend with increasing crystal thickness after an apparent threshold thickness of approximately 3 layers is exceeded. At or below the threshold thickness, vibration-assisted

colloidal crystal assemblies are dominated by hexagonally packed regions with small but measurable fractions of (100) fcc crystal domains. The small fraction of (100) fcc domains are attributed to localized regions marking transitions in the number of multi-layers in the colloidal crystal, resulting from confinement effects[13] .

As shown in Figure2.12, as the threshold colloidal crystal thickness is exceeded, the mechanism responsible for the generation of (100) fcc structures due to vibration becomes increasingly dominant. Colloidal crystals comprised of nearly 40% (100) fcc domains are achieved for samples as thick as just ten layers. The extensive (100) fcc domains appear to form independent of the aforementioned thickness-transition effects[12,13,24,25]. CLSM analysis at grain boundaries in the colloidal crystal (e.g., Figure 2.7c) has confirmed that square-packed domains generally have identical numbers of particle layers as bordering hexagonally-packed regions such that the colloidal crystals have a remarkably uniform overall thickness. Perhaps as noteworthy as the facile formation and extent of the (100) fcc domains is the apparent robustness of the process to a wide range of system conditions and material properties. Figure 2.12 shows remarkably good agreement for the threshold number of colloidal layers (i.e., ca. 3) and the measured fraction of (100) fcc domains with increasing thickness for crystals for which the thickness was tuned by different means (i.e., deposition rate, evaporative flux). Furthermore, the monotonically increasing fraction of (100) fcc regions appears insensitive to variations in chemical composition of the substrate. Similar results were obtained for assemblies of PS particles on glass as well as glass-supported 2 μm thick polystyrene films.

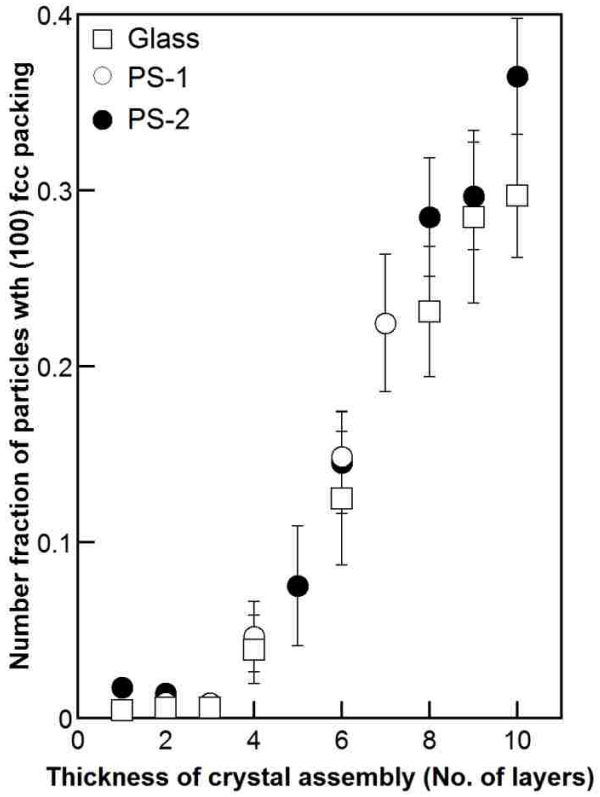

Figure 2.12:Sensitivity of fraction of (100) fcc domains to colloidal crystal thickness and substrate chemistry Variation of the number fraction of (100) fcc domains with number of layers for colloidal-crystal assemblies of 0.93 μm PS particles, on plain glass (□) where colloidal crystal thickness has been changed by tuning the vibration-assisted convective deposition rate from 6 μm/s (monolayer colloidal crystal) to 2 μm/s (10-layer colloidal crystal) in the presence of a fixed relative humidity of 55 %. Complementary analysis is shown of colloidal crystals deposited on a polystyrene film (circles), for which the thickness of the multi-layered colloidal crystal has been tuned by variation in deposition speed, PS-1 (○), and variation in humidity, PS-2(●)

2.3.2 Effect of blade angle on generation of FCC (100)

The preliminary studies on conventional self-assembly procedures performed in the group by Kumnorkaew et. al.[15] showed a high degree of dependence of assembled colloidal crystal on the blade geometry. However this was found to be negligible in the case of vibration assisted process, the results in Figure 2.13 obtained with a hydrophobic blade end for various angles in the range of 20-70 degrees. These results signify that the characteristics of the colloidal crystal assembly depends only on the nature of the thin liquid meniscus, and not the bulk suspension characteristics.

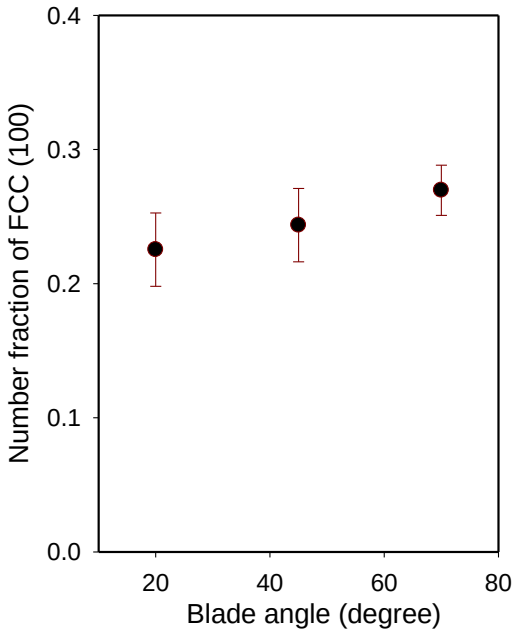

Figure 2.13: Variation of square-packing with deposition blade angle

2.3.3 Effect of vibration conditions on generation of FCC (100)

The formation of square packing in colloidal crystal samples were analyzed for various vibration conditions- namely frequency and amplitude of vibration. These were aimed at identifying the conditions beyond which the formation of square packing might be suppressed within the crystals. To achieve an accurate estimate of the vibration conditions, calibration studies were initially performed on the set-up to correlate the amplitude units (V_{pp}) to its micrometer counterpart. This was achieved by recording the movement of the stage for a definite amplitude and frequency using a high speed camera, followed by an estimation of the amplitude values using feature tracking tools. The calibration curves thus obtained for various frequencies are shown in Figure A1 and Figure A2 (Appendix).

The range of frequencies which could be studied by parametric studies were limited by the constraints with regards to obtaining a uniformly thick sample of sufficient investigable area at a given condition. To eliminate the dependence of square packing formation on colloidal crystal thickness, multiple samples were prepared with a given amplitude-frequency combination, achieved by varying the deposition speed or relative humidity. Of these multiple samples fabricated, only those with eight layers as confirmed using a confocal microscopy z-scan were chosen for analysis. This enables an accurate estimation of frequency and amplitude on square packing formation. Furthermore, the range of frequencies used for experiments were varied only in the range of 30 Hz – 60 Hz. At lower frequencies, the oscillatory nature of vibration makes it unworkable to restrain the liquid suspension within the angular volume bounded by the deposition blade, whereas suspension instabilities result in significant streak formation at higher frequencies.

For the range of frequencies from 35 Hz- 60 Hz, three amplitude values were chosen for experiments:

(i) Low amplitude – 325 μm

(ii) Medium amplitude – 620 μm

(iii) High amplitude – 1200 μm

The results for these studies are shown in Figure 2.14. From the plots, it could be observed that the fraction of square packing remains relatively unchanged, at least for the range of frequencies considered. It could be postulated that the range of vibration conditions employed in these studies are higher than the threshold conditions sufficient to realize the formation of square packed nucleates within the suspension. Even though these studies were not successful in identifying a threshold parameter for square packing formation, it nevertheless demonstrates the robustness of the reported technique to achieve these assemblies.

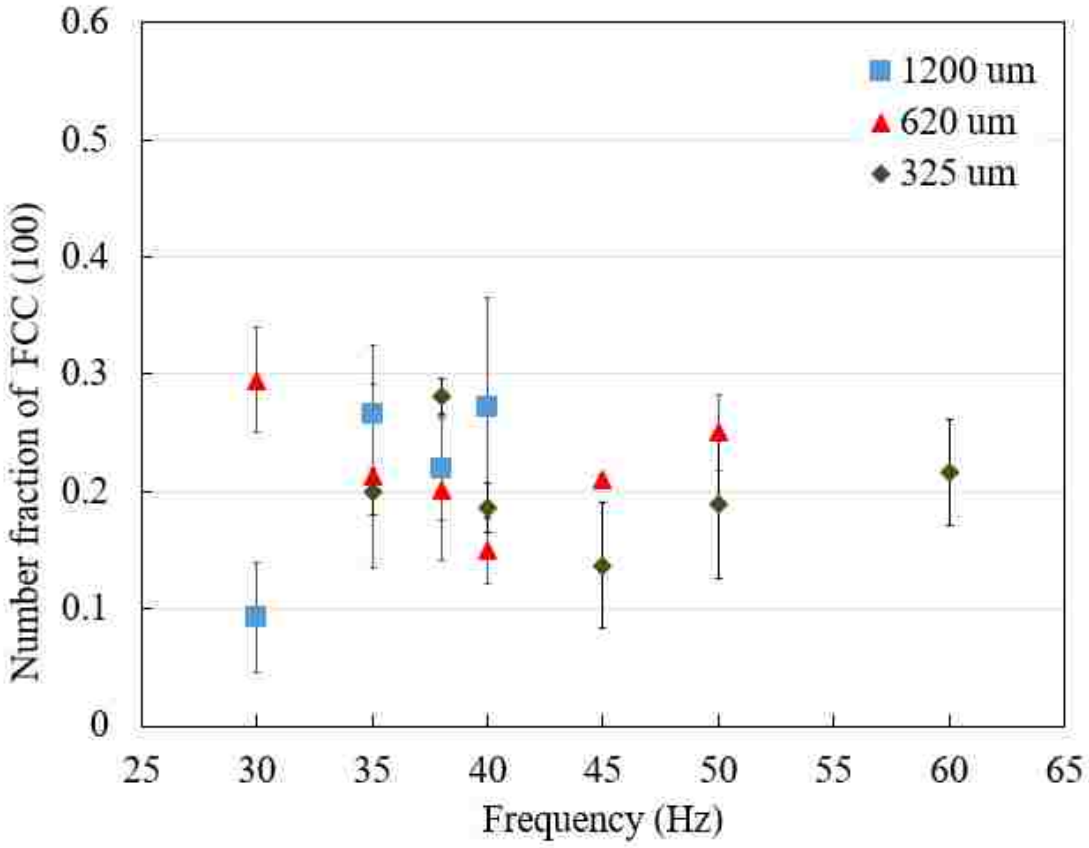

Figure 2.14: Variation of square-packing with frequency and amplitude of the sinusoidal vibrations. From the plots, it could be observed that for the colloidal crystals fabricated with a thickness of eight layers, the fraction of square packing remains close to 0.2 (as observed in Figure 2.12)

2.4 Applications of self-assembled (100) fcc structures

The square-packed arrangement of particles in the self-assembled colloidal crystal has several applications, both in their assembled form as well as the inverse-opal structure. The inverse-opal structure can be derived from the colloidal crystal assembly by infiltrating the voids with a suitable precursor salt, followed by reduction of the salt to the respective organic/ inorganic phase and subsequent removal of the template. These colloidal crystal assemblies as well as the inverse opal structures can be used for the following applications:

2.4.1 As template to obtain non close-packed structures

The square-packing structures obtained can be used as a template to obtain body-centered cubic arrangement of particles. In comparison to close packed structures, the non-close packed structures possess a much lower packing efficiency, and this provides it with unique photonic properties[44]. The higher void fractions of these non-close packed structures makes them easier to infiltrate[44],in addition to several applications in photonic fields. They also provide superior electronic and photonic properties, with enhanced optical, electronic and photovoltaic device performance. [45]

The fabrication of bcc structures from the square-packed fcc structure involves employing the latter as a template, thereby directing the colloidal particles of a reduced size onto the surface-voids of the square-packed structures. This, when implemented in a layer-by-layer fabrication approach (as shown in Figure 2.15) enables the manipulation of the packing fraction of the hierarchically assembled colloidal crystal system. A few preliminary experiments were performance to test the compatibility of this approach to obtain non-close packed structures. The initial colloidal-crystal assembly with square-

packing arrangement of particles were obtained with 1.5 μm PS particles which was heat-treated to improve the mechanical stability of the assembly and then rendered hydrophilic by plasma-treatment. A colloidal suspension of 0.93 μm PS particles, when dragged over the colloidal-crystal assembly at an optimal velocity results in these particles getting selectively captured into the voids present in the surface layer of the colloidal crystal. The resulting structure after the deposition of a single layer is shown in Figure 2.16 (a,b)

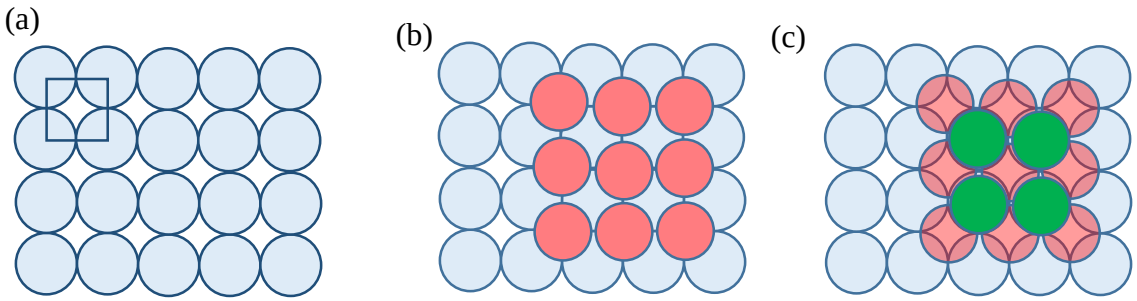

Figure 2.15: Fabrication procedure of non-close packed (ncp) structures by layer-by-layer assembly procedure on a square-packed colloidal crystal, (a) Surface layer of square-packed crystal (b) First layer of ncp structure (c) Second layer of ncp arrangement

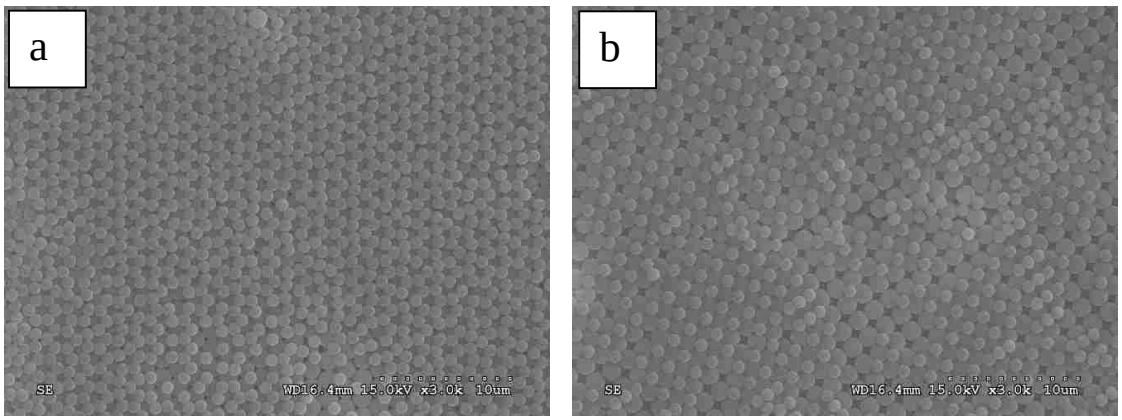

Figure 2.16: Non-close packed (ncp) structures by layer-by-layer assembly procedure
(a) Layer of 0.93 µm PS particles packed into the voids of hexagonally packed colloidal crystal of 1.5 µm (b) 0.93 µm PS particles packed into the voids of square-packed regions

2.4.2 Photonic crystal applications

The as-assembled colloidal-crystal assemblies of polystyrene particles with air voids has a low refractive-index contrast and hence does not exhibit a photonic band gap (PBG)[46]. However, these structures can be tuned to the required PBG by infiltrating the voids with a suitable sol-gel, followed by calcination to obtain the corresponding inorganic matrix. The photonic properties of this colloidal crystal assembly of particles can be tuned to obtain various band gaps by varying the lattice parameter, void fraction of the periodic structures, refractive indices of the materials involved or by obtaining new structures by infiltration of the void space with a suitable precursor salt[47]. It has been reported that the inverse replicas obtained by the infiltration of colloidal crystals with silicon salt and subsequent heat treatment yields a wider band gap of 9.59 % [48] with a non-close packed structure compared to a close-packed structure[44].

The successful implementation of such inverse-opal structures for photonic applications requires a colloidal-assembly with a well-interconnected and mechanically stable pore structure. To demonstrate the void-space architecture of the fabricated colloidal structures, the colloidal-crystal assembly was infiltrated with an MgO precursor and subsequently heat treated to obtain MgO. The resulting structure (Figure 2.17) shows a 3-D interconnected void-space architecture.

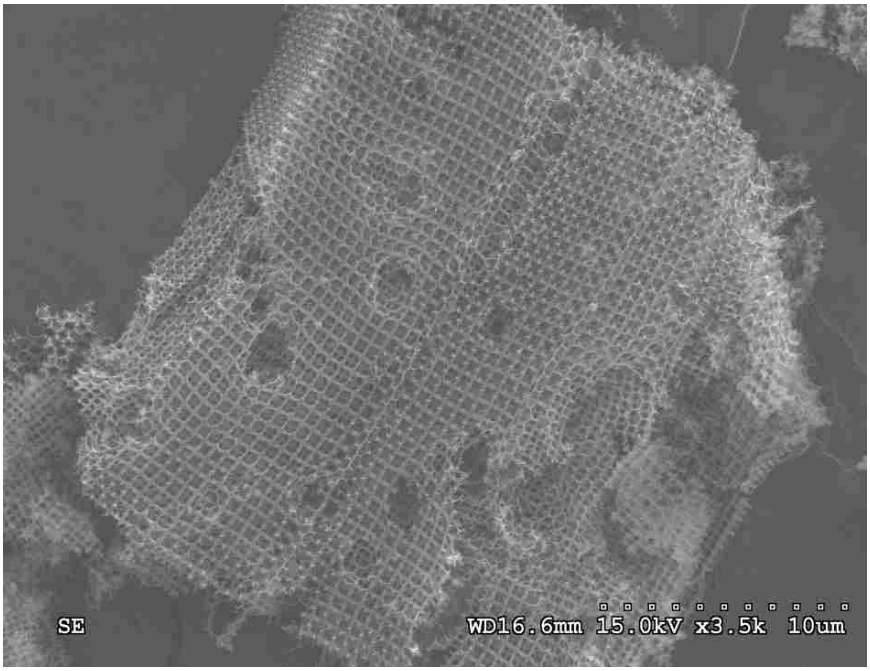

Figure 2.17: Inverse opal MgO structure with the square-packed colloidal crystal as the template

2.5 Conclusion

The realization of flow-induced (100) fcc domains by vibration-assisted convective deposition may eliminate the need for accurate substrate patterning and highly-controlled crystal growth that is critical for achieving colloidal crystals of similar crystalline symmetry by alternative state-of-the-art colloidal epitaxy approaches. The robustness of the process coupled with the intrinsic scalability of convective deposition holds exciting potential for realization of large area (100) fcc crystals. The ease with which the colloidal crystal films can be delaminated from the substrate upon which they were deposited for the purpose of generating free standing structures also circumvents one of the key limitations of epitaxial grown structures for which such delamination is more difficult. Yet, scalability hinges, at least in part, upon the ability to tune properties such as the size and orientation of the (100) fcc domains, a prospect demanding fundamental insight into the underlying mechanisms of their formation and their sensitivities to system parameters and flow conditions intrinsic to vibration-assisted convective deposition.

2.6 References

1. Pusey, P. N. & Megen, W. van. Phase behaviour of concentrated suspensions of nearly hard colloidal spheres. *Nature* **320,** 340–342 (1986).

2. Philp, D. & Stoddart, J. F. Self-assembly in natural and unnatural systems. *Angew. Chemie* **35,** 1154–1196 (1996).

3. Min, Y., Akbulut, M., Kristiansen, K., Golan, Y. & Israelachvili, J. The role of interparticle and external forces in nanoparticle assembly. *Nat. Mater.* **7,** 527–38 (2008).

4. Bishop, K. J. M., Wilmer, C. E., Soh, S. & Grzybowski, B. A. Nanoscale forces and their uses in self-assembly. *Small* **5,** 1600–1630 (2009).

5. Whitesides, G. M. & Grzybowski, B. Self-assembly at all scales. *Science (80-.).* **295,** 2418–2421 (2002).

6. Park, S. H., Qin, D. & Xia, Y. Crystallization of Mesoscale Particles over Large Areas. *Adv. Mater.* **10,** 1028–1032 (1998).

7. Jiang, P. & McFarland, M. J. Large-scale fabrication of wafer-size colloidal crystals, macroporous polymers and nanocomposites by spin-coating. *J. Am. Chem. Soc.* **126,** 13778–13786 (2004).

8. Ruhl, T., Spahn, P. & Hellmann, G. P. Artificial opals prepared by melt compression. *Polymer (Guildf).* **44,** 7625–7634 (2003).

9. Shereda, L. T., Larson, R. G. & Solomon, M. J. Boundary-driven colloidal crystallization in simple shear flow. *Phys. Rev. Lett.* **105,** 228302 (2010).

10. Hayward, R. C., Saville, D. A. & Aksay, I. A. Electrophoretic assembly of colloidal crystals with optically tunable micropatterns. *Nature* **404,** 56–59 (2000).

11. Smoukov, S. K., Gangwal, S., Marquez, M. & Velev, O. D. Reconfigurable responsive structures assembled from magnetic Janus particles. *Soft Matter* **5,** 1285–1292 (2009).

12. Dimitrov, A. & Nagayama, K. Continuous convective assembling of fine particles into two-dimensional arrays on solid surfaces. *Langmuir* **12,** 1303–1311 (1996).

13. Prevo, B. G. & Velev, O. D. Controlled, rapid deposition of structured coatings from micro- and nanoparticle suspensions. *Langmuir* **20,** 2099–2107 (2004).

14. Ghosh, M., Fan, F. & Stebe, K. J. Spontaneous pattern formation by dip coating of colloidal suspensions on homogeneous surfaces. *Langmuir* **23,** 2180–2183 (2007).

15. Kumnorkaew, P., Ee, Y. K., Tansu, N. & Gilchrist, J. F. Investigation of the deposition of microsphere monolayers for fabrication of microlens arrays. *Langmuir* **24,** 12150–12157 (2008).

16. Vlasov, Y. A., Bo, X. Z., Sturm, J. C. & Norris, D. J. On-chip natural assembly of

silicon photonic bandgap crystals. *Nature* **414,** 289–293 (2001).

17. Jin, C. *et al.* Optical properties of tetragonal photonic crystal synthesized via template-assisted self-assembly. *J. Appl. Phys.* **99,** 116109 (2006).

18. Yang, Z., Huang, X., Li, S. & Zhou, J. Photonic bandgap and photoluminescence in TbPO4 inverse opal with coexistence of the (001) and (111) orientations. *J. Am. Ceram. Soc.* **92,** 1596–1598 (2009).

19. Sun, S., Murray, C. B., Weller, D., Folks, L. & Moser, A. Monodisperse FePt nanoparticles and ferromagnetic FePt nanocrystal superlattices. *Science (80-.).* **287,** 1989–1992 (2000).

20. Kazakova, O., Hanson, M., Blomqvist, P. & Wäppling, R. Interplay between shape and magnetocrystalline anisotropies in patterned bcc Fe/Co(001) multilayers. *Phys. Rev. B* **69,** 094408 (2004).

21. An, X. Z. & Yu, A. B. Analysis of the forces in ordered FCC packings with different orientations. *Powder Technol.* **248,** 121–130 (2013).

22. Sirota, E. B., Ou-Yang, H. D., Sinha, S. K. & Chaikin, P. M. Complete phase diagram of a charged colloidal system: A synchrotron x-ray scattering study. *Phys. Rev. Lett.* **62,** 1524–1527 (1989).

23. Woodcock, L. V. Entropy difference between the face-centred cubic and hexagonal close-packed crystal structures. *Nature* **385,** 141–143 (1997).

24. Pieranski, P., Strzelecki, L. & Pansu, B. Thin colloidal crystals. *Phys. Rev. Lett.* **50,** 900–904 (1983).

25. Meng, L. *et al.* The role of thickness transitions in convective assembly. *Nano Lett.* **6,** 2249–2253 (2006).

26. Blaaderen, A. Van, Ruel, R. & Wiltzius, P. Template-directed colloidal crystallization. *Nature* **385,** 321–324 (1997).

27. Zhang, J. *et al.* Template-directed convective assembly of three-dimensional face-centered-cubic colloidal crystals. *Appl. Phys. Lett.* **81,** 3176–3178 (2002).

28. Yi, D. K., Seo, E. M. & Kim, D. Y. Surface-modulation-controlled three-dimensional colloidal crystals. *Appl. Phys. Lett.* **80,** 225–227 (2002).

29. Lee, W., Chan, A., Bevan, M. A., Lewis, J. A. & Braun, P. V. Nanoparticle-mediated epitaxial assembly of colloidal crystals on patterned substrates. *Langmuir* **20,** 5262–5270 (2004).

30. Hoogenboom, J. P. *et al.* Template-induced growth of close-packed and non-close-packed colloidal crystals during solvent evaporation. *Nano Lett.* **4,** 205–208 (2004).

31. Jin, C., McLachlan, M. A., McComb, D. W., Rue, R. M. D. La & Johnson, N. P. Template-assisted growth of nominally cubic (100)-oriented three-dimensional crack-free photonic crystals. *Nano Lett.* **5,** 2646–2650 (2005).

32. Yin, Y., Li, Z. Y. & Xia, Y. Template-directed growth of (100) -oriented colloidal crystals. *Langmuir* **19,** 622–631 (2003).

33. Tanaka, M., Shimamoto, N., Tanii, T., Ohdomari, I. & Nishide, H. Packing of submicrometer-sized polystyrene particles within the micrometer-sized recessed patterns on silicon substrate. *Sci. Technol. Adv. Mater.* **7,** 451–455 (2006).

34. Fan, F. & Stebe, K. J. Assembly of colloidal particles by evaporation on surfaces with patterned hydrophobicity. *Langmuir* **20,** 3062–3067 (2004).

35. Fudouzi, H., Kobayashi, M. & Shinya, N. Assembly of microsized colloidal particles on electrostatic regions patterned through ion beam irradiation. *Langmuir* **18,** 7648–7652 (2002).

36. Winkleman, A., Gates, B. D., McCarty, L. S. & Whitesides, G. M. Directed self-assembly of spherical particles on patterned electrodes by an applied electric field. *Adv. Mater.* **17,** 1507–1511 (2005).

37. Gregory M.Gratson, Mingjie Xu, J. A. L. Direct writing of three- dimensional webs. *Nature* **428,** 2481 (2004).

38. Zarzar, L. D. *et al.* Direct Writing and Actuation of Three-Dimensionally Patterned Hydrogel Pads on Micropillar Supports. *Angew. Chemie* **123,** 9528–9532 (2011).

39. Campbell, M., Sharp, D. ., Harrison, M. ., Denning, R. . & Turberfield, A. . Fabrication of photonic crystals for the visible spectrum by holographic lithography. *Nature* **404,** 53–56 (2000).

40. Macfarlane, R. J. *et al.* Assembly and organization processes in DNA-directed colloidal crystallization. **106,** (2009).

41. Vossen, D. L. J., Hoogenboom, J. P., Overgaag, K. & Blaaderen, A. Van. Building Two and Three-dimensional Structures of Colloidal Particles on Surfaces using Optical Tweezers and Critical Point Drying. **705,** 1–6 (2002).

42. Muangnapoh, T., Weldon, A. L. & Gilchrist, J. F. Enhanced colloidal monolayer assembly via vibration-assisted convective deposition. *Appl. Phys. Lett.* **103,** 181603 (2013).

43. Crocker, J. C. & Grier, D. G. Methods of digital video microscopy for colloidal studies. *J. Colloid Interface Sci.* **310,** 298–310 (1996).

44. Meseguer, F. & Fenollosa, R. Non-close packed colloidal crystals. *J. Mater. Chem.* **15,** 4577 (2005).

45. Tan, K. W. *et al.* Colloidal Self-Assembly-Directed Crystalline Silicon Nanostructures. *ACS Nano* 7960–7966 (2011).

46. Shishkin, I. I. *et al.* Inverted Yablonovite-like 3D photonic crystals fabricated by laser nanolithography. in *Proc. SPIE Vol. 8425* (Míguez, H. R., Romanov, S. G., Andreani, L. C. & Seassal, C.) **8425,** 84252C–1–84252C–5 (2012).

47. Arpin, K. a *et al.* Multidimensional architectures for functional optical devices. *Adv.*

Mater. **22,** 1084–1101 (2010).

48. Doosje, M., Hoenders, B. J. & Knoester, J. Photonic bandgap optimization in inverted fcc photonic crystals. *J. Opt. Soc. Am. B* **17,** 600 (2000).

49. Snezhko, A. & Aranson, I. S. Magnetic manipulation of self-assembled colloidal asters. *Nat. Mater.* **10,** 698–703 (2011).

50. Tohver, V., Smay, J. E., Braem, a, Braun, P. V & Lewis, J. a. Nanoparticle halos: a new colloid stabilization mechanism. *Proc. Natl. Acad. Sci. U. S. A.* **98,** 8950–4 (2001).

51. Lin, Y. *et al.* Self-directed self-assembly of nanoparticle/copolymer mixtures. *Nature* **434,** 55–59 (2005).

52. Jenekhe, S. A. & Chen, X. L. Self-Assembly of Ordered Microporous Materials from Rod-Coil Block Copolymers. *Science (80-.).* **283,** 372–375 (1999).

3

Investigation of the mechanism for generation of square packing in colloidal crystals

3.1 Introduction

The dynamics of the crystal assembly and the resulting packing structure in vibration-assisted processes is driven by the combined effects of inter-particle forces and hydrodynamic effects generated by the experimental conditions. The studies being discussed in this chapter pertains to gaining an insight into the underlying mechanism for the observed square packing in colloidal crystals, which could in addition provide a clue to tailor the process to achieve high-quality colloidal crystals with a greater degree of structural diversity.

A clear mechanistic understanding of the generation of varying packing structures with the introduction of external vibration demands a proper understanding of the processes involved, each of them analyzed separately to discern its individual contribution to the overall results observed. The generation of a multilayer crystal in a conventional convective assembly process progresses via a single planar growth and is driven by the "convective steering" of colloidal particles towards the growth front. In contrast, the growth of a colloidal crystal in vibration-assisted deposition follows a mechanism with significant variation with respect to the growth front characteristics. The addition of

external periodic vibration creates a back-and-forth movement of the meniscus, resulting in a dynamic meniscus shape and high shearing forces exerted on the suspension.

The suspension 'microstructure' (which refers to the interparticle ordering in a suspension) at equilibrium as well as non-equilibrium conditions is determined by a variety of factors, the major ones being the relative magnitude of brownian forces (or diffusive forces) and hydrodynamic forces (convective forces) in suspension, concentration of the suspension and electrostatic interaction between the particles (attractive or repulsive). For dilute suspensions (~0.1 wt. %) at rest, various microstructures have been reported – liquid like uniform ordering with characteristic Debye-Scherrer ring (when brownian forces dominate), crystalline orderings with bcc or fcc configurations (repulsive interaction between charge stabilized particles), crystalline orderings with rhcp or fcc configurations (repulsive interaction between sterically stabilized particles) as well as formation of aggregates or gels (attractive interaction between particles). In addition, a fully crystalline state is also observed when the suspension concentration is high (>~ 50 wt. %).

When a suspension in equilibrium is subjected to shearing forces (e.g. arising from flow), the hydrodynamic forces becomes dominant[1]. A measure of the relative effect of both driving forces – Brownian forces and hydrodynamic forces on the suspension microstructure in such a scenario can be characterized by the Peclet number, given by:

$$Pe = \frac{Convective\ forces}{Diffusive\ forces} = \frac{\dot{\gamma} a^2}{D_0} = \frac{6\pi\eta_0 a^3 \dot{\gamma}}{k_B T}$$

At low Peclet numbers (Pe<< 1), the microstructure is isotropic in nature. However, they become increasingly distorted at higher Peclet number values due to the hydrodynamic forces acting on the microstructure along the compressional and extensional axes, thus

making the suspensions ‘Non-newtonian’ in nature. The evolution of these microstructures have been analyzed both by in-situ experimental techniques (light scattering, confocal imaging, neutron scattering, x-ray scattering etc) as well as by theoretical and numerical methods. These techniques permit a characterization of the microstructures, both their structure factor (representative of the interparticle ordering in microstructures) as well as the orientation with respect to the velocity – velocity gradient – vorticity planes of the shearing forces (a schematic of the various planes investigated shown in Figure 3.1 for a concentric cylinder geometry).

Research work pertaining to shear-induced ordering in suspensions has mainly focused on two scenarios – steady-state shear and oscillatory shear (predominantly at high amplitude and referred to as ‘Large-amplitude oscillatory shear’), either of them differentiated based on whether the direction of velocity component remains constant (steady-state shear) or periodically oscillates in direction (oscillatory shear) during the course of experimental investigation. While a steady state shear of the suspension can be observed in a conventional convective deposition process, oscillatory shear becomes dominant in vibration-assisted deposition, and would be the focus in this chapter.

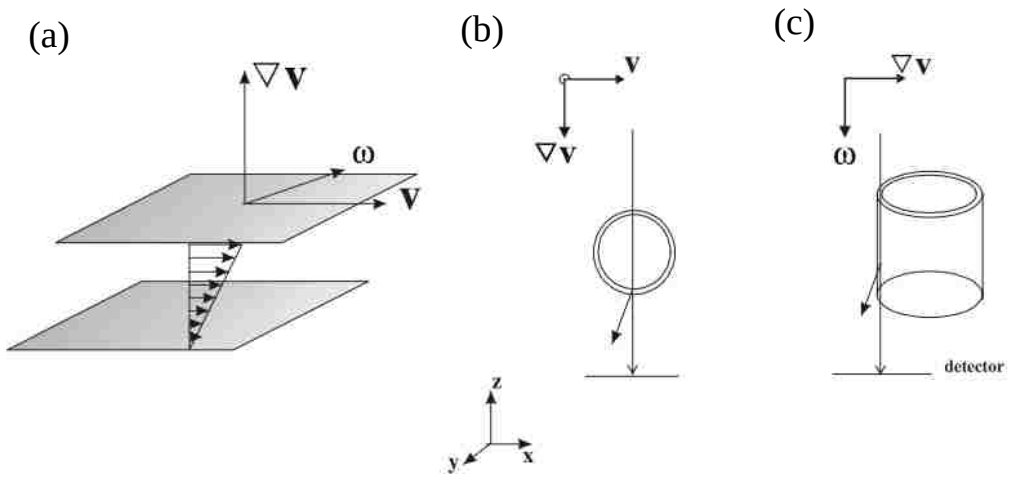

Figure 3.1: Analysis of suspension microstructures in a shear cell[2] (a) Representative shear cell geometry showing the velocity (V), velocity gradient (ΔV) and vorticity (ω) directions (b) Propagation of scanning incident beam along the velocity gradient direction, giving a projection of the microstructure in V-ω plane for a couette-cell geometry (c) Incident beam along the vorticity direction with the resulting projection in ΔV-ω plane. (Figures shown were adapted from the corresponding references)

3.1.1 Phase transitions in suspensions under shear

In addition to generation of particle clusters (nuclei), the addition of shearing forces has also been shown responsible for affecting a long-range ordering in the suspension, an observation first reported by Hoffman[3] and further investigated in detail by Ackerson group. When a colloidal suspension in equilibrium is subjected to shear, reversible phase transitions occur in the microstructures of the colloidal assemblies. The non-equilibrium structures thus generated in a sheared colloidal suspension depends both on the suspension properties (size, shape, concentration and surface charge of colloidal particles, ionic strength of solvent etc.) as well as the magnitude and nature of shearing forces.

At low particle concentration (~ 0.1 wt. %), a charged colloidal suspension generates body centered cubic crystal (bcc) at equilibrium[4]. Under shearing, these structures initially undergoes a transition into freely slipping two-dimensional hexagonal layers capable of slipping past one another in the velocity direction[5,6]. At higher shear rates, the shear melting of the crystal results in an amorphous phase. These phase transitions in dilute colloidal suspensions does not significantly alter the measured shear viscosity values of the suspension owing to the negligible effect of low particle densities[4].

The shear-induced ordering in suspensions becomes more pronounced with an increase in the concentration of the suspensions[7]. At high particle concentrations (> ~15 wt. %), shear induced phase transitions are highly reflected in the measured shear viscosity of suspensions, with the colloidal suspensions exhibiting a high viscosity at low shear rate, reduced viscosity at intermediate shear rates (shear thinning) and an increase in value at high shear rates (shear-thickening). Similar phase transitions have been reported for both steady-shear and oscillatory shear in colloidal suspensions of charged particles at high

volume fractions, however they are initiated at a much lower shear rates for oscillatory flow compared to steady shear (only at shear rates >100 s^{-1})[8]. The predominant microstructures generated in either scenarios are of four major categories – twinned fcc structure, layered structure, string-like structure and amorphous liquid-like structure, with phase transitions between various microstructures reported to be gradual with co-existing phases. The images in Figure 3.2 shows the scattered intensity distributions of these structures obtained using laser diffraction experiments in a shear cell, with the laser beam aligned parallel to the shear direction (direction of velocity gradient), the images being obtained corresponding to the velocity-vorticity plane. The inset image of each intensity distribution pattern represents a real-space reconstruction of the associated microstructure.

The evolution of various microstructures have been presented in detail in the paper by Ackerson[7], with similar transitions observed in the case of non-aqueous suspensions[9] as well for oscillatory shear. As reported by Ackerson, the equilibrium phase for concentrated aqueous suspensions (0.41 < volume fraction < 0.50) was amorphous or liquid like ordering yielding Debye-Scherrer rings (Figure 3.2f), which was maintained even at low strain amplitudes / applied stress. However, with increasing strain amplitudes, the intensity distribution reveals a three-fold symmetry pattern similar to an fcc structure, which oscillates between two mirror-image like patterns at the two extremes of an oscillation cycle. The origin of these twinned fcc structures have been attributed to easy slippage of (111) planes over one another giving rise to ABCA…. or ACBA… stacking sequence in fcc. The (111) planes of the fcc structure lies parallel to the shear-cell surface aligned along the velocity-vorticity plane, with each (111) plane representing a streamline of constant velocity. However, the close-packed direction of the (111) plane is aligned parallel to the

vorticity direction at low strain amplitudes (also reported for steady-shear experiments), they become aligned to the velocity direction at higher strain values (schematic of both orientations shown in Figure 3.3).

At higher strain amplitudes, the intensity distribution pattern generates a six-fold symmetry pattern, representative of a three-dimensional fcc crystal composed of randomly stacked close-packed planes of particles, with the close-packed direction now aligned in the direction of the velocity axis. Under the influence of shear, these layers continuously slip past one another either in a zig-zag fashion (Figure 3.2c) or in a straight path (Figure 3.2d).While a free slipping of planes is possible up to a volume fraction of 0.58 (wt. %), it becomes restricted to zig-zag movement above 0.58. At further high amplitudes, the (111) planes of the fcc structure (with close packing in direction of velocity) breaks up generating strings of particles oriented in the velocity direction – as observed in the intensity distribution plot of Figure 3.2e.

The phase-diagram representing the phase transitions in concentrated colloidal suspensions with increasing strain amplitudes in oscillatory shear conditions is given in Figure 3.4. The shear induced ordering has been investigated in flat-plate, couette-cell as well as concentric cylinder geometries and has been further developed upon by several groups to generate long-range ordered colloidal crystal assemblies by spin coating[10], shear flow crystallization[11], melt compression[12] etc. To obtain a long-range ordered colloidal assembly, the two underlying factors- direction of flow streamlines and magnitude of velocity gradient (which generates the shear stress) requires to be maintained uniform throughout the region of interest[11].

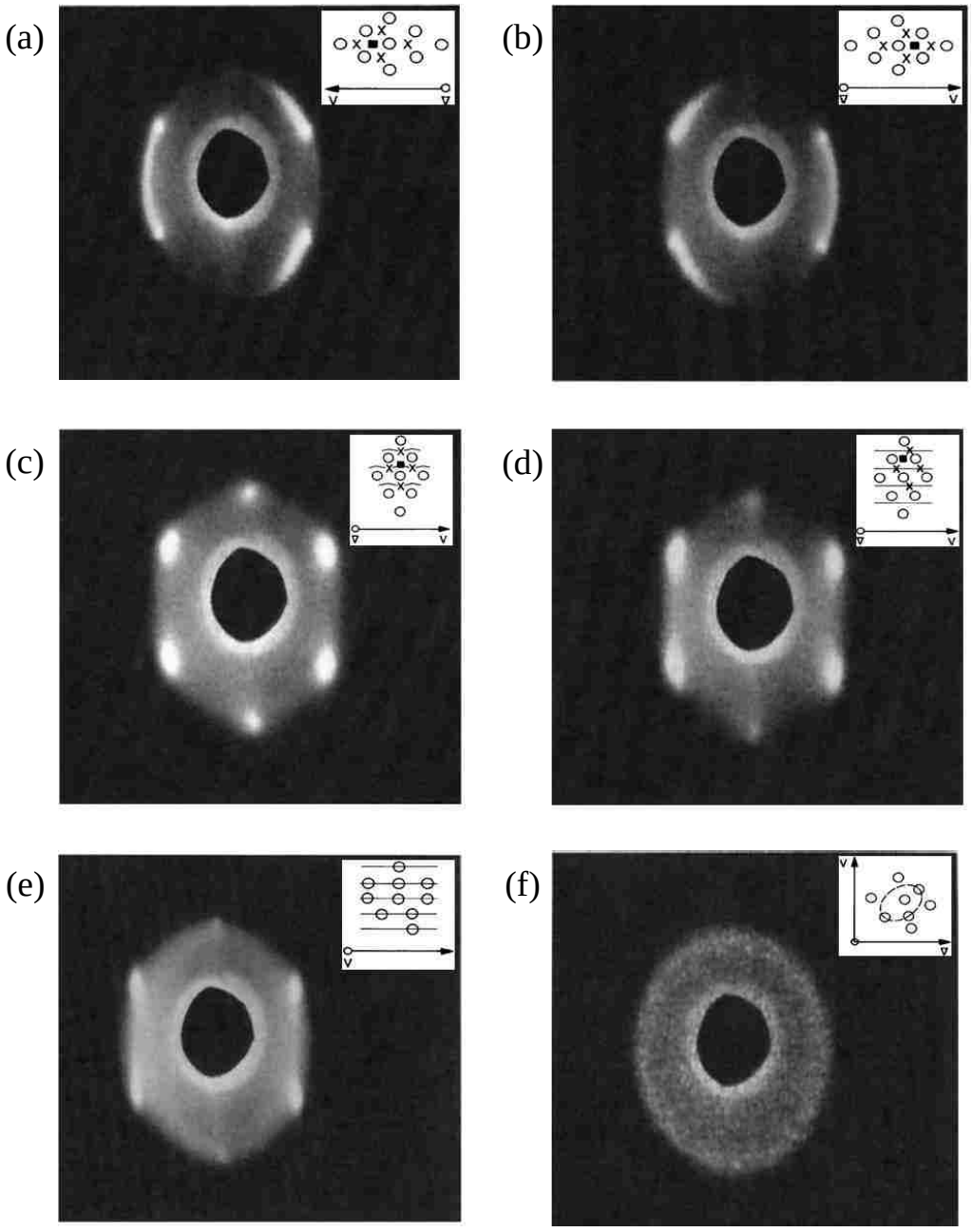

Figure 3.2: Scattered intensity distributions of various microstructures observed under steady shear and oscillatory shear in suspensions at high volume fractions, inset images represent the real space structures of the intensity patterns[7]**.** (a),(b) Twinned fcc structure (c) Six-fold symmetry pattern by randomly stacked layers (zig-zag movement) (d) Four-fold pattern by slipping of layers in straight line (e) String-like ordering and (f) Amorphous liquid-like ordering. (Figures shown were adapted from the corresponding references)

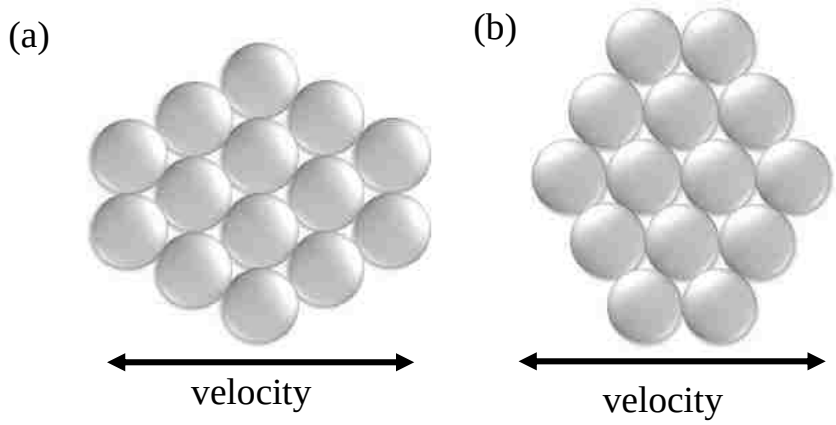

Figure 3.3: Orientation of close-packed direction of (111) fcc plane at various strain amplitudes (a) At low strain amplitudes, the close packed direction is oriented in vorticity direction (b) At higher strain amplitudes, the orientation is in the direction of velocity axis

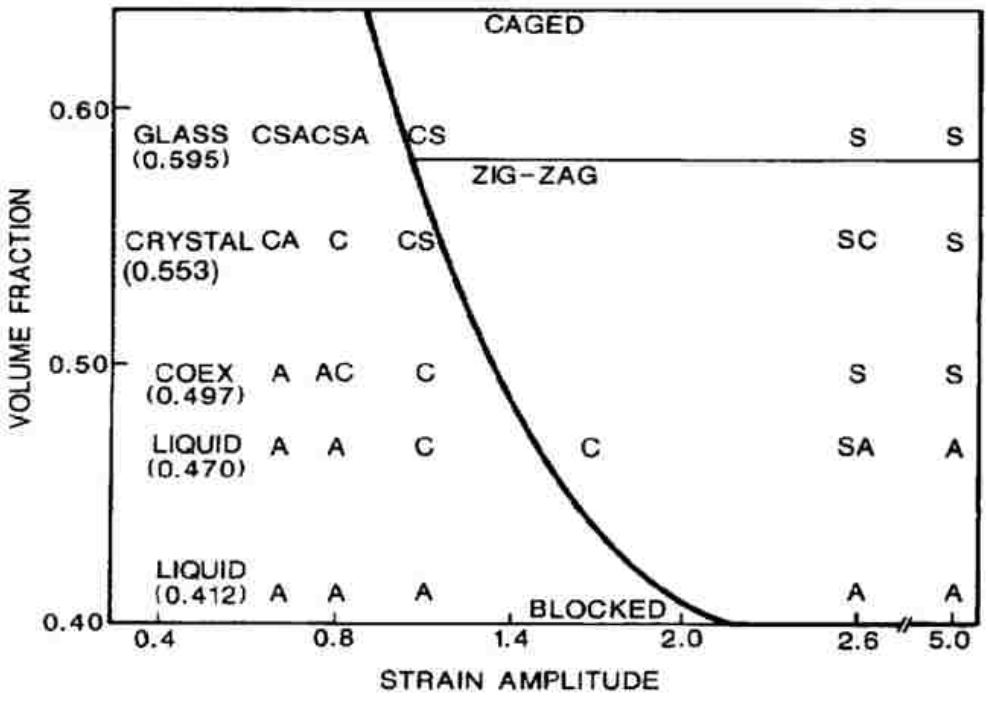

Figure 3.4 : Phase diagram for the microstructure transitions in colloidal suspension at high volume fraction subjected to oscillatory shear[7] (frequency = 3.5 Hz). The various phases are C: fcc, S: layer ordering, A: amorphous liquid. In the case of phases co-existing (CA,CS etc.), the first character denotes the predominant phase. (Figure shown was adapted from the corresponding reference)

3.1.2 Nucleation and growth in colloidal suspensions under shear

There are two dominant factors which drives the formation of polycrystalline particle arrangements in colloidal suspension subjected to an oscillatory shear. While the rate of homogeneous nucleation determines the overall number of stable nuclei (with size larger than critical nucleus size) which can be generated in the suspension, the rate of growth of these nuclei regulates the size distribution of various crystalline arrangements within the suspension. Significant research has been performed on the phenomenon of homogeneous nucleation and growth in suspensions under shear, both experimentally and theoretically by several research groups, summarized by the following observations:

(i) Colloidal suspensions subjected to an oscillatory shear exhibits contrasting behavior with regard to the nucleation rate, depending on the volume fraction of the suspension. At high volume fractions, the presence of shear has been observed to cause an increase in the homogeneous nucleation rate, attributed to the stable layered packing in suspension microstructures with hexagonal packing configuration at high strain amplitudes[13,14] (discussed in detail in Section 3.1.1). However at low particle fractions, the rate of homogeneous nucleation is suppressed when dilute suspensions of charged particles are subjected to oscillatory shear, demonstrated theoretically[15,16] as well as experimentally for weak shear. This results in limited number of stable nuclei being generated with size larger than the critical nucleus size. This has been investigated theoretically to discern if it occurs due to suppression of nucleation or due to breaking up of nuclei due to shear, with the theoretical inferences attributing it to the former. In suspensions at rest, the particles initially form local ordering within the suspension, which later converts to isolated particle clusters or nuclei. The presence of an

oscillatory shear significantly reduces the probability of particles to form these pre-ordered arrangements, thus resulting in limited number of stable nuclei in the suspension[16].

(ii) The presence of shear enhances the growth rate of nuclei: Another characteristic observation in shear-induced nucleation processes is that once a stable nucleus is formed beyond the critical nucleus size, the presence of shear enhances its growth. This may be due to the fact that under shear, the nucleus undergoes reorganization to adopt a favorable orientation with respect to the flow streamlines,which enables it to capture more approaching particles[15,16]. In addition, more particles are being driven to the growth front of the nucleus by convective forces in this case, enabling a faster growth of the generated nuclei.

3.2 Analysis of packing assemblies in vibration-assisted deposition

Two methodologies were adopted to gain an understanding of the underlying mechanism for the simultaneous formation of square and hexagonal packing assemblies in vibration-assisted deposition – a systematic analysis of the as-obtained packing structures and in-situ confocal studies. A detailed analysis of the packing assemblies involved extensive confocal imaging of the sample, followed by extracting significant information from the images by employing image analysis tools.

3.2.1 Analysis algorithm

The development of analysis algorithms was intended to obtain qualitative information about the packing configuration of the assembled colloidal crystal structures- both with respect to their local bond order as well as the relative orientation. While the former has been detailed in Chapter 2, the analysis in this chapter deals with identifying the square domains in the assembly and calculating their orientation with respect to the flow direction.

3.2.1.1 Identification of (100) fcc domains

A (100) fcc domain represents a grouping of particles belonging to 4 nearest neighbor (NN) category and lying adjacent to each other forming a continuous region. The particle grouping based on the characteristics of its nearest neighbors uses a relaxed criteria of two particle diameters for the scaled centroid co-ordinates. A representational grouping of 4 NN particles into various domains is shown in Figure 3.5b. The typical grouping of 4 NN particles is considered to be a domain only if there are at least 100 particles in the grouping and has at least ten 4 NN particles with $|\psi_4| \geq 0.77$.

3.2.1.2 Calculation of orientation of (100) fcc domains

The calculation procedure for the estimation of cubic-domain orientations is a two-step process, in which the local orientation of the particles is first calculated, which is then averaged to obtain the orientation of the entire domain. For each particle identified as a part of any fcc(100) domain (and actually containing 4 NN) , the local orientation of the particle is calculated as the average of the bond angles of the particle with each of its four neighbors.

$$\theta_{orient,p}{}' = \frac{1}{4}\left(\left|\theta_{1,p} - 0\right| + \left|\theta_{2,p} - 90\right| + \left|\theta_{3,p} - 180\right| + \left|\theta_{4,p} - 270\right|\right)$$

where $\theta_{i,p}(\, i = 1,2,3,4)$ is the bond-angle of 'p' with each of its four neighbors

$\theta_{orient,p} = modulus(\theta_{orient,p}{}', 90)$

if $\theta_{orient,p} > 45, then\ \theta_{orient,p} = 90 - \ \theta_{orient,p}$

The orientation of a domain is calculated by averaging the orientation of the individual particles constituting the domain, a representational sketch given in Figure 3.5b.

.

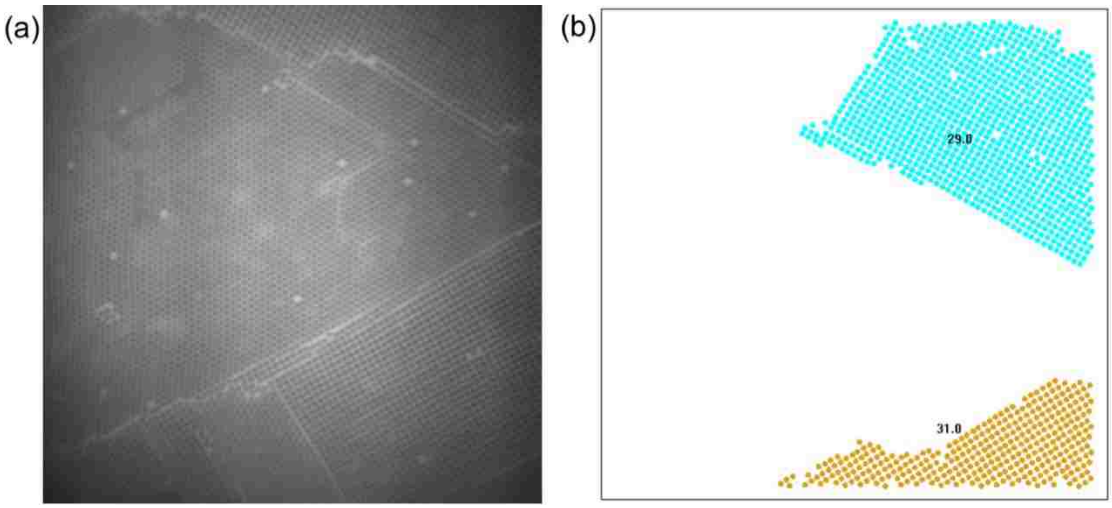

Figure 3.5: Grouping of square-packed particles into (100) fcc domains and calculation of the average orientation of these domains. (a) A representational confocal image of the sample (b) A reconstructed image showing the square packed domains and its orientation with respect to flow direction

3.2.2 Observations on orientation of square-packed domains

Confocal laser scanning microscopy (CLSM) imaging and subsequent image analysis were performed in order to fully quantify the size and distribution of the (100) fcc crystalline domains and surrounding rhcp domains as well as to assess whether the domains are preferentially oriented. Whereas, laser diffraction experiments suggest that some crystalline domains are as large as several millimeters, CLSM at a resolution enabling accurate determination of single particle locations is limited to analysis only of sequential regions containing ca. 4500 particles. Owing to inaccuracies associated with the correlation of particle locations across neighboring frames, CLSM-based calculations of domain size and domain orientation were carried out by treating each confocal frame as a separate entity.

Figure 3.6a-d shows four representative confocal scans with various specified fractions of (100) fcc crystalline domains, that have been further parsed according to their relative size based upon the number, *n*, of particles contained within each. Figure 3.6e shows a rendered image obtained by combining several consecutive confocal frames along the direction of deposition. In addition to underscoring the extent of the (100) fcc crystalline domains, Figure 3.6e also reveals an orientation of the large (100) fcc crystalline domain analyzed therein of $\alpha=30^{o}$ relative to the direction of deposition. For reference, the orientation of domains of various sizes is also specified in Figures 3.6a-e.

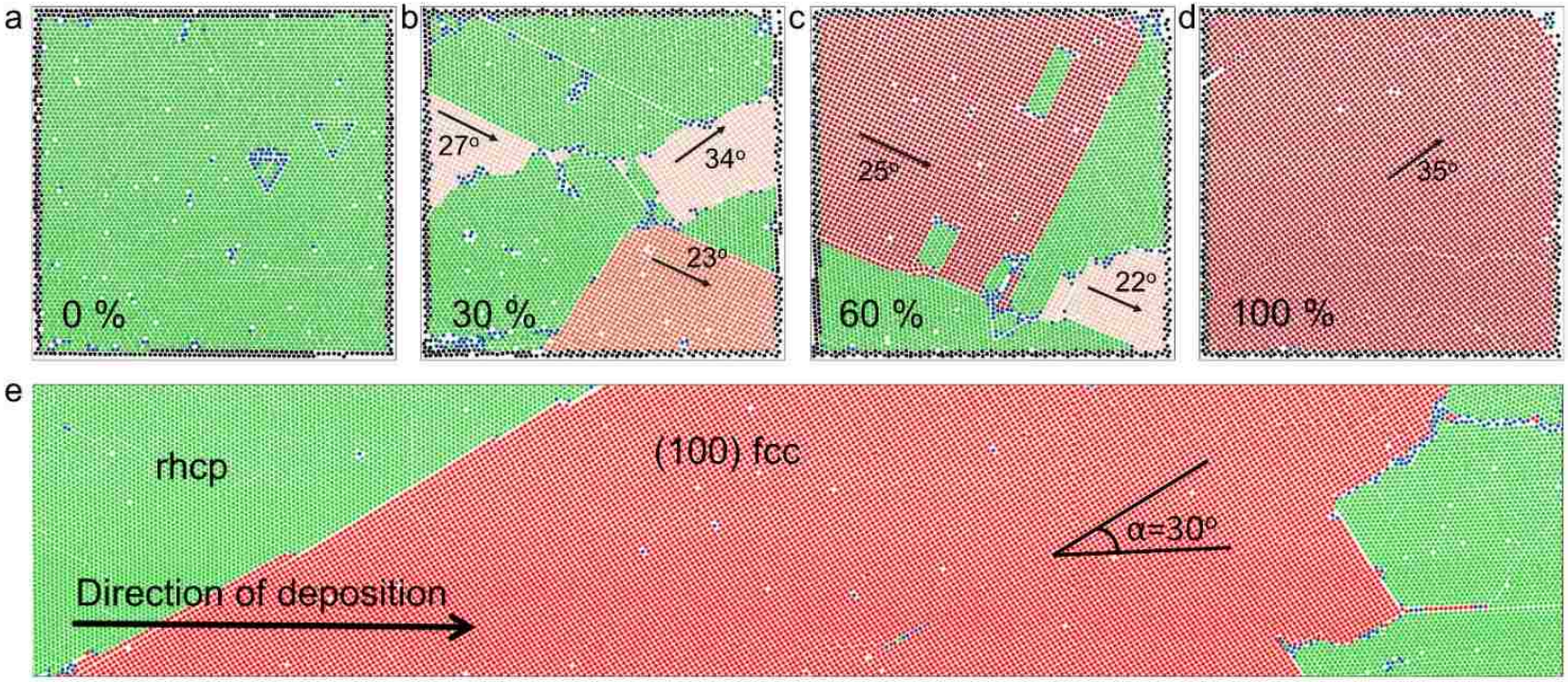
a
0 %
b
27°
34°
23°
30 %
c
25°
22°
60 %
d
35°
100 %
e
rhcp
(100) fcc
α=30°
Direction of deposition

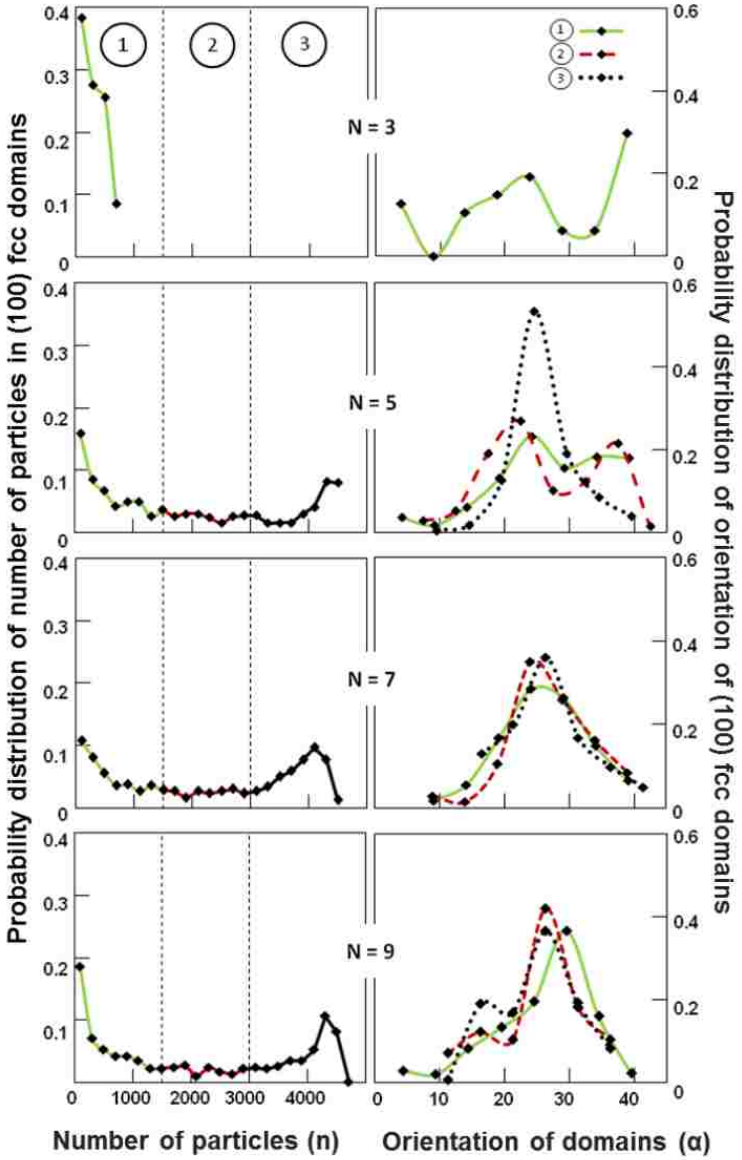

Figure 3.7. Probability of (100) fcc domain size, orientation Probability of domain size in terms of number of particles, *n*, (left column) and corresponding domain orientation, α, (right column) for multi-layer colloidal crystals comprised of specified numbers of layers, N. Line style is used to denote domain size according to number, *n*, of particles included: (1) solid (small, n < 1500 particles), (2) dashed (medium, 1500 ≤ n ≤ 3000), and (3) dotted (large, n>3000).

The result of more extensive analysis beyond the snapshots shown in Figure 3.6of the size, distribution, and orientation of (100) fcc domains within vibration-assembled colloidal crystals of various multi-layer thickness, N, is shown in Figure3.7. To help facilitate analysis, the (100) fcc domains were categorized into bins of relative sizes ranging from (1) those having less than 1500 particles on the surface, or roughly one third of the image size, to (3) crystals covering the majority of the image and clearly spanning beyond it. The probabilities of (100) fcc domains of various sizes are shown in the left column. While small domains ($n<1500$ particles) exist in the thinnest ($N = 3$ multi-layers) to the thickest ($N=9$ multi-layers) colloidal crystals, the distribution of fcc (100) domain size shifts dramatically from small to large with increasing colloidal crystal thickness. For relatively thin colloidal crystals having $N = 3$ layers, square-packed structures exist entirely as small domains. These domains arise at regions of transition between grains for changes in thickness as has been reported previously[17]. As the overall colloidal crystal thickness increases to $N \geq 5$, the fraction of such small domains becomes insignificant, with the majority associated with the edges of larger domains (i.e., identified as small domains in Figure 3.6b,c). This is accompanied by a shift toward larger square-packed domains that extend across multiple CLSM images.

The orientation, α, of the (100) fcc domains in relation to the direction of deposition is likewise sensitive to the number of particle layers comprising the colloidal crystal. The smallest domains found for colloidal crystals comprised of $N = 3$ particle layers have no clear orientation, only weakly favoring $20^o < \alpha < 30^o$. Small and medium-sized (100) fcc domains found in samples assembled into $N = 5$ layers also have no clear orientation, however, they are more strongly aligned at an angle $\alpha = 25^o$ relative to the assembly

direction. For colloidal crystal of $N \geq 7$ particle layers, a clear preferential alignment of the (100) fcc along $25^o \leq \alpha \leq 30^o$ is observed, with the smaller and medium-sized domains drawing alignment through association with larger domains not visualized in their entirety. The reduction in the standard deviation associated with domain orientation as the domains become larger corresponds to the overall tendency of the domains to be aligned at ~ 30^o in the colloidal crystal assembly obtained through vibration-assisted convective deposition. In samples that are predominantly rhcp, there is no correlation in the crystal lattice with regard to the deposition direction, nor has it been reported previously in non-epitaxial convective deposition.

This observation of aligned fcc (100) domains supports the development of a hypothesis where the underlying mechanism is related to the meniscus and suspension flow characteristics regulated by the addition of vibration to the convective deposition process. It is apparent that the mechanism for colloidal assembly in vibration-assisted convective deposition differs significantly from conventional (i.e., vibration-free) convective assembly. Conventional convective assembly procedures for multilayer synthesis having a static meniscus remains unaltered in shape throughout the process wherein particles assemble predominantly by convective steering[18,19] . Previous studies have suggested the optimal growth front is a (311) fcc plane[18] oriented at an angle of 100^o based on the assumption that the free surface has hexagonal symmetry.

3.2.3 In-situ confocal studies

Experiments were performed for in-situ observation of the progress of colloidal crystal assembly in vibration-assisted deposition, which would enable an identification of various stages involved in the assembly process. The actual deposition conditions for the results presented in this chapter involved vibrations at 40 Hz and 1200 μm amplitude. To enable an observation of the thin film region of the suspension, a set-up similar to the actual one was designed with an added functionality of real time observation of particles using confocal microscope. However, the limitations associated with the imaging capabilities of the confocal microscope restricts the amplitude of oscillating particles which could be directly observed during the experiments. The amplitude was hence lowered to ~ 2 μm for imaging purposes.

Figure 3.8a shows a reconstructed image-frame obtained during in-situ imaging of the assembly process, which shows the presence of both hexagonally and square packed regions amidst several individual particles. In addition to these dual packing configurations, another characteristic observation is the inclined orientation of the square region which would enable it to capture more of the incoming particles and grow into a large domain. Based on this in-situ confocal observation, a nucleation-growth based mechanism could be proposed for the observed square packing structures – the process initiated with the nucleation of square-packed nucleates in the thin film region, followed by its rotation to a growth favored orientation and finally its growth by the addition of incoming particles. A schematic of this model is given in Figure 3.8b.

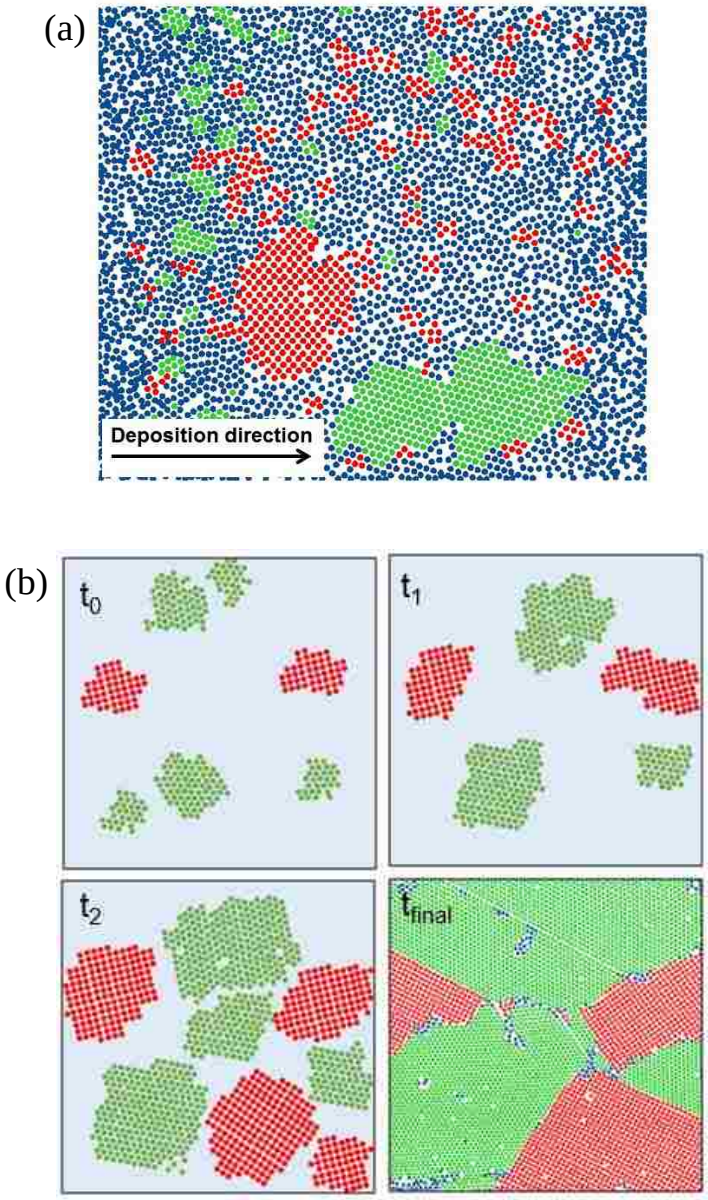

Figure 3.8.Image analysis of in situ structure during assembly (a) Simultaneous formation of square and hexagonally packed regions through a nucleation-growth mechanism demonstrated by a color-rendered in-situ confocal image. The image obtained using 0.93 µm PS particles and at 40 Hz and amplitude of ~10 µm, comprises of both hexagonal (green) and square (red) packed nucleates being generated in the suspension (blue), suggesting a nucleation-growth mechanism during convective assembly.(b) A schematic of the proposed nucleation-growth model for the observed packing assemblies

3.2.4 Proposed mechanism

One possible mechanism for the distinct formation of (100) fcc crystalline domains in vibration-assisted convective deposition could be that the resulting shearing of charge-stabilized particle suspensions assists colloidal assembly into structures other than rhcp symmetries. This has been investigated in many other non-equilibrium experimental studies of simple sheared colloidal systems[6,20–22] as well as order induced by flow in Couette devices[7] as well as planar geometries[23] and Poiseuille flow[11]. When a metastable particle aggregate in a suspension undergoes oscillatory shear, the resulting structure depends on the direction of shear forces as well as the relative magnitudes of shear and inter-particle forces[8,24,25].

Alternatively, another explanation of the generation of colloidal crystals with a combination of hexagonal and square-packing arrangement of the constituent particles having alignment with respect to the direction of deposition can consider the preferential growth of randomly oriented colloidal nucleates. As the suspension is concentrated as it approaches the thin film region, it crosses the liquid-crystal coexistence concentration, either that found in equilibrium systems or at a concentration where crystallization is assisted by the imposed shear from vibration. These fcc nucleates, having random orientation, grow in directions relative to the deposition direction. Those having their (100) plane aligned with the substrate grow without disrupting their lattice arrangement at a comparable or faster rate than nucleates having other orientations. This can be observed in Figures 3.6,3.7 in which the large (100) fcc domains have a preferential orientation of 30^{o} with respect to the deposition direction. Moreover, although numerous square-packed (red)

nucleates can be observed in Figure 3.8a, those domains which can grow need to possess a preferential orientation with respect to the incoming particles.

3.3 Conclusion

This chapter strives to gain a mechanistic understanding of the observed square packed regions in the colloidal crystals generated by vibration-assisted deposition. A review of the literature as well as in-situ confocal studies supports the notion of a nucleation-growth mechanism being responsible for the observed structures. In select experiments performed on the CLSM enabling *in situ* scanning during assembly, evidence of this mechanism is suggested by coexistence of rhcp and fcc (100) substrate-aligned nucleates in the region just upstream of the final arrested polycrystalline colloidal assembly. While only heuristics can be derived through this experiment, the evidence motivates further studies into nucleation and preferential growth that may favor coupling of crystalline microstructure and convection direction toward assembly of a polycrystalline thin film leading to large flow- and substrate-aligned fcc crystalline domains. Perhaps only studies allowing experimental particle tracking during vibration-assisted convective assembly or multiscale time-resolved simulations that track both the particle phase and the dynamic motion of the interface can give further insight into the mechanism of assembly.

3.4 References

1. Wagner, N. J. & Brady, J. F. Shear thickening in colloidal dispersions. *Am. Inst. Phys.* 27–32 (2009).

2. Vermant, J. & Solomon, M. J. Flow-induced structure in colloidal suspensions. *J. Phys. Condens. Matter* **17,** R187–R216 (2005).

3. Hoffman, R. L. Discontinuous and Dilatant Viscosity Behavior in Concentrated Suspensions. I. Observation of a Flow Instability. *J. Rheol. (N. Y. N. Y).* **16,** 155 (1972).

4. Ackerson, B. J., Hayter, J. B., Clark, N. a. & Cotter, L. Neutron scattering from charge stabilized suspensions undergoing shear. *J. Chem. Phys.* **84,** 2344 (1986).

5. Ackerson, B. & Clark, N. Shear-Induced Melting. *Phys. Rev. Lett.* **46,** 123–126 (1981).

6. Ackerson, B. J. & Clark, N. A. Sheared colloidal suspensions. *Phys. A Stat. Mech. its Appl.* **118,** 221–249 (1983).

7. Ackerson, B. J. Shear induced order and shear processing of model hard sphere suspensions. *J. Rheol. (N. Y. N. Y).* **34,** 553–590 (1990).

8. Besseling, T. H. *et al.* Oscillatory shear-induced 3D crystalline order in colloidal hard-sphere fluids. *Soft Matter* **8,** 6931–6939 (2012).

9. Yan, Y. D. Oscillatory-shear-induced order in nonaqueous dispersions of charged colloidal spheres. **202,** 68–80 (1994).

10. Jiang, P. & McFarland, M. J. Large-scale fabrication of wafer-size colloidal crystals, macroporous polymers and nanocomposites by spin-coating. *J. Am. Chem. Soc.* **126,** 13778–13786 (2004).

11. Sawada, T., Suzuki, Y., Toyotama, A. & Iyi, N. Quick fabrication of gigantic single-crystalline colloidal crystals for photonic applications. *Japan J. Appl. Phys.* **40,** L1226–L1228 (2001).

12. Ruhl, T., Spahn, P. & Hellmann, G. P. Artificial opals prepared by melt compression. *Polymer (Guildf).* **44,** 7625–7634 (2003).

13. Ackerson, B. J. & Pusey, P. N. Shear-induced order in suspensions of hard spheres. *Phys. Rev. Lett.* **61,** 1033–1036 (1988).

14. Yan, Y. D., Dhont, J. K. G., Smits, C. & Lekkerkerker, H. N. W. Oscillatory-shear-induced order in nonaqueous dispersions of charged colloidal spheres. *Phys. A Stat. Mech. its Appl.* **202,** 68–80 (1994).

15. Blaak, R., Auer, S., Frenkel, D. & Hartmut, L. Crystal Nucleation of Colloidal Suspensions under Shear. 1–5

16. Lander, B., Seifert, U. & Speck, T. Crystallization in a sheared colloidal suspension. *J. Chem. Phys.* **138,** (2013).

17. Pieranski, P., Strzelecki, L. & Pansu, B. Thin colloidal crystals. *Phys. Rev. Lett.* **50,** 900–904 (1983).

18. Brewer, D. D. *et al.* Mechanistic principles of colloidal crystal growth by evaporation-induced convective steering. *Langmuir* **24,** 13683–13693 (2008).

19. Born, P., Munoz, A., Cavelius, C. & Kraus, T. Crystallization mechanisms in convective particle assembly. *Langmuir* **28,** 8300–8308 (2012).

20. Dozier, W. D. & Chaikin, P. M. Periodic structures in colloidal crystals with oscillatory flow. *J. Phys.* **43,** 843–851 (1982).

21. Chen, L. B. *et al.* Structural changes and orientational order in a sheared colloidal suspension. *Phys. Rev. Lett.* **69,** 688–691 (1992).

22. Chen, L., Chow, M., Ackerson, B. & Zukoski, C. Rheological and microstructural transitions in colloidal crystals. *Langmuir* **36,** 2817–2829 (1994).

23. Stancik, E. J., Hawkinson, A. L., Vermant, J. & Fuller, G. G. Dynamic transitions and oscillatory melting of a two-dimensional crystal subjected to shear flow. *J. Rheol. (N. Y. N. Y).* **48,** 159–173 (2004).

24. Haw, M. D., Poon, W. C. K. & Pusey, P. N. Direct observation of oscillatory-shear-induced order in colloidal suspensions. *Phys. Rev. E* **57,** 6859–6864 (1998).

25. Panine, P., Narayanan, T., Vermant, J. & Mewis, J. Structure and rheology during shear-induced crystallization of a latex suspension. *Phys. Rev. E* **66,** 022401 (2002).

26. Born, P., Blum, S., Munoz, A. & Kraus, T. Role of the meniscus shape in large-area convective particle assembly. *Langmuir* **27,** 8621–8633 (2011).

4

Periodic defects in square packing crystals through stress relaxation

4.1 Introduction

Self-assembled colloidal crystal assemblies of monosized colloidal particles in suspension offers a versatile technique to attain the desired physical, optical, surface and volume properties, making them suitable candidates for technological and engineering applications. Moreover, the periodic variations of dielectric constant in these self-assembled structures generate the highly sought after interference diffraction effects which enables their use for photonic and optical applications. The development of technologies for the fabrication of the periodic structures as well as the incorporation of these structures in engineering devices is governed by the inherent characteristic features of these structures as well as its quality. While the former signifies the packing arrangement of particles within the structure and the orientation of packing assembly with respect to the substrate, the quality of the obtained crystal is governed by factors such as the extent of uniform packing arrangement, the reproducibility of the technique to generate the desired structure and the density of defects in the final assembled structure, each of which demands careful control and tuning to yield the desired packing assembly best suited for the end application.

4.1.1 Intrinsic defects in self-assembled colloidal crystals

One of the major limitations which limits the potential of self-assembly techniques in becoming an alternative to the microfabrication procedures to generate periodic arrangements is the presence of unavoidable defects within the crystal assembly. The presence of these defects often alter the theoretically predicted properties of the bulk structure, with significant reduction in the end-use capabilities. Defects in the self – assembled colloidal crystal arises due to the dynamics of the processes responsible for the assembly of particles into a long range ordered arrangement, and may occur during various stages like the assembly stage (when particles uniformly dispersed in suspension attain a directional movement towards the assembly front where they are packed into a long range order) or during the drying phase (when these assembled particles are rendered immobile by complete removal of the solvent). These defects further vary in their extent and may be grouped as either macroscopic or microscopic defects[1].

The macroscopic defects in colloidal crystal assemblies are observed over extended length scales, can be detected using the naked eye, and includes band-like regions in assemblies, formation of streaks characterized by accumulation of particles along distinct regions of the sample as well as the formation of cracks in the final film. The generation of band-like regions in colloidal assemblies is often attributed to the stick-slip motion of the liquid meniscus when the suspension is dragged across the substrate[2]. This results in band like regions in which the particles are deposited separated by vacant regions of the substrate, a control of which could be obtained by ensuring sufficient wettability of the substrate[2] aided by prior surface treatment or use of surfactants. On the other hand, the generation of streaks in the final assembled film is due to the generation of localized

instabilities in the thin film meniscus at the three-phase contact line. Another significant macroscopic defect observed in colloidal assemblies is the formation of cracks in the film, generated due to the volume shrinkage of particles – giving rise to tensile stresses which develops within the film on the removal of the liquid double layer surrounding the particle[1,2]. Although the cracks cannot be completely eliminated, it can nevertheless be suppressed to a significant extent by reducing the thickness of the liquid double layer by a variation of the zeta potential[1] or by drying of the film under controlled rate and humidity.

In comparison to the macroscopic defects, the crystal possesses several microscopic defects which occur localized within the crystal and can be observed as point defects (voids, interstitial defects), line defects (surface steps, dislocations) or volume defects (stacking faults). The formation of interstitial defects can be attributed to the presence of foreign particles or impurities with different diameters trapped within the assembly, while voids are generated due to the brownian motion, possessed by the particles when they are assembled into the packing configuration with a double layer of water around it which imparts it a certain degree of mobility. Furthermore, the crystal assembly procedure demands a perfect match between the velocity at which the particles are driven to the drying front and the velocity at which they are assembled, a mismatch of which leads to the variation in number of layers within the assembly, visible as a surface step. Also, several volume defects like stacking faults also occur due to the nearly equal free energies of hcp and fcc packing configuration in close packed assemblies. A control of these stacking faults could be achieved by employing colloidal epitaxy methods[3], slow sedimentation[4] as well as gravitational tempering[5,6], making them better suited for high end photonic applications.

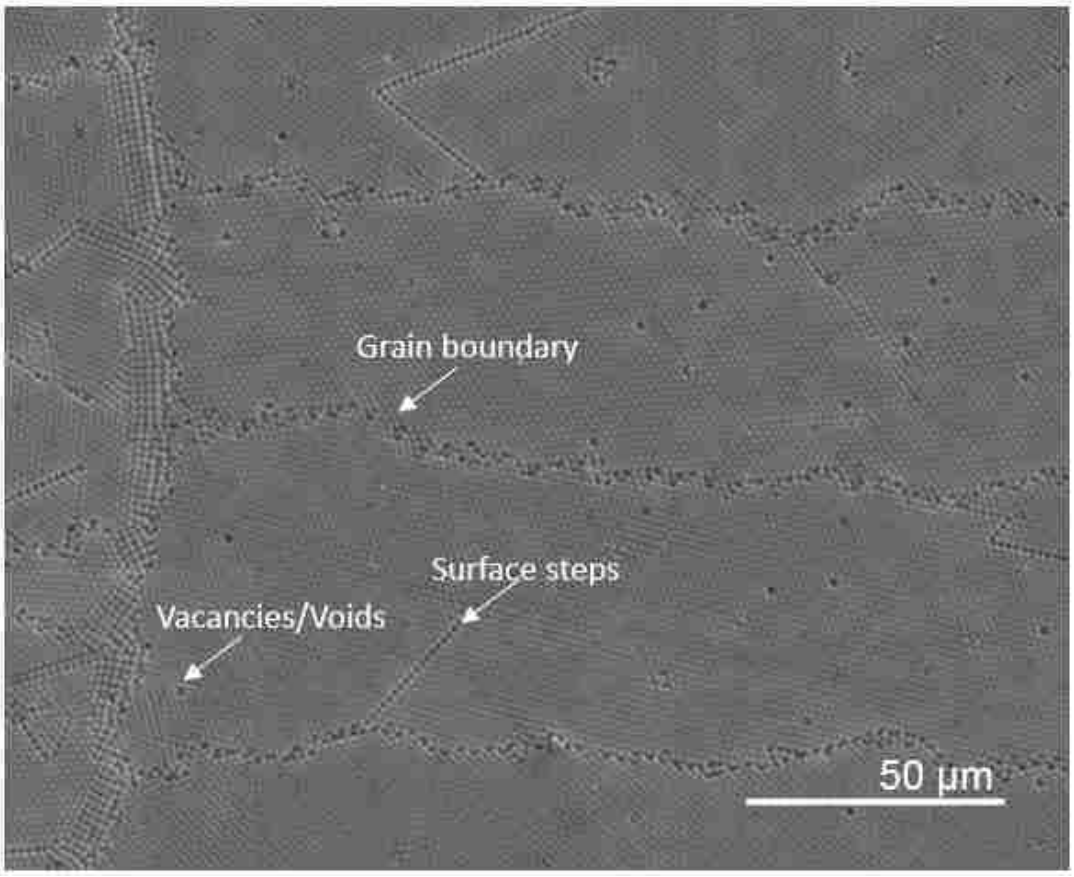

Figure 4.1: Intrinsic microscopic defects in colloidal crystals. The image shows various intrinsic defects in a self-assembled colloidal crystal like vacancies, surface steps and grain boundary.

4.1.2 Dislocations in crystalline materials

Dislocations are localized line defects in crystalline materials and are observed as discontinuous boundary in an otherwise perfectly packed crystal along which a set of particles are shifted with respect to the adjacent plane[7,8]. The nucleation of dislocations in crystalline materials and their dynamics have been extensively investigated for conventional materials owing to their significance in plastic deformation (irreversible deformation) and fatigue failure of materials. The research into the theory of dislocations was initiated by the observation that crystalline materials undergo deformation at stress values several orders of magnitude lower than the stress required to affect a planar displacement of atoms relative to the adjacent layer (theoretical shear strength) – plastic deformation at low shear values attributed to the movement of large number of dislocations present within the crystal lattice. Research on improving the strength of alloys by limiting plastic deformations caused by dislocations thus focusses on either eliminating the dislocations in the structure or limiting the movement of dislocations by pinning it using solute atoms dispersed within a bulk phase or generating tangled dislocations which are unable to move[9,10].

The dislocations observed in crystal systems can be described by the parameter 'Burgers vector', which is constructed around a dislocation core such that the magnitude and direction of the vector quantifies the extent of lattice mismatch due to the incorporation of the dislocations when compared with a perfect crystal. These dislocations can be classified into various types depending on the relative magnitude of atomic plane shifts with respect to a fixed dislocation line – screw dislocations, edge dislocations and mixed dislocations, a schematic of each of which represents the direction of atomic shifts with

respect to the dislocation line and the corresponding Burger's vector shown in Figure 4.2 (c,d). While edge dislocations are characterized by Burgers vector perpendicular to the dislocation line, screw dislocations have Burgers vector lying parallel to the dislocation line. The actual dislocations observed in real crystal are however of mixed nature with both edge and screw components, Burgers vector of which is at an angle to the dislocation line.

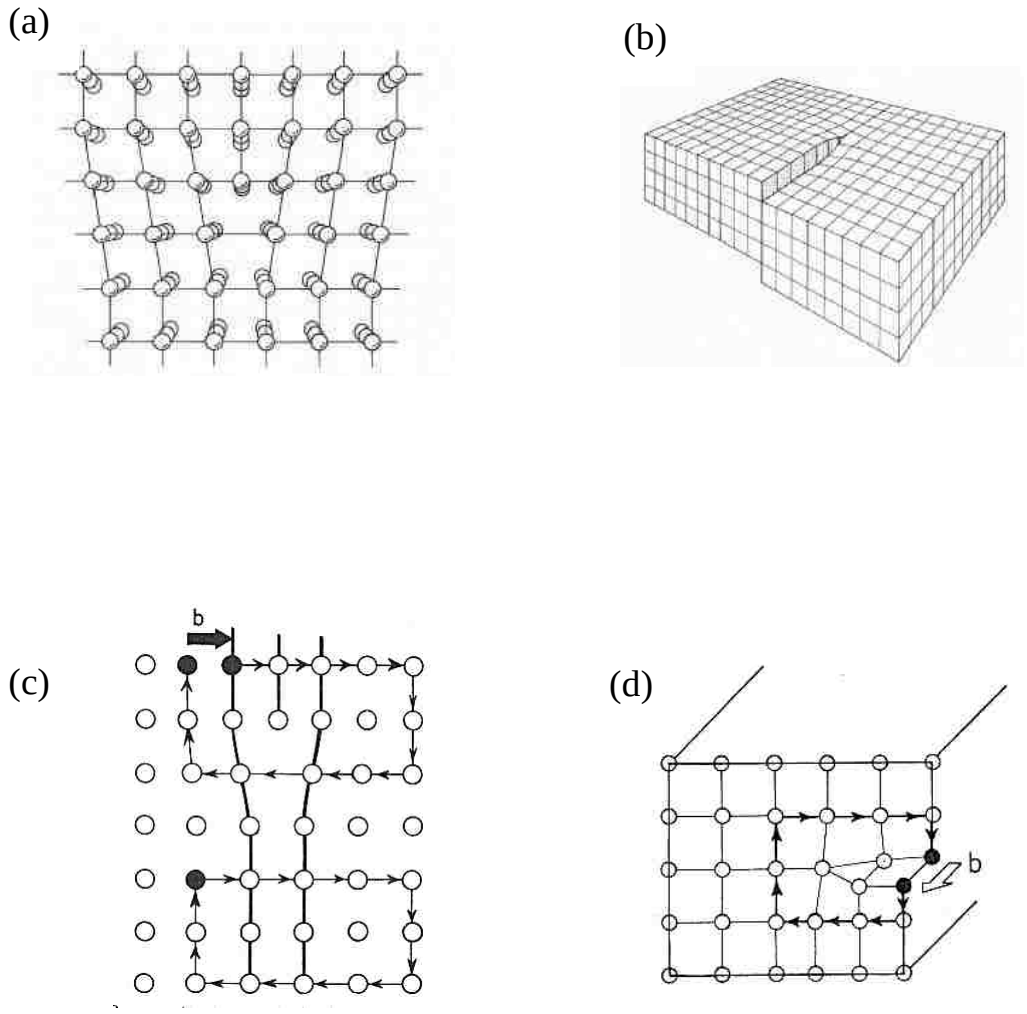

Figure 4.2: Edge and screw dislocations in a simple cubic crystal. (a) An edge dislocation[11] (b) a Screw dislocation[11] (c) Construction of Burgers circuit and calculation of Burgers vector for edge dislocation[7] and (d) Burgers vector calculation for edge dislocation[7]. (Figures shown were adapted from the corresponding references)

4.1.2.1 Self-energy of dislocations

The application of stress on a body results in a corresponding deformation (strain) with a linear relationship established between the two through Hooke's law (the proportionality constant being the Young's modulus). The energy stored within the system during the application of stress is thus directly proportional to the work required to produce the observed strain magnitude and is referred to as the 'self-energy' of a dislocation[7].

The self-energy of the screw dislocation is given by[7]:

$$\zeta = \frac{\mu b^2}{4\pi}\log\frac{R}{5b} \qquad \text{where } R \text{ is the outer dimension of the crystal}$$

For edge dislocation[7],

$$\zeta = \frac{\mu b^2}{4\pi(1-\nu)}\log\frac{R}{5b} \qquad \text{with } \nu = \text{Poisson ratio} = \frac{\lambda}{2(\lambda+\mu)}$$

$$\lambda, \mu : \text{Lamē constants}$$

For mixed dislocations[7],

$$\zeta = \frac{\mu b^2}{4\pi(1-\nu)}\ (1-\nu\ Cos^2\theta)\ \log\frac{R}{5b}$$

Approximating the above relations, the self-energy of dislocations of any type can be approximated to be directly proportional to the squared magnitude of the corresponding Burger's vector (b^2).

4.1.2.2 Nucleation of dislocations

When a uniformly packed crystal is subjected to shearing forces, there is a built-up of considerable amount of strain energy within the crystal. The crystal tends to relieve the stored strain energy by the nucleation of topological defects or dislocations within the structure, which involves breaking of definite number of inter-particle bonds within the crystal. Such dislocations generated in crystalline materials have their dynamics and intrinsic behavior characterized predominantly by three factors- nucleation of dislocations which represents regions at which there is a disruption of periodic lattice arrangement, their mobility (referred to as slip) and their interactions with other dislocations (dislocation reactions). While the nucleation of dislocations refers to the generation of dislocations in a material with definite characteristics and occurs when the resolved shear stress component acting on the crystal is higher than the dislocation barrier, the mobility of these dislocations refers to the translation of these topological defects through the volume of a crystal with its identity preserved[12].

The generation of dislocations in a crystal (dislocation nucleation) can occur through two pathways – heterogeneous dislocation nucleation and homogeneous nucleation, the classification based on the mechanism originally responsible for their generation[12]. A heterogeneous nucleation of dislocations is caused when pre-existing defects in the crystal act as focal points at which strain energy gets accumulated resulting in the formation of dislocations even at low or medium strain rates. Such energetically activated regions in the crystal correspond to either a lattice defect or a pre-existing dislocation in an adjacent plane which is capable of generating a new dislocation. Conversely, homogeneous nucleation of dislocations occurs without any aid from pre-

existing defects and is commonly observed in a defect-free prefect stress when subjected to suitable stress fields. Since homogeneous dislocation is devoid of any locally activated regions which may act as localized strain concentrators, they require high strain rates for their generation in a defect-free crystal. Once a dislocation is nucleated within the crystal, it grows and multiples rapidly thereby facilitating a partial release of the shear stress.

4.1.2.3 Dislocation movement in crystals

In addition to the density of dislocations nucleated within the crystal, the behavior of the material modified by the presence of dislocations is also intricately related to the dislocation dynamics, which includes dislocation movement and dislocation reactions. The movement of dislocation occurs along a definite crystal plane in a preferential direction, the magnitude of which enables a classification of dislocation as either perfect dislocation or partial dislocation. In a perfect dislocation, the movement of slip plane shifts the atoms in the plane to identical lattice locations – i.e. the magnitude of the displacement is a complete lattice vector such that a perfect lattice structure is left behind. However, in partial dislocations (imperfect dislocations), the magnitude of displacement is not in terms of multiples of the lattice vector, thereby resulting in a structural configuration different from the original one being left behind. Two major types of partial dislocations identified in crystals are Frank partials and Shockley partials. The Frank partial dislocation is immobile in nature as its slip plane is perpendicular to the {111} plane[7]. On the other hand, Shockley partial dislocations are mobile with the slip plane lying on the {111} plane[7].

For Frank partial dislocation, $\bar{\boldsymbol{b}} = \frac{a}{3} < 111 >$

For Shockley partial dislocation, $\bar{\boldsymbol{b}} = \frac{a}{6} < 112 >$

Dislocation movement in a crystal may occur through two routes – dislocation glide (slip) or dislocation climb, with dislocation glide being more commonly observed in materials. The 'slip' is characterized by a simultaneous coordinated movement of atoms on the slip plane relative to the adjacent plane, in the direction of Burger's vector of the dislocation. When slip occurs, the regions of the crystal between the slip planes remains unchanged, as can be observed in Figure 4.3a. In conventional materials, the slip movement of dislocations through the volume enables it to emerge out from the surface of the material, appearing as slip steps and are referred to as 'Luder's bands'[13]. On the other hand, dislocation climb occurs when the dislocation moves in a direction perpendicular to the Burgers vector.

Slip systems in fcc crystal:

The dislocation movement in a crystal subjected to a distorting force field is associated with a definite slip system, comprising of slip plane (a plane along which the slip occurs in the crystal) and slip direction (the direction in which the slip plane moves). The slip plane in a crystal is usually the most densely packed plane in the crystal (smoothest plane), which is observed in the {111} group of planes in fcc structure with hexagonal packing of constituent particles. Such a plane in the crystal would offer lowest resistance to the movement of dislocations on the plane (referred to as Peierls stress)[7]. Another factor which favors a preferential selection of the {111} family of planes in an fcc crystal is that it provides an opportunity for the dislocations to dissociate into imperfect dislocations with a further reduction in their self-energies[7]. The slip direction, on the other hand, is usually the direction in which the atoms are most closely spaced. This in turn corresponds to the direction in which a perfect dislocation can move with the shortest displacement.

Considering a crystal with a lattice parameter ‘a’, the Burgers vector associated with a perfect dislocation along the <110> direction is given by, $\overline{\boldsymbol{b}} = \frac{a}{2} < 110 >$

For a perfect dislocation along the <100> direction, $\overline{\boldsymbol{b}} = a < 100 >$.

Since the self-energy of a dislocation is proportional to b^2, the amount of energy stored is lowest in the case of <110> direction ($b^2 = \frac{a^2}{2}$ for $< 110 >$, $b^2 = a^2$ for $< 100 >$). Since dislocations with smaller self-energy are more preferable from a thermodynamic stand point, the fcc crystal tends to generate a dislocation in the <110> directions.

The preference of an fcc crystal to slip along the {111} plane has also been demonstrated experimentally using uniaxial tensile loading on an fcc copper crystal, in which von Mises stress was calculated for various loading directions. It was then observed that loading along the {111} plane generated the highest magnitude of von Mises stress, thus making the nucleation of dislocations easier on the {111} plane[14]. The various slip systems possible in materials depend on the crystal configurations, and can be identified using Thompson tetrahedron. An fcc unit cell thus has 12 slip systems comprising of four {111} plane and each {111} plane possessing three <110> directions.

(a)

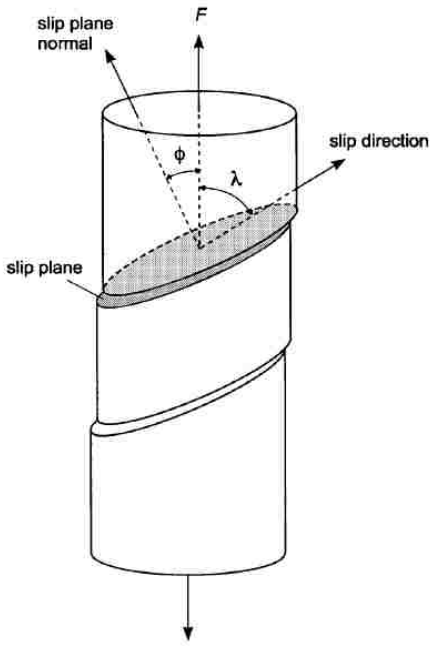

(b)

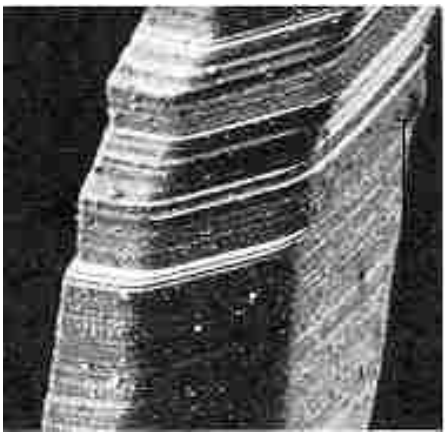

Figure 4.3: Dislocation movement (slip) in crystalline materials (a) A schematic of slip in a crystal structure showing the slip plane and slip direction[8] (b) Slip bands resulting from dislocation movement in a hexagonal cobalt crystal[15] (Figures shown were adapted from the corresponding references)

Calculation of critical resolved shear stress:

In crystals, slip occurs when the component of the shear stress acting on the slip system is higher than the resistance to dislocation motion. This critical shear stress value required to initiate slip can be calculated based on Schmidt's law.

Consider the schematic of a crystal as shown in Figure 4.3a with a definite slip plane and slip direction and a uniaxial tensile force (F) acting on the crystal. Assume an angle ϕ between the normal to the slip plane and direction of force and the angle between slip direction and direction of force to be λ.

The tensile stress (τ) acting on the crystal in the same direction as, $\tau = \frac{F}{A}$

The shear stress acting on the slip plane of crystal in slip direction,

$$\tau_R = \frac{Force\ acting\ on\ slip\ plane}{Cross-sectional\ are\ of\ slip\ plane} = \frac{F\ Cos\ \lambda}{\left(\frac{A}{Cos\ \phi}\right)} = \tau\ Cos\ \lambda\ Cos\ \phi$$

The parameter $Cos\ \lambda\ Cos\ \phi$ is referred to as the Schmidt factor. Thus, the possibility of a crystal plane slip under the effect of shearing forces is reliant on the values of twin angles (λ, ϕ), the maximum value obtained for Schmidt factor when $\lambda = \phi = 45^o$.

4.1.2.4 Dislocation Reactions

Another significant aspect of dislocation dynamics involves the dissociation of dislocations into several components. The dissociation of a perfect dislocation into two partial dislocations occurs when there is a reduction in the net self-energy of the system (Frank's rule). Thus, for dislocations with Burger's vector $\overline{\boldsymbol{b_1}}, \overline{\boldsymbol{b_2}}$ and $\overline{\boldsymbol{b_3}}$, the dissociation reaction:

$\overline{\boldsymbol{b_1}} \rightarrow \overline{\boldsymbol{b_2}} + \overline{\boldsymbol{b_3}}$ occurs only if $(b_2^2 + b_3^2) < b_1^2$

In an fcc crystal, a perfect dislocation may split into two partial dislocations, which may be either Shockley type or Frank type or a combination of both, as shown below.

Dissociation of a perfect dislocation into two Shockley partials[7]:

$$\frac{a}{2}<110> \quad \rightarrow \quad \frac{a}{6}<211> + \frac{a}{6}<12\bar{1}>$$

$$b_1^2 = \frac{a^2}{2} \qquad\qquad b_2^2 + b_3^2 = \frac{a^2}{6} + \frac{a^2}{6} = \frac{a^2}{3}$$

Dissociation of a perfect dislocation into a Shockley partial and a Frank partial[7]:

$$\frac{a}{2}<01\bar{1}> \quad \rightarrow \quad \frac{a}{6}<\bar{2}1\bar{1}> + \frac{a}{3}<11\bar{1}>$$

$$b_1^2 = \frac{a^2}{2} \qquad\qquad b_2^2 + b_3^2 = \frac{a^2}{6} + \frac{a^2}{3} = \frac{a^2}{2}$$

The above reaction has nevertheless been shown to be favorable when the anisotropy of the elastic constants was taken into account[7].

4.1.2.5 Propagation of dislocations in crystal through cross-slip mechanism

Dislocations generated in a crystal moves along well-defined slip planes, which is {111} types of planes in an fcc crystal. The screw dislocations in the crystal has also the ability to switch from its original slip plane to an intersecting slip plane of the same type, provided that the new slip plane contains the required slip direction. This phenomena, referred to as 'cross-slip'[7,8] results in a heterogeneous nucleation of dislocations in the crystal, with an existing dislocation nucleating a new one on the intersecting plane with similar characteristics. This generation of new dislocations by cross-slip is referred to as a Koehler source[7], contrasting it from a Frank-Read source and is responsible for multiplication of dislocations in crystals like LiF[16] as well as Aluminum single crystal[17].

The cross-slip associated with a perfect dislocation is demonstrated in Figure 4.4a, the various sequence of events leading up to the cross-slip labeled as (i),(ii) and (iii). In this figure, it could be observed that the screw dislocation which originally glides on the (111) plane gets transferred to the $(1\bar{1}1)$ plane at point S, both the planes containing the Burgers vector $\overline{\boldsymbol{b}} = \frac{a}{2}[\bar{1}01]$. However, in comparison to a perfect dislocation, imperfect dislocations like Shockley partials cannot directly undergo cross-slip due to limitations associated with its slip plane[7,8]. For example, a Shockley partial with $\overline{\boldsymbol{b}} = \frac{a}{6}[112]$ can lie on only one of the {111} family of planes. Cross-slip in this case, occurs through the formation of 'constrictions' in which the partial dislocations are brought together by the application of stress. Once a constriction is formed, they possess characteristics of a perfect dislocation and can undergo cross-slip. The sequence of steps involved in cross slip of partial dislocations is shown in Figure 4.4b, in which formation of constrictions is followed by cross slip into adjacent plane and finally dissociation of screw dislocation into partials.

(a)

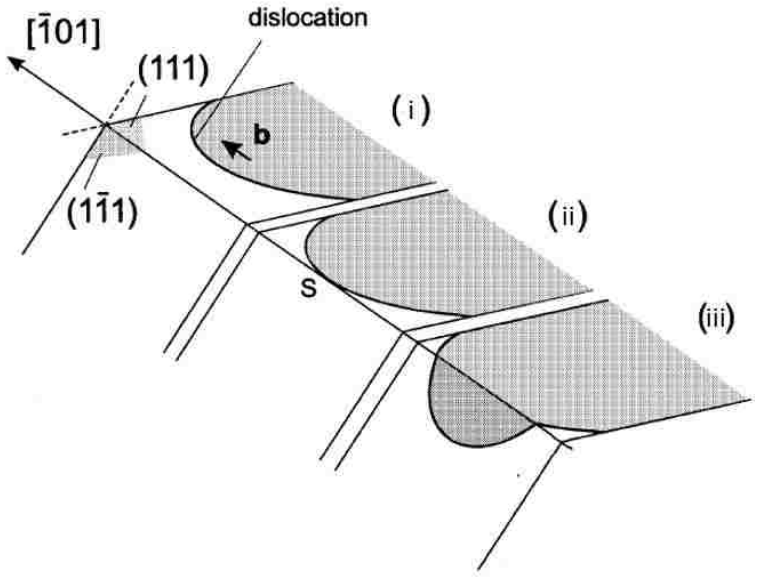

(b)

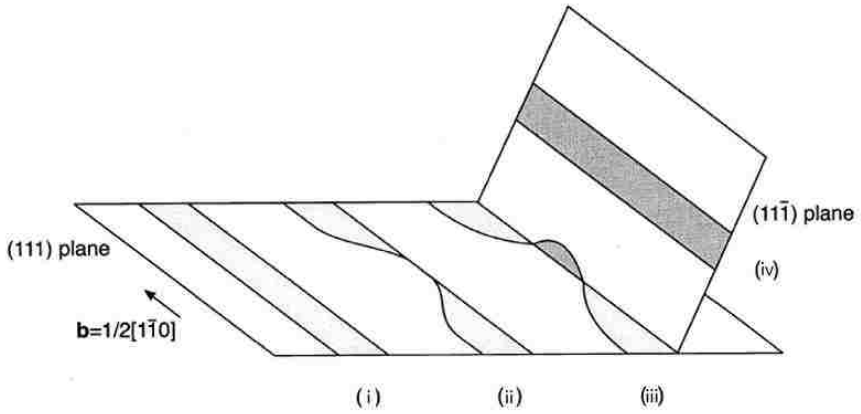

Figure 4.4: Propagation of dislocations through cross-slip mechanism. (a) Cross slip in perfect dislocations[8], in which dislocation on (111) plane slips to form a dislocation on (1$\bar{1}$1) plane at S (b) Cross-slip involving partial dislocations progressing though a four-step sequence[8] in which the partials initially combine to form a perfect dislocation, undergoes cross-slip and then splits again into partials on the new plane. The figures were adapted from the corresponding reference.

4.1.2.6 Band-like patterns reported in conventional materials

When single crystals are subjected to a deforming stress field, they undergo plastic deformation characterized by the nucleation and movement of dislocations (referred to as slip or dislocation glide) – slip occurring along several well defined planes in the crystal. These dislocation movements associated with the strain relaxation processes result in slip bands when the dislocations escape from the crystal structure at the free surface which creates surface markings on the crystal surface – the lines corresponding to active slip planes. These slip bands commonly observed in materials are randomly distributed within the volume, with each band nucleated from a distinct dislocation source isolated from other sources. In addition to these bands, the literature also reports the observation of a spatially correlated set of slip bands in fcc and bcc materials as well as in non-metals like silicon[18]. This section of the chapter attempts at a general discussion on these periodic line patterns, which might enable an extrapolation of this observed phenomenon and its underlying mechanism towards similar results observed in colloidal crystal structures.

The generation of a correlated family of slip bands observed in crystals has been attributed to the instabilities associated with dynamic strain aging in crystals[18] – a phenomenon in which the diffusion of interstitial solute atoms in an alloy temporarily obstructs the movement of dislocations, until the dislocations can overcome the obstacle with significant stress. This results in a discontinuous variation of crystal stress with time and is manifested in the form of a family of parallel bands when the crystals are oriented for a single slip. These bands, classified as Luder's bands[13] or Portevin Le Chatelier (PLC) bands[19] are usually initiated at one end of the specimen and propagates inwards[18]. In these

bands (Luders bands and PLC Bands Type B,C), the generation of a new slip band occurs adjacent to the pre-existing one by cross-slip mechanism, resulting in a periodic pattern[18].

In addition to the observation of periodic slip bands associated with dynamic strain aging, these patterns (which are visually similar to the bands reported in Results & Discussions section) has also been observed when a crystal experiences an accumulation of stress at internal points, which act as nucleation spots for spatially correlated set of parallel slip bands. In one such reported work, LiF crystals (with fcc structure) cleaved along the (001) faces are subjected to stress treatment followed by chemical treatment with a selective etching agent, thus generating etch-pits at the dislocation points[20]. The reported results of alternating bending and etching repeated multiple times shows the formation of multiple sets of tech pits, each set corresponding to a single stress treatment event. Another similar result has been reported in the growth of SiGeC ternary alloys on a Si (001) substrate surface[21]. In this work, it was reported that ledge-shaped defects are formed within the crystal when the substitutional carbon content in the alloy exceeded 1.5 %. This has been attributed to the nucleation and spatially correlated propagation of dislocations when the internal stress crosses a threshold after a definite deposition thickness of the SiGeC alloy. Similar patterns have also been reported in the molecular dynamics simulation of an (001) oriented fcc crystal when subjected to tensile stress[22], however, the orientation of defect lines with respect to that of square packed particles are different in this case when compared to the results obtained in our work.

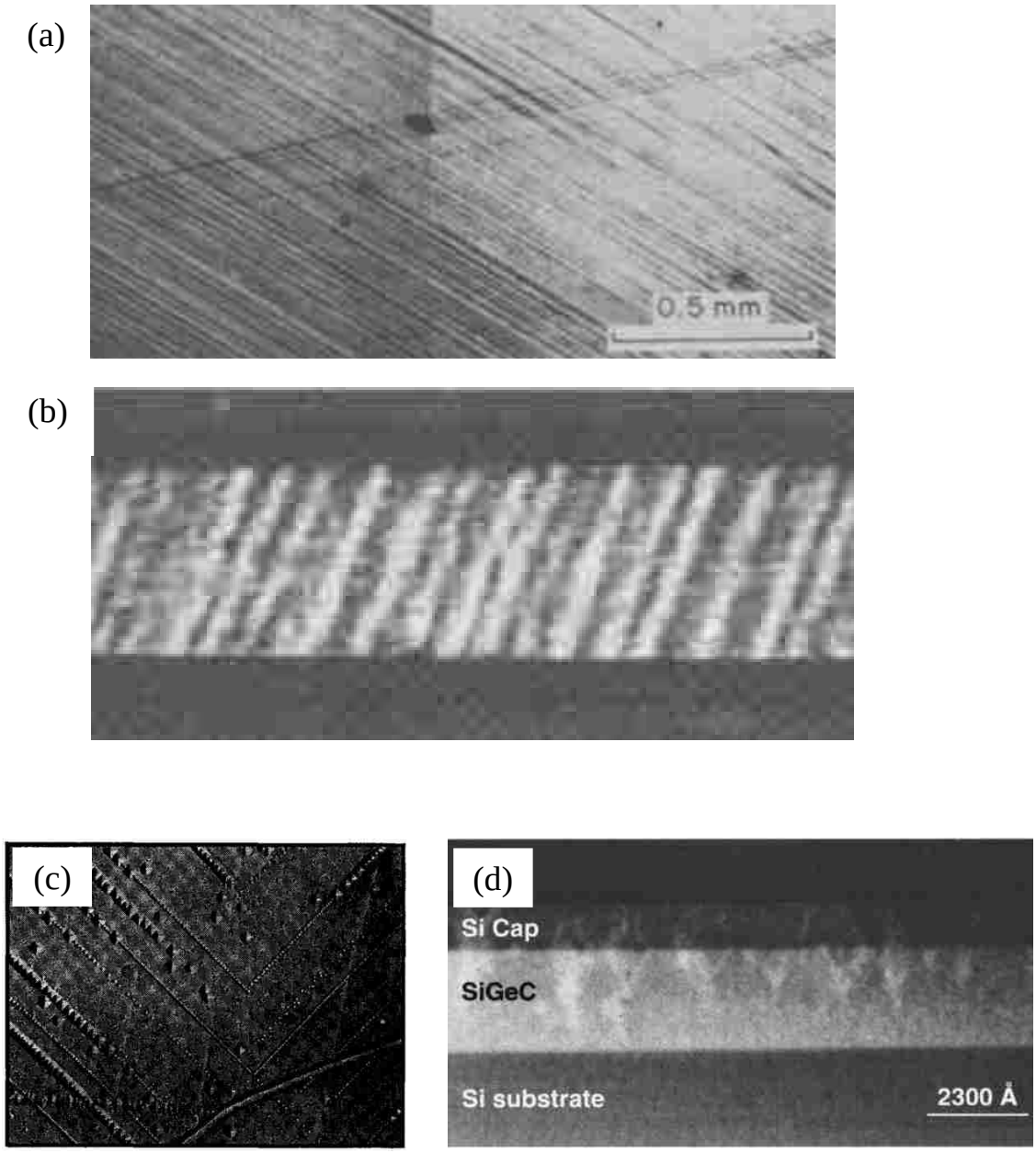

Figure 4.5: Periodic band patterns observed in crystalline materials due to stress relaxation. (a) Luder's bands observed in Si crystal deformed under compressive strain[13] and (b) Portevin-Le-Chatlier bands in Al-Mg alloy , both the Luders bands and PLC bands generated due to strain hardening in materials (c) Periodic band patterns in LiF crystals due to dislocation glide when subjected to bending forces[20] (d) Ledge-shaped patterns in SiGeC alloys grown on Si(001) surface, due to stacking faults beyond a threshold thickness[21] (The figures were adapted from the corresponding references)

4.1.2.7 Dislocations in three-dimensional colloidal crystals

Colloidal crystal assemblies which possess a long range ordered arrangement of particles in a three dimensional space can be utilized as analogues for atomic crystal systems to investigate the nucleation, growth and propagation of dislocations, as well as their interactions with one another[23]. The performance of these colloidal crystals as equivalent periodic structures to atomic crystals has been made possible owing to the size of its individual building blocks being several orders of magnitude larger than the corresponding building units in atomic systems, thus enabling a real time observation of the dynamics associated with the dislocation. Moreover, it is easier to generate dislocations in colloidal crystals compared to their atomic systems counterparts due to the lower magnitude of inter-particle forces. In atomic crystals, strain relaxation occurs in sub nanosecond time scale, whereas it is millisecond time scale in colloidal crystals which enables a direct visualization of the dislocation dynamics through confocal microscopy techniques.

Dislocations commonly observed in colloidal crystals arise either due to imperfections during the growth processes (trapped impurities which may act as point defects), misfit dislocations (generated due to the mismatch in lattice parameter when the crystal assembly is grown on lithographically patterned templates) – collectively referred to as heterogeneous dislocation nucleation or may be homogeneously generated in an otherwise perfect crystal due to the application of stress[23]. These dislocations in colloidal crystals are generally investigated by laser diffraction microscopy techniques which helps to identify the location of these dislocations, with microscopic scale data of the same at particle level resolution generated using confocal microscopy. The latter enables a

characterization of the relative displacements of individual particles around a dislocation core, thus facilitating an in-situ observation of the dislocation dynamics.

The extension of the principles of dislocation dynamics to colloidal crystal systems was first investigated in the seminal work by Schall et.al, the reported experiments involving colloidal crystal assemblies of 1.55 μm silica particles grown epitaxially on a (100) patterned template. The nucleation of dislocations in these crystal assemblies were obtained through two distinct approaches – misfit dislocations and by application of shear. In the first approach, the crystal was grown on a template with a stretched lattice parameter (d=1.63um) by sedimentation process[24]. Gradual layer by layer growth on the stretched template leads to a built up of strain energy within the crystal with increasing thickness, eventually resulting in the nucleation of misfit dislocations. The critical thickness for nucleation of these dislocations was found to be 31 μm, a height at which the crystal was observed to possess a high dislocation density. A yet another approach reported by the same group involved the generation of dislocations in a perfectly crystalline fcc (100) crystal by the application of a necessary shearing force[25]. This approach utilizes the principles of nano-indentation experiments in which the surface of the crystal was indented with a needle of hemispherical tip at a controlled rate. A temporal and spatial investigation of the indented colloidal crystal by employing laser diffraction method to image the strain fields (visible inference about the same obtained from the variation in brightness when illuminated with laser) and individual particle imaging through confocal microscopy were utilized to observe the nucleation and spread of dislocations (which would enable a visualization of strain fields within the crystal). Analysis of the strained lattice revealed that the strain energy arising from the crystal being surface-indented gradually builds up at

an interior point of the crystal away from the surface. This eventually nucleates a stable defect (dislocation) visible as a distinct shift of particles from their original lattice positions, which gradually grows in size with time. Another significant observation in the same work was that the stable slanting dislocation thus generated was capable of nucleating second dislocation on the adjacent intersecting plane.

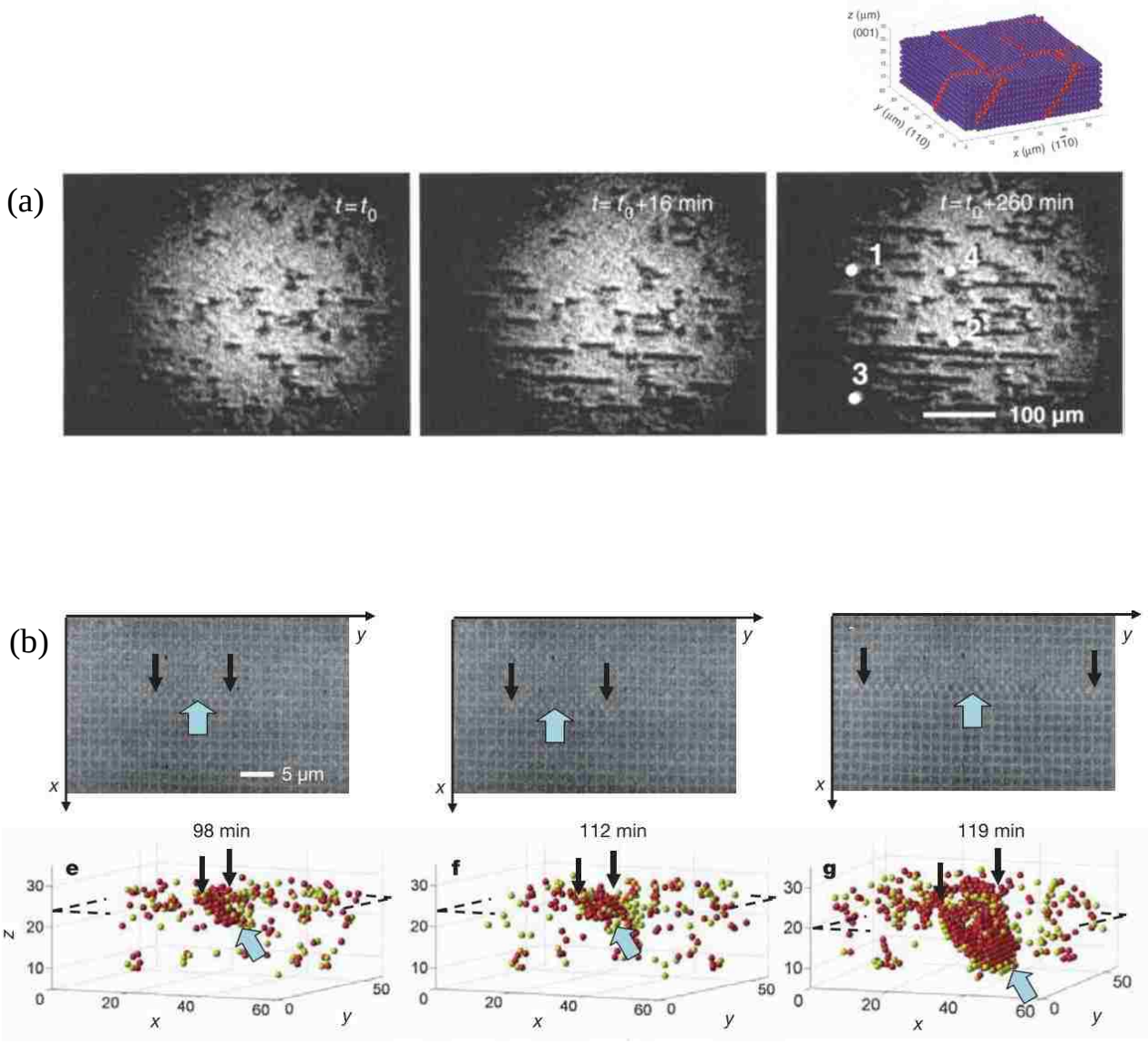

Figure 4.6: Nucleation and propagation of dislocations in an epitaxially grown fcc (100) crystal. (a)Shockley partial dislocations due to misfit in lattice parameters of the substrate pattern and crystal assembly, with the images showing the growth of dislocations with time. A reconstruction of defect is also shown[24] (b) Dislocations generated due to the indentation of the free surface, with the three images showing the growth of dislocation line[25]. The images shown in this figure were adapted from corresponding references.

4.1.3 Engineered defects in colloidal crystals

The randomly generated intrinsic defects in colloidal crystals which are governed by the dynamics of the assembly process are detrimental for the proper utilization of the assembly for device fabrication. Conversely, various controlled defects can be incorporated extrinsically into the crystal, which would impart it several unique functionalities which cannot otherwise be realized. A strategy to successfully incorporate defects with tunable morphology and desired dimensionality (point, line, planar or volume defects) into the self –assembled colloidal crystal structures is crucial in realizing the objective of miniaturized self-assembled optical circuits. With an analogy established between photonic crystals and electronic semiconductors, the former referred to as 'semiconductors of light', the introduction of artificial defects into the crystals can be compared to the incorporation of dopants into the semiconductor. The dimensionality and quality of these defects regulates the additional optical functionalities derived from its incorporation. While point defects embedded in a uniform and periodic crystal serves the purpose of micro cavities to localize and concentrate light[26], the line, planar and volume defects in the medium acts as channels for guiding and splitting electromagnetic wave propagating through the bulk medium in the respective dimensions[26]. Moreover, when used for photonic applications, the incorporation of these tuned defects disrupts the periodicity of the colloidal crystal, thus creating defect bands (pass band) in the photonic band gap region[27].

In spite of the high potential of engineered defects in colloidal crystals, the procedures for the same remain only partially successful due to the inherent challenges involved. The current techniques reported in literature to fabricate these structures employ a combination of top-down (lithography) and bottom-up (self-assembly) techniques. While

the self-assembly process yields the bulk of the uniformly crystalline phase, microfabrication-based procedures are used to introduce defects, the commonly adopted one being the post-processing of a crystal using lithographic[28] or photon polymerization technique[26,27,29,30]. In the lithography based methods, selected regions of the crystal assembly are etched away using electron lithography, thereby yielding the desired line patterns on the crystal surface. These patterns originally generated on the surface can be translated into line defect buried within the crystal by further growth of the assembly on the exposed surface. In comparison to the electron lithographic technique which is inherently a three-step process (crystal assembly – line pattern fabrication – final assembly), photon polymerization based procedures yield the desired line defects by a multistep process. In this technique, the assembled crystal is infiltrated with a photosensitive monomer which is selectively polymerized using a focused multiphoton beam, the beam being gradually swept across the substrate in accordance with the desired line defect pattern. Replacement of the residual monomer with the inverse opal salt followed by etching away of the original crystal assembly yields the inverse opal structure with incorporated air-core line defect within the structure. Although successfully demonstrated to yield a defect band within the forbidden energy gap (photonic band gap) of a photonic crystal, this methodology suffers from significant scattering loses due to the rough edges of the line defect[31].

An yet another procedure reported for incorporating line or planar defects involves depositing an additional layer of desired thickness and dielectric constant on a colloidal crystal assembly, which can be either converted into a planar defect or line defect (achieved by employing a photoresist layer converted into a line defect by photolithography[31–33]). In

either scenarios, deposition of a second overlying layer of the colloidal crystal with subsequent treatment steps (infiltration, template removal, photoresist removal) results in a buried planar or line defect with the conditioned architecture. Similar results have also been reported for planar defect fabrication with the photoresist layer replaced with a semiconductor salt deposition using CVD methods[34].

Research in the last decade has focused on extracting the real potential of self-assembly route as a viable alternative to the microfabrication procedures with respect to defect engineering in colloidal crystal. This research domain is investigated by concurrent research by several groups, albeit with limited success and definite realization of defects predominantly confined to simple geometries. A theoretical investigation of the self-assembly technique to create point defects achieved using substitutional or interstitial doping of the crystal assembly with particles of different diameter or dielectric constant showed promising potential for the substitutional defect based technique to affect changes in the photonic band gap[35,36]. However, actual implementation procedures for the same suffers from a random and unmodulated distribution of foreign atoms (substitutional defects) within the assembly. Self-assembly based route has also been proposed for planar defects by employing templated substrate with an intentional mismatch between particle orientation and height in selected regions of the template aimed at inducing defects in the final assembled structure. This procedure which yields planar defects slanted to the substrate needs significant control over the template design[37] (demonstrated only for square templates) and growth environment of the assembly process. A combination of various self-assembly techniques performed sequentially have been suggested for generating planar defects within the assembly. For example, spin coating[38] or Langmuir-Blodgett

deposition method[39] can be used to deposit an assembled monolayer of particles with a desired diameter on the surface of an already fabricated crystal, which would act as the substrate for further crystal growth. Similarly, a layer-by-layer deposition of particles with varying dimeter and controlled thickness of each layer[40] would also yield a planar defect structure within the final assembly.

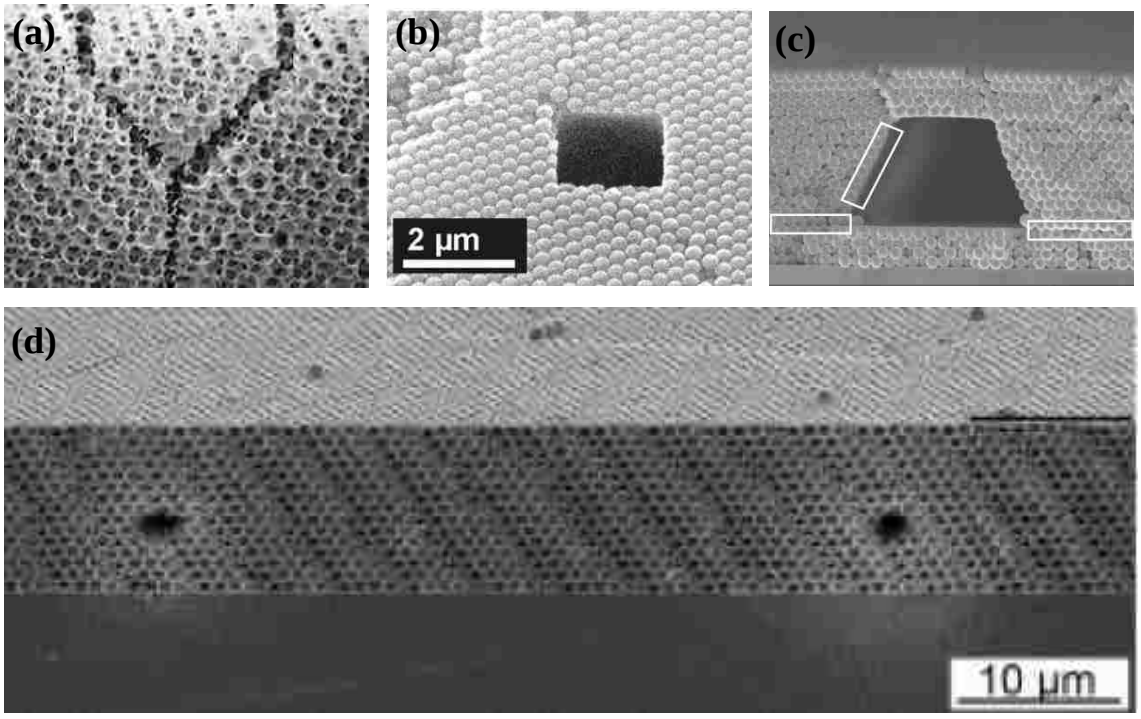

Figure 4.7: Defect patterns incorporated into colloidal crystal assemblies through microfabrication techniques. (a) Line defects generated by FIB milling[41] (b) Hole pattern by electron beam lithography[28] (c) Defect pattern using photoresist method[31] and (d) Line defects generated using multiphoton polymerization[30]. (All the figures shown were adapted from the corresponding references)

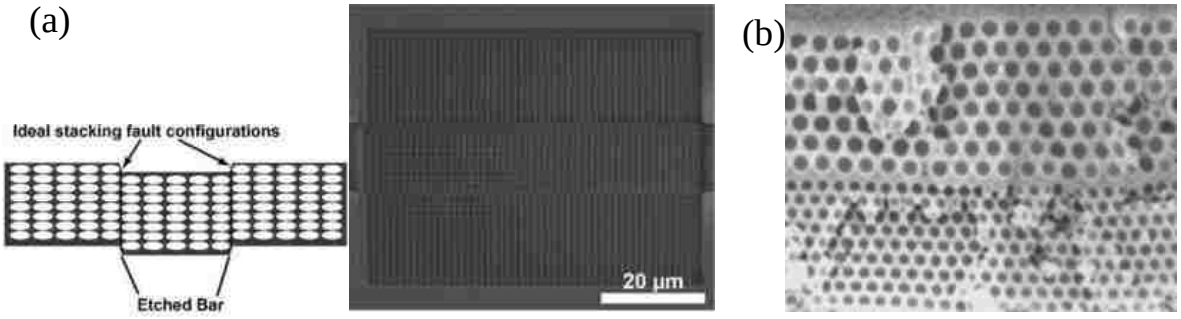

Figure 4.8: Fabrication of controlled defects in colloidal crystals through self-assembly techniques. (a) Fabrication of sedimentary colloidal crystal assembly with slanting planar defects through epitaxial procedures[37] (b) Fabrication of an embedded planar defect utilizing a two-step colloidal assembly process[34].

4.2 Analysis algorithm for characterizing bands in colloidal crystals

The colloidal crystal samples discussed in this chapter were obtained using a vibration assisted deposition process, a detailed discussion of which can be found in Chapter 2 of the dissertation. These crystal assemblies were observed to have significantly large domains with both hexagonal and square packing configuration, which corresponds respectively to fcc (111) and fcc (100) planes of the crystal oriented parallel to the substrate. While these results (in Chapter 2) signifies a long-ranged periodicity at particle level of the crystal assembly, the same samples are also characterized by regions which possess a periodicity at much larger length scales – a length scale spanning across several hundreds of particles in the crystal. Such regions with a higher hierarchy of periodical arrangements were observed in the square-packed regions of the sample in the form of parallel lines with a definite periodicity associated with them. Although these self-generated defects could be observed via planar scanning of the sample using SEM and confocal microscopy techniques, a detailed analysis of the same is a prerequisite to deduce the characteristics of these observed patterns, attain an in-depth understanding of the generation mechanism as well as to explore the potential for tuning the inherent morphology of these structures.

The analysis procedure for the colloidal crystal samples involves performing both a two-dimensional scan of the bottom-most layer of the assembled crystal as well as a three-dimensional volume scan. While the former would yield quantitative information regarding the density and periodicity of these defects when coupled with particle identification routines in IDL, the latter would help gain an understanding of the nucleation and growth dynamics of these volume defects in the crystal. The analysis algorithm discussed in this section was utilized to analyze the data obtained from a two-dimensional confocal scan of

the sample, with the objective of characterizing the periodic bands observed in the square-packed regions of the sample and involves the following calculations:

1) Identifying the particles in the frame which forms the band-like patterns

2) Group the particles thus identified into various continuous bands, accounting for the possible errors which may arise from a less-than-ideal confocal scan and incorrect estimation of the particle centroids

3) Calculations to determine the characteristics of the bands, namely, the periodicity of the bands, density of the occurrence of bands in a sample and their orientation with respect to the direction of deposition of the crystal assembly.

The analysis procedure adopted to achieve the aforementioned goals consists of several sequential steps, as has been outlined below based on a representative confocal scan image:

4.2.1 Identification of particles which constitute the band-like patterns

The particles which would form the band-like parallel lines visible in a two-dimensional confocal scan actually lies in a different plane with respect to the bulk square packing particles, and are not usually identified as discrete particles in usual calculations (discussed in Chapter 2). To perform computational analysis of the periodic bands, it is however essential to add these particles to the calculations, and are identified by lowering the intensity and particle diameter thresholds as to enable locating these particles in the confocal scan image. Once all the significant particles in a frame are identified, they are grouped into various categories, namely, square-packed regions (represented as red color), hexagonally packed regions (green color) and remaining particles which belong to neither of the two above groupings (blue color) – the grouping based on the initial steps of the

algorithm discussed in Chapter 2.The calculations being implemented to characterize the particles in a confocal image utilizes both the number of nearest neighbors of the particle as well as their local-crystallinity value (ψ) and consists of the following steps:

(i) Preliminary grouping of particles into square or hexagonal (or others) based on the number of nearest neighbors and ψ- values (as discussed in detail in Chapter 2)

(ii) For each of the particle classified as 'others' (blue particles), recalculations are done to explore if they could be added to the square-packing group (red) or hexagonal-packing group (green) depending on the it's nearest neighbor particles (as discussed in Chapter 2).

(iii) The particles which were originally blue, but then modified to be added to the square or hexagonal groupings are checked for their ψ- values to account for any possible errors in particle groupings. The steps (i), (ii) and (iii) yield groupings of particles, as shown in the color-coded reconstructions in Figure 4.9 b-d.

(iv) The particles represented as blue-colored spheres in Figure 4.10a may actually correspond to particles associated with either voids or bands. A discriminating feature of the particles actually associated with the bands is that they have similar local bond angles associated with them, which could be used to distinguish these particles from those associated with the voids. This is achieved by plotting a histogram of the particle angles and screening out the particles which have their angles highly deviating from the local peaks of the histogram. (The frame may in reality contain multiple sets of parallel bands- this results in multiple local peaks in the particle orientation histogram).

The particles which were identified to constitute the band based on the above listed calculations are shown in yellow color in Figure 4.10 b.

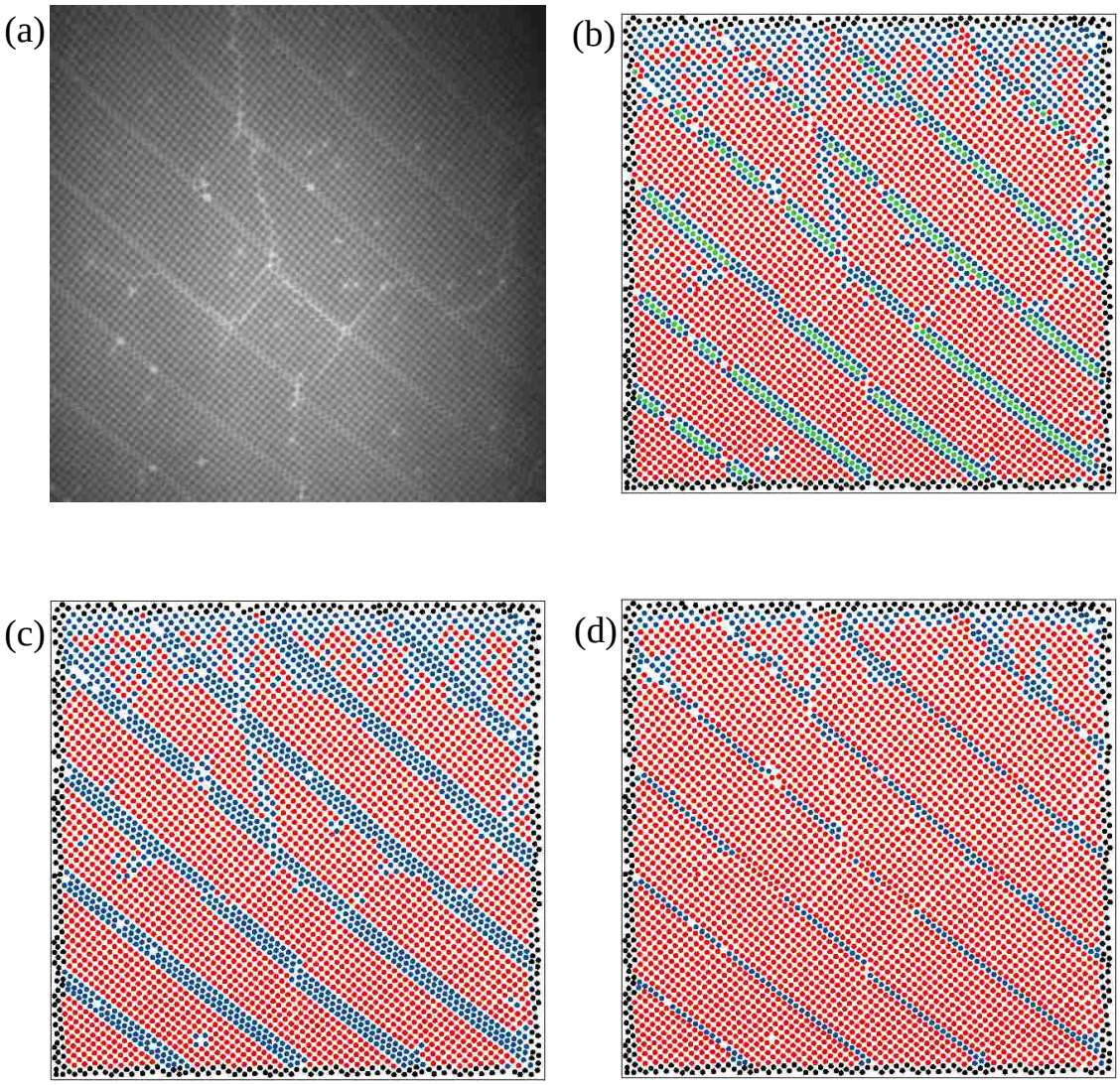

Figure 4.9: Calculations to identify particles constituting the band lines. (a) Representative confocal image used for demonstration of calculation algorithm (b) Reconstruction of particle types after calculating the number of neighbors (c) Recalculation based on ψ- values to eliminate any possible errors in particle groupings (d) Color-coded reconstruction after excess of blue particles were added to the square group (red) or hexagonal group (green)

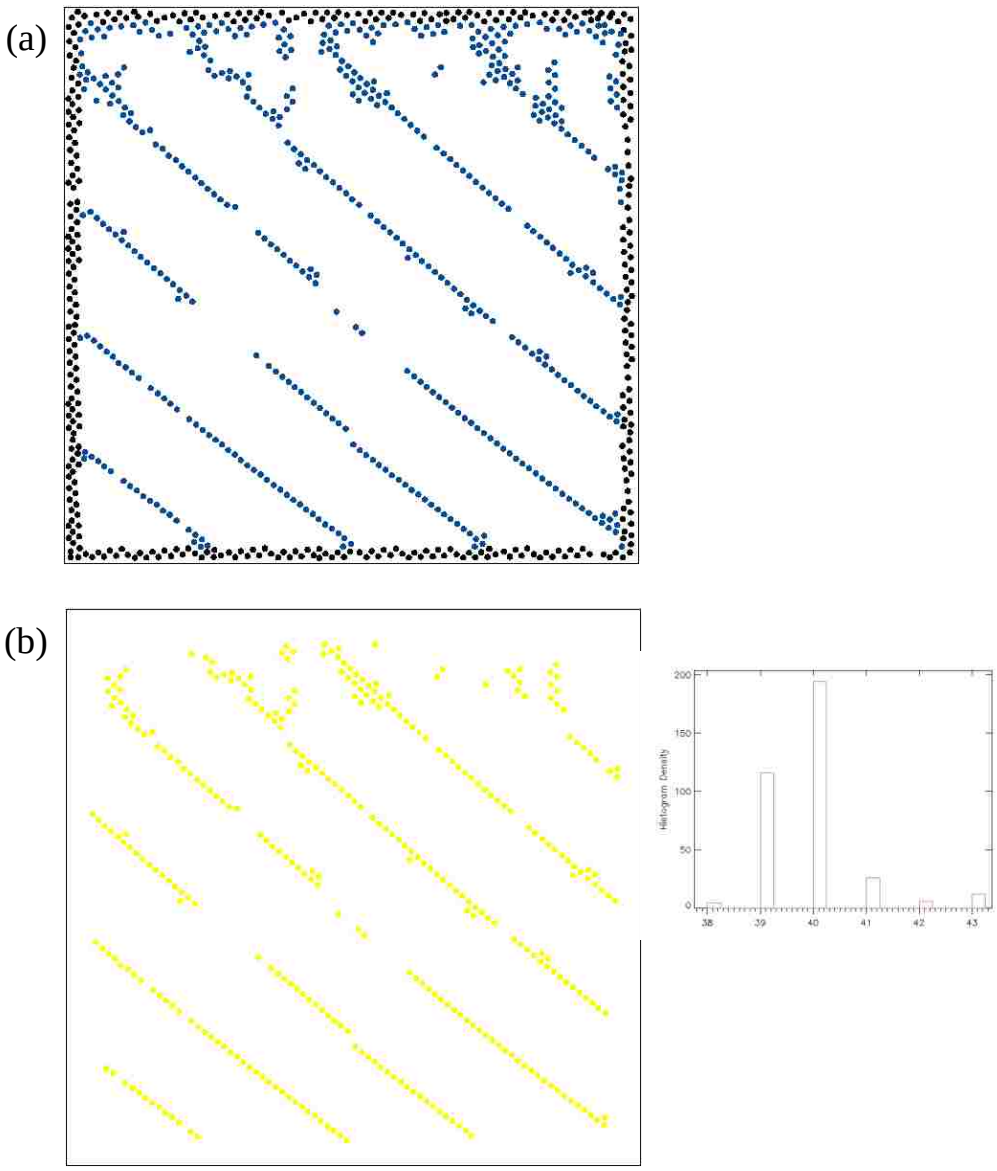

Figure 4.10: Calculations to identify particles constituting the band lines (Continued from Figure 4.9). (a) Reconstructed image showing the blue particles which were identified in Figure 4.9d (b) Particles which were identified to be constituting the band lines based on the histogram of local particle orientations, shown in yellow color. The histogram is shown adjacent to the figure.

4.2.2 Grouping of particles into various band lines

Once the individual particles possibly forming the band lines have been identified, they need to be grouped into distinct bands before any further analysis can be done. This is implemented by utilizing the local histogram peaks of particle angles, each peak in the plot corresponding to a distinct family of bands. The calculation involves the following steps:

(i) The yellow colored particles are initially grouped into various sets depending on their local orientation, with the number of such sets equal to the number of local peaks in the histogram (which in turn corresponds to the number of sets of parallel bands that can be identified in the confocal image under investigation).

(ii) For each set of particles thus identified (with similar orientation angles), a nearest neighbor calculation is done to identify the particles lying close to it and might belong to the same band line. To accomplish this, an inclined rectangular geometry with extended major axis and a shorter minor axis is considered as the region of interest around a reference particle, the enclosed region then probed for any particles with centroids lying within the rectangular geometry. Such a non-spherical geometry is considered in this case owing to the fact that not all the particles in the band-line might have been identified in Step 1. This hence demands a proper selection of the geometry parameters – inclination, length and width of the rectangle to effectively identify particles which might lie on the same band line.

(iii) Once the yellow particles were grouped into various sets (each set corresponding to a distinct line in the frame), the orientation of the band-line and standard deviation of the particles in the band line were calculated, along with an identification of the starting (top-most) and ending (bottom-most) particle co-ordinates.

(a)

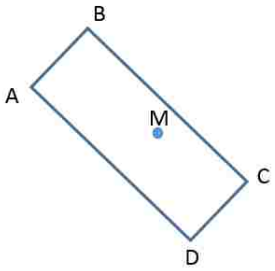

A particle M with co-ordinates (x,y) lies within a rectangle ABCD if and only if:

$$0 < AM.AB < AB.AB \quad and$$
$$0 < AM.AD < AD.AD$$

(b)

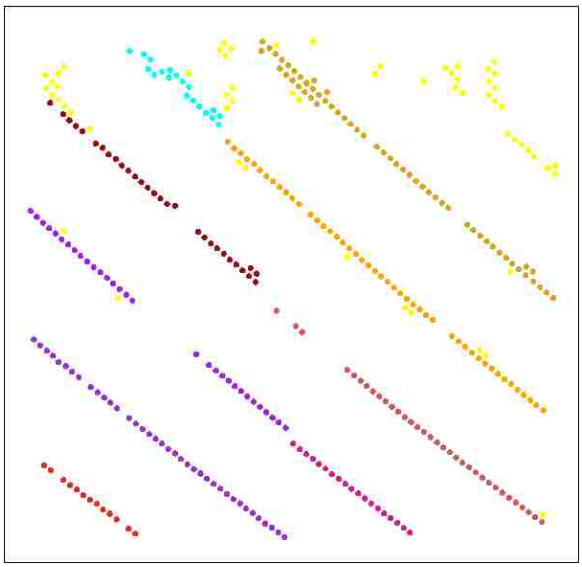

Figure 4.11: Grouping of band particles into distinct lines (a) Inclined rectangular geometry considered for grouping the particles into band lines (b) The particles which were grouped into various lines shown in non-yellow colors. The particle grouping assumes a minimum of ten particles within each group and groups with less than 10 particles are eliminated from further calculations.

4.2.3 Calculation to identify the characteristic attributes of the bands

For the band lines identified in the frame, the following calculations are then performed:

(i) Combining multiple lines into a single one

In certain scenarios, the particle identification in Step 1 might leave out several particles in the band, which might result in a single continuous band-line being identified as several disjoint lines with vacant regions between them. A set of calculations are performed which explores if the discrete lines identified in Step 2 might actually correspond to broken segments of the same band-line – the analysis based on the y-intercept of these lines (disjoint segments of the same band-line would have same values for the y-intercept). Once such possible combination is identified, the slope of the combined line is compared with that of discrete lines to eliminate possible errors in calculation.

(ii) Grouping the bands into various sets

After all the unique band-lines are identified, each set of parallel bands are grouped into various categories – each category (or family) of bands associated with a characteristic angle and with all of the constituting individual bands lying parallel to each other. The relative positions of the individual band-lines in each family are then identified based on their position in the frame in the direction of left to right.

(iii) Calculations on each family of bands

Once the various families of bands in a frame have been identified (with each family comprised of a set of parallel band-lines), the perpendicular distance between the band-lines are calculated. To obtain an accurate estimation of this distance, the perpendicular distance is calculated at various points along two adjacent parallel bands. The averaged

distance thus obtained directly corresponds to the periodicity of the bands. Furthermore, the area between the bands is also calculated, which would yield a quantitative estimate of the fraction of square packing in the sample confined within the band regions. An inherent challenge in area estimation is that in some cases, the entire span of the band-lines may not be identified due to missing particles which results in an underestimation of the area. Suitable approximations are adopted in such scenarios to get reliable estimates of the actual length of the band-lines.

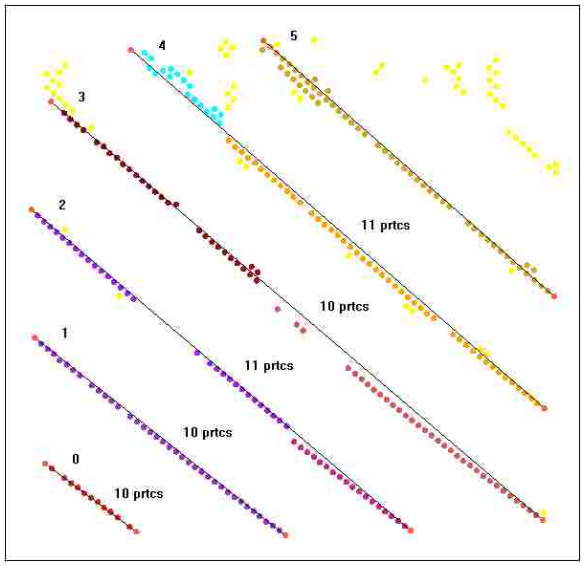

Figure 4.12: Calculation of periodicity of bands. A reconstructed image which shows the band patterns after multiple band lines with similar y-intercepts were combined together and the periodicity of the band-lines calculated.

4.3 Results and Discussions

The ability of the vibration-assisted deposition process to affect the generation of non-hexagonal packing assemblies in colloidal crystals has been discussed in Chapter 2 of the dissertation, thus opening up an alternate approach to fabricate such structures without relying on colloidal epitaxy procedures. From the discussions in Chapter 2 and 3, it could be concluded that the aforementioned procedure in fact simultaneously generates both uniformly packed hexagonal and square domains of millimeter-sized length scale, as could be inferred from the diffraction experiments employing large mm-scale-diameter laser beams. The simultaneous generation of these packing assemblies could be attributed to the generation of particle-nucleate microstructures in the suspension with both square and hexagonal packing which occurs due to hydrodynamic stresses acting in thin film region.

In addition to the formation of large continuous regions with square packing configuration, the generated crystal assemblies were also observed to have a high density of defects in the square packed regions. However, a novel characteristic which distinguishes these defects and sets them apart in comparison to intrinsic defects in other self-assembly techniques was the long ranged order associated with these defects, which corresponds to the periodicity of these packing assemblies at a higher level of hierarchy than the periodicity at particle level. These defects were visible as a family of periodic band-lines on the surface of the crystal, associated with a unique periodicity maintained over dimensions of several thousands of monosized particles –the ‘periodicity of defects’ referred to in this discussion corresponding to the number of particles along a perpendicular line between two adjacent band lines. On a detailed analysis of the crystal volume using confocal microscopy techniques, it was inferred that these band-lines on the surface

actually corresponds to ledge patterns (continuous zig-zag or V-shaped volume defects) generated within the assembly.

4.3.1 Morphology of ledge-shaped defect patterns

The co-generated defects in the crystal assembly were analyzed for their topography and intrinsic characteristics through extensive confocal-based methods. While a two-dimensional confocal scan enables an investigation of the extent of spread of these defects within the square domain, density of these patterns and conservation of its periodicity, a three-dimensional confocal scan in the z-direction enables a volume reconstruction of these patterns which could stimulate an investigation into the underlying mechanisms.

The confocal images in Figure 4.13a,b shows a set of defects running parallel to each other with definite periodicity, these images being representative of the two patterns of defects observed in the sample. While both images show a localized distortion of the bulk four-particle packing symmetry at periodic length intervals, they are characterized by a dissimilar planar location and local orientation of the particles lying within the distorted region. On careful inspection, it could be observed in Figure 4.13a that the particles at localized crystal imperfections lie on a plane different from the perfectly packed particles on its either side, and these types of defects are referred to as ‘Type A’ in the following discussions. Conversely, the image in Figure 4.13b has all the particles in the frame lying on the same plane but with a distortion along two adjacent groups of particles. This type of defects is referred to as “Type B” for the sake of clarity in the subsequent discussions. While the former could be visualized as a localized (110) fcc packing at certain regions,

the latter is similar to simultaneous slipping of a set of particles in the (100) direction relative to the adjacent particles, displacement vector magnitude being less than the lattice parameter which would yield the observed pattern. When a detailed analysis of the sample was done to establish a relative generation frequency of either of these patterns, it was observed that the patterns consist predominantly of Type A, with Type B rarely observed (discussed further in mechanism section).

The reconstructed panorama images in Figures 4.14 and Figure 4.15 were obtained by combining several coded individual frames of the defect patterns. In these images, it could be observed that the generated defects conserve its periodicity throughout the entire region of its presence, which makes these defects different from the intrinsically generated defects reported for colloidal crystals. Furthermore, these defects could be observed to have a spread spanning the entire region of the fcc (100) domain from one grain boundary to the other, with their alignment directed along the minor dimension of the crystal as could be seen in Figure 4.15. Another significant inference which could be derived from the reconstructed images is the presence of fully developed defect lines as well as partially developed ones, represented using white and grey squares respectively in Figure 4.14 a,b. The inset images of Figure 4.14a show a magnified view of the local particle orientations at the three representative regions of a single family of defect lines – at the grain boundary, at one of the partially developed defects and a fully developed defect. From the inset images, it could be observed that the periodicity of the defects remains the same at all the three points.

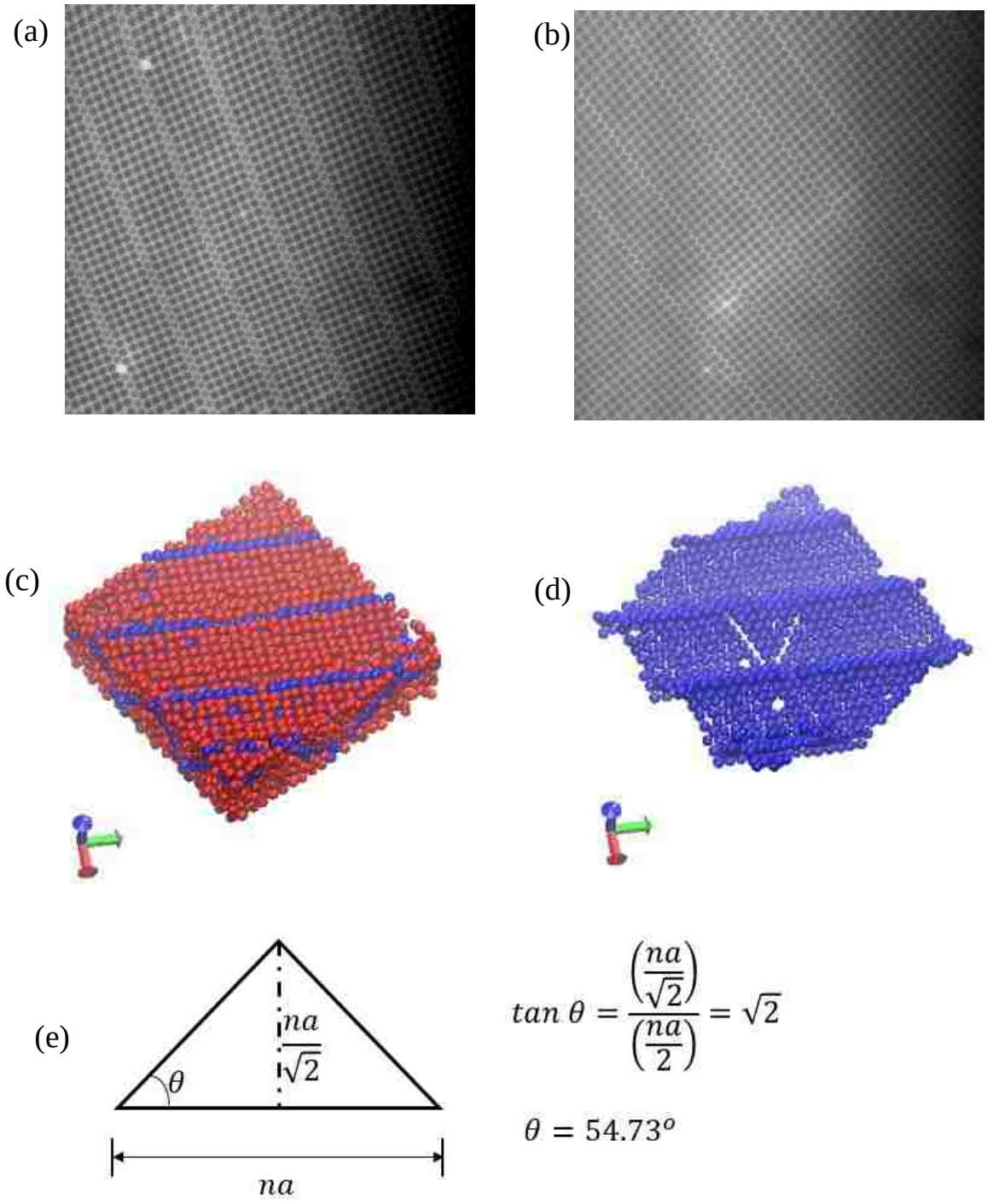

Figure 4.13: Periodic defect patterns observed in fcc (100) colloidal crystals. (a) Defect patterns generated by slipping of particles in the fcc crystal in a <110> direction (b) Defect patterns in fcc (100) formed by the slipping of particles relative to one another in same plane (c) 3-D reconstructed image of the periodic defect (d) A reconstruction of the defect plane which shows the ledge-shaped pattern and hexagonal packing of particles in the defect plane and (e) Geometric calculations to confirm the identity of the defect plane as fcc (111) plane.

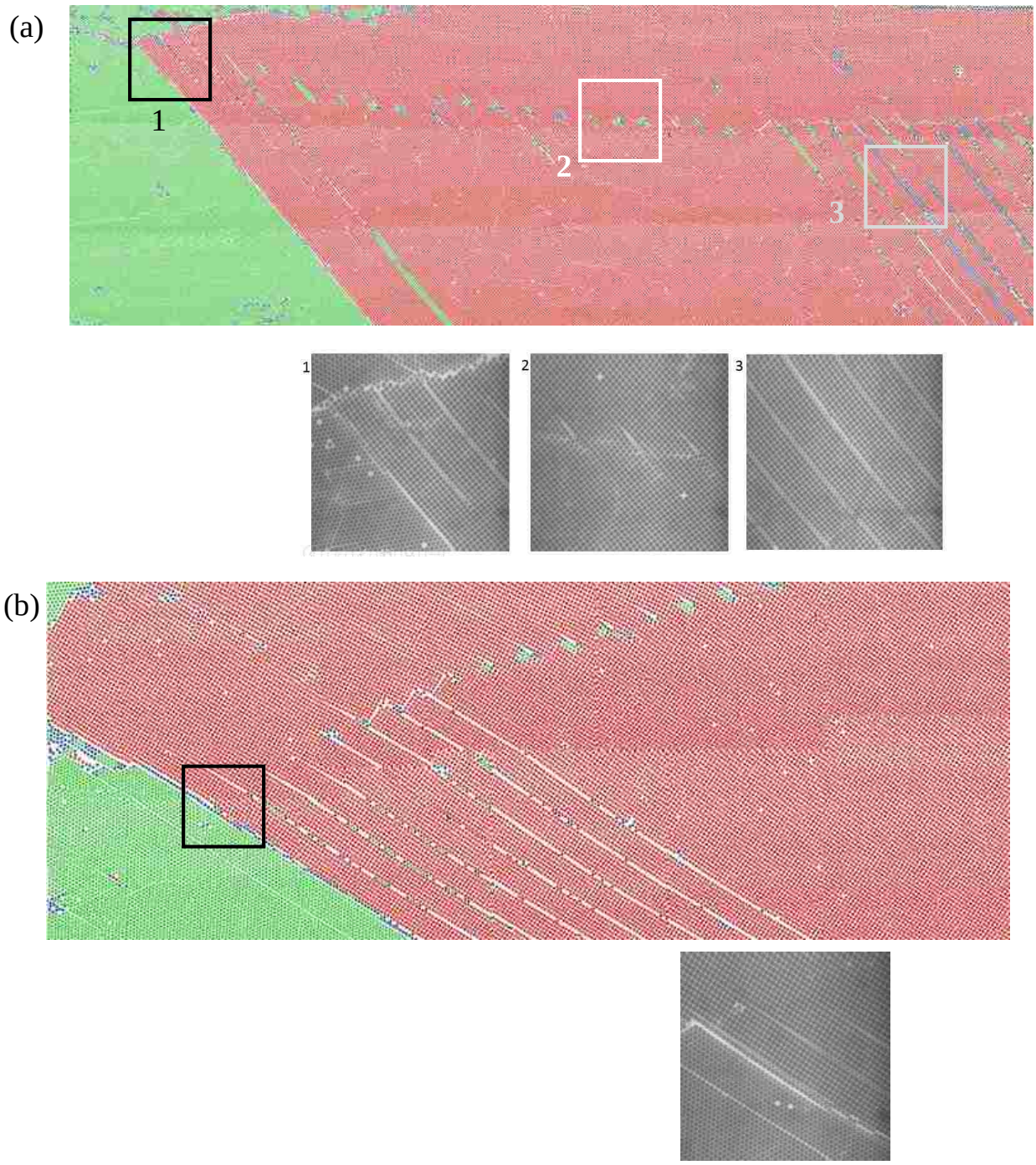

Figure 4.14: Reconstructed panorama images of the defect patterns in colloidal crystals. The images use following color representation for packing assemblies: square-packing (red), hexagonal packing (green) (a) Panorama image with three representative regions: grain boundary, under-developed defects and fully developed defects shown as black, white and grey colors respectively, a magnified image of each shown underneath (b) Another panorama image with a magnified view of the region adjacent to the grain boundary. The as-observed 'under-developed' and 'fully-developed defects' could be attributed to perfect dislocations and imperfect dislocations, discussed in details in following sections.

Figure 4.15: Reconstructed panorama image of defect pattern which shows the defects running along the minor dimension of the crystal

The observed patterns were also analyzed for their 3-D structure using a volume based confocal scan, a reconstructed image of which is shown in Figure 4.13c. In this figure, the assembled particles of the bulk matrix with a four-fold particle symmetry is shown in red color, whereas all other particles are shown in blue. A reconstructed image with the blue particles isolated from the volume matrix is shown in Figure 4.13d, with a definite hexagonal packing symmetry associated with it. An analysis of the 3-D reconstructed pattern also showed that the periodicity of the defects is equal to the number of layers of the fcc (100) colloidal crystal domain. A schematic of this geometry could be reconstructed as shown in Figure 4.13e, with the base angle of the geometry calculated to be equal to 54.73^{o}.

Considering an fcc crystal, the angle between (100) and (111) planes is given by:

$$\theta' = Cos^{-1}\left(\frac{1}{\sqrt{3}}\right) = 54.7^{o}$$

Thus, it could be confirmed that the defects observed in the fcc (100) oriented colloidal crystal are confined to the (111) planes of the crystal.

4.3.2 Proposed mechanism for the observed defects in fcc (100) crystals

The formation of periodic band like defects could be attributed to a sequential initiation and propagation of defects in the volume of the crystal, the underlying mechanism being spatially correlated. This hypothesis derives its motivation from the observation that the parallel lines observed in the sample have their periodicity conserved throughout the assembled region of the crystal, spanning several thousands of particles.

The defects observed in the square packed regions of the colloidal assembly can be visualized to be a result of the strain relaxation of the crystals when subjected to a deforming force. The initial indication regarding this mechanism was inferred from the 3-D reconstructed image of the defect pattern which showed a hexagonal packing of particles in the defect plane, with the individual defect patterns resembling an fcc (110) packing arrangement. These observations could be coupled with the dislocation theory- involving processes like nucleation, growth, propagation and dissociation reactions, which have been extensively studied for conventional materials and recently demonstrated for colloidal crystals. These strain relaxation processes occur only in the square packed regions of the assembly, as is evident from the complete absence of such patterns in the hexagonally packed regions of the assembly- the distinguishing factor being the stress acting on the crystal for particle configuration and mobility of the individual packing units in the respective regions.

4.3.2.1 Hydrodynamic stresses acting on fcc (100) and mobility of assembled particles

The deforming stress fields which eventually generates the observed defect patterns have their origin in the hydrodynamic forces acting on the square crystal domain in the post-assembly phase, after the individual particles have been assembled into a long-range ordered arrangement featuring a rectangular domain with sharp boundaries as shown in Figure 4.16a. Due to the large amplitude of vibrations employed in the deposition process (> 1 mm), the square domains remain subjected to the periodic back and forth movement of the liquid meniscus over it, with the solvent undergoing Darcy flow through the voids in the packing assembly. The resistance of the packing assembly to this Darcy flow depends predominantly on the void structure of the assembly perpendicular to the direction of flow streamlines. Considering the two crystal assemblies simultaneously observed in the sample (fcc(111) and fcc(100) oriented parallel to the substrate), an fcc(100) crystal offers lowest resistance to flow if the voids are aligned parallel to the direction of flow. However, a contrasting scenario comes into play if the fcc (100) packing and the direction of Darcy flow are both oriented parallel to the substrate, in which case the crystal face of the fcc (100) domain oriented perpendicular to flow offers a significant resistance to the flow of liquid through it. This resistance to flow offered by the square domains perhaps could be the origin of the hydrodynamic stresses acting on the crystal, which could then transform into a shearing force owing to the 30^{o} preferential orientation of the square domains with respect to the flow direction.

In addition to a stress field of sufficient magnitude, another prerequisite to effect changes in a particle structure during its post-assembly stage is the mobility of individual units within the assembled structure, without the distortion of the bulk particle

configuration. For the crystal assembly discussed in this chapter, this is made possible by the presence of solvent (DI water) within the void structure of the crystal prior to its complete drying. This imparts a restricted mobility to the individual packing units in the crystal, with the particles free to move about their mean position in the assembly, keeping the bulk packing unperturbed.

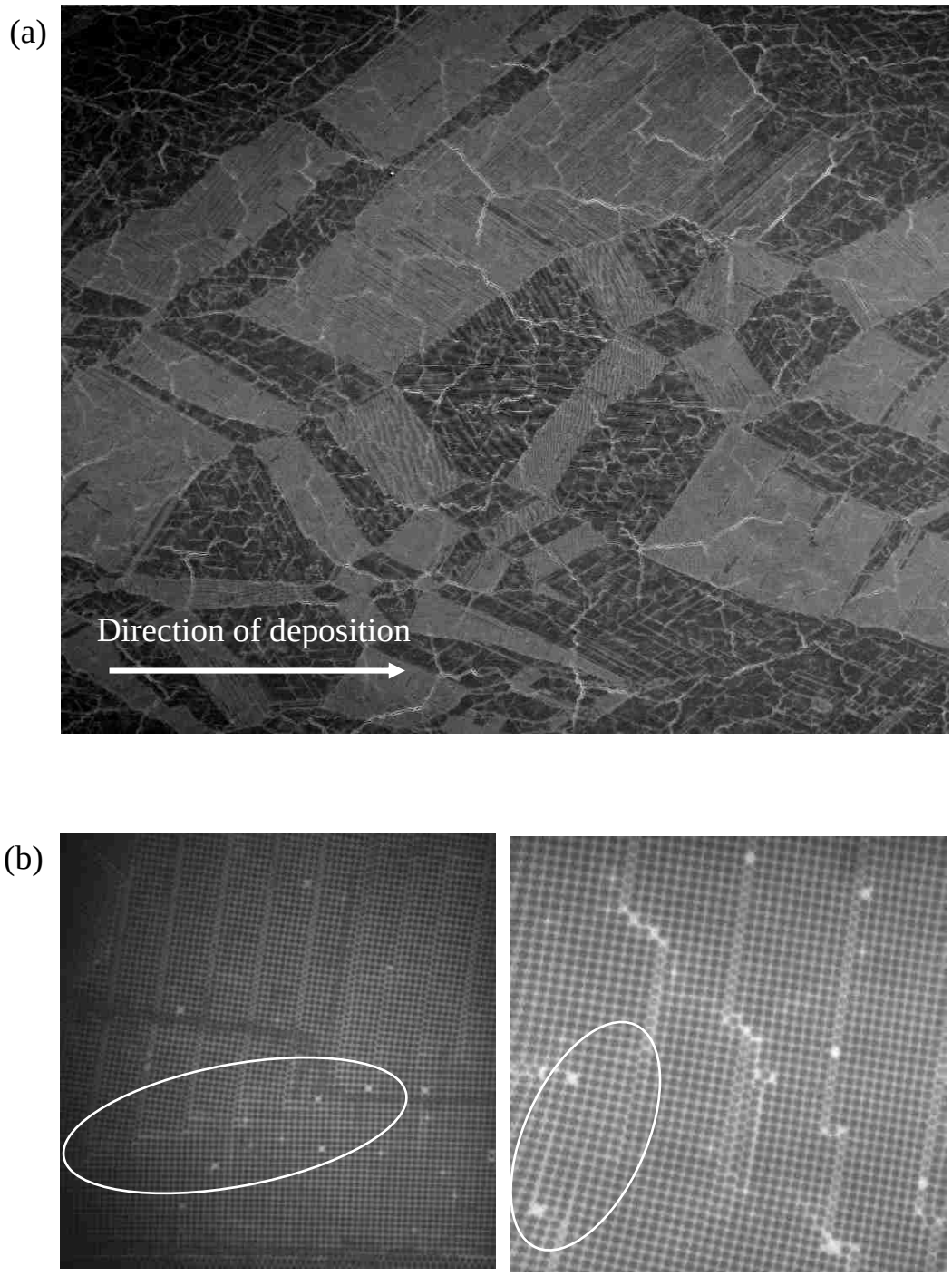

Figure 4.16: Investigation of the hydrodynamic stresses acting on fcc (100) crystal. (a) A SEM image of the sample showing the fcc (100) domains (bright color). The image shows the rectangular shape of domains, their aspect ratios and relative orientation of these domains with respect to flow direction (b) Representative images which shows the distortion in relative particle orientations at the edges of bands. The presence of arrays of dislocations in the crystal could be verified by the observed low angle grain boundaries highlighted in the images.

4.3.2.2 Slip system based analysis of the fcc (100) colloidal crystal

When a uniformly packed crystal domain experiences built-up of strain energy, the crystal attempts to effect a reduction in the stored energy, the adopted pathway for strain relaxation being the nucleation and propagation of dislocations within the crystal volume. The movement of such dislocations, generally referred to as 'slip' or 'dislocation glide' results in patterns visible as distinct lines on the surface of the crystal where the dislocation escapes out of the crystal volume. The inherent characteristics of these defects can be derived based on identifying the corresponding slip system of the fcc crystal, comprising of slip plane and slip direction. For the fcc crystal reported in this study, the slip plane is the {111} family of planes with <110> set of directions being the dominant slip direction.

The occurrence of two distinct defect patterns in Figure 4.13a,b (referred to as Type A and Type B) however requires a more detailed analysis of the dislocation processes and associated energetics in an fcc crystal.

For an fcc {111} plane, a few possible directions in which it can undergo slip are:

(i) <110> direction, which has a Burger vector of $\overline{\boldsymbol{b}} = \frac{a}{2} < 110 >$

(ii) <100> direction, for which Burger's vector is given by: $\overline{\boldsymbol{b}} = a < 100 >$

Comparing the self-energy of dislocations (approximated as the square of the Burger's vector (b^2)), for dislocation slip in $< 110 >$ direction, $b^2 = \frac{a^2}{2}$

For dislocation slip in $< 100 >$ direction, $b^2 = a^2$

Since the dislocations with lowest self-energy are preferred by the crystal, the dislocation patterns obtained in an fcc crystal prefers a movement of particles in the $< 110 >$ direction.

The preference of the {111} crystal planes to adopt a movement in the <110> direction could be easily observed in the case of Type A defects. This has been further illustrated by the set of schematics in Figure 4.17, which compares a perfectly crystalline fcc structure to a distorted one characterized by a simultaneous movement of particles in the <110> direction. The magnitude of particle movement in this scenario can be observed to generate an imperfect / partial dislocation instead of a perfect one, the generation of which requires a displacement magnitude of $\frac{a}{2}$ in <110> direction, whereas the observed magnitude is only $\frac{a}{4}$. ($'a'$ being the lattice parameter). The formation of such partial dislocations could be explained based on the tendency of the crystal to reduce the energy associated with a dislocation pattern, achieved by dissociation reaction of the form:

$$\frac{a}{2}<110> \quad \rightarrow \quad \frac{a}{4}<110> + \frac{a}{4}<110>$$

$$b_1^2 = \frac{a^2}{2} \qquad b_2^2 + b_3^2 = \frac{a^2}{8} + \frac{a^2}{8} = \frac{a^2}{4}$$

Although the dislocation reactions of this type has not been reported for conventional solids, its occurrence in the colloidal systems under consideration could be attributed to the low energy threshold of these systems in comparison to its atomic counterparts. Moreover, in the case of crystals considered in this chapter, the crystal assembly has water within the voids which imparts additional mobility for the particles.

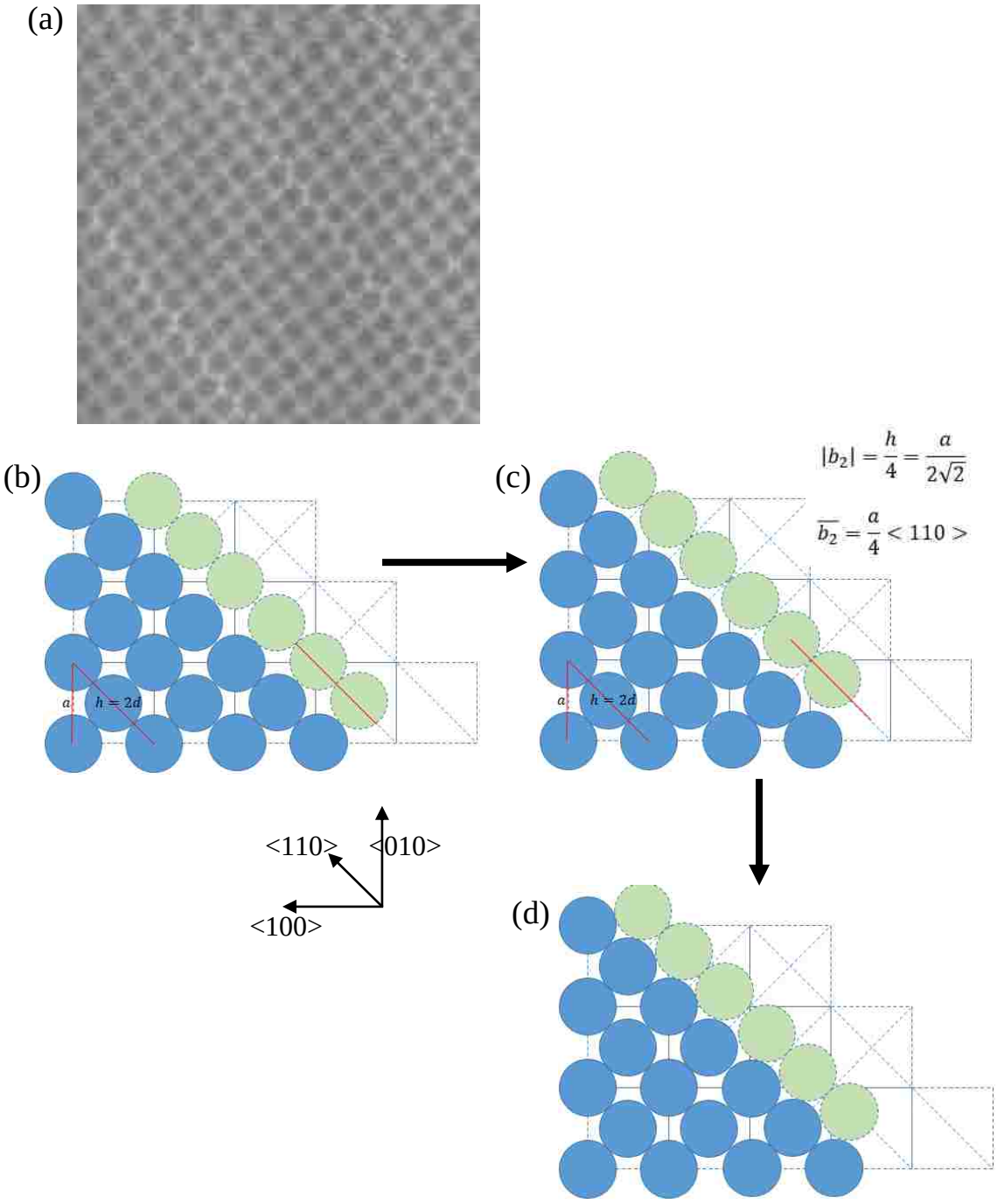

Figure 4.17: Analysis of Type 'A' defects. (a) A magnified confocal image of the defect pattern obtained at the bottom-most layer of the crystal (b-d) A sequential representation of the pattern generation from a perfect crystal. (b-c) Movement of particles in <110> direction (c-d) Movement of particles in $<1\bar{1}0>$ direction. This step can however be ignored as the energy is required by crystal only to overcome the threshold barrier for its movement and only (b-c) transition needs to be considered.

While Type 'A' patterns features a single vertical plane for the bulk square particles as well as the boundary particles of the bands (which has localized hexagonal packing), the Type B patterns have a different z-position or height for both sets of particles. This could be confirmed by the distinct difference in intensities of both sets of particles which could be observed in the two-dimensional confocal image obtained with the bulk square packed particles in focus (Figure 4.18a) and further confirmed experimentally using a three-dimensional confocal scan of the crystal sample. The formation of these patterns can also be explained based on dislocation reactions as was postulated for Type A defects, but with a different set of component directions which moves the particles out of the bulk plane.

The dislocation dissociation reaction in the crystal could be represented as:

$$\frac{a}{2}<110> \quad \rightarrow \quad \frac{a}{6}<211> + \frac{a}{6}<12\bar{1}>$$

$$b_1^2 = \frac{a^2}{2} \qquad\qquad b_2^2 + b_3^2 = \frac{a^2}{6} + \frac{a^2}{6} = \frac{a^2}{3}$$

Although the partial dislocations reported in fcc crystals could be Shockley partials or Frank partials, we postulate that the observed dislocations are of Shockley type as they are mobile dislocations with their slip plane on {111}. Frank dislocations, on the other hand, are immobile in nature.

Geometric calculations were performed to confirm the presence of <112> movement as the underlying reason for the patterns of Type B. From a representative confocal image corresponding to the bottom-most layer of the sample, the horizontal separation distance (projected distance) of both sets of particles was calculated to be 0.49 μm, while the vertical distance of separation between the centroids (bottom-most set of either particles) was evaluated to be 0.27 μm. This gives an angle of 29^o which is equal to the theoretical inclination angle between {110} and {112} planes (Figure 4.18b).

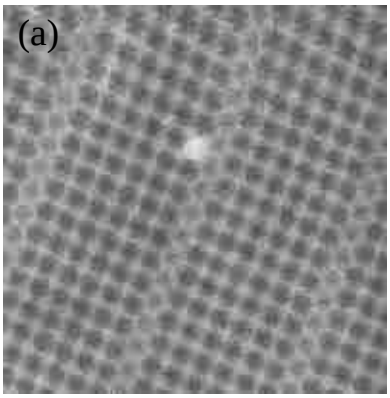

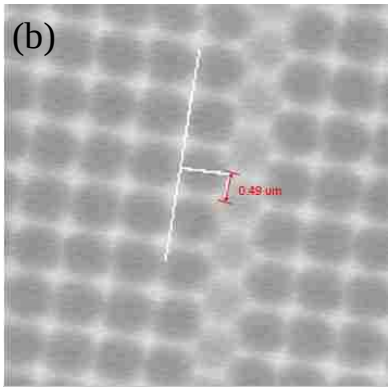

(c)

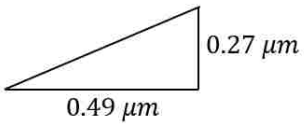

$$\tan\theta = \frac{0.27}{0.49}$$

$$\theta = 28.8^{o}$$

(d)

$$\bar{u} = \frac{a}{6} < 211 >$$

$$\bar{n}_{\{100\}} = < 001 >$$

$$a = \sqrt{2}\mathrm{d} = \sqrt{2}\ \mathrm{x}\ 0.93\ \mu m = 1.32\ \mu m$$

$$projection\ vector, \bar{p} = \bar{u} - \frac{\bar{u}.\bar{n}}{|n|^2}\bar{n}$$

$$\bar{p} = \frac{a}{6} < 211 > - \frac{\frac{a}{6}(1)}{1}.< 001 >$$

$$= \frac{a}{6} < 211 > - \frac{\mathrm{a}}{6} < 001 >$$

$$= \frac{a}{6} < 210 >$$

$$|p| = \frac{a}{6}\sqrt{(4+1)} = \frac{\sqrt{5}}{6}a = 0.49\ \mu m$$

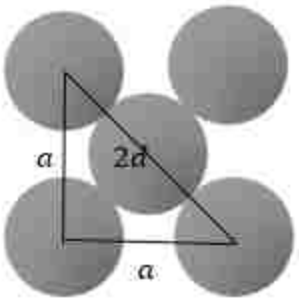

Figure 4.18: Analysis of Type 'B' defects. (a) A magnified confocal image of the defect pattern obtained at the bottom-most layer of the crystal – The difference in the height location of both sets of particles are evident from the different intensities of the particles (b,c) Geometric calculation to confirm the presence of <112> direction. Considering the band-edge particles with the bulk square particles, horizontal projected distance = 0.49 μm, vertical distance of separation between the centroids = 0.27 μm. This gives an angle value of 29°, equal to the angle between a {110} plane and {112} plane (b,d) Another set of calculations to support the hypothesis which measures the horizontal projected distance of the vector, $\bar{u}$ with the {100} plane where $\bar{n}$ is the unit normal vector

4.3.2.3 Nucleation and propagation of dislocations

The generation and distinct characteristics of Type A and Type B patterns could be explained based on the concept of slip system in fcc crystals and dislocation reactions which generates the respective in-plane and out-of-plane patterns. However, the spatially correlated generation of hundreds of such patterns with uniform periodicity and spanning across several thousands of particles demands an in-depth understanding of the dislocation dynamics, which investigates the nucleation and propagation of these defects. The pre-requisite of spatial correlation eliminates a possible mechanism whereby the bands are randomly nucleated on the surface of the substrate and propagates upwards the crystal along the slip plane.

The observed periodic bands in the fcc (100) crystal could be attributed to two possible mechanisms, both of which are spatially correlated. In the first possible mechanism, there is a homogeneous nucleation of dislocation at the grain boundary. This corresponds to a scenario in which there is localized accumulation of stress within the bulk of the crystals, which eventually act as nucleation spots. When these dislocations reached the free surface of the crystal, they perhaps nucleated another dislocation on the intersecting {111} plane by the phenomenon of 'cross-slip' (discussed further in Section 4.3.2.4), which could aid in the spread of these patterns in opposite direction in the crystal. With cross-slip phenomenon occurring alternatively at the free-surface of the crystal and the surface of the substrate, there is a gradual propagation of these patterns in the downstream direction of the crystal with preservation of its periodicity. A schematic of this is shown in Figure 4.19a. The development of a new dislocation by cross-slip has been demonstrated by various groups for conventional materials[17] as well as colloidal crystals[25].

In a second possible mechanism, the nucleation of dislocations occurs at interior points within the bulk crystal, as has been demonstrated for plasma crystals[42] in which a dislocation initially splits into a dislocation pair which are then gradually separated from each other and moves out in opposite directions. This could be considered analogous to the observed ledge-shaped patterns, which might have been generated from a single source and gradually progressed in opposite directions. The simultaneous generation and movement of two dislocations in opposite directions relives the accumulated stress within a definite volume of the crystal. This process is then repeated one by one within the crystal volume, whereby a V-shaped pattern is nucleated on the surface of the substrate which grows till the crystal surface. A schematic of this scenario is represented in Figure 4.19b. A work which demonstrates a similar observation involves a molecular dynamics based analysis of dislocation nucleation in a defective crystal with voids[43]. For the considered system, two branches of dislocations were simultaneously generated from the void surface within the crystal volume when subjected to deforming forces.

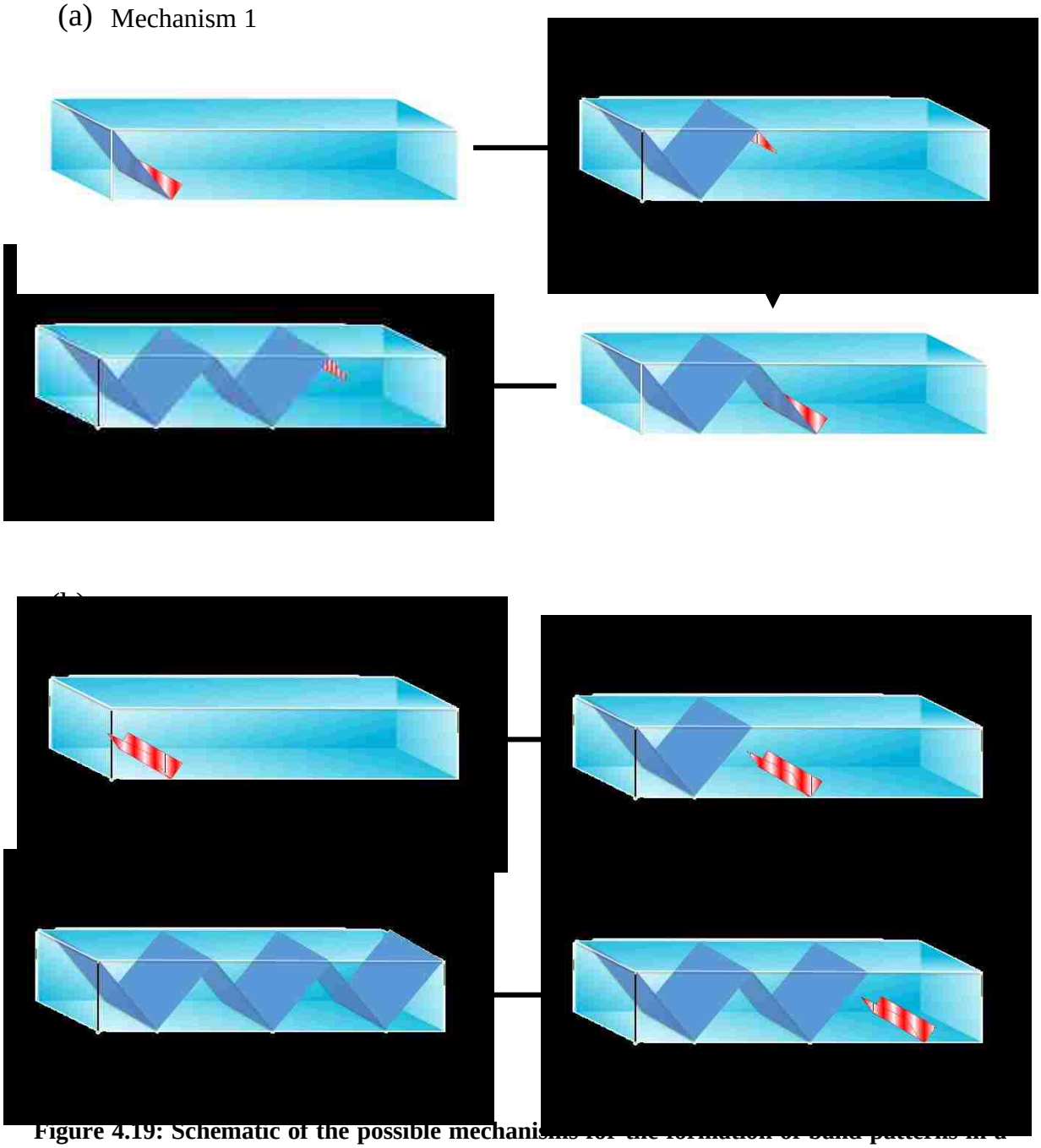

Figure 4.19: Schematic of the possible mechanisms for the formation of band patterns in a square packed domain. The red colored patterns in the figure represents a nucleation event whereby a new dislocation is generated on the {111} plane in the direction as indicated. (a) A schematic which shows the sequence of steps by which the dislocation spreads throughout the crystal starting from the grain boundary. The propagation is achieved by 'cross-slip' occurring alternatively at the free surface of the crystal and the surface of the substrate (b) Another possible mechanism whereby two dislocation branches are simultaneously generated at a single point on the substrate.

A nucleation hypotheses based on a single nucleation event at the grain boundary (Mechanism 1) appears more plausible based on similar observations for conventional solids as well as colloidal crystals, unlike the second scenario which has been shown only for heterogeneous nucleation from a pre-existing void. Another factor supporting the former mechanism is the observation that the periodicity of the defects is maintained even at grain boundary. With multiple fcc (111) planes, it is possible that the dislocation nucleated away from the boundary may terminate at the grain boundary along any of these planes, which might yield a band spacing which would be different from the periodicity maintained within the bulk of the crystal. Hence, a more plausible hypothesis would be that the dislocations are nucleated at the grain boundary due to the fluid stress acting on the square-packed domain, and gradually progresses unidirectional within the crystal volume.

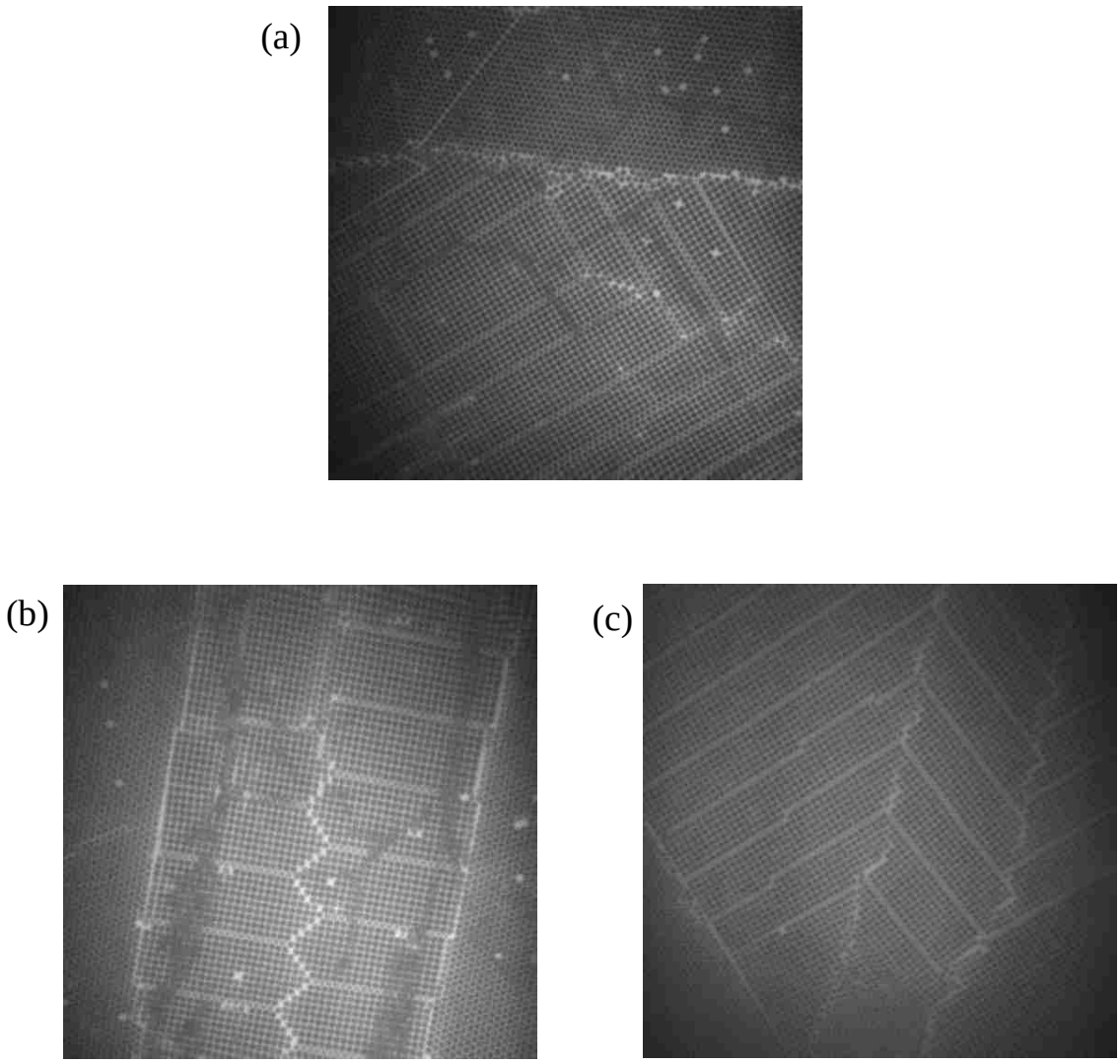

Figure 4.20: Multiple families of band lines observed in the fcc (100) domains of the colloidal crystal assembly.

4.3.2.4 Propagation of dislocations within the crystal

The observation of conserved periodicity within a family of dislocation lines lends credence to the observation that the multiple dislocations in the sample are spatially correlated, instead of being independently generated within the volume. A stress field acting on a crystal may result in the homogeneous nucleation of a single dislocation event, and other dislocations in the family are generated sequentially from an adjacent dislocation. This could be observed in the multiple families of lines in Figure 4.20a,b, where each family has its distinct periodicity and intersects with bands of another family at perpendicular angles (Figure 4.20a). In these images, the origin of an entire family could be traced back to a single nucleation event. The slight variations in periodicity observed in the images could possibly be due to the localized variations in the thickness of the fcc (100) crystal.

The generation of a new dislocation from a pre-existing one could be attributed to a heterogeneous nucleation process, in contrast to the homogeneous nucleation which generated the initial dislocation of the family. In this process, when a (111) plane containing a dislocation slips out of its original lattice in the <110>direction, there is a built-up of strain energy in the adjacent (111) plane which lies at an angle to the previous one. Thus, there is a transfer of strain energy between two intersecting (111) planes at the two surfaces of the crystal – at the crystal-substrate contact-plane and crystal-air contact-plane. This explains the generation of a new branch of dislocation from the pre-existing ones which then undergoes a slip movement in a negative direction relative to the previous one. This phenomenon, referred to as cross-slip (discussed in detail in Section 4.1.2.5), has been observed in LiF crystals[16] as well as in colloidal crystals subjected to indentation[25].

4.3.2.5 Effect of crystal domain orientation

The intrinsic feature of slip bands including its pattern, density and orientation observed in the fcc (100) crystal in turn depends on the magnitude and direction of the shearing forces acting on the crystal. This hypothesis has been demonstrated in detail for the observed Lauder's bands generated during the deformation in mild steel[44] – with study focusing on the effect of gran size and cross-sectional geometry on the generated band patterns within the single crystal. These observations could be extended to the current scenario, in which the generation of a high density of bands in the fcc (100) structure attributed to the macroscopic geometry of the square-packed domains. From the SEM image in Figure 4.16a, it could be observed that the square domains (which appear as bright regions) are predominantly rectangular in shape, with similar aspect ratios for several domains. Another distinguishing feature is the preferential orientation of these domains, which was calculated to be 30^{o} with respect to the flow direction. Geometrical considerations of a body subjected to shearing forces indicates that the slip bands could be generated more easily in bodies which have their aspect ratios much different from 1. Furthermore, the orientation of the bands would be such that they run parallel to the minor dimension as could be observed in Figure 4.15.

4.3.3 Tunability of defect periodicity in self-assembled crystals

From Figure 4.13d, it could be observed the defects are confined within the {111} set of planes in the crystal, with the planes appearing to diverge from each other from a reference line. This in turn results in the ledge patterns possessing a separation distance directly related to the number of layers of the colloidal crystal assembly. This characteristic of the patterns opens up a strategy to devise structures with a controlled periodicity of these patterns by varying the number of layers of the crystal assembly. To further investigate this possibility, colloidal crystal samples with (100) fcc regions were fabricated by varying the deposition speed and humidity of the growth environment – the periodicity of defect patterns in these crystal assemblies as given by Figure 4.21a-f . With the number of layers varying from four layers to 13 layers, a similar proportional increase could be observed in the periodicity of the crystal.

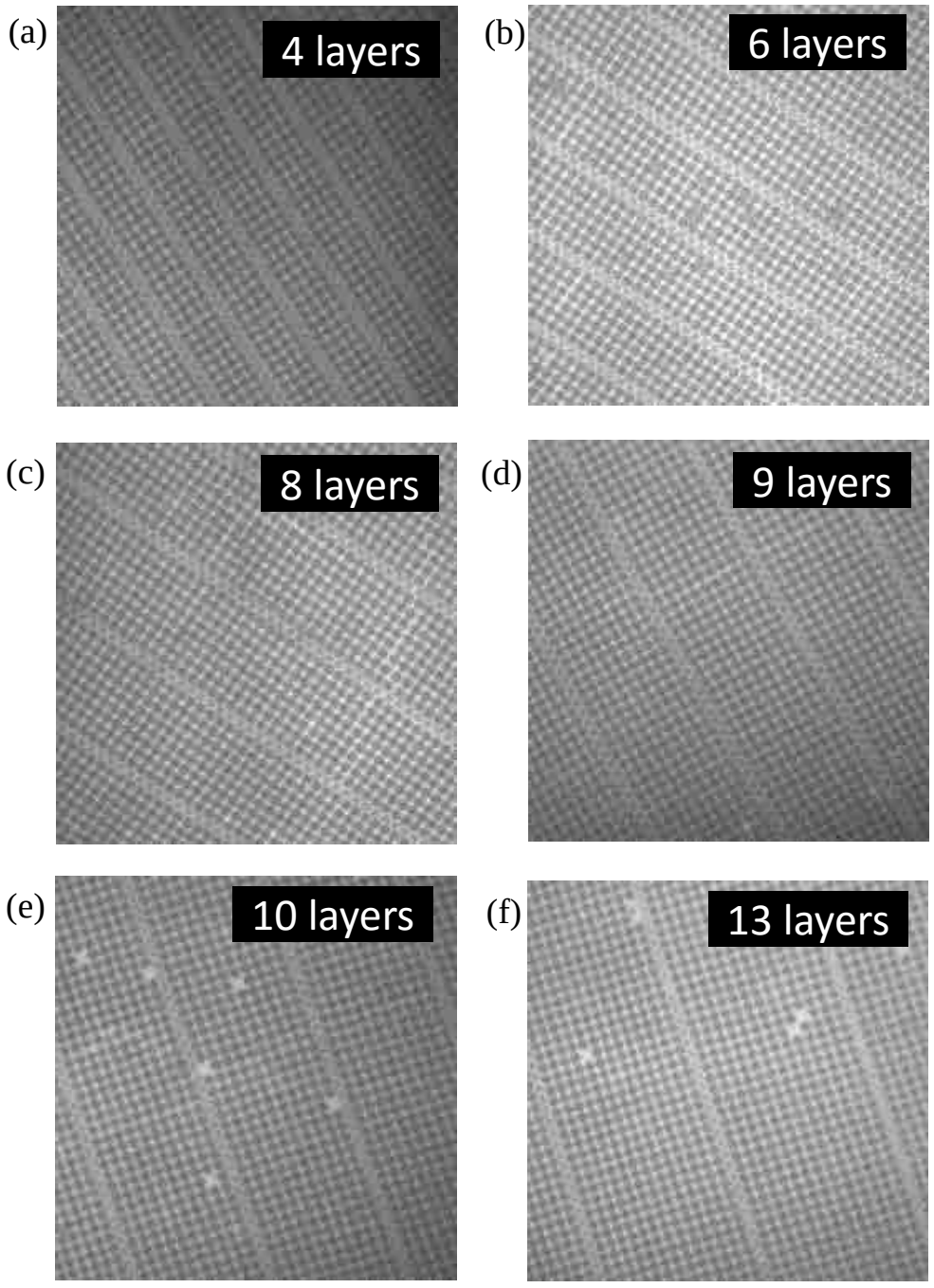

Figure 4.21: Defect patterns with varying periodicities generated in colloidal crystals. The confocal images (a-f) corresponds to fcc (100) colloidal crystals with numbers of layers as shown in the respective images. A proportional increase in the periodicity of the bands with increasing number of layers of the crystal assembly can be seen in the figures.

4.3.4 Parametric studies to investigate formation of bands in FCC (100) domains

Detailed studies were performed to identify the factors responsible for the formation of band patterns and to analyze the parameters which could be utilized to control their extent of formation in square packed FCC (100) domains. The prior discussions on the mechanism of formation of these patterns (Section 4.3.2) attributes their origin to the stress relaxation undergone by the crystal when subjected to a suitable deforming force. It could be hence postulated that the density of these patterns in FCC (100) domains could be controlled by a variation in two factors:

(i) Magnitude and characteristics of the deforming force exerted on the crystal and

(ii) Crystal response to the deforming force

Various ways in which the former parameter (deforming force acting on the crystal) could be controlled includes varying the frequency-amplitude conditions of film formation as well as varying the curvature of the thin film meniscus, which could be achieved by either varying the hydrophobicity of the substrate, blade angle of deposition or even the volume of thin film suspension. On the other hand, the response of a crystal to a deforming force acting on it could be postulated to be dependent on the number of layers of the crystal and the binding force between the particles constituting the crystal. With increased thickness of assembly, it would perhaps become more difficult for the crystal to undergo stress relaxation which might yield the observed patterns.

Figure 4.22 shows the variation in the density of bands with varying thickness of the crystal as well as volume of suspension used for deposition. The bands present in the confocal scans of the sample were identified using the algorithm outlined in Section 4.2 of the chapter. Once the band lines were identified, the particles in the sample confined within the band lines were counted and the density of bands is given by the ratio:

$$\text{Density of bands} = \frac{\text{Total number of particles lying within the band}}{\text{Total number of particles in the FCC(100) domain}}$$

In Figure 4.22, it could be observed that a variation in the number of layers generates a corresponding variation in the number of bands observed in the sample, albeit with opposing trends depending on the volume of suspension. For a suspension volume of 75 µl, the band formation could be observed to be enhanced with increasing thickness of the crystal. However, an opposite trend was obtained with 200 µl. The observed results could be attributed to a combination of both the relative ease at which the crystal could undergo a stress relaxation as well as the deforming force generated within the thin film region which depends on the Laplace pressure and hence the curvature of the meniscus.

Studies were also performed to analyze the effect of frequency and amplitude of the sinusoidal vibrations, with the amplitudes chosen for study being 1200 µm, 620 µm and 325 µm. For each of the selected amplitudes, colloidal crystals with a thickness of eight layers were fabricated for the range of frequencies varying from 30 Hz to 60 Hz (within the limitations of the instruments for each amplitude). Such an approach helps eliminate the effect of thickness on the formation of bands, the results as shown in Figure 4.23. From the plots, it could be observed that the density of bands shows a minor peak around 35 Hz for the low amplitude scenarios (325 µm). It however becomes more visible as the amplitude is increased to 620 µm and further enhanced at 1200 µm. A suitable explanation for this observation however could not be derived during the course of this work and demands a detailed study.

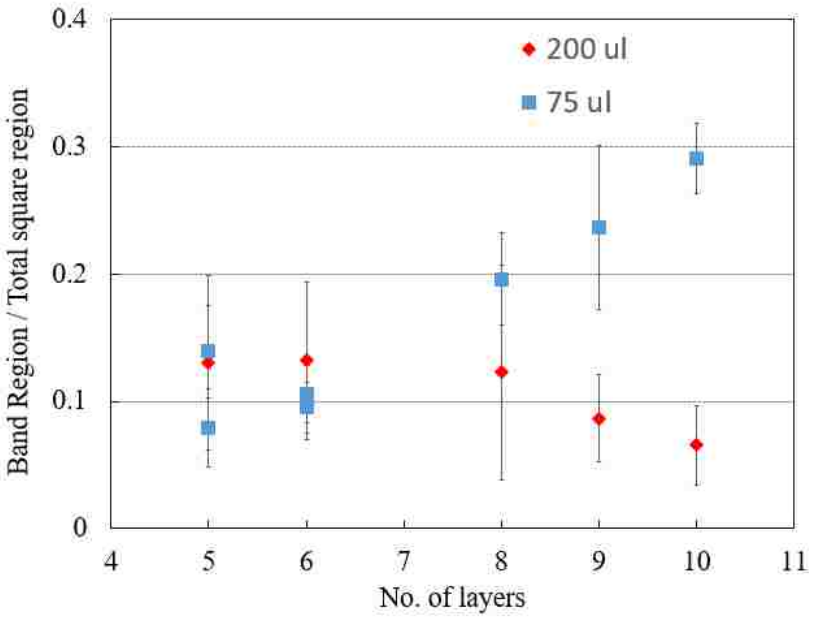

Figure 4.22: Variation of the banded fraction of the sample with colloidal crystal thickness. Two opposing trends were observed when the volume of the colloidal suspension used was varied from 75 µl of suspension (an increasing trend with colloidal thickness) to 200 µl (a decreasing trend with colloidal thickness). The observed results could be attributed to a combination of factors like Laplace pressure within the curvature of the meniscus as well as the threshold shearing forces necessary to create dislocations within the crystal volume.

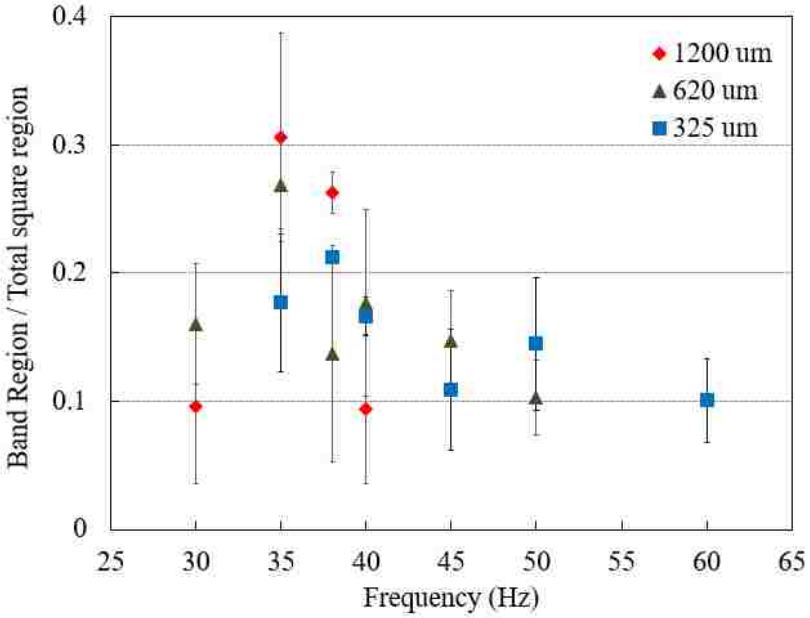

Figure 4.23: Variation of banded fraction of sample with frequency and amplitude. The results correspond to samples with eight layers. Although the banded fraction lies close to 2 % (as observed in Figure 4.22 for No. of layers =8), a variation could nevertheless be observed across multiple frequencies. A peak could be observed around 35 Hz, which becomes more pronounced with increasing amplitudes.

4.4 Conclusion

The chapter presents a description of the observed periodic defect structures in colloidal crystal assemblies, the generation of which could be attributed to the stress relaxation mechanism in the periodic lattice structure. Although the current understanding of the underlying dynamics does not permit high degree of control over the initiation of these patterns, their periodicity can however be suitable tuned by varying the number of layers of the crystal assembly. Moreover, the relative ease with which these patterns could be generated opens up potential pathways to explore the incorporation of these structures in lieu of microfabrication techniques for engineered defects in periodic structures.

4.5 References

1. Koh, Y. K., Teh, L. K. & Wong, C. C. Defects in self assembled colloidal crystals. *Adv. Mater. Micro- Nano-Systems* (2005). at <http://hdl.handle.net/1721.1/7361>

2. Teh, L. K., Tan, N. K., Wong, C. C. & Li, S. Growth imperfections in three-dimensional colloidal self-assembly. *Appl. Phys. A* **81,** 1399–1404 (2004).

3. Blaaderen, A. Van, Ruel, R. & Wiltzius, P. Template-directed colloidal crystallization. *Nature* **385,** 321–324 (1997).

4. Hoogenboom, J. P., Derks, D., Vergeer, P. & van Blaaderen, A. Stacking faults in colloidal crystals grown by sedimentation. *J. Chem. Phys.* **117,** 11320 (2002).

5. Chaikin, P. M. *et al.* Crystallization of hard-sphere colloids in microgravity. *Nature* **387,** 883–885 (1997).

6. Mori, A., Suzuki, Y. & Sato, M. Gravitational Tempering in Colloidal Epitaxy To Reduce Defects Further. *Cryst. Growth Des.* **14,** 2083–2086 (2014).

7. Weertman, J. & Weertman, J. R. *Elementary Dislocation Theory*. (1992).

8. Hull D.J. D and Bacon. *Introduction to Dislocations (fourth edition). Butterworth-Heinemann* (2001).

9. Charles, K. *Introduction to solid state physics*. *John Wiley Sons, Inc* (2005). doi:10.1007/s13398-014-0173-7.2

10. Zhu, T., Li, J., Ogata, S. & Yip, S. Mechanics of Ultra-Strength Materials. *MRS Bull.* **34,** 167–172 (2009).

11. Hirth, J. P. & Lothe, J. *Theory of Dislocations*. **4,** (1992).

12. Li, J. The mechanics and physics of defect nucleation. *Mater. Res.* **32,** 151–159 (2007).

13. Mahajan, S., Brasen, D. & Haasen, P. Luders bands in deformed silicon crystals. *Acta Metall.* **27,** 1165–1173 (1979).

14. Pang, W.-W., Zhang, G.-C., Zhao, X.-G. & Zhang, P. Dependence of dislocation creation on tensile orientation in face-centered-cubic ductile metals under high strain rate loading. *J. Appl. Phys.* **118,** 124301 (2015).

15. Guy, A. G. *Introduction to Materials Science*. (McGraw-Hill, 1972). doi:10.1016/B978-2-84299-286-6.50009-3

16. Flinn, J. E., Duvall, G. E., Fowles, G. R. & Tinder, R. F. Initiation of dislocation multiplication in lithium fluoride monocrystals under impact loading. *J. Appl. Phys.* **46,** 3752 (1975).

17. Oh, S. H., Legros, M., Kiener, D. & Dehm, G. In situ observation of dislocation nucleation and escape in a submicrometre aluminium single crystal. *Nat. Mater.* **8,** 95–100 (2009).

18. Mesarovic, S. D. Dynamic strain aging and plastic instabilities. *J. Mech. Phys. Solids* **43,** 671–700 (1995).

19. Chihab, K., Estrin, Y., Kubin, L. P. & Vergnol, J. The kinetics of the Portevin-Le Chatelier bands in an Al-5at% Mg alloy. *Scr. Metall.* **21,** 203–208 (1987).

20. Gilman, J. J. & Johnston, W. G. Observations of dislocation glide and climb in lithium fluoride crystals. *J. Appl. Phys.* **27,** 1018–1022 (1956).

21. Lethanh, V., Calmes, C., Zheng, Y. & Bouchier, D. Multilayer-array growth of SiGeC alloys on Si(001). *Appl. Phys. Lett.* **80,** 43–45 (2002).

22. Liu, P., Zhang, Y. W., Fox, B. & Lu, C. Molecular dynamics study of dislocation formation in a [001] face-centered-cubic epitaxial island under tensile stress. *Appl. Phys. Lett.* **84,** 714–716 (2004).

23. *Dislocations in Solids*. (Elsevier, 2010).

24. Schall, P., Cohen, I., Weitz, D. a & Spaepen, F. Visualization of dislocation dynamics in colloidal crystals. *Science* **305,** 1944–1948 (2004).

25. Schall, P., Cohen, I., Weitz, D. A. & Spaepen, F. Visualizing dislocation nucleation by indenting colloidal crystals. *Nature* **440,** 319–23 (2006).

26. Sun, C.-H. & Jiang, P. Photonic Crystals: Acclaimed defects. *Nat. Photonics* **2,** 9–11 (2008).

27. Rinne, S. A., García-Santamaría, F. & Braun, P. V. Embedded cavities and waveguides in three-dimensional silicon photonic crystals. *Nat. Photonics* **2,** 52–56 (2008).

28. Ferrand, P. *et al.* Direct electron-beam lithography on opal films for deterministic defect fabrication in three-dimensional photonic crystals. *Microelectron. Eng.* **73-74,** 362–366 (2004).

29. Lee, W., Pruzinsky, S. A. & Braun, P. V. Multi-Photon Polymerization ofWaveguide StructuresWithin Three-Dimensional Photonic Crystals. *Adv. Mater.* **14,** 271–274 (2002).

30. Jun, Y., Leatherdale, C. A. & Norris, D. J. Tailoring Air Defects in Self-Assembled Photonic Bandgap Crystals. *Adv. Mater.* **17,** 1908–1911 (2005).

31. Yan, Q., Zhou, Z., Zhao, X. S. & Chua, S. J. Line Defects Embedded in Three-Dimensional Photonic Crystals. *Adv. Mater.* **17,** 1917–1920 (2005).

32. Vekris, E. *et al.* Buried linear extrinsic defects in colloidal photonic crystals. *Adv. Mater.* **17,** 1269–1272 (2005).

33. Ye, Y.-H. *et al.* Self-assembly of three-dimensional photonic-crystals with air-core line defects. *J. Mater. Chem.* **12,** 3637–3639 (2002).

34. Palacios-Lidón, E., Galisteo-López, J. F., Juárez, B. H. & López, C. Engineered planar defects embedded in opals. *Adv. Mater.* **16,** 341–345 (2004).

35. Pradhan, R., Tarhan, I. & Watson, G. Impurity modes in the optical stop bands of doped colloidal crystals. *Phys. Rev. B* **54,** 13721–13726 (1996).

36. Chan, D. L. C., Lidorikis, E. & Joannopoulos, J. D. Point defect geometries in inverted opal photonic crystals. *Phys. Rev. E - Stat. Nonlinear, Soft Matter Phys.* **71,** 1–6 (2005).

37. Hilhorst, J., de Winter, D. a M., Wolters, J. R., Post, J. A. & Petukhov, A. V. Defect engineering in sedimentary colloidal photonic crystals. *Langmuir* **29,** 10011–10018 (2013).

38. Wang, L., Yan, Q. & Zhao, X. S. From planar defect in opal to planar defect in inverse opal. *Langmuir* **22,** 3481–3484 (2006).

39. Wostyn, K. *et al.* Insertion of a two-dimensional cavity into a self-assembled colloidal crystal. *Langmuir* **19,** 4465–4468 (2003).

40. Jiang, B. P., Ostojic, G. N., Narat, R., Mittleman, D. M. & Colvin, V. L. The fabrication and bandgap engineering of photonic multilayers. *Adv. Mater.* **13,** 389–393 (2001).

41. Rinne, S. a., García-Santamaría, F. & Braun, P. V. Embedded cavities and waveguides in three-dimensional silicon photonic crystals. *Nat. Photonics* **2,** 52–56 (2008).

42. Nosenko, V., Zhdanov, S. & Morfill, G. Supersonic Dislocations Observed in a Plasma Crystal. *Phys. Rev. Lett.* **99,** 025002 (2007).

43. Hatano, T. Dislocation nucleation in shocked fcc solids: Effects of temperature and preexisting voids. *Phys. Rev. Lett.* **93,** 1–4 (2004).

44. Lomer, W. M. The yield phenomenon in polycrystalline mild steel. *J. Mech. Phys. Solids* **1,** 64–73 (1952).

5

Enhancing light capturing efficiency in dye sensitized solar cells

5.1 Introduction

The field of renewable energy resources has received immense attention in recent years due to several reasons, the major ones being the depleting fossil fuel reserves and an increased awareness about environmental protection. The mean global energy consumption is currently estimated to be 150,000 TW.hr[1]and is projected to increase up to 210,000 TW.hr by the year 2035[2].This huge demand for energy could be met only through non-conventional sources of energy, the most promising ones among them being the fusion reaction and solar energy. Solar energy, which is produced by nuclear fusion reaction of Deuterium and Tritium in the sun's core, is one of the most versatile forms of renewable energy, available in such abundance that it can meet the energy needs of the whole global population with zero emission of greenhouse gases. The supply of solar energy to earth is estimated to be 8 x 10^9TW hr./year[3], which when harnessed at even 10 % efficiency over 0.1 % of earth's surface would satisfy the current needs.

Solar energy can be harnessed into a usable form through various ways, the primary ones being the solar thermal technologies and photovoltaic technology. Solar power technologies were conventionally focused on photovoltaics to convert solar energy to electric power. The thin film organic photovoltaic technology, while less efficient than

silicon technologies, are attractive because of their relative ease and low cost of fabrication and implementation. Within this sector, dye-sensitized solar cells (DSSCs) represent a burgeoning technology with promise to overcome some of the materials and performance gaps plaguing solid state semiconductor devices (e.g., cost/performance ratio, ease of manufacture, mechanical robustness, and low-light operability). Pioneering work by Grätzel[4] more than a decade ago first demonstrated the concept of DSSCs. These multicomponent devices operate on the basis of favorable differential kinetics governing charge mobility, electron hole generation, and recombination. By coupling an optically transparent conductive anode sensitized with photoactive (i.e., electron injecting) dye molecules with a counter-electrode across a suitable electron donor (i.e., conventionally a liquid electrolyte solution), DSSCs are able to convert solar energy into electrical power even under low-light conditions. Device efficiencies, however, currently remain a drawback at just over 13%[5] such that commercial realization of this promising technology demands device optimization. Efforts to realize higher overall device efficiencies are confounded, in part, by challenges associated with optimizing this multicomponent system as it relates to intra- and inter-component phenomena. Despite the realization of sensitizer external quantum efficiencies (incident photon to current efficiency) of as much as 90%,[6] only marginal improvements over the near 10% efficiency initially reported by Grätzel in 1991 (η=7.9%)[4] have been realized in over 20 years (maximum lab-scale demonstrated η =13.0 %[7], commercial cell efficiency = 11.9 %[8]).

5.1.1 Major components of Dye sensitized solar cells

A DSSC cell has a sandwich structure, with a photoelectrode (anode) and counter electrode (cathode) and a redox electrolyte confined between the electrodes, as shown in Figure 5.1. Both the electrodes are fabricated on a transparent glass/flexible substrate with an electrically conducting layer which performs the function of charge collection within the cell. The various components of a DSSC, which includes the transparent conducting oxide(TCO) coated glass as mechanical support, photoelectrode comprising of semiconductor oxide and a suitable photosensitizer or dye, redox electrolyte and the counter electrode demands individual as well as concurrent engineering and optimization for an efficient performance of the overall device[9].

Photoelectrode

The photoelectrode/ the working electrode acts as the anode of a DSSC cell, and consists of a mesoporous layer of interconnected semiconductor oxide nanoparticles deposited on a supporting surface. Glass as well as several flexible substrates have been investigated as the supporting surface, with the prerequisites of the same being optical transparency to the incident solar radiation in the visible-near IR region and high electrical conductivity of the surface. This is achieved by coating the glass surface with a Fluorine-doped tin oxide (FTO) or Indium-doped tin oxide (ITO) layer for enhanced electrical conductivity of the surface, FTO being the preferred candidate owing to its higher electrochemical stability.

The mesoporous layer of the photoelectrode comprises of nanometer sized particles of oxide semiconductor materials like TiO_2, ZnO, SnO_2, of which TiO_2 –anatase phase is the preferred choice owing to its cheap cost, low toxicity and good chemical stability in

solution. Compared to rutile and brookite phases, anatase TiO_2 has a slightly higher bandgap and can absorb more sunlight in the near UV-visible region, which makes it the preferred choice for DSSC fabrication. The TiO_2 film is typically fabricated to be 10-15 μm in thickness, the overall thickness and porosity designed to achieve efficient harvesting of incident light by ensuring sufficient dye loading and retention of incident photons within the photoactive region to generate photoelectrons. In addition, the porosity of the film also plays a dominant role in ionic diffusion of charge carrier species within the electrolyte. In addition to mesoporous structure, several morphologies have been analyzed in literature for TiO_2 photoelectrode like core-shell structures[10,11], one-dimensional nanostructures like nanowires[12], three-dimensional nanostructures, with emphasis on both high surface area and effective light harvesting, charge transport and collection. The deposition of the TiO_2 film is done by several techniques like doctor-blading[13], screen printing[14], spray pyrolysis[15], electrophoretic deposition[16] etc. After deposition, the TiO_2 film is sintered at 500- 550 C, which provides a continuous path for electron conduction as well as converting TiO_2 to crystalline anatase form.

Semiconductor oxide materials are covered with a monolayer of a suitable photosensitizer molecule or the 'dye', which absorbs the incoming solar radiation thus generating photoelectrons. An ideal photosensitizer should have high absorption coefficient in the visible-near IR region of the solar spectrum, in addition to good solubility in organic solvents and high thermal and chemical stability. The selection of the dye species should also ensure that the excited state of the dye is at a higher energy level than the conduction band edge of the associated semiconductor oxide. Several organic and inorganic metal complexes, porphyrins and phthalocyanines have been used for DSSCs in

association with TiO_2 as semiconductor oxide, the highest efficiencies being reported with coordination complexes of transition metals (Ru dyes of polypyridine family[17]). Suitable anchoring groups like carboxylic acid and carboxylate groups are attached to the dye molecule for effective interaction of the dye with the oxide surface. This helps to attain higher charge injection efficiencies through a coupling of donor energy level (of the dye) and acceptor energy level (of the semiconductor oxide). Recent research has focused on panchromatic engineering involving multiple dyes[18] for enhanced spectral and absorption properties as well as the use of quantum dots as sensitizing medium. Quantum dots, with their tunable bandgap and high extinction coefficient offers a good alternative to achieve higher photon capture, but the device performance involving quantum dots suffers from low overall efficiency due to limited surface coverage and higher recombination losses.

Redox electrolyte

The redox electrolyte mediates electron transport between the working electrode and the counter electrode, the preferred choice being the I^-/I_3^- system in an organic solvent (mixture of acetonitrile and valeronitrile) owing to its excellent chemical stability and reversibility, low viscosity which provides high ion diffusion rates as well as low absorption of visible light. The redox electrolyte performs the function of regenerating the oxidized dye species into the ground state, thus accomplishing the generation of photoelectrons within the cell without any permanent chemical conversion of the dye. The I^-/I_3^- redox system however suffers the limitation of long-term stability of DSSC due to high vapor pressure of the solvent, which limits their use in high-temperature applications (>80 C). The use of molten salt electrolytes like dialkyl imidazolium salts[19] enables to overcome this limitation with their high thermal stability and negligible vapor pressure.

However, the efficiency of these systems are limited by the high charge diffusion resistance in the electrolyte due to the extremely high viscosity of the solvent, and has been demonstrated to be enhanced using high-hole-mobility semiconductor salts of $CsSnI_{2.95}F_{0.05}$type[20].

Counter electrodes

The counter electrode aids in the regeneration of the redox species from their oxidized forms. The counter electrode comprises of materials with good electro catalytic properties coated on a TCO glass surface, preferred catalyst being finely divided platinum owing to its excellent chemical stability to the electrolyte under working conditions. Recent research has focused on developing cheaper alternatives to platinum, the focus being carbon counter electrodes in various forms like carbon black[21] and carbon nanotubes.

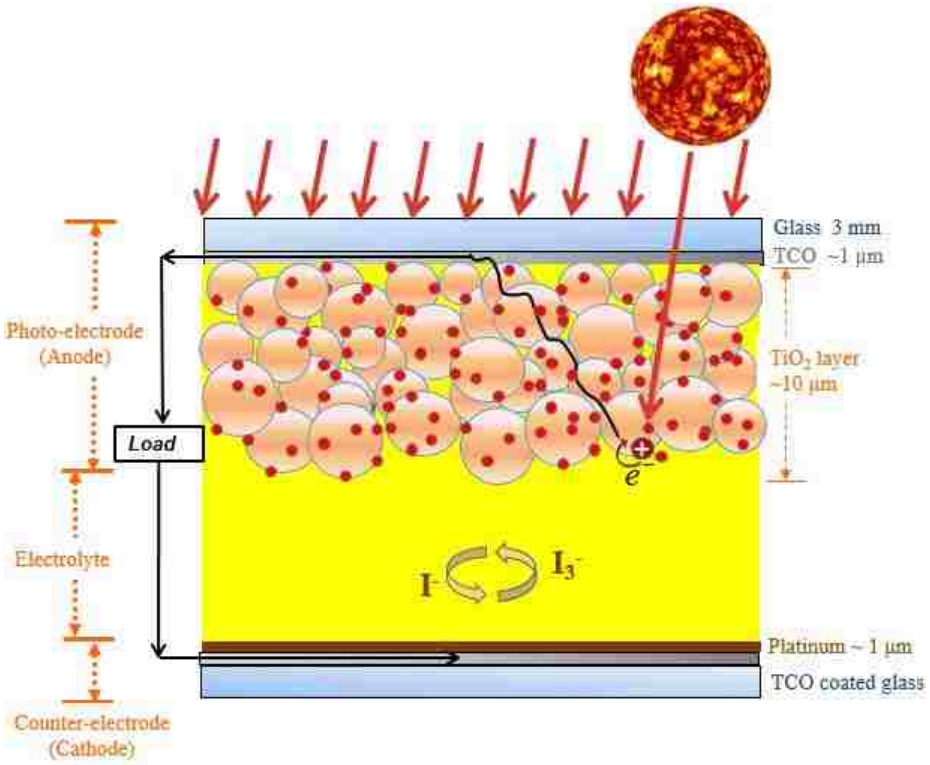

Figure 5.1: Sandwich structure of a Dye Sensitized solar cell (DSSC) showing the photoelectrode, counter electrode and the electrolyte. The typical thickness of the various components is also shown.

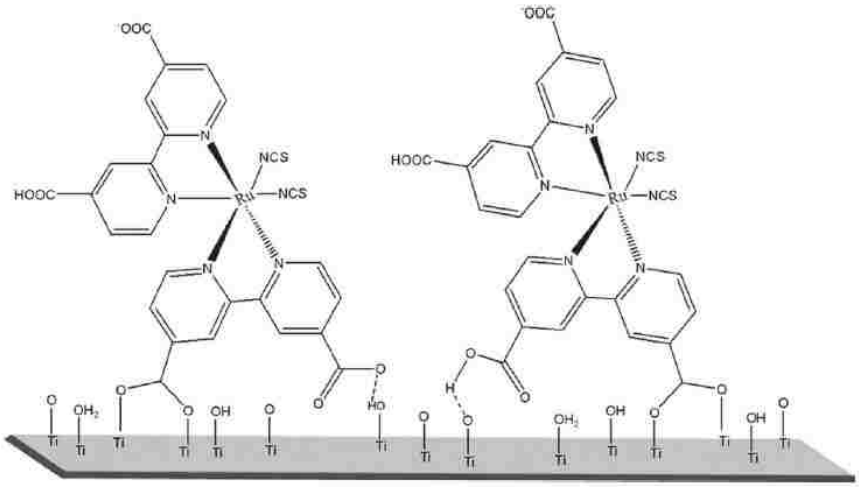

Figure 5.2 : Adsorption of *Di-tetrabutylammonium cis-bis(isothiocyanato)bis(2,2'-bipyridyl-4,4'-dicarboxylato)ruthenium(II)* (N719 Dye) onto the TiO_2 surface through the formation of bidentate bond and H-bond[22] by the carboxylic acid and carboxylate groups of the dye molecule. (Figure shown was adapted from the corresponding reference)

5.1.2 Working Principle of DSSC

A DSSC converts incident photon energy into useful electricity, the working of which involves a separation of electron generation and charge transport processes unlike in conventional photovoltaic devices. In a DSSC, the generation of photoelectrons occurs at the dye-semiconductor oxide interface, while the charge transport occurs within the interconnected network of nanoparticles and the redox electrolyte.

The operation of a DSSC[23] involves the sensitizing dye molecules which act as the photon capture medium, the absorption of incident photons resulting in an excitation of the dye molecules. The excited dye species then injects an electron into the conduction band of the semiconductor oxide, thereby generating an anionic species of the dye.

$$S_{(adsorbed)} + h\nu \rightarrow S^{*}{}_{(adsorbed)}$$

$$S^{*}{}_{(adsorbed)} \rightarrow S^{+}{}_{(adsorbed)} + e^{-}{}_{(TiO_2)}$$

The electrons injected into the conduction band of TiO_2 are conducted through adjacent TiO_2 particles and reaches the conducting glass substrate (TCO), from which it passes through the external load and finally reaches the counter electrode.

The oxidized dye molecule is regenerated to the ground state by accepting electrons from the I^- ion of the electrolyte, thereby oxidizing it to I_3^-.

$$S^{+}{}_{(adsorbed)} + \frac{3}{2} I^{-} \rightarrow S_{(adsorbed)} + \frac{1}{2} \mathrm{I_3}^{-}$$

The oxidized I_3^- ion diffuses towards the counter electrode and is reduced to I^- ions by the electrons flowing through the external load.

$$I_3^- + 2\, e^{-}{}_{(cathode)} \rightarrow 3\, I^-$$

The photoelectrons generated in the active layer may undergo recombination with the oxidized dye or electrolyte species on the TiO2 surface, resulting in a reduced efficiency of the device.

$$S^{+}_{(adsorbed)} + e^{-}_{(TiO_2)} \rightarrow S_{(adsorbed)}$$

$$I_3^- + 2\, e^{-}_{(TiO2)} \rightarrow 3\, I^-$$

The current output from a DSSC cell (maximum value being the short-circuit current I_{sc}) under illumination depends on the number of photoelectrons which are collected by the electrode surfaces, while voltage output is dependent on the electrochemical properties of the dye, semiconductor oxide and the electrolyte. The choice of a dye for a particular semiconductor-oxide/ electrolyte system is based on the HOMO (Highest occupied molecular orbital) and LUMO (lowest unoccupied molecular orbital) energy levels of the former, with the energy level values determining the efficiency of charge injection processes from excited dye molecule to conduction band of semiconductor –oxide and the efficiency of dye regeneration by the electrolyte[24]. The maximum voltage output from the cell (Open circuit voltage – V_{oc}) is theoretically equal to the difference between the fermi level of the semiconductor oxide and the Nerst potential of the electrolyte. However, the measured V_{oc} values are lower than the theoretical ones due to losses arising in the cell due to competing recombination reactions.

An equivalent circuit of a DSSC consists of the current source, diode, one parallel resistance and three series resistances[25,26]. The current source generates the photocurrent in proportion to the irradiation of sunlight. The shunt resistance $R_{SH}$is due to the recombination losses or the back-electron transfer. There is also a set of series resistances due to resistance on the surface of counter electrode (R_{Pt}), impedance of carrier transport

through ions in the electrolyte (R_{ELEC}), resistance due to the TCO layers (R_T) and the resistance at the metal contacts (R_m).

The effective resistance of TCO layer and metal contacts is given by[25] :

$$R_T = R_{TCO}\frac{W}{L} \ , R_m = \rho_m \frac{L_m}{W_m h_m}$$

where W, L are the dimensions of TCO glass sheet;ρ_m : resistivity of metal contact;

L_m, W_m, h_m : dimensions of metal contact

The current flowing through the diode and the shunt resistance is given by[25]:

$$I_D = I\left\{exp\left(q\ \frac{V+IR_S}{nkT}\right)-1\right\}\ ,\ I_{SH} = \frac{V+IR_S}{R_{SH}} \quad where\ R_s = R_{Pt} + R_{ELEC} + R_T + R_m$$

Hence, the output current is given by:

$$I_O = I - I_D - I_{SH} = I - I\left\{exp\left(q\ \frac{V+IR_S}{nkT}\right)-1\right\} - \frac{V+IR_S}{R_{SH}}$$

The maximum obtained efficiency of DSSC is only 10-11 %, compared to the theoretical predicted one of ~ 20 %[3]. There are several factors limiting the cell performance among which the light harvesting efficiency is the most dominant one[17], followed by the energy losses arising due to charge recombination, electron trapping, optical reflection etc[3].The boosting of light harvesting efficiencies can be achieved by developing photo sensitizers with broader spectral response, while reducing the energy losses in the cell and this demands the design of suitable anode morphologies.

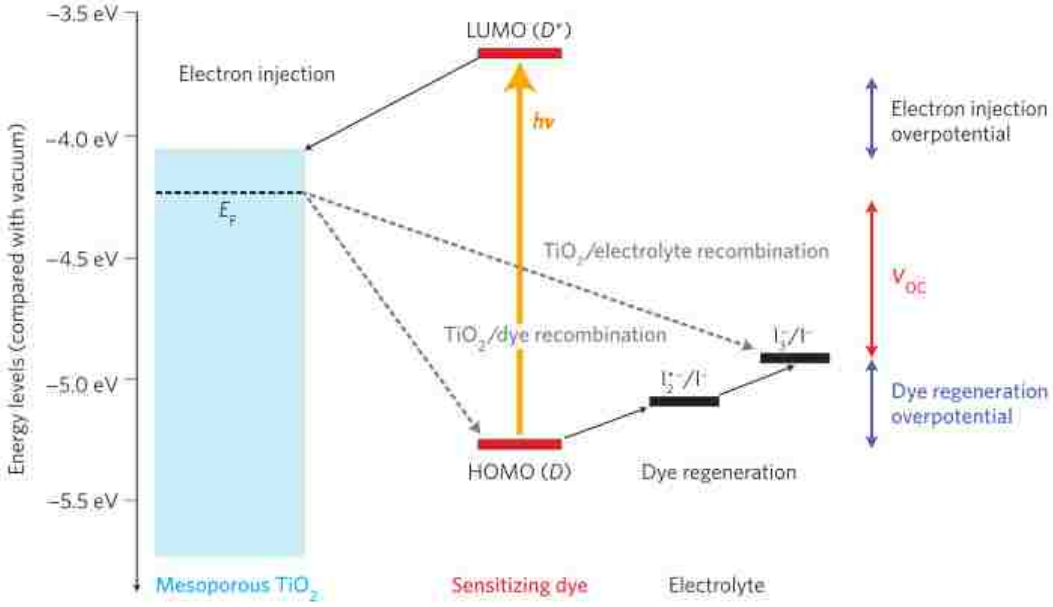

Figure 5.3: Schematic energy diagram of DSSC[27]outlining the various processes involved in the working of cell namely, photoexcitation, electron injection and dye regeneration. The potentials associated with the dye, semiconductor oxide and redox electrolyte are also shown. The open circuit voltage, V_{OC} is the difference between the fermi-level of semiconductor oxide and redox potential of the electrolyte. (Figure shown was adapted from the corresponding reference)

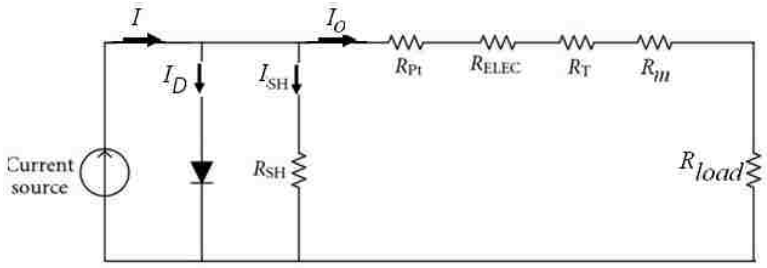

Figure 5.4: An equivalent circuit representation of DSSC[25]. The various resistances accounted for in developing a phenomenological model of the DSSC is also shown.

5.1.3 Measurement of Performance characteristics of DSSC

The intensity of solar radiation reaching the earth is influenced by several atmospheric factors as well as the orientation of the sun with respect to earth, maximum solar radiation achieved with the sun directly overhead when the radiation travels the shortest path length to reach the earth through the atmosphere. This shortest path length is referred to as the Air Mass (AM) and is approximated as AM = 1/Cos ϕ where ϕ is the angle of elevation of the sun. For performance measurements of solar cells, the standard of 1.5 AM is used, with ϕ = 42^o.

Consider the voltage-current characteristics of a typical DSSC given by Figure 5.5.For each point on the I-V curve, the power output is given by the area of the rectangle *OACB.* The voltage-current values which maximizes the area of the rectangle giving the maximum power output of the solar cell (P_{max}) corresponds to the Open-circuit voltage (V_{oc}) and Short-circuit current (J_{sc}). The Fill factor (FF) of a cell is given by the ratio of the maximum obtainable power from cell (P_{max}) to the area of the rectangle *OA'C'B'*.

$$FF = \frac{Area\ of\ OACB}{Area\ of\ OA'C'B'} = \frac{P_{max}}{J_{sc}V_{oc}}$$

The efficiency of a cell is given by the ratio of maximum power of the solar cell per unit area(P_{max}) to intensity of the incident light (P_{in})

$$\eta = \frac{P_{max}}{P_{input}} = \frac{V_{oc}\,J_{sc}\,FF}{P_{input}}$$

The fill factor has values ranging from 0 to 1, a lower value denoting higher internal resistances in the cell[25]and poor probe connection.

The Incident photon-to-current conversion efficiency (IPCE) of a DSSC, also referred to as "External quantum efficiency" represents the overall performance of the device under illumination with a monochromatic light with a wavelength λ. IPCE can be defined as the ratio of photocurrent density in external circuit under illumination to the incident photon flux, assuming monochromatic illumination.

$$IPCE\ (\lambda) = 1240\ \frac{J_{sc}(\lambda)}{\lambda\ P_{in}(\lambda)}$$

$$IPCE\ (\lambda) =\ LHE\ (\lambda).\eta_{inj}.\eta_{coll}$$

where $LHE\ (\lambda)$ is the efficiency of absorption of incident light (a definite wavelength determined by absorption coefficient of the dye and photon path length of the incident radiation within the photoactive region), η_{inj} is the efficiency of charge injection from the excited state of the dye into conduction band of TiO_2 and η_{coll} is the efficiency of charge collection at the TCO glass surface of the electrode.

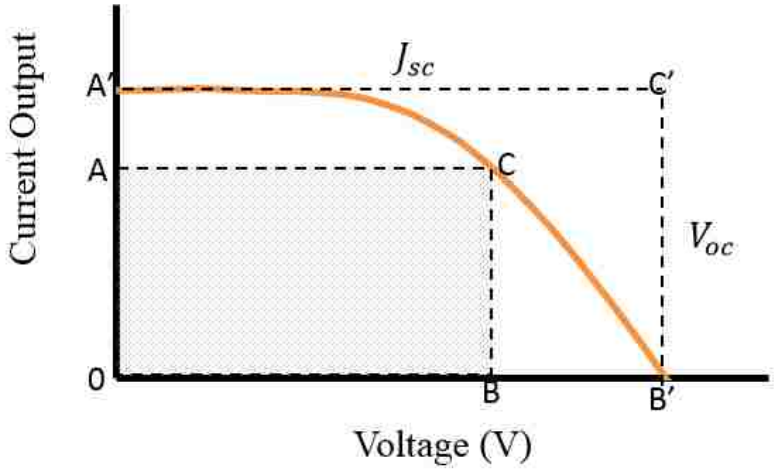

Figure 5.5: Typical Current-voltage characteristics of a DSSC under illumination.

5.1.4 Photon management in DSSC

The commercialization of DSSC technology is often limited by the low efficiency of the devices in comparison to other solar energy harvesting techniques. An enhancement in device performance demands a concurrent engineering and optimization of various device components, namely the anode, cathode and the electrolyte. An increase in solar cell efficiency can be achieved either by an increased photovoltage (by using a semiconductor with a higher negative potential than TiO_2[28]) or by increasing the photocurrent, which is attained by an enhanced light capturing efficiency in the device resulting in the generation of higher number of photoelectrons as well as by reduced recombination losses within the device, leading to enhanced charge collection efficiencies at the outer electrode surface.

The incorporation of photon management techniques for enhanced light harvesting in DSSC is further necessitated by the fact that only a fraction of incident solar radiation can be effectively captured by the sensitizing dye. The solar spectrum incident on the earth's surface has wavelength ranging from 300 – 1300 nm. However, a significant fraction of the spectrum cannot be captured by the dye (N719 for the current work), whose spectral response is limited to the 300 – 800 nm as shown in the figure. An analysis of the spectral curve of N719 reveals that the absorption coefficient is significantly lowered for wavelengths in the range of 600-800 nm. The objective of light management techniques in DSSC is to effectively improve the absorption efficiency of DSSC for sensitizing dye wavelengths which overlap the solar spectrum (600-800 nm for N719 dye as highlighted in figure), without adversely affecting the photoelectron generation and charge collection efficiencies.

The absorption efficiency of a medium associated with a definite wavelength is given by Beer Lambert's law as:

$$\eta_A = 1 - \exp(-\alpha L)$$

where α is the wavelength dependant absorption coefficient and L is the photon length. Hence, the objective of enhanced capturing of certain wavelengths of the solar spectrum effectively translates to ensuring increased photon path lengths of the corresponding wavelengths within the photoactive region of the DSSC device.

Photon management techniques in DSSC demand a concurrent engineering of light harvesting approaches and anode architecture for optimal performance of the overall device. A default approach towards enhancing the photon path length in DSSC would be to increase the thickness of TiO2 active layer. This is however constrained by a corresponding increase in the electron diffusion length of photoelectrons towards the collecting electrode. Furthermore, the diffusivities of ionic species I^-/I_3^- in the electrolyte is low due to the high viscosity of the solvent[29], the associated mass transport resistance further worsened by the increase in diffusion length with increased active layer thickness. This constraints the overall thickness of the TiO_2 active layer and is limited to a 10-12 μm thickness for optimal performance. In addition, the TiO_2 particles in the active mesoporous layer ought to be transparent in nature and involves particles with 20-25 nm diameter. Owing to their small diameters (20-25 nm) in comparison to the wavelength of incident light (300-1000 nm), these particles are weak scatterers and are capable of only affecting a Rayleigh scattering of incident light[30].

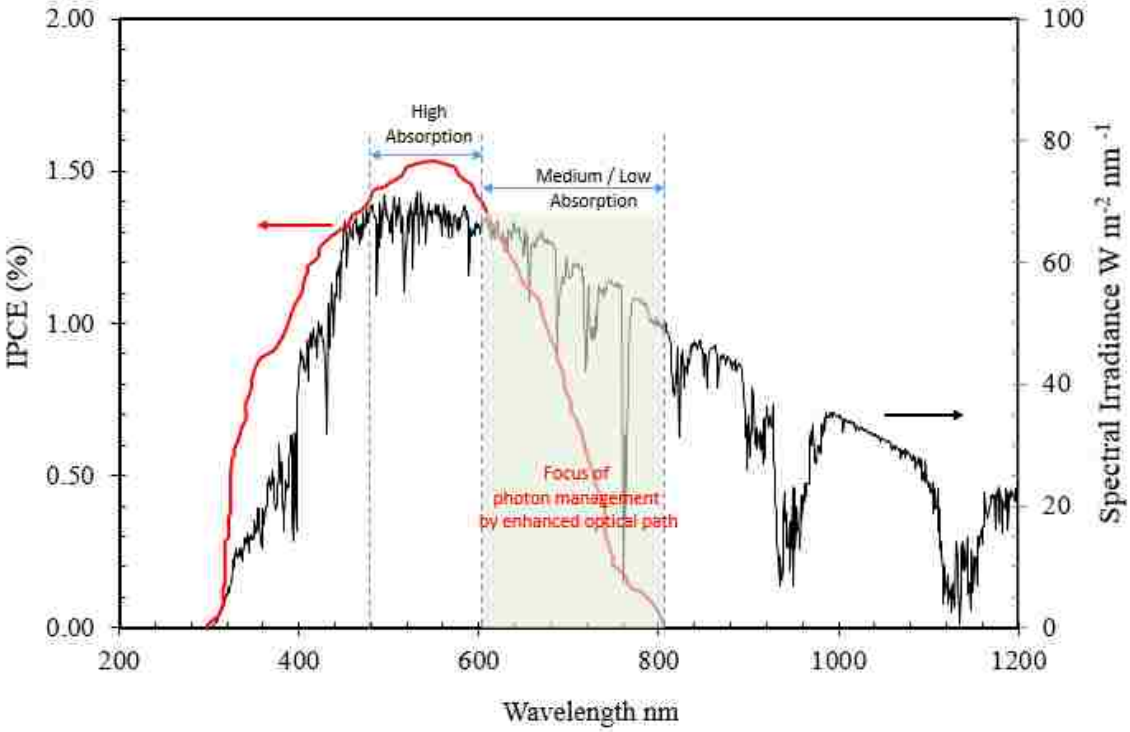

Figure 5.6: Performance of sensitizing dye in DSSC for capturing incident solar radiation, with a plot of spectral irradiance of AM 1.5[31] solar radiation compared with the IPCE Spectrum [32] of N719 Dye. The shaded region represents the range of wavelengths which is the focus of photon-path enhancement procedures.

Research into enhanced light harvesting in DSSC cells employs various architectures utilizing the principle of scattering (point scatterers[33] or scattering layers[34–37]), refraction (prisms[38] and microlens[39] on outer glass surface), diffraction (periodic gratings[40]) as well as interference reflection (photonic crystals[41,42]) for achieving enhanced photon path lengths within the active region of the DSSC cell. The use of larger particles which act as point-scatterers dispersed within the active TiO_2 layer or distinct scattering layers within the active layer offers a versatile approach to effect Mie scattering of incident photons[30,34], thereby providing an enhanced photon path length within the TiO_2 layer. According to theoretical calculations based on Mie theory, ideal scattering is achieved with 250-300 nm diameter TiO_2 particles dispersed within the TiO2 layer[43]. The relative enhancement of photon path length arising from the incorporation of external scatterers is dependent on the difference in refractive index of mesoporous TiO2 layer and scatterers[35], diameter and shape of the particles[34,37] as well as the position of scattering layers within the photoanode[36]. However, the use of scatterers diminishes the available surface area for dye loading and increases the amount of backscattering, leading to a reduction in the generation of photoelectrons. These limitations have been overcome to a certain extent by fabricating spherical TiO2 beads which are mesoporous in nature[44] for active layer (ensures light scattering and higher dye loading) or oriented nanotube arrays[45] (light scattering coupled with higher charge collection efficiencies). In addition, the use of metallic[46] nanoparticles as plasmons have also been investigated which increases the probability of photon capture by the dye molecules by localized surface plasmon resonances.[46] However the approach is limited by the increase in recombination losses due to the presence of

metallic ions within the active layer, minimized to an extent by the use of core-shell metal-insulator[47] nanoparticles.

In this chapter, we consider the effect of placing internal microlens arrays to increase the amount of light entering the device and refocus the light within the nanostructured dye support. By effectively patterning the internal surface of the external protective conductive layer, the aim is to widen the injection cone and alter the light distribution into the photoactive layer. The microlens arrays developed in this study are comprised of either titania or titania/silica nanocomposites. Due to the ease of fabrication of traditional DSSCs, these microlens arrays are readily incorporated into the fabrication process.

5.2 Experimental Section

5.2.1 Materials

The DSSC electrodes were fabricated on fluorine-doped tin oxide (FTO) glass purchased from Pilkington Group Ltd. (TEC-7, 3mm thickness, 81 % light transmittance, 7 Ω/sq.). A dense coating of titania on glass surface was achieved using a sol-gel prepared from 13.5 % titanium butoxide , 2.8 % ethyl acetoacetate (Fisher Scientific), 3.8 % 2,4-pentanedione (Fisher Scientific) and 2.8 % 2,3-butanedione (Fisher Scientific) in 200 proof ethanol (VWR), all chemicals listed in this section used without any further purification unless otherwise stated. Mesoporous titanium dioxide layer for photoanode was obtained using TiO_2 paste comprising of 1.75 g of 25 nm anatase titania powder (Sigma-Aldrich, heated at 500 C for 3 hours prior to use) suspended in a solution of 25 µl titanium (IV) isopropoxide and 7.5 ml of 200 proof ethanol. The sensitizing dye solution for working electrode has the composition of 0.3 mM of di-tetrabutylammonium cis-bis(isothiocyanato)bis(2,2'-bipyridyl-4,4'-dicarboxylato)ruthenium(II) dye (N 719, Sigma Aldrich) dissolved in a solution of equal volumes of acetonitrile (Fisher Scientific) and t-butanol (Fisher Scientific). A platinum counter electrode was utilized for DSSC in this work, synthesized from a solution of chloroplatinic acid in ethanol (Platisol- Solaronix), and I^-/I_3^- redox couple was chosen as the electrolyte which was prepared from 0.6 M 1-butyl-3-methylimidazolium iodide, 0.03 M iodine, 0.10 M guanidinium thiocyanate and 0.5 M 4-tertbutylpyridine in a 85:15 solution of acetonitrile and valeronitrile respectively. The fabrication of microlens structures employed monosized 1 µm diameter silica particles (ÅngströmSphere –Fiber optic center) dispersed in deionized water to 20 % volume fraction, 100 nm polystyrene nanoparticles (8 % volume, Emulsion Polymer Institute,

Lehigh University) and 0.93 µm polystyrene microspheres(10 % volume, Thermo Scientific).

5.2.2 Fabrication of DSSC device

The FTO coated glass pieces of 1 in x 1 in were cleaned in a 0.1 M solution of concentrated HCl in ethanol immersed in a sonicator bath, rinsed subsequently with 200 proof ethanol and dried under a stream of N_2. For the working electrodes, the cleaned glass pieces were coated with a 10 nm thick titania sol-gel layer and heated at 500^o C for 3 hours to convert the sol-gel into crystalline anatase phase. The microlens structure, which can be chosen to have either a convex or concave morphology was fabricated on the titania coating, but beneath the mesoporous dye-sensitized TiO_2 layer using convective deposition techniques which has been outlined in previous work[48–50]. To develop convex microlens structures on glass surface, a binary suspension comprising of 14 % SiO_2 and 4 % PS polystyrene in DI water was deposited on the glass surface, followed by thermal treatment at 400 C for 30 minutes to yield a monolayer of silica particles. The silica monolayer was then infiltrated with titania sol-gel and subsequently heated at 500 C for sol-gel phase transformation into crystalline anatase. The synthesis of concave microlens structures employs heat-degradable microspheres like PS, a monolayer of which was infiltrated with the titania sol-gel and subsequently burnt off via heat treatment to reveal a surface topography with concave shaped microlenses. DSSC working electrodes with an active area of 1 cm x 1 cm were shaped by removing the excess microlens coatings from glass surface. TiO_2 paste was then applied on the selected area, dried at room temperature, exposed to UV-ozone environment for 3 hours and finally sintered at 500 C for 3 hours.

The glass pieces, once sufficiently cooled was immersed in the sensitizing dye solution overnight for dye loading.

The counter electrode/ cathode was prepared by depositing H_2PtCl_6 solution on cleaned TCO glass and heat treated at 400 C for 1 hour. 1 mm diameter holes were drilled in the glass-pieces which would act as counter-electrodes, after which both the working and counter electrodes were assembled into a sandwich type cell using a hot-melt gasket made of Surlyn film with the aperture in the sealing film designed to yield a clearance of a couple of millimeters from the active area of TiO_2 electrode. After the assembly had been properly sealed, the prepared electrolyte was injected into the cell by vacuum back-filling, followed by sealing the drilled hole using Surlyn film and microscope glass slide. Copper tapes were used to provide electrical contacts for current-voltage measurements.

5.2.3 Characterization of DSSC Cells

The performance of the so-fabricated DSSC cells under illumination were characterized using a Solar simulator (Abet Technologies-Model No: 10500), which features a Xe short arc lamp and an AM 1.5 G filter. The optical system of the simulator is focused to produce a collimated beam of desired diameter and an intensity of 100 mW/cm^2 on the exposed surface of the device, verified using a solar power meter. The I-V curve of the device under irradiation was obtained using suitable data acquisition units (Agilent Measurement unit, Model No: U2722A).

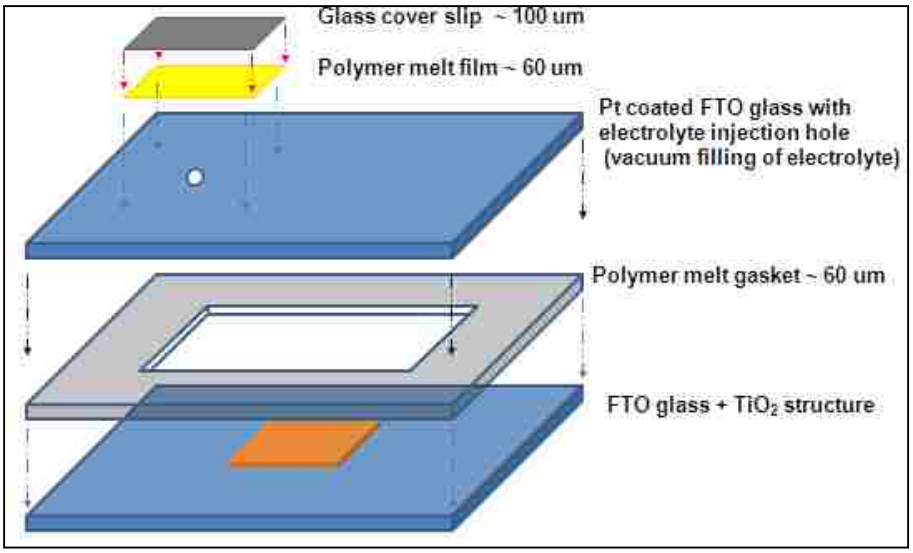

Figure 5.7: Schematic of the fabrication procedure and packaging of sandwich structure of a DSSC

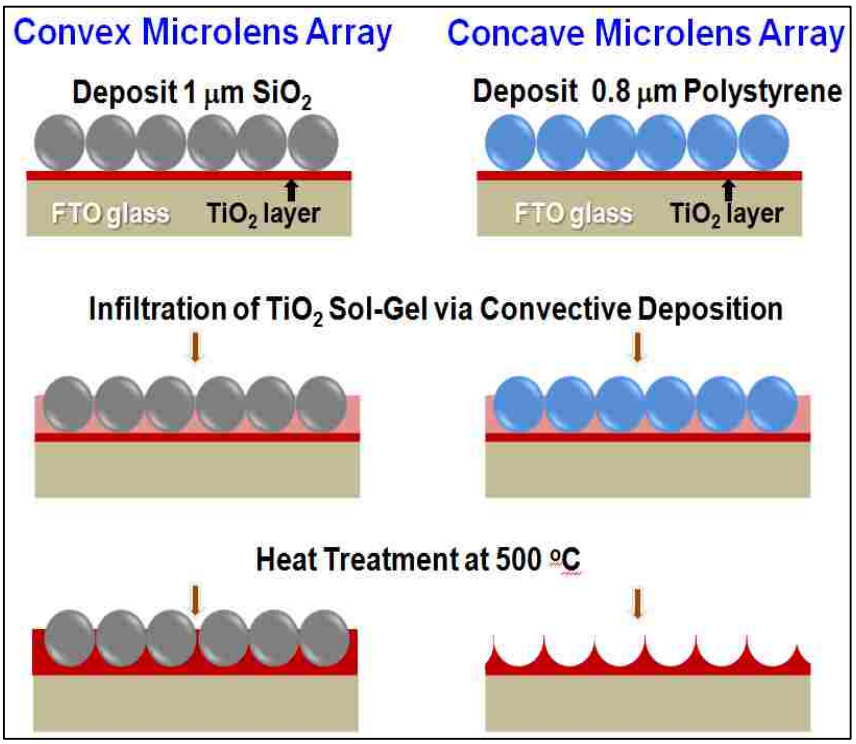

Figure 5.8: Fabrication of DSSC with Convex and concave microlens array. Both Microlens structures involves a monolayer deposition of silica or polystyrene microspheres, infiltration with the titania salt and final heat treatment procedure

5.3 Results and Discussion

The overall efficiency of a DSSC is dependent on the individual efficiencies of the processes involved in the cell, namely the efficiency of the incident photons to generate photoelectrons, electron injection efficacy into the semiconductor conduction band and the efficiency of generated electrons being captured at the electrode surface, thereby generating a photocurrent. In an actual device, only a limited region of the incident photon spectrum can be effectively captured by the sensitizing dye, thereby imposing limitations on the optimal utilization of the incident light. The focus of the work is to enhance the probability and efficiency of the incident light to generate photoelectrons by devising suitable methodologies and device architecture to enable a sustained retention of the incident photons within the photoactive region comprising of the dye-semiconductor mixture, which yields an improved probability for photoelectron generation. This objective was realized by incorporating a regular array of micrometer sized lenses with semicircular curvature, which would aid in bending of the photons as it traverses through the lens structure. The fabrication of the so-called microlens structure however demands a robust and scalable fabrication technique, the pre-requisite of which can be achieved comfortably by the convective deposition technique. The efficacy of this procedure to generate uniform structures with high periodicity and control over the number of layers makes it an enticing approach to fabricate the microlens structures, the performance of which can be further improved upon by the addition of periodic vibrations to yield monolayered uniform structures of desired extent over the required surface.

Figure 5.8 outlines the fabrication procedure and the resulting microlens structures proposed and analyzed in this work for enhanced light capturing efficiencies in DSSC

devices. For optimal performance, the microlens structures were confined to a monolayer thickness and incorporated between the treated FTO glass surface and mesoporous TiO2 layer. The various process parameters exert a profound influence on the final morphology of the microlens structure and their ability to effect a significant performance enhancement over plain DSSC devoid of these structures. These parameters includes the size of particles involved to generate microlens structures (silica and polystyrene), the thickness of coatings, extent of sol-gel infiltration as well as the temperature employed for the thermal treatment to generate crystalline anatase phase, each of which demands individual consideration to achieve optimal performance enhancement from microlens incorporation. The DSSC cells thus fabricated under varying conditions were characterized and optimal conditions chosen based on scanning electron microscopy (SEM) observations and performance measurements.

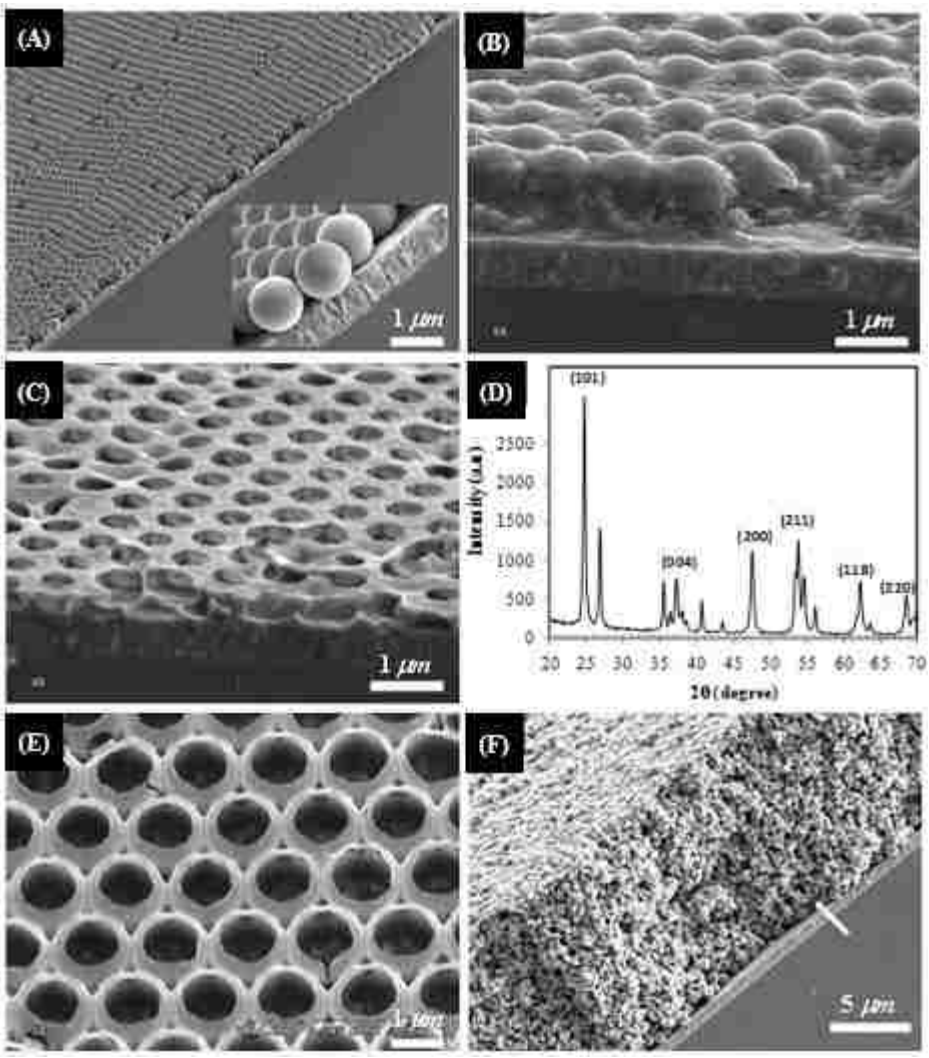

Figure 5.9 : SEM images and XRD analysis of Microlens structures: (A) monolayer of 1 µm SiO_2 particles on ultrathin titania salt coated transparent electrode (B) Convex microlens arrays made of monolayer of SiO_2 infiltrated with TiO_2 sol-gel (C) Concave microlens array made of TiO_2 sol-gel after removing polystyrene monolayer template (D) Powder diffraction from XRD showing the anatase and rutile phases of TiO_2 after heat treatment at 500 ^oC (E) Concave microlens with excess TiO_2 sol-gel infiltration (F) Titanium dioxide mesoporous layer on top of microlens array

5.3.1 Enhancement in performance with microlens

Figure 5.10 compares the performance of DSSC with the incorporation of microlens and devoid of these additional structures. The plots featuring continuous lines with markers in the figure compares the ideal scenarios of plain DSSC, convex microlens and concave microlens. The incorporation of microlens into the actual structure of a DSSC aids in the scattering of light rays, which leads to an increased utilization of the incoming photons to generate photocurrent. The microlens possess two unique features which aids in this enhanced light scattering – a medium with a different refractive index as well as the convex/ concave architecture which serves as internal lenses. A convex microlens contains silica particles embedded in a crystalline anatase titania, whereas concave microlens resembles an inverse-opal like structure composed of a continuous titania phase (which is predominantly anatase). The initial bending of the light occurs when it encounters the continuous titania phase in the DSSC structure, and is further bent due to the lens –like action owing to the curved architecture of the microlens. This also serves to reflect back the photons reflected from the TiO_2particles of the photoanode back into the device.

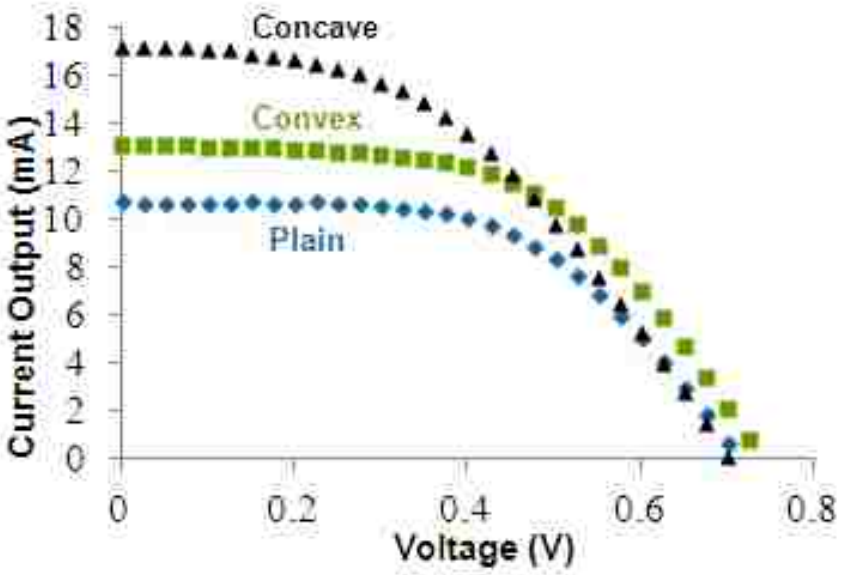

Figure 5.10: I-V curves of DSSC for (1) TiO_2 concave Microlens (2) SiO_2/TiO_2 convex Microlens (3) Plain DSSC

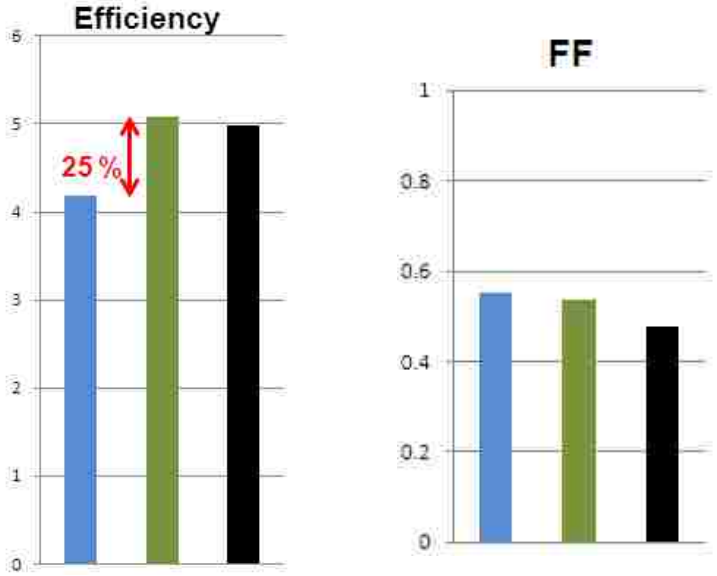

Figure 5.11: Comparison of FF and Efficiency of Plain (blue), Convex microlens (green) and Concave microlens (black)

The V_{oc} curve shows a similar value for the case of a Plain cell, Convex and concave microlens. The V_{oc} value, given by the difference of the redox potential of electrolyte and conduction band of TiO_2 remains unchanged, which indicates that the microlens structures improves the light harvesting efficiency of the device, without altering its inherent dynamics. On the contrary, the addition of Microlens into the DSSC structure leads to a significant improvement in I_{sc} value over that of a Plain cell, which can be attributed to an increased utilization of the incoming photons, resulting in an increase in the generation of photoelectrons. The FF of a cell, which represents how close the actual performance of the cell is to the ideal case indicates the internal resistance in the cell. The incorporation of an additional microlens layer increases the internal resistance of the cell, which can be observed from the reduction of FF values for the convex and concave microlens over that of a Plain cell. The maximum power output from the cell, which is the product of FF,V_{oc} and I_{sc} determines the overall efficiency of the cell. The incorporation of microlens leads to a reduction in the FF. However, it is more than compensated by the significant increase in short-circuit current, with an improvement of almost 25 % in overall performance.

5.3.2 Farfield measurement set-up

Far field measurements were performed on the DSSC cells, with the performance of the anode with incorporated microlens compared with that of plain DSSCs. The objective of these measurements were to analyze the angular variation in optical fields with the introduction of microlens, when a collimated white light (with similar spectral characteristics as AM 1.5 solar radiation) was incident on the structure. A higher angular spread across multiple wavelengths of the incident spectrum would signify a bending of the incident light when it encounters the convex/ concave microlens structure. This would directly result in an increased photon path length and thereby, an increased residence time of incident photons within the device, thus enabling a mechanistic proof of enhanced photocurrent generation with microlens.

The far field measurements were performed on the experimental set up designed, fabricated and operated by the Optics lab of Prof. Nelson Tansu in the Department of Electrical Engineering, Lehigh University. A schematic of the experimental set-up is shown in Figure 5.12. The measurement system consists of a collimated beam of light obtained using a suitable light source, polarizer and a spherical aperture of desired diameter. The aperture size and position is adjusted to illuminate the desired region of interest of the device. For the purpose of far field characterization, the measurements were performed on an undyed DSSC anode (TCO glass surface coated with microlens and further coated with TiO_2 nanoparticles). The optical fields emerging out of the device at various angles were measured using an adjustable photodetector which was rotated about a semicircular path and kept equidistant from the illuminated area of the device. The

intensity of the optical signals and its spectral composition were analyzed using a spectrometer.

The results of far field measurements are shown in Figure 5.13, with the normalized average intensity of the transmitted light evaluated for three different configurations – plain DSSC, DSSC with convex microlens and DSSC with concave microlens. This was calculated by measuring the intensity of each individual wavelength in the transmitted light which was then averaged to obtain the intensity of light over entire wavelength spectrum. The values thus obtained were normalized to with respect to its maximum and minimum intensity values to obtain a range of values from 0 -1. From the figure, it could be observed that there is an enhanced spread of incident light with the addition of microlens structure.

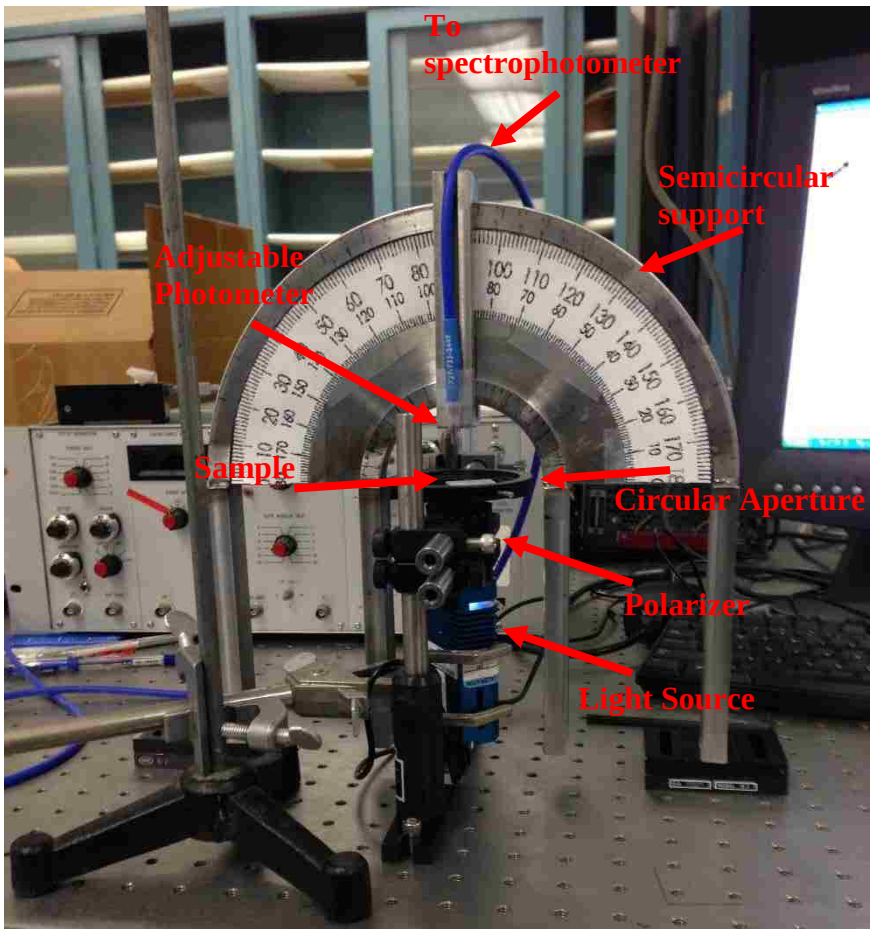

Figure 5.12: Experimental set-up for far field measurement. The various components in the set-up are labeled in the figure. A polarized and collimated light is incident on the microlens structure of the DSSC. The transmitted light is then analyzed across various angles using a spectrophotometer.

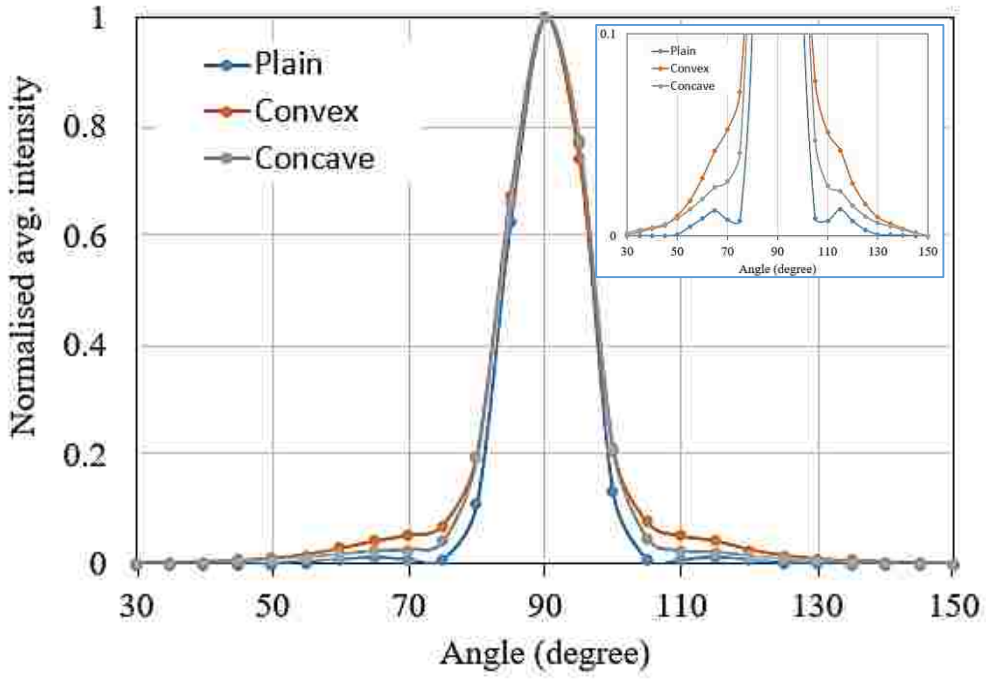

Figure 5.13: Normalized intensity of the transmitted light from specimen (averaged over multiple wavelength) plotted for plain DSSC, convex microlens and concave microlens. The inset image shows a magnified view of the angular spread with the incorporation of microlens. The twin minor peaks observed in the inset figure could be attributed to the bending of light around the aperture.

5.4 Studies on anode fabrications for enhanced cell performance

In addition to enhanced light harvesting in DSSC through photon management techniques, several attempts were made for improving the overall performance of cell through higher charge collection efficiency and reduced recombination losses in the photoelectrode.

5.4.1 Incorporation of blocking layer to reduce recombination losses

The major part of the recombination losses occurs at the working electrode, when the electrons recombine with the oxidized redox initiator at the surface of the glass substrate, thereby reducing the photocurrent. To circumvent these losses, the TCO substrate was coated with a high density titania film, which reduced the recombination probability at the electrode. In addition to the titania salt coating discussed in the fabrication procedure, DSSCs were fabricated with titania salt obtained by magnetic stirring of ethanol, Titanium (IV) isopropoxide and Acetic acid over a period of 12 hours. The cells thus fabricated showed marginal improvement in performance as can be observed from Table 5.1.

Configuration	**No Ti Salt**	**Original Ti Salt**	**New Ti Salt**
Avg. efficiency (%)	5.00 ± 0.32	5.23 ± 0.19	5.56 ± 0.24

Table 5.1: Comparison of average efficiency with various titania salts

The titania salt creates a high density non-porous film on the working electrode TCO substrate, resulting in improved performance efficiency attributed to the reduced recombination of the electrons with the oxidized redox species at the working electrode.

5.4.2 Configuration of the probe

The charge collection efficiency of the cell varies with the configuration of the probe (as depicted in Figure 5.14(a). The results averaged over 3 cells and summarized in Figure 5.14(b) show the optimal configuration to be the one spanning both the length and breadth of the cell. The results show an improvement in the collection of photoelectrons when the metal contacts span all sides of the electrodes. Further improvements in the charge collection can be realized by using high-conductivity silver pastes for making external contacts from the cell.

5.4.3 Active area of the photoelectrode

The performance efficiency of the cell, measured on a unit area basis showed a remarkable increase with the reduction in the active area. A handful of plain DSSC cells of each type, fabricated with active area ranging from 2 cm^2 to 0.125 cm^2 , all other parameters remaining the same, (as depicted in Figure 5.15) gave an exponential increase in the efficiency values (given in Figure 5.15(b)). A similar trend was observed for the DSSC with micro lenses incorporated in it, with average efficiency values of 5 and 11.5 for active areas of 1 cm^2 and 0.125 cm^2 respectively. The I-V curves of the individual cells of each type show a decreasing FF with increase in the active area. The increase in FF and efficiency with decreasing active area can be attributed to the reduced resistances associated with the TCO glass surface for both the electrodes.

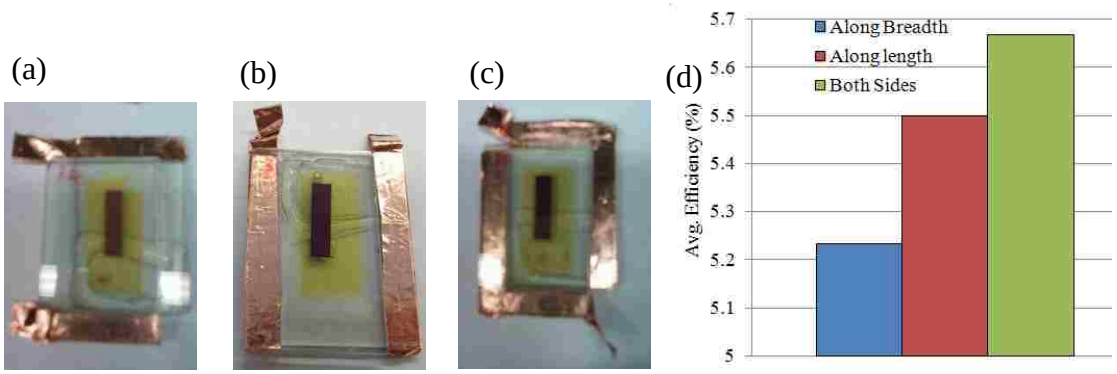

Figure 5.14: Effect of probe configuration (a) along the breadth (b) along the length (c) On both sides (d) Comparison of average efficiencies for various probe configurations

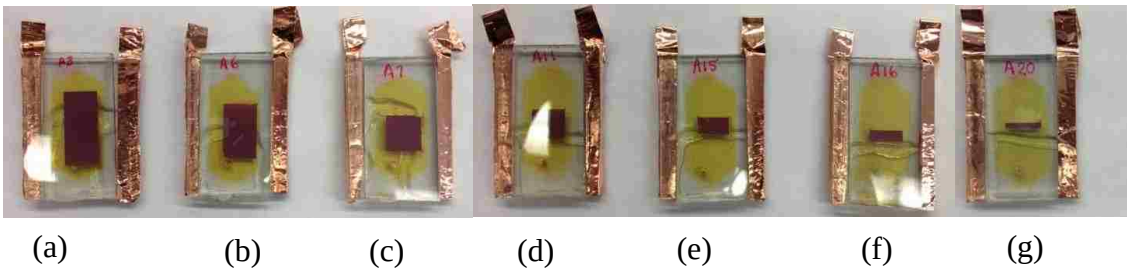

Figure 5.15: DSSC with different active areas (a) 2x1 (b) 1.5x1 (c) 1x1 (d) 0.75x1 (e) 0.5x1 (f) 0.25x1 (g) 0.125x1 (all dimensions in cm)

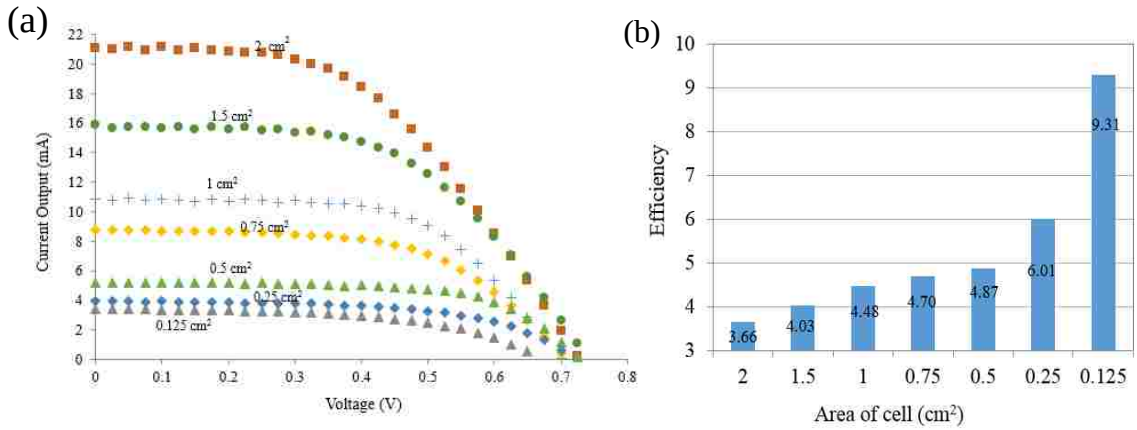

Figure 5.16: (a) Voltage-Current characteristics and (b) Performance comparison of DSSC with varying active area on photoelectrode. The averaged efficiency values of each type has been shown on the respective bar plots.

5.5 Scale-up of DSSC technology for commercial applications

Commercial applications require the fabrication of a large number of cells to meet the power requirements. This scale-up in the load capacity of the DSSC can be achieved either by fabricating small cells and interconnecting them to form a single circuit or by fabricating a cell with a large continuous area.

5.5.1 Small cells externally interconnected into a series / parallel connection

In this approach, nine 1 cm x 1 cm cells were fabricated under similar conditions and their performances were measured. Thereafter the cells were interconnected in series and parallel fashion, with the circuitry as given in the inset of Figure 5.17(b)(c).

In series configuration, the opposite terminals of adjacent cells are connected together forming a single path, whereas in the parallel connection, all the like terminals of the individual cells are connected to a single point. The series connection of cells gives a higher output voltage, whereas the parallel connection gives a higher output current. The values shown to the right for each plot helps to make a comparison of the efficiency and fill factor values for the individual cells as well as for the series and parallel configurations. The experimental results show a higher efficiency and fill factor when the cells are connected in a series fashion than when measured individually. As can be observed from the results, as well as the performance curves of Figure 5.17(a)(b)(c), the series interconnection of the cells gives a higher efficiency and fill factor than the average of the individual cells, and definitely fares better than parallel interconnection.

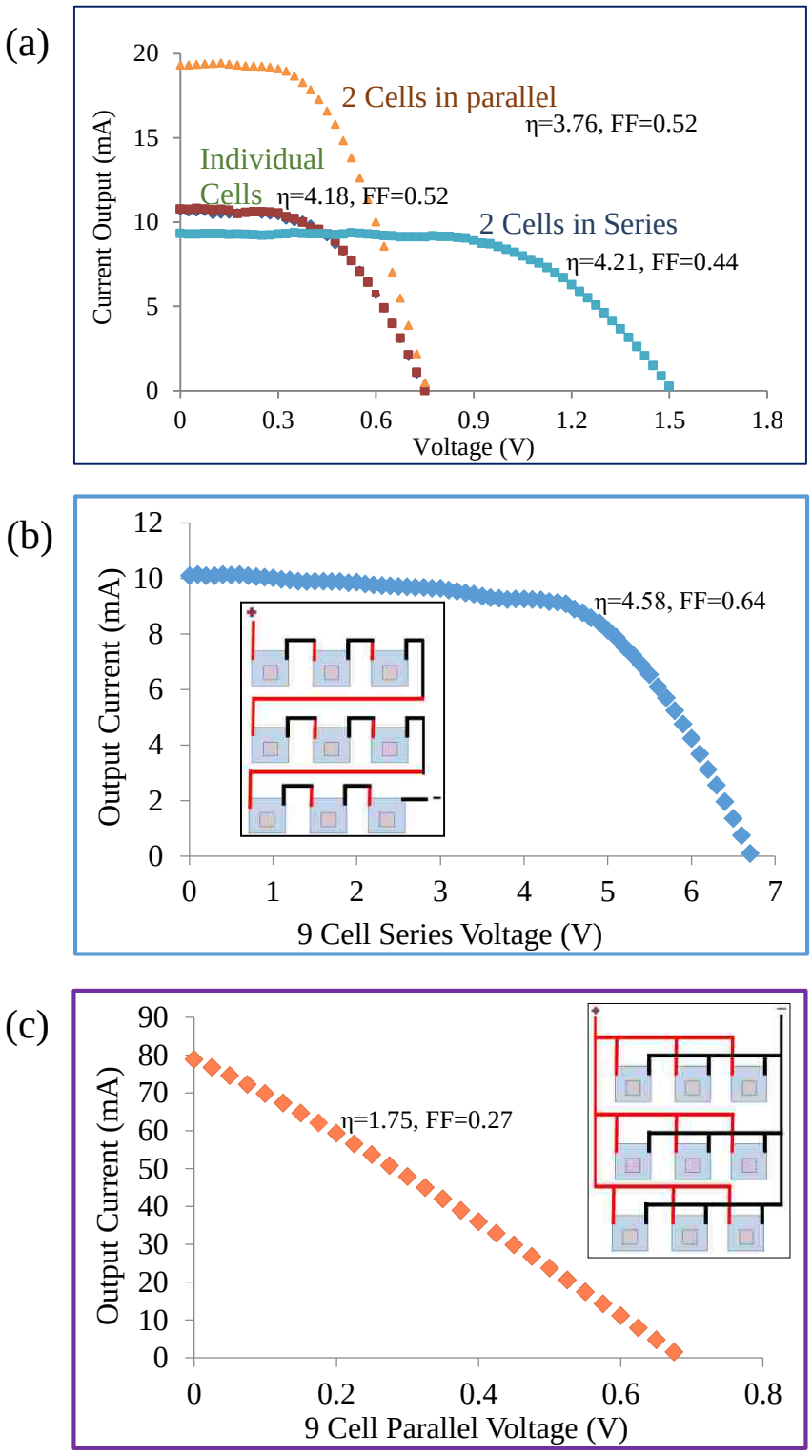

Figure 5.17: Comparison of individual cell performance, along with the series and parallel configurations (a) V-I characteristics of nine individual cells, along with two cells in series and parallel connection (b) V-I characteristics of all nine cells connected in series (circuitry in inset) (c) V-I characteristics of all nine cells in parallel, with the corresponding circuitry in inset. The efficiency and fill factor values for each configuration are also shown adjacent to the corresponding plot, showing a better performance for the series configuration.

5.5.2 A **single large cell with the required area**

In this approach, two cell patterns were fabricated: one with nine discontinuous segments each of 1 cm^2 area on the same glass sheet and the other with a single continuous area of 9 cm^2on the glass. A schematic of both configurations as well as images of the actual device are shown in Figure 5.18(a),(b). The performance characteristics of these cells were evaluated and compared with the series and parallel configuration of cells which was discussed in Figure 5.17.

Figure 5.18(c) describs the charcteristics of the cells fabricated by the aforementioned configurations. The performance of both the discontinuous-segment-type (Figure 5.18a) as well as the continuous-type (Figure 5.18b) are similar, with negligible differences in key performance parameters like V_{OC},I_{SC},η and FF. Moreover, the performance of either configurations are similar to the results obtained when separate cells are connected in a parallel circuit (Figure 5.17c), with an efficiency value much lower than that could be obtained with a series configuration. It can thus be concluded that to obtain a desired power output, the optimal choice is to fabricate several small cells and then connect them in a series arrangement.

(a)

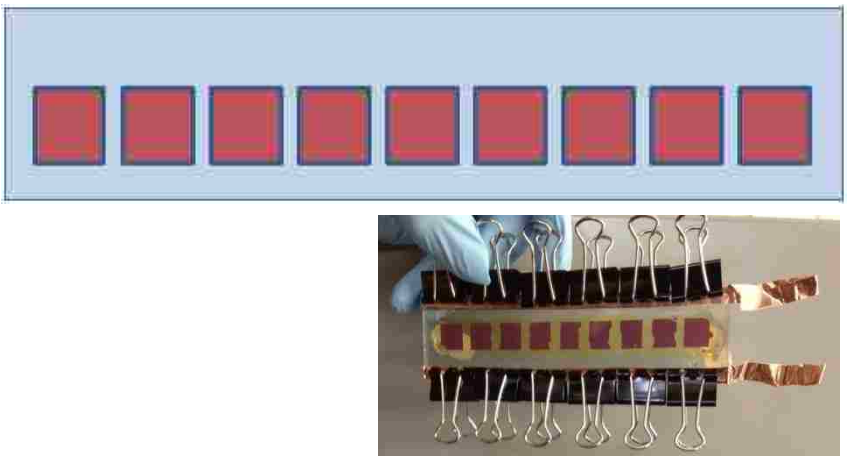

(b)

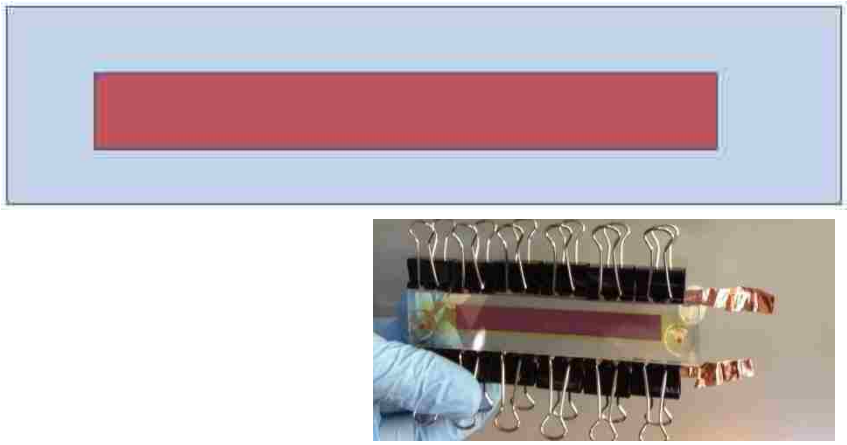

(c)

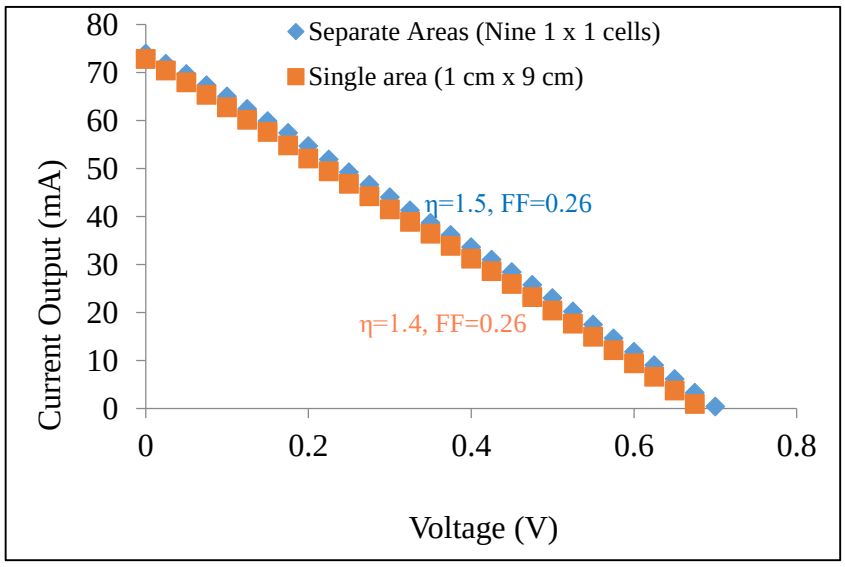

Figure 5.18: Schematic and performance comparison of DSSC fabricated as single large cell (a) Schematic of a DSSC comprised of nine discontinuous areas (image of actual device shown beneath) (b) Schematic of DSSC as a single continuous area (c) V-I characteristics of both configurations, with the efficiency and fill factor values.

5.5.3 Working and counter electrodes on the same glass substrate

From the discussion in Section 5.5.1 and 5.5.2, it could be inferred that a single large cell gives much reduced performance compared to multiple cells connected in series and with same total area, owing to sheet resistance. This section further investigates this observation by obtaining a DSSC module of multiple cells in series connection, with all constituting cells of the device confined to a single sandwich structure -i.e., a monolithic cell with serially connected individual modules. Two configurations were investigated for this purpose- Configuration 1 in which a series connection between cells was achieved using external copper tapes, Configuration 2 in which the device architecture was modified to provide a series connection between adjacent cells in an internal manner.

The aforementioned architecture demands that alternating regions of the same glass surface should act as the working electrode (TiO2 layer) and counter electrode (Pt layer) – separation between various compartments achieved by etching off the TCO layer from the glass as shown schematically in Figures 5.19a,b. In Configuration 1 (with external series connection), the etching on both glass surfaces coincides with each other, but is staggered in Configuration 2 (internal series connection). Both the configurations adopt a similar approach for their fabrication. The desired regions are first coated with titania sol gel and then the TiO2 layer with heat treatment of 500 C for both. The platinum layer is then deposited on the designated regions of the same glass surface and heated at 400 C. This is followed by immersion of glass sheets for dye loading and final packaging and electrolyte injection. While the various individual modules are isolated with respect to electrolyte in Configuration 1, they have a continuous volume in Configuration 2. The performance of both architectures were investigated outdoors.

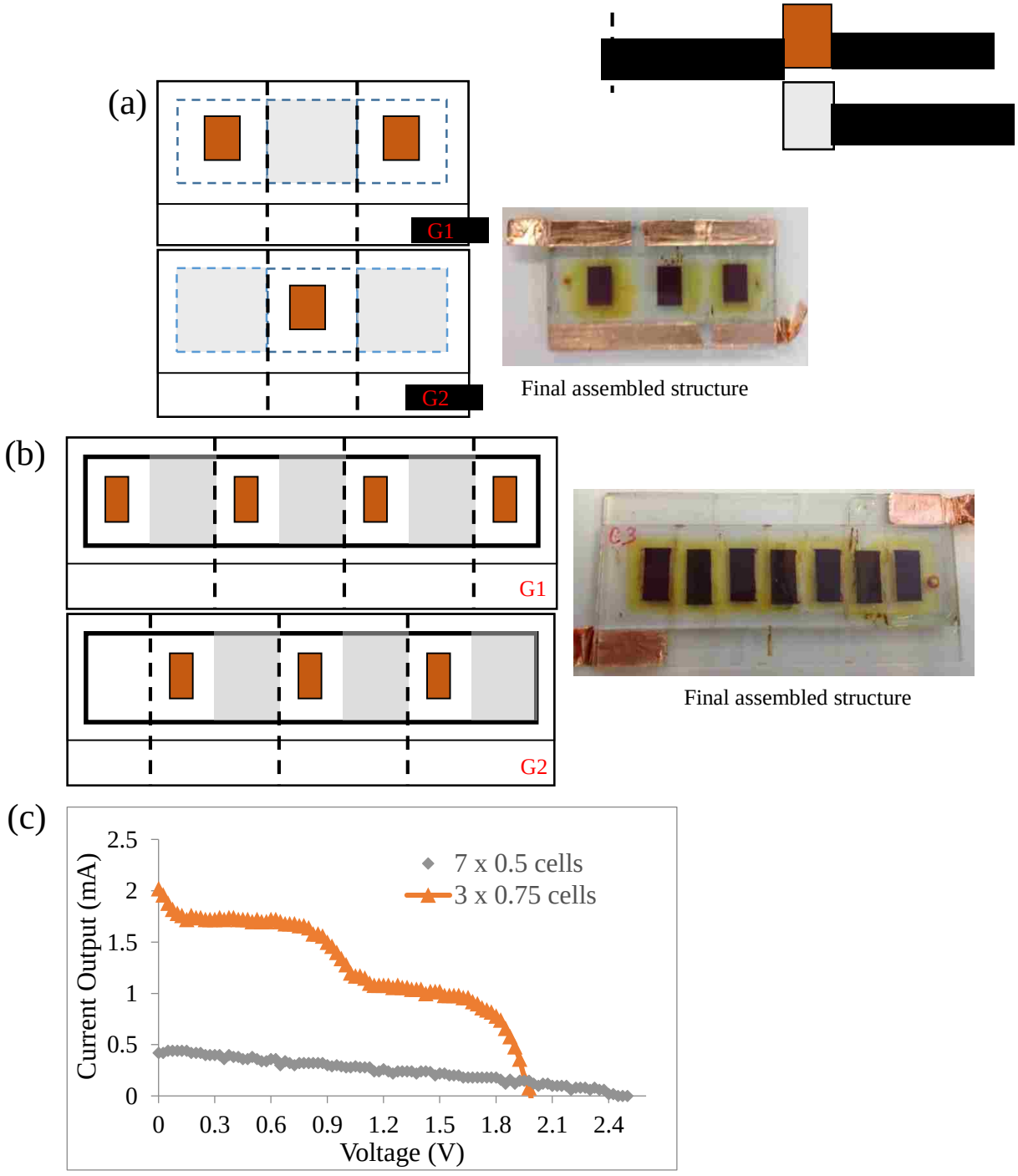

Figure 5.19: Schematic of fabrication procedure to obtain a monolithic DSSC structure in series configuration, with alternating working electrode and counter electrode on same glass sheet (a) Schematic of configuration 1 (series connection between segments through copper tapes), with an image of the final assembled device (b) Schematic of Configuration 2 (series connection through selective etching of glass surface) with the final assembled device. For both schematics, the notations G1 and G2 represents the two glass sheets used for sandwiched DSSC structure (c) V-I characteristics for both Configuration 1and Configuration 2

For both the configurations of the monolithic type, the performance was not as per the expected results, perhaps due to the cross-contamination of the electrodes. When different regions of the same glass sheet is used to develop the TiO2 layer and platinum layer, there is unavoidable contamination of the TiO2 particles with platinum vapors. This perhaps acts as recombination sites for the photoelectrons, severely reducing the overall performance. Hence, developing this architecture needs a design to isolate the various regions during the fabrication technique to avoid a loss of performance and activity by contamination.

5.6 Summary and Future Work

The current work focuses on developing an understanding of the basic phenomena as well as the factors which affects the performance of the DSSC, with special emphasis on the anode morphology. Cells have been fabricated with different anode structures and their performances were characterized, thereby providing an insight into the various factors which affect the overall efficiency of a dye-sensitized solar cell. The studies on the scale-up technologies for commercial applications revealed a better performance for series interconnection of the cells over that of a single large cell, which has the potential for further improvement by the fabrication of monolithic DSSC architectures.

5.7 References

1. British Petroleum. BP Statistical Review of World Energy June 2015. 48 (2015). doi:bp.com/statisticalreview

2. British Petroleum. BP Energy Outlook 2016 edition. Outlook to 2035. (2016).

3. Zhang, Q. & Cao, G. Nanostructured photoelectrodes for dye-sensitized solar cells. *Nano Today* **6,** 91–109 (2011).

4. O'Regan, B. & Grätzel, M. A low-cost, high-efficiency solar cell based on dye-sensitized colloidal TiO2 films. *Nature* **353,** 737–740 (1991).

5. Green, M. A., Emery, K., Hishikawa, Y., Warta, W. & Dunlop, E. D. Solar cell efficiency tables (version 41). 1–11 (2013). doi:10.1002/pip

6. Grätzel, M. Recent advances in sensitized mesoscopic solar cells. *Acc. Chem. Res.* **42,** 1788–1798 (2009).

7. Mathew, S. *et al.* Dye-sensitized solar cells with 13% efficiency achieved through the molecular engineering of porphyrin sensitizers. *Nat. Chem.* **6,** 242–247 (2014).

8. Green, M. A., Emery, K., Hishikawa, Y., Warta, W. & Dunlop, E. D. Solar cell efficiency tables (version 47). *Prog. Photovoltaics Res. Appl.* **24,** 3–11 (2016).

9. Grätzel, M. Perspectives for dye-sensitized nanocrystalline solar cells. *Prog. Photovoltaics Res. Appl.* **8,** 171–185 (2000).

10. Yu, Y.-Y. *et al.* A hierarchical homogeneous core–shell structure of TiO2 hollow microspheres for high efficiency dye-sensitized solar cells. *Adv. Powder Technol.* **26,** 1072–1078 (2015).

11. Law, M. *et al.* ZnO - Al 2 O 3 and ZnO - TiO 2 Core - Shell Nanowire Dye-Sensitized Solar Cells. *J. Phys. Chem.* **101,** 22652–22663 (2006).

12. Law, M., Greene, L. E., Johnson, J. C., Saykally, R. & Yang, P. D. Nanowire dye-sensitized solar cells. *Nat. Mater.* **4,** 455–459 (2005).

13. Hagfeldt, A., Boschloo, G., Sun, L., Kloo, L. & Pettersson, H. Dye-Sensitized Solar Cells. *Chem. Rev.* **110,** 6595–6663 (2010).

14. Ito, S. *et al.* Fabrication of Screen-Printing Pastes From TiO 2 Powders for Dye-Sensitised Solar Cells. 603–612 (2007). doi:10.1002/pip

15. Natarajan, C., Fukunaga, N. & Nogami, G. Titanium dioxide thin film deposited by spray pyrolysis of aqueous solution. *Thin Solid Films* **322,** 6–8 (1998).

16. Chen, H.-W. *et al.* Electrophoretic deposition of TiO2 film on titanium foil for a flexible dye-sensitized solar cell. *Electrochim. Acta* **56,** 7991–7998 (2010).

17. *Handbook of Photovoltaic Science and Engineering*. (John Wiley & Sons, Ltd, 2003).

18. Yum, J.-H., Baranoff, E., Wenger, S., Nazeeruddin, M. K. & Graetzel, M. Panchromatic engineering for dye sensitized solar cells.pdf. 842 (2011).

19. Papageorgiou, N. *et al.* The Performance and Stability of Ambient Temperature Molten Salts for Solar Cell Applications. *J. Electrochem. Soc.* **143,** 3099 (1996).

20. Chung, I., Lee, B., He, J., Chang, R. P. H. & Kanatzidis, M. G. All-solid-state dye-sensitized solar cells with high efficiency. *Nature* **485,** 486–9 (2012).

21. Murakami, T. N. *et al.* Highly Efficient Dye-Sensitized Solar Cells Based on Carbon Black Counter Electrodes. *J. Electrochem. Soc.* **153,** A2255 (2006).

22. Lee, K. E., Gomez, M. A., Elouatik, S. & Demopoulos, G. P. Further Understanding of the Adsorption Mechanism of N719 Sensitizer on Anatase TiO2 Films for DSSC Applications Using Vibrational Spectroscopy and Confocal Raman Imaging. *Langmuir* **26,** 9575–9583 (2010).

23. Nazeeruddin, M. K., Baranoff, E. & Gr??tzel, M. Dye-sensitized solar cells: A brief overview. *Sol. Energy* **85,** 1172–1178 (2011).

24. Hagberg, D. P. *et al.* Tuning the HOMO and LUMO energy levels of organic chomophores for dye sensitized solar cells. *J. Org. Chem.* **72,** 9550–6 (2007).

25. Huang, Y. *et al.* Theoretical modeling of the series resistance effect on dye-sensitized solar cell performance. *Appl. Phys. Lett.* **95,** 243503 (2009).

26. Lee, K.-J. *et al.* A Study on a Solar Simulator for Dye Sensitized Solar Cells. *Int. J. Photoenergy* **2012,** 1–11 (2012).

27. Hardin, B. E., Snaith, J. & Mcgehee, M. D. The renaissance of dye-sensitized solar cells. *Nat. Photonics* **6,** 162–169 (2012).

28. Kubo, W., Sakamoto, A., Kitamura, T., Wada, Y. & Yanagida, S. Dye-sensitized solar cells: Improvement of spectral response by tandem structure. *J. Photochem. Photobiol. A Chem.* **164,** 33–39 (2004).

29. Ito, S. *et al.* High-efficiency organic-dye-sensitized solar cells controlled by nanocrystalline-TiO2 electrode thickness. *Adv. Mater.* **18,** 1202–1205 (2006).

30. Hore, S. *et al.* Scattering spherical voids in nanocrystalline TiO2- enhancement of efficiency in dye-sensitized solar cells. *Chem. Commun.* 2011–3 (2005). doi:10.1039/b418658n

31. *Reference Solar Spectral Irradiance: Air Mass 1.5*. at <http://rredc.nrel.gov/solar/spectra/am1.5/>

32. Fabregat-Santiago, F., Garcia-Belmonte, G., Mora-Sero, I. & Bisquert, J. Characterization of nanostructured hybrid and organic solar cells by impedance spectroscopy. *Phys. Chem. Chem. Phys.* **13,** 9083–9118 (2011).

33. Hore, S. *et al.* Scattering spherical voids in nanocrystalline TiO2- enhancement of efficiency in dye-sensitized solar cells. *Chem. Commun. (Camb).* 2011–2013 (2005). doi:10.1039/b418658n

34. Koo, H.-J. *et al.* Size-dependent scattering efficiency in dye-sensitized solar cell. *Inorganica Chim. Acta* **361,** 677–683 (2008).

35. Hore, S., Vetter, C., Kern, R., Smit, H. & Hinsch, A. Influence of scattering layers on efficiency of dye-sensitized solar cells. *Sol. Energy Mater. Sol. Cells* **90,** 1176–1188 (2006).

36. Liu, H. *et al.* Enhance the performance of dye-sensitized solar cells by balancing the light harvesting and electron collecting efficiencies of scattering layer based photoanodes. *Electrochim. Acta* **132,** 25–30 (2014).

37. Zheng, Y. Z. *et al.* Novel ZnO-based film with double light-scattering layers as photoelectrodes for enhanced efficiency in dye-sensitized solar cells. *Chem. Mater.* **22,** 928–934 (2010).

38. Dominici, L. *et al.* Angular refractive path for optical enhancement and evaluation of dye solar cells. *Sol. Energy* **98,** 553–560 (2013).

39. Chen, Y. *et al.* Microlens array induced light absorption enhancement in polymer solar cells. *Phys. Chem. Chem. Phys.* **15,** 4297–302 (2013).

40. Barettin, D., Di Carlo, A., De Angelis, R., Casalboni, M. & Prosposito, P. Effect of dielectric Bragg grating nanostructuring on dye sensitized solar cells. *Opt. Express* **20,** A888–97 (2012).

41. Guldin, S. *et al.* Dye-sensitized solar cell based on a three-dimensional photonic crystal. *Nano Lett.* **10,** 2303–2309 (2010).

42. Nishimura, S. *et al.* Standing wave enhancement of red absorbance and photocurrent in dye-sensitized titanium dioxide photoelectrodes coupled to photonic crystals. *J. Am. Chem. Soc.* **125,** 6306–10 (2003).

43. Ferber, J. & Luther, J. Computer simulations of light scattering and absorption in dye-sensitized solar cells. *Sol. Energy Mater. Sol. Cells* **54,** 265–275 (1998).

44. Huang, F., Chen, D., Zhang, X. L., Caruso, R. a. & Cheng, Y.-B. Dual-Function Scattering Layer of Submicrometer-Sized Mesoporous TiO 2 Beads for High-Efficiency Dye-Sensitized Solar Cells. *Adv. Funct. Mater.* **20,** 1301–1305 (2010).

45. Zhu, K., Neale, N. R., Miedaner, A. & Frank, A. J. Enhanced charge-collection efficiencies and light scattering in dye-sensitized solar cells using oriented TiO2 nanotubes arrays. *Nano Lett.* **7,** 69–74 (2007).

46. Hägglund, C., Zäch, M. & Kasemo, B. Enhanced charge carrier generation in dye sensitized solar cells by nanoparticle plasmons. *Appl. Phys. Lett.* **92,** 2006–2009 (2008).

47. Brown, M. D. *et al.* Plasmonic dye-sensitized solar cells using core-shell metal-insulator nanoparticles. *Nano Lett.* **11,** 438–445 (2011).

48. Kumnorkaew, P., Ee, Y. K., Tansu, N. & Gilchrist, J. F. Investigation of the deposition of microsphere monolayers for fabrication of microlens arrays. *Langmuir*

24, 12150–12157 (2008).

49. Kumnorkaew, P., Weldon, A. L. & Gilchrist, J. F. Matching constituent fluxes for convective deposition of binary suspensions. *Langmuir* **26,** 2401–5 (2010).

50. Muangnapoh, T., Weldon, A. L. & Gilchrist, J. F. Enhanced colloidal monolayer assembly via vibration-assisted convective deposition. *Appl. Phys. Lett.* **103,** 181603 (2013).

6

Magnesium oxide based membrane separators for thermal batteries

6.1 Introduction

Thermal batteries refer to a class of primary batteries which uses molten salts as electrolytes[1,2]. They are characterized by their high temperature of operation (high temperature power sources), with the operating temperatures in the range of 350^{o}C – 550^{o}C. These batteries derive its name from the fact that they are 'thermally activated'[2] – the operation of the battery is reliant on an internal heat source which brings the device into operating conditions.

The prominent feature of a thermal battery is its ability to store the device for over 25 years over a wide range of temperatures without any significant degradation of the device. This is made possible by the solid and inactive state of the inorganic salt which constitutes the electrolyte. Since the components of the battery are stored in an inactive stage, it eliminates the degradation of the active materials during storage as well as capacity loss due to self-discharge. The battery, could nevertheless be activated instantly within a span of seconds by converting the electrolyte into a molten form using a suitable internal heat source, thus rendering the electrolyte into an excellent ionic conductor. In comparison to a typical electrolyte employed in Li-ion batteries, the molten salt electrolytes have a conductivity of 1850 mS cm^{-1} at 500 ^{o}C[2], which is several orders of magnitude higher than

the conventional electrolytes in batteries. This high ionic conductivity associated with the electrolytes results in a high power output and a high energy output when the device is thermally activated. The limitations of these thermal batteries arise from its mode of operation, with the incorporation of them as a source of power limited by its one- time usage, low activated life and high surface temperatures. The inherent features of thermal batteries make it a suitable source of power for military and defense applications, which includes powering rockets, missiles and torpedoes[2]. In addition, the ability to maintain the battery in an inert condition without significant degradation enables its usage in space exploration systems – to power critical electronic components in space flights[2].

6.1.1 Construction of Thermal batteries

The major components of a thermal battery comprise of cathode, anode, electrolyte and an internal heat source placed between the cells in the battery stack. A schematic of the construction of a thermal battery is shown in Figure 6.1.

Thermal batteries employ a metal salt as cathode, with suitable materials investigated being sulfides of iron (FeS_2), cobalt (CoS_2), nickel (NiS_2,NiS) and transition metals (MoS_2,Sb_2S_3, Bi_2S_3), transition metal halides ($NiCl_2$, $FeCl_2$, $SbCl_3$, $CuCl_2$) and transition metal oxides (WO_3, V_2O_5, MnO_2)[3]. Of these various suitable candidates, metal sulfides like CoS_2 and FeS_2 are commonly preferred for the construction of thermal batteries[1,4]. In comparison to other salts, CoS_2 has the advantages of a higher decomposition temperature, higher conductivity and better voltage stability[1]. In the case of thermal batteries which employ FeS_2 as cathode, detailed studies performed have shown a

high degree of dependence of thermal stability and decomposition temperature on the inherent microstructure of the corresponding salt[5].

The decomposition of FeS_2 when heated at an inert atmosphere follows the reaction:

$$FeS_2 \rightarrow \ FeS + S_2$$

While a microscale FeS_2 undergoes decomposition at 360^{o}C, nanostructured FeS_2 is stable up to 500^{o}C[5]. In addition, nanostructuring when applied to cathode materials enables an increased pellet density with higher surface area and compactness, which enables a reduction in the volume of the cell. Furthermore, it ensures an enhanced reaction rate and a higher power density resulting from the improved Li ion diffusion in the nanostructured cathode[5].

The construction of anodes for thermal batteries are currently based on various materials like Ca (and its alloys like Ca-Al, Ca-Si), Mg, Al and Li (and alloys like Li-Al, Li-Si)[6]. Of the various alloys investigated, optimal anode performance was obtained with the binary and ternary alloys of Lithium. However, a major limitation of the Li based alloys is their high sensitivity to external environmental conditions comprising of oxygen and water vapor, which are significantly pronounced for Li-Si and Li-Al alloys. This necessitates the packaging of the anode to be performed in a dry environment with a relative humidity less than 3 %[6].

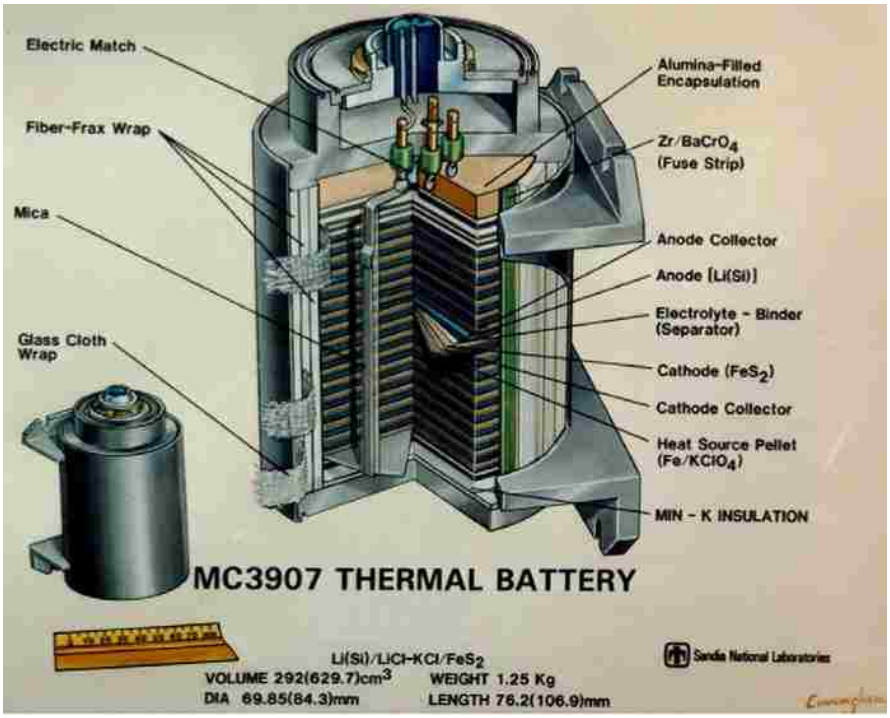

Figure 6.1: Construction of a thermal battery with Li-Si as anode and FeS_2 as cathode[2]. The image was adapted from the corresponding reference.

The selection of a suitable molten salt as electrolyte is reliant on the physical, chemical and electrochemical properties of the material considered. The desirable characteristics of the electrolyte for its successful incorporation could be summarized based on the following characteristics[7]:

Physical properties	Chemical properties	Electrochemical properties
• Low vapor pressure • Suitable melting point • Suitable wetting angle with the separator materials and electrodes	• High ionic conductivity • Stable towards O_2 and moisture • Low solubility of anode and cathode materials	• No reaction between electrolyte and electrodes • No redox reaction of the electrolyte

Table 6.1: Characteristics of electrolyte for use in thermal batteries

The current transport in the electrolytes in its molten state occurs as a result of the migration of the ionic species. Hence, Li based electrolytes are usually preferred for the thermal battery construction as the high mobility of Li+ cations gives the highest ionic conductivity, most preferred one being LiCl-KCl eutectic mixture with melting temperature of 352 ^oC[2].

6.1.2 Operation of thermal batteries

The activation of a thermal battery is achieved using pyrotechnic or heat pellets incorporated within the battery stack, commonly used ones being a mixture of Fe and Potassium Chlorate ($KClO_4$). This combustible mixture is ignited directly by firing directly through a hole or using a fuse strip, whereby the electrolyte is melted into a molten form and rendered ironically conductive by the heat of combustion.

The sequence of discharge reaction of FeS_2 in molten LiCl-KCl is given by[2]:

$$FeS_2 \rightarrow Li_3Fe_2S_4 \rightarrow Li_{2-x}Fe_{1-x}S_2(x{\sim}0.2) + Fe_{1-x}S \rightarrow Li_2FeS_2 \rightarrow Li_2S + Fe$$

The discharge reaction at the anode with Li-Al alloy as the anode material is given by[2]:

$$Li_{0.47}Al_{0.53} \rightarrow \ Li_{0.0578}Al_{0.53} + 0.411\ Li^{+} + 0.411\ e^{-}$$

6.1.3 Separators for thermal batteries:

The separators are three-dimensional porous membrane structures which separate the cathode and anode in a cell, and are responsible for the immobilization of the molten electrolyte within the battery. This is achieved by capillary action of the electrolyte confined within the pores of the binder materials constituting the separator membrane, the retention efficiency within the pores determined by the magnitude of the surface tension for the electrolyte-binder system. The inability of the binder materials to completely immobilize the molten electrolyte results in dewetting of the same when the battery is activated, resulting in electrolyte leakage and shorting between the cathode and anode[7].

The design of the separator membrane plays a dominant role in the overall performance of a thermal battery, a choice of the suitable material and structure for its fabrication regulated by the physical, chemical and electronic properties of the constituent materials. Being a high temperature power source, it is essential that the separator membrane remain thermally stable in the range of operating temperatures. Furthermore, it should be resistant to the high levels of mechanical stress experienced by the battery during its manufacture and assembly[7].

The construction of a suitable separator membrane is based on inorganic oxides, the early investigated ones being silica, alumina and magnesia owing to the electrically insulating nature of the binder materials. Of these, MgO is more preferred due to its chemical inertness, thermal stability and desirable wetting properties. The MgO particles

are assembled into membrane structures with desired morphology, the final ionic conductivity of the separator membrane determined by its porosity and tortuosity.

This chapter of the dissertation reports on various methodologies which were investigated to fabricate MgO based separator membranes for thermal batteries. The techniques investigated relies on the convective assembly procedures studied in the previous chapters, which has the benefits of ease of scalability and high quality of the obtained periodic structures. The study mainly focusses on developing suitable prototypes of the membrane with a high porosity and uniform periodicity of the structure.

6.2 Fabrication of MgO based membrane separators

The fabrication of magnesium oxide based separator membranes used two distinct approaches:

(i) Fabrication of membrane using stabilized Magnesium oxide nanoparticles

(ii) Infiltration of a colloidal crystal assembly of soft sphere with a suitable precursor salt and subsequent heat treatment

6.2.1 Membrane fabrication using stabilized magnesium oxide nanoparticles

In this approach, the membrane fabricated was attempted by directly assembling magnesium oxide nanoparticles into a suitable porous membrane, with the aid of soft spheres which would generate the necessary void spaces on being heat treated. This approach, however, has the inherent limitation that MgO nanoparticles readily undergoes hydration reaction to generate Magnesium hydroxide - $Mg(OH)_2$ in an aqueous, alcohol based or alkaline (NaOH, KOH) medium. On being heat treated at high temperatures,

$Mg(OH)_2$ undergoes decomposition to yield MgO, the resulting variation in density during processing unsuited for thermal battery applications.

The fabrication approach initially investigated techniques whereby stabilized MgO suspension could be synthesized, which could then be used to develop membrane structures. This was achieved by dispersing commercially purchased MgO nanoparticles in an aqueous solution with lignin sulfonate salt added to it[8]. The stabilizing action of lignin sulfonate could be attributed to the behavior of these salts to act as polyelectrolytes (polymers with an electrolyte group in the repeating units). When dissolved in an aqueous solution, the electrolyte groups undergo dissociation to generate negatively charged species, which gets adsorbed on the positively charged magnesia surface. This acts as a protective coating for the particles, whereby hydration of MgO to $Mg(OH)_2$ could be significantly suppressed[9,10]. The suspension thus prepared was then thoroughly dispersed, allowed to settle and supernatant liquid siphoned off. SEM studies were performed to verify that the supernatant liquid comprises of MgO nanoparticles, while the sediment contained predominantly $Mg(OH)_2$.

Figure 6.2 and shows the structure of membranes generated using stabilized MgO nanoparticles. In Figure 6.2a, a binary suspension of ~20 nm MgO nanoparticles and 0.93 μm Polystyrene particles was co-deposited on a suitable substrate. Contrary to the uniform structures reported elsewhere with binary suspension[11], the structure obtained in this case was predominantly disordered owing to the opposite surface charge of particles in the binary suspension. Being positively charged in an aqueous suspension, MgO particles exhibited a tendency to attach itself to the surface of the negatively charged polystyrene microspheres, thereby resulting in a disordered film structure. Heat treatment at 500 ^oC for

3 hours was utilized to burn off PS particles, leaving behind the porous membrane structure as could be seen in Figure 6.2.

An alternate procedure investigated involved the infiltration of MgO nanoparticles into a 3-D colloidal crystal assembly of PS particles, with the prospect that the thermal treatment of PS particles would yield an ordered MgO inverse structure. This approach was however limited by the adhesion of MgO particles to PS surface, which hindered the infiltration of the MgO nanoparticles to completely fill the pore volume of the colloidal crystal structure.

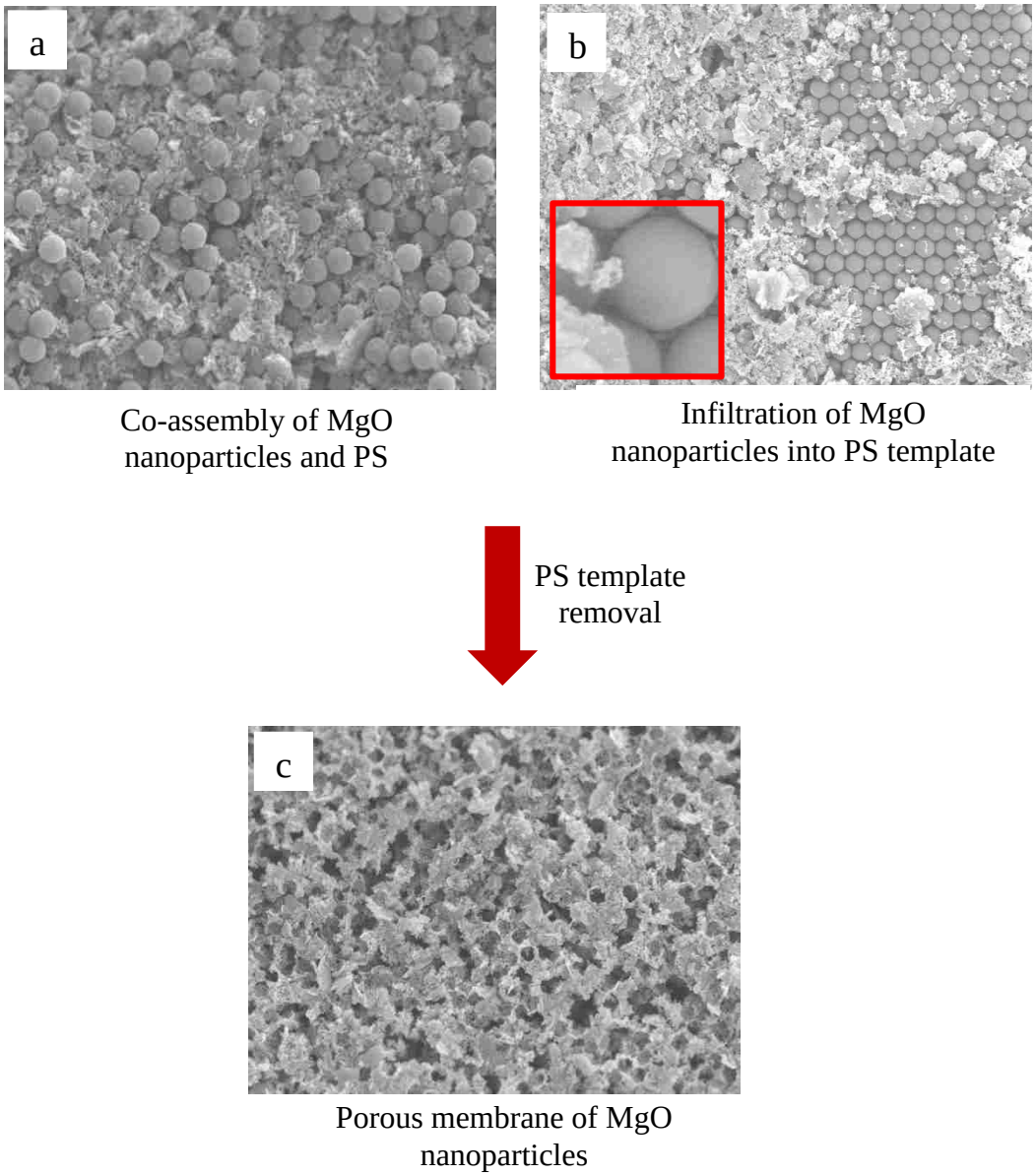

Figure 6.2: Membrane fabrication using MgO nanoparticles (a) Co-assembled structure obtained from binary suspension of PS microspheres and MgO nanoparticles (b) Infiltration of MgO nanoparticles into PS template (c) Structures (a,b) after heat treatment at 500 C for 3 hours

6.2.2 Fabrication of MgO membrane using precursor salt

In this approach, a uniform and three dimensionally periodic colloidal crystal structure was fabricated using vibration assisted convective deposition techniques. The assembled structure was then infiltrated with a suitable magnesium oxide precursor salt, with subsequent heat treatment of the infiltrated structure to obtain the inverse opal membrane.

The prerequisite for this approach is a uniformly ordered colloidal crystal structure comprised of soft spheres, with polystyrene microspheres being chosen due to its monodispersity and ease of availability. The particles in the suspension were assembled into a colloidal crystal structure with long ranged crystallinity using vibration assisted convective deposition techniques. The film was then dried and partially melted at 70 C to enhance the adhesion of the film to the substrate and improve the mechanical strength. The colloidal crystal film was then infiltrated with the precursor salt, Magnesium nitrate hexahydrate $Mg(NO_3)_2.6H_2O$ dissolved in ethanol, with the infiltration performed under vacuum conditions for almost 2 hours. The film was then taken out of the solution, excess liquid drained off and top surface of the film wiped with Kimwipes (Kimberly-Clark). This enables a removal of excess liquid which might be retained on the colloidal crystal, the retention of which may lead to an excess non-porous layer of magnesium oxide over the final structure.

This procedure however had the limitation associated with the melting temperature of PS particles and softening temperature of Magnesium nitrate salt before it underwent decomposition to MgO. The melting temperature of PS is ~ 240 ^oC, while the infiltrated magnesium nitrate salt has a melting temperature of 89 ^oC. This resulted in a disordered structure for the final inverse opal film. This limitation was partially resolved by adding

citric acid to magnesium nitrate solution[12], which enabled a suppression of the melting process. The colloidal structure infiltrated with an ethanol –based solution of magnesium nitrate and citric acid was then heat treated at 500 C for 3 hours. This results in a decomposition of Magnesium nitrate to magnesium oxide, in addition to the removal of PS particles yielding the inverse opal structure.

The MgO structure obtained in the above outlined procedure is shown in Figure 6.3. It could be observed that the procedure yielded a MgO porous membrane structure, with its porosity and tortuosity regulated by the characteristics of the original colloidal structure. This could be observed in the inverse structures with both hexagonal as well as square morphology.

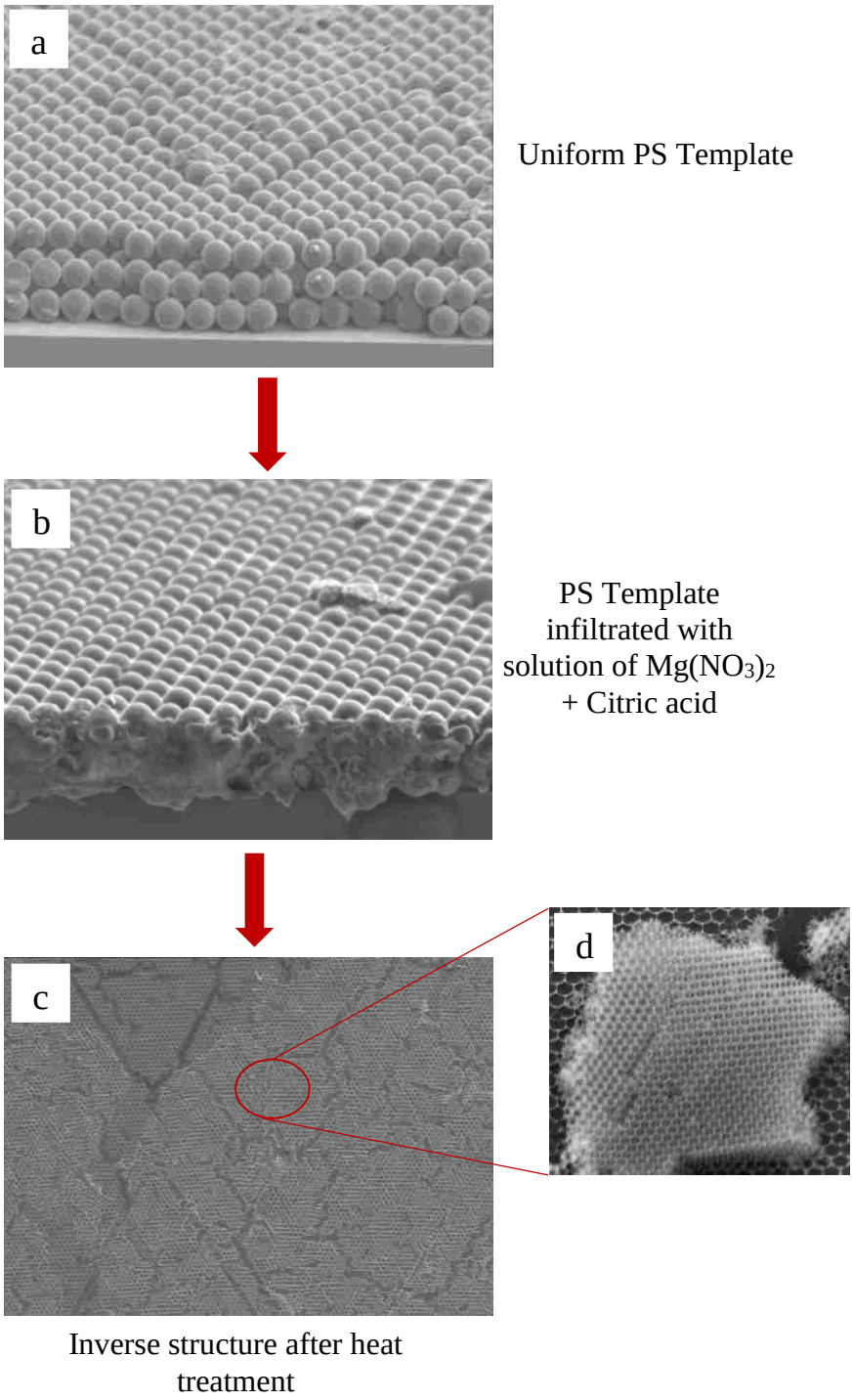

Figure 6.3: Membrane fabrication using MgO precursor salt(a) Uniform PS template obtained by vibration-assisted convective deposition of PS microspheres (b) PS template after vacuum infiltration of precursor salt (c) ,(d) Inverse structure of MgO after heat treatment at 500 C for 3 hours

6.3 Conclusion

The chapter presents a convective deposition based approach for the fabrication of membrane separators for thermal batteries. Although the procedure yielded a highly porous membrane structure, the suitability of the technique for commercial applications is limited by the extensive cracking observed in the structures during heat treatment. This could be attributed to the shrinkage of the polystyrene particles when subjected to heat, thereby resulting in cracks. Suitable methodologies need to be developed to minimize cracks, which might include precursor modification which would enable a solidification of the infiltrated salt at a temperature lower than the melting temperature of polystyrene. Another possible route would be to use hard spheres (like silica) for the colloidal crystal template, which could be etched away to generate the inverse structure. This however needs to be performed in a way such that the MgO particles in the membrane does not undergo hydration into magnesium hydroxide.

6.4 References

1. Butler, P., Wagner, C., Guidotti, R. & Francis, I. Long-life, multi-tap thermal battery development. *J. Power Sources* **136,** 240–245 (2004).

2. Guidotti, R. A. & Masset, P. Thermally activated (‘thermal’) battery technology. Part I: An overview. *J. Power Sources* **161,** 1443–1449 (2006).

3. Masset, P. J. & Guidotti, R. A. Thermal activated (‘thermal’) battery technology. Part IIIb. Sulfur and oxide-based cathode materials. *J. Power Sources* **178,** 456–466 (2008).

4. Masset, P. J. & Guidotti, R. A. Thermal activated (‘thermal’) battery technology. Part IIIa: FeS2 cathode material. *J. Power Sources* **177,** 595–609 (2008).

5. Au, M. Nanostructured thermal batteries with high power density. *J. Power Sources* **115,** 360–366 (2003).

6. Guidotti, R. A. & Masset, P. J. Thermally activated (‘thermal’) battery technology. Part IV. Anode materials. *J. Power Sources* **183,** 388–398 (2008).

7. Masset, P. & Guidotti, R. A. Thermal activated (thermal) battery technology. Part II. Molten salt electrolytes. *J. Power Sources* **164,** 397–414 (2007).

8. Hollis, J. W. & M., L. L. Stable Lignosulfonate emulsions. (1987).

9. Amaral, L. F., Oliveira, I. R., Bonadia, P., Salomao, R. & Pandolfelli, V. C. Chelants to inhibit magnesia (MgO) hydration. *Ceram. Int.* **37,** 1537–1542 (2011).

10. Amaral, L. F., Oliveira, I. R., Salomao, R., Frollini, E. & Pandolfelli, V. C. Temperature and common-ion effect on magnesium oxide (MgO) hydration. *Ceram. Int.* **36,** 1047–1054 (2010).

11. Kumnorkaew, P., Weldon, A. L. & Gilchrist, J. F. Matching constituent fluxes for convective deposition of binary suspensions. *Langmuir* **26,** 2401–5 (2010).

12. Li, H., Dai, H., He, H. & Au, C. T. Facile Route Using Highly Arrayed PMMA Spheres as Hard Template for the Fabrication of 3D Ordered Nanoporous MgO. *Chinese J. Chem. Phys.* **20,** 697–700 (2007).

7

Summary and Future Outlook

7.1 Summary

The research work has demonstrated vibration-assisted convective deposition procedure to be an effective tool to induce non-thermodynamically favored packing arrangements in self-assembled colloidal crystals. The versatility of this approach has been established by the results discussed in the dissertation for varying systems of colloidal suspensions, substrate conditions as well as growth environments. Through this work, it was demonstrated that the use of vibrations in convective deposition technique results in non-conventional packing assemblies observed at multiple levels of hierarchy- (i) at single particle level which is evident as the square-packing of colloidal particles instead of the commonly observed hexagonal packing configuration and (ii) at multi-particle level in the form of periodic band patterns in the colloidal assembly. The work also attempts a mechanistic understanding of the observed packing assemblies through a combination of theoretical and experimental approaches. The final chapters of the work investigate an incorporation of these techniques to achieve suitable structures which could enable an enhanced performance of the devices for energy applications.

7.2 Future directions

The future work in this field could be focused on further improving the quality of the packing assemblies, which could be explored for various substrates and particle types. The incorporation of colloidal crystal assemblies with square-packing arrangement can also be investigated for other scientific and technological devices like sensors, magneto-crystalline anisotropic[1] applications as well as catalytic supports. These require an optimal choice of the colloidal particles which constitutes the fundamental building blocks of these structures as well as fine-tuned methodologies to fabricate the desired structure. In addition, the enhancement of structural diversity by vibration-assisted processes can also be investigated using binary colloidal systems involving nanoparticle haloing[2] or with particles with functionalized polymer strands[3,4] or DNA molecules. These would enable a degree of structural diversity in self-assembled colloidal crystals which is currently realized only with microfabrication techniques.

The set of experiments designed for further studies of the procedure could also be focused on elucidating a mechanistic understanding of the observed results as well as devising methodologies to further enhance the structural diversity associated with self-assembled colloidal crystals and their incorporation into commercially significant macroscopic devices.

7.2.1 Experimental confirmation of proposed mechanism for FCC (100) formation

The objectives of the future set of experiments which could be designed for further investigation of the observed phenomenon could be to explore the growth conditions which would optimize the overall formation of square packing and other non-hexagonal

packing structures as well as to gain a mechanistic understanding of the underlying phenomenon so as to enable the tailoring of the procedure to commercially fabricate devices with desired properties. The design of experiments towards this objective would focus on analyzing in detail, both the nucleation of clusters as well its growth into large domains.

The microstructure studies pertaining to surfactant-stabilized micron-sized polystyrene suspensions under shearing rates similar to the experimental conditions can either be performed on the original geometry or on a representational one. The experiments on original geometry is highly challenging due to the unconstrained and dynamic shape of the meniscus under vibration. This is further limited by the observation and imaging capabilities of the confocal microscope when the suspension is vibrated at a frequency of 40 Hz and amplitude of 200 μm. Another approach would be to use representational geometry such as a closed channel in which similar magnitudes of shearing rates can be generated, which would enable a comparison of the variation in results for multiple Peclet numbers with a progressing time frame. A trade-off in the designed set of experiments is demanded between the accuracy of the results and extending the results across multiple flow geometries.

The use of external vibration in convective self-assembly procedures yields a long-range arrangement of particles, with negligible variation in thickness. The relative absence of thickness variation in the assembled colloidal crystal can be attributed to the flat meniscus obtained at 40 Hz and 200 μm amplitude, which for very high withdrawal velocities has been demonstrated to yield a homogeneous colloidal crystal formation[5]. The shape of the thin film meniscus,which is characterized by its curvature and contact angle

with the substrate, plays a dominant role in determining the long range ordering and thickness[5] of the assembled colloidal crystals. Previous studies regarding the role of meniscus shape in convective self-assembly process have shown that a moderately curved meniscus yields a colloidal crystal assembly with negligible variations in thickness due to the localization of the perturbations[6]. Furthermore, it plays a significant role in determining the magnitude of convective flux of particles towards a drying front as well as the dynamics of crystallization processes at the drying front. A proper understanding of the structural diversity in a vibration assisted process however, necessitates an analysis of the flow patterns associated with colloidal particles within the meniscus.This could be achieved by experiments involving tracer particles, and tracking of their relative displacement with time using particle image velocimetry (PIV) procedures, performed for both meniscus-elongation and meniscus-compression regimes. The characterization of the meniscus shape and flow streamlines generated during the course of periodic fluctuation of the meniscus enables a description of the shearing forces experienced by individual colloidal particles and colloidal-clusters in the suspension. This would also provide an understanding of the generation of square-packed nucleates as well as the final orientation of particles associated with the square-packed regions of the colloidal crystal assembly.

7.2.2 Influence of meniscus shape and flow streamlines on colloidal crystal-packing

The shape of the thin film meniscus,which is characterized by its curvature and contact angle with the substrate, plays a dominant role in determining the long range ordering and thickness[5] of the assembled colloidal crystals. Previous studies regarding the role of meniscus shape in convective self-assembly process have shown that a moderately

curved meniscus yields a colloidal crystal assembly with negligible variations in thickness due to the localization of the perturbations[6]. Furthermore, it plays a significant role in determining the magnitude of convective flux of particles towards a drying front as well as the dynamics of crystallization processes at the drying front.

The use of external vibration in convective self-assembly procedures yields a long-range arrangement of particles, with negligible variation in thickness. The relative absence of thickness variation in the assembled colloidal crystal can be attributed to the flat meniscus obtained at 40 Hz and 200 μm amplitude, which for very high withdrawal velocities has been demonstrated to yield a homogeneous colloidal crystal formation[5]. A proper understanding of the structural diversity in a vibration assisted process however, necessitates an analysis of the flow patterns associated with colloidal particles within the meniscus. The previous studies on flow streamlines in convective self-assembly procedures have employed tracking of tracer particles in the thin film region[6] as well as numerical simulations in COMSOL[7]. A direct extension of these procedures to the current experimental conditions is limited by the following factors:

(i) The analysis of the meniscus flow-profiles for the usual convective assembly processes is based on a static meniscus which remains relatively unaltered during the course of the experiment. For this geometry, the velocity profiles observed were parallel to the substrate with increasing velocities closer to the drying front. Such an approximation is not possible with the current scenario in which the meniscus has an unconstrained and dynamic shape and alternates between an elongated and a compressed shape during each half-cycle of the external sinusoidal vibration, and is expected to result in a highly altered flow profile.

(ii) The analysis of flow profiles within the meniscus using COMSOL is based on the bulk suspension constrained within the wedge-shaped volume created between the deposition blade and the substrate. However, preliminary results from our parametric studies have shown that the characteristics of the colloidal crystal assembly depends only on the nature of the thin liquid meniscus and not on the bulk suspension characteristics, which was the focus of the studies using simulated flow profiles.

Hence, a reliable understanding of the flow profiles demands a completely revamped set of experiments involving tracer particles, and tracking of their relative displacement with time using particle image velocimetry (PIV) procedures, performed for both meniscus-elongation and meniscus-compression regimes. The characterization of the meniscus shape and flow streamlines generated during the course of periodic fluctuation of the meniscus enables a description of the shearing forces experienced by individual colloidal particles and colloidal-clusters in the suspension. This would also provide an understanding of the generation of square-packed nucleates as well as the final orientation of particles associated with the square-packed regions of the colloidal crystal assembly.

7.2.3 Analysis of band patterns

Future work in this field could be focused on attaining a better insight into the mechanism as well as to explore the feasibility of these structures for commercial applications. Possible avenues of interest with regards to mechanistic understanding would involve quantifying the stress fields acting on the crystal during the deposition process, an analysis of which could provide a valuable tool in controlling the generation of these structures. Moreover, this would also enable one to explore whether further variations in

defect patterns could be possibly obtained by a similar approach. Such a characterization and analysis of stress fields would involve an in-depth study of the Darcy flow patterns through the void structures of the crystal and relative variations in pressure drop for different packing configurations. A simulation based analysis of various scenarios would definitely aid in accomplishing this objective.

The current industrial focus on microelectronic devices would also provide an impetus towards analyzing the performance of these structures as potential photonic waveguides. This could be achieved by selective infiltration of the bulk matrix with a high refractive index salt and subsequent etching away to yield air-core defects in place of the original planar defect patterns. A systematic study based on finite difference time domain (FDTD) calculations could be helpful in analyzing the capabilities of such a fabrication technique towards achieving the intended results.

7.3 References

1. Snezhko, A. & Aranson, I. S. Magnetic manipulation of self-assembled colloidal asters. *Nat. Mater.***10,** 698–703 (2011).

2. Tohver, V., Smay, J. E., Braem, a, Braun, P. V & Lewis, J. a. Nanoparticle halos: a new colloid stabilization mechanism. *Proc. Natl. Acad. Sci. U. S. A.***98,** 8950–4 (2001).

3. Lin, Y. *et al.* Self-directed self-assembly of nanoparticle/copolymer mixtures. *Nature***434,** 55–59 (2005).

4. Jenekhe, S. A. & Chen, X. L. Self-Assembly of Ordered Microporous Materials from Rod-Coil Block Copolymers. *Science (80-.).***283,** 372–375 (1999).

5. Born, P., Blum, S., Munoz, A. & Kraus, T. Role of the meniscus shape in large-area convective particle assembly. *Langmuir***27,** 8621–8633 (2011).

6. Born, P., Munoz, A., Cavelius, C. & Kraus, T. Crystallization mechanisms in convective particle assembly. *Langmuir***28,** 8300–8308 (2012).

7. Xiao, J. & Attinger, D. Simulations of Meniscus Motion and Evaporation for Convective Deposition Manufacturing. *Excerpt from Proc. COMSOL Conf. 2010 Bost. Simulations* (2010). at <http://www.uk.comsol.com/papers/9101/download/xiao_paper.pdf>

Appendix

Calibration of Signal Generator

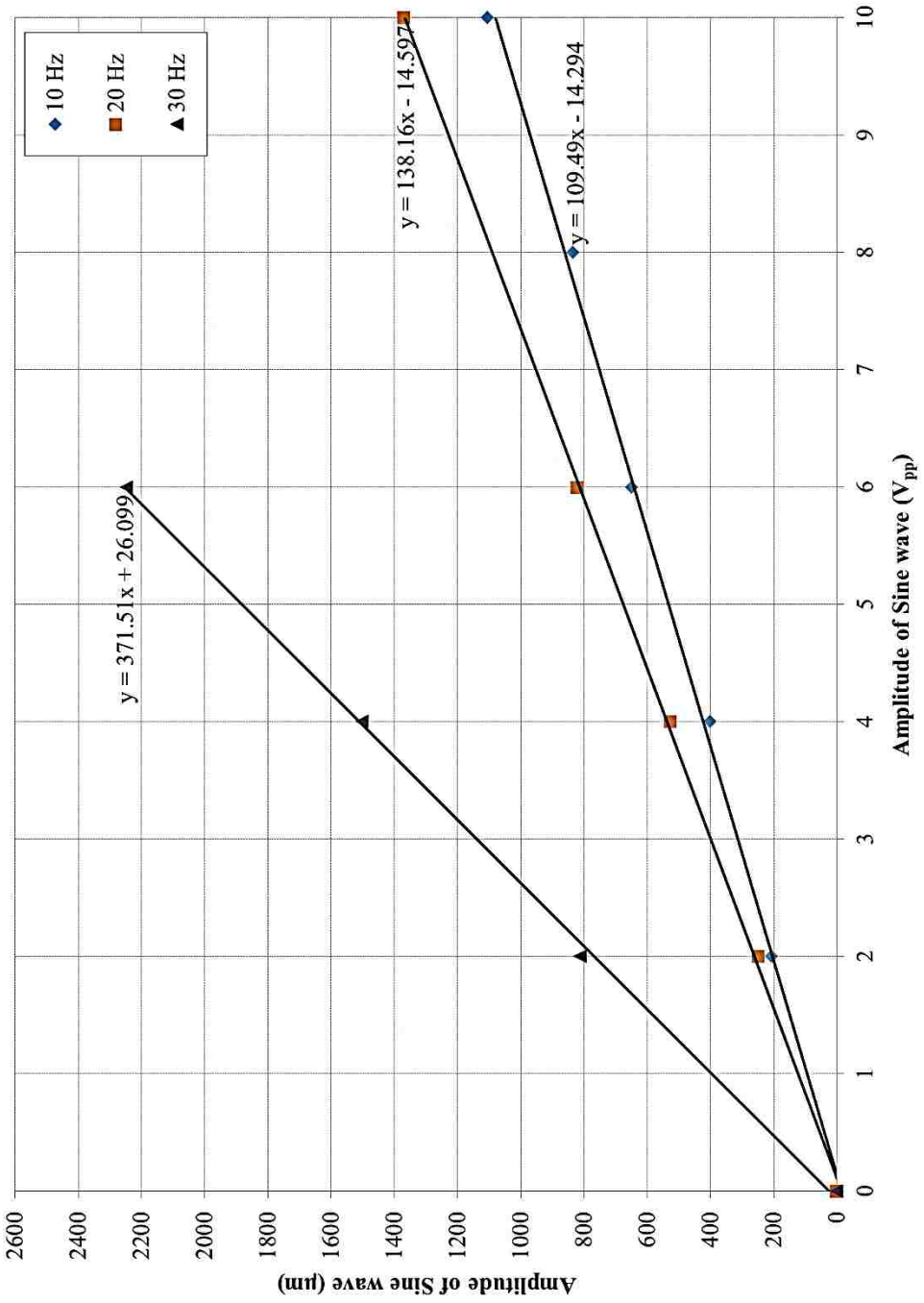

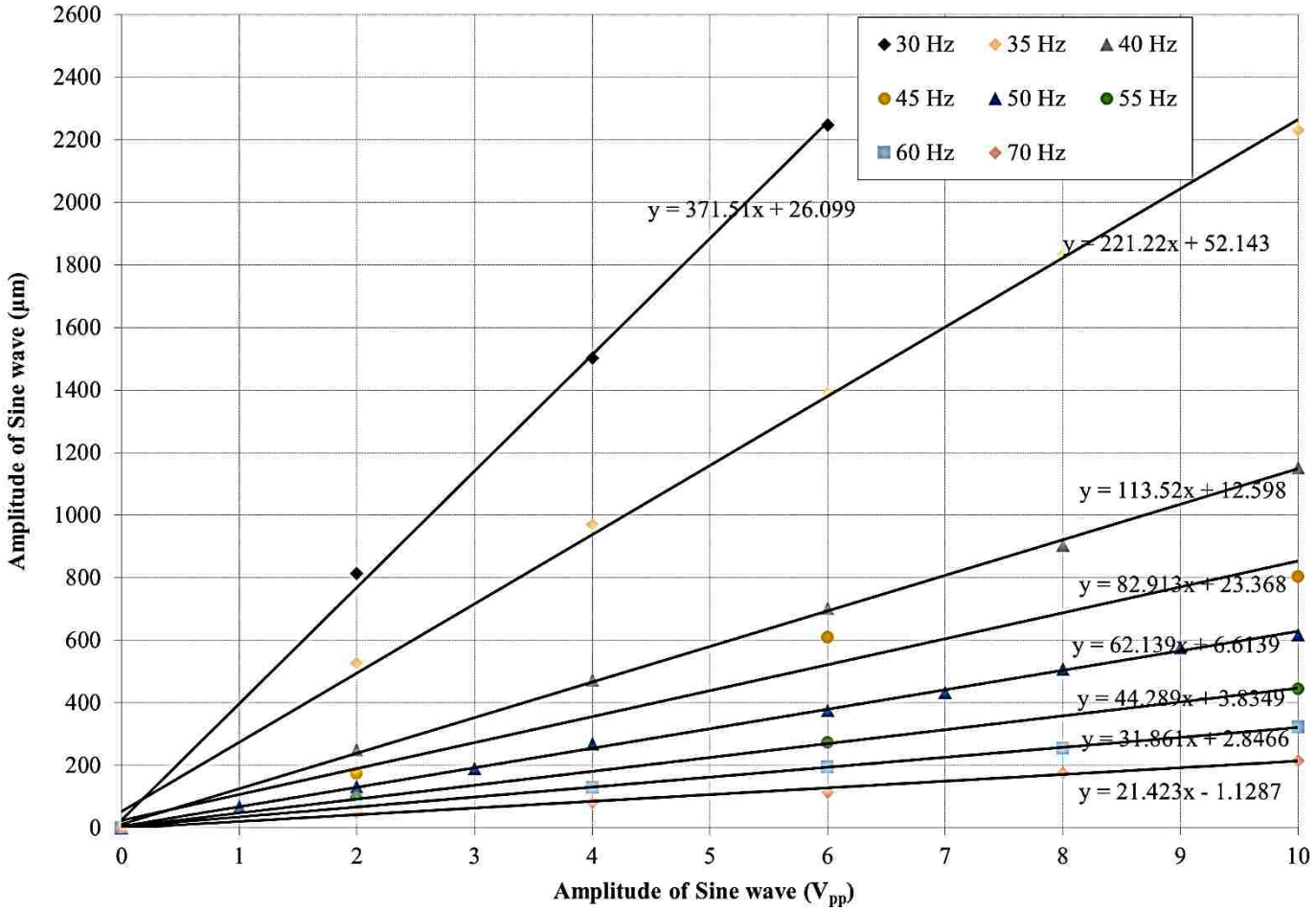
30 Hz
35 Hz
40 Hz
45 Hz
50 Hz
55 Hz
60 Hz
70 Hz
y = 371.51x + 26.099
y = 221.22x + 52.143
y = 113.52x + 12.598
y = 82.913x + 23.368
y = 62.139x + 6.6139
y = 44.289x + 3.8349
y = 31.861x + 2.8466
y = 21.423x - 1.1287
Amplitude of Sine wave (µm)
Amplitude of Sine wave (Vpp)
0
200
400
600
800
1000
1200
1400
1600
1800
2000
2200
2400
2600
0
1
2
3
4
5
6
7
8
9
10

[redacted]

Vitae

EDUCATION

Ph.D. Chemical Engineering *2011-2016*
Department of Chemical and Biomolecular Engineering, Lehigh University
Advisors: Professor James F. Gilchrist and Professor Mark A. Snyder
Dissertation: Flow-templated fabrication of colloidal crystals

M.Tech. Chemical Engineering *2008-2010*
Department of Chemical Engineering, IIT Madras, India
Advisor: Professor Niket Kaisare

B.Tech. Chemical Engineering *2004-2008*
Department of Chemical Engineering, Government Engineering College, Thrissur, India

RESEARCH AND WORK EXPERIENCE

Doctoral Research, Lehigh University *September 2011-July 2016*

• *Investigation of techniques to generate atypical self-assembled structures*

This focuses on scalable strategies for realizing periodically structured films through controlled assembly of micrometer sized building blocks. The technique adopted involved incorporation of periodic lateral vibrations to convective assembly technique, with the twin benefits of yielding an enhanced quality of films as well as generation of square-packing configuration within the crystal. It was also demonstrated how periodicity could be controlled across higher length scales through generation of uniform periodic crystalline defects in assembled crystal through stress relaxation.

• *Enhancement of light extraction efficiency in dye-sensitized solar cells (DSSCs)*

The project involved development of techniques which could enhance light capturing efficiency of DSSCs. The effect of microlens structure for achieving an enhanced photon path length within the device was investigated, resulting in 25 % efficiency improvement of the device. Studies were also performed to identify suitable scale up strategies for commercial applications.

• *Design of membranes for thermal batteries*

This involved the development of an optimal architecture for the separators in thermal batteries. The research investigated a sacrificial templating approach to fabricate structured MgO films, with the obtained structure characterized by high pore volume and ordered periodicity.

• *Design of simulation algorithms for systematic analysis of various systems*

The work involved the design and formulation of software routines which could enable an accurate, comprehensive and faster analysis of various systems. The range of systems investigated includes particles coatings on substrates, suspension microstructure under shear as well as thermophoretic processes.

Development Engineer, Flowmaster Inc., India *June 2010-July2011*

My work involved the development, analysis and enhancement of various simulation routines for Flowmaster V7 software, a thermo-fluid simulation software for steady state and transient analysis. This enables an easy conceptualization and optimization of fluid system designs for industrial research.

• *Heat transfer modeling in automobile cooling systems*

The work involved spearheading the development of routines for modeling heat transfer in the system in the absence of flow. In such a scenario, the fluid conduction and natural convection currents arising due to density differences becomes the dominant driving force for heat transfer. The energy balance equations were formulated, which were implemented for various components of the cooling system.The component development was performed in C# language in a Visual Studio-2010 environment.

Master's Research, IIT-Madras, India *Aug. 2009-June2010*

• *Control of distributed parameter systems using Approximate Dynamic Programming*

Distributed Parameter Systems (DPS) are characterized by the variation of the state variables in spatial as well as time domains. The research work involved the implementation of the ADP based control strategy for such systems. The results obtained for ADP policy underlined an improved performance of the same over conventional Proportional-Integral-Derivative (PID) and model predictive control (MPC) approaches. The work also explored the versatility of the model-free ADP methods, specifically the Q-learning approach.

• *Implementation of Value Iteration & Policy Iteration schemes to obtain optimal policy*

The concepts of Machine learning / Reinforcement Learning were utilized to obtain an optimal control policy for the scenarios under consideration. The convergence characteristics were studied for different parameter settings. In addition, learning control algorithms like Q-learning and SARSA were also implemented for training an agent to reach its destination by traversing through a puddle world.

• *Estimation of empirical models using system identification techniques*

This involved the use of non-parametric and parametric modeling (ARX,ARMAX,OE etc) concepts to describe the input-output relationship of a given system. The quality of the models were analyzed based on their predictive ability and variance of the parameter estimates**.**

PUBLICATIONS (REFEREED JOURNAL ARTICLES)

[1] **M. Joy**, T. Muangnapoh, M.A. Snyder, and J. F. Gilchrist, "Template-free fabrication of partially aligned (100) fcc thin film colloidal crystals", *Soft Matter,* 2015,11:7092-7100

[2] J. Boettcher, **M. Joy**, K. Joshi, T. Muangnapoh and J.F. Gilchrist, “Spacing of seeded and spontaneous streaks during convective deposition”, Accepted in *Langmuir*

[3] P. Kumnorkaew, **M. Joy**, M. A. Snyder, and J. F. Gilchrist, “Dye sensitized solar cell enhancement incorporating convectively assembled internal microlens arrays”, In preparation

[4] **M. Joy**, M. A. Snyder, and J. F. Gilchrist, “Periodic defects in thin film colloidal crystals fabricated from convective assembly”, In preparation

[5] **M. Joy** and N. S. Kaisare, "Approximate dynamic programming based control of distributed parameter systems," *Asia Pacific Journal of Chemical Engineering*.,2011, 6: 452-459

CONFERENCE PRESENTATIONS

[1] **M. Joy** (speaker), T. Muangnapoh, M. A. Snyder and J. F. Gilchrist, “Flow-Templated Fabrication of FCC (100) Colloidal Crystal Structures”,89th ACS Colloid & Surface Science Symposium, June 2015, Pittsburg

[2] **M. Joy**, T. Muangnapoh, M. A. Snyder and J. F. Gilchrist (speaker), “Non-Templated fabrication of partially aligned FCC thin film colloidal crystals, AIChE Annual Meeting, November 2014, Atlanta

[3] **M. Joy** (speaker), T. Muangnapoh, M.A. Snyder and J. F. Gilchrist, “Deposition of non-templated FCC (100) colloidal crystals”, Society of Rheology 86th Annual Meeting, October 2014, Philadelphia

[4] P. Kumnorkaew, **M. Joy**, J.F. Gilchrist and M.A. Snyder (speaker), “Multiscale anode assemblies for improving efficiency and versatility of dye-sensitized solar cells”, AIChE Annual Meeting, Oct. 2012, Pittsburg

[5] **M. Joy** and N. S. Kaisare (speaker) , “Approximate dynamic programming based control of distributed parameter systems,” PSE-Asia 2010: 5th International Conference on Design, Operation and Control of Chemical Processes, July 2010, Singapore